Opposite Sign Dimuon Production in High Energy Neutrino-Nucleon Interactions.

by

Boris Strongin

Submitted in Partial Fulfillment of the

Requirements for the Degree of Doctor of

Philosophy

at the

Massachusetts Institute of Technology

May, 1989

Signature of Author Boris Strongin

Department of Physics

May 5, 1989

Certified by Frank E. Taylor

Frank E. Taylor

Thesis supervisor

Accepted by .....

George F. Koster

Chairman, Department Committee on Theses

Opposite Sign Dimuon Production in High Energy Neutrino-Nucleon Interactions

by

Boris Strongin

Submitted to the Department of Physics on May 5, 1989 in partial fulfillment of the requirements for the Degree of Doctor of Philosophy

Abstract

The results of a study of opposite sign dimuons produced in the Lab C detector exposed to the Fermilab quadruplet neutrino beam are presented. The amount of the strange sea in the nucleon, the semileptonic branching ratio of the D meson, the elements U_{cd} and U_{cs} of the Kobayashi-Maskawa matrix, and the mass of the charm quark are measured. Various kinematic properties of the standard charm model of opposite sign dimuons are compared with data. The amount of strange sea relative to the up and the down sea is found to be $\kappa = 0.56 \pm 0.06 \pm 0.07$. The semileptonic branching ratio is $B = 0.084 \pm 0.03 \pm 0.014$. The matrix elements U_{cd} and U_{cs} are found to be $U_{cd} = 0.225 \pm 0.038 \pm 0.019$ and $U_{cs} = 0.973 \pm 0.061\ ^{+0.036}_{-0.019}$. The mass of the charm quark is found to be consistent with $M_c = 1.5$ GeV/c^2. No discrepancy between the data and the standard charm model of opposite sign dimuons is found.

Thesis supervisor: Dr. Frank E. Taylor

Title: Senior Research Scientist

To my mother

ACKNOWLEDGMENTS.

No experiment in high energy physics can be done by one man alone, and this one is no exception. I am deeply indebted to a great many people for their guidance, encouragement and support during my years in graduate school.

First and foremost I wish to thank my adviser Frank Taylor. He taught me a lot about what it really means to be an experimental physicist, about attention to detail and the importance of "back of an envelope" calculations. His unwavering enthusiasm for physics has been a great inspiration for me.

Stu Fuess, our software czar, created much of the E-733 software framework and showed all of us how to do it right. He contributed substantially to this analysis, but even more importantly, he has always been there for me when I needed to discuss a tricky point or to go over a particularly complicated piece of software.

Randy Pitt made a great contribution to the drift electronics effort. Linda Stutte created our on-line computer system and to a large extent designed the neutrino beam line. Mike Tartaglia and Uwe Schneelkloth analyzed the test data.

The Michigan State contingent has always worked tirelessly at whatever had to be done. To the " hunchbacks of MSU", my fellow graduate students George Perkins, Robert Hatcher, and Bill Cobau, with whom we shared countless hours of night shifts and working on (or under) the detector, I wish a speedy completion of their analyses. Ray Brock deserves my special thanks for keeping me on my toes by being ever so skeptical about my results.

After all these years I want to say that I am very grateful to David Frisch for bringing me to M.I.T.

Last but not least, I owe a debt of gratitude to all my friends in Chicago who made my years at Fermilab a much more pleasurable experience.

Table of contents.

List of figures.

Table of tables.

CHAPTER I.
THEORY.

1.1 Introduction.

Since their first observation in neutrino reactions in 1974 [1.1], opposite sign dimuons have been extensively investigated. The present data are consistent with their origins being the production and decay of the charmed quark[1.2]. One of the most interesting aspects of opposite sign dimuons is that they provide a window into the "sea" of non-valence quarks inside the nucleon. In particular, they allow the determination of relative strengths of the strange versus the up and the down sea components. According to the present understanding of the quark model, the strange quark can only be present inside the nucleon as a virtual particle, and therefore the strength of its presence depends on the resolution (i.e. momentum) of the probe with which one tries to detect it. That fact makes it particularly interesting to repeat the experiment whenever higher energies become available. The experiment reported in this thesis used the highest energy neutrino beam available in the world provided by the Fermilab Tevatron.

1.2 Deep Inelastic Neutrino-Nucleon Scattering.

According to the minimal quark-parton model, hadrons are composed of point-like spin 1/2 constituents - quarks. The proton contains two up quarks of charge +2/3 and one down quark of charge -1/3; the neutron contains two down quarks and one up quark. The u and d quarks are called valence quarks; they are always present in the nucleon. However, all the other quarks are also present in the nucleon in the form of virtual particles - the so called sea. Thus deep inelastic lepton-nucleon scattering is actually elastic scattering of leptons on the constituent quarks of the nucleon.

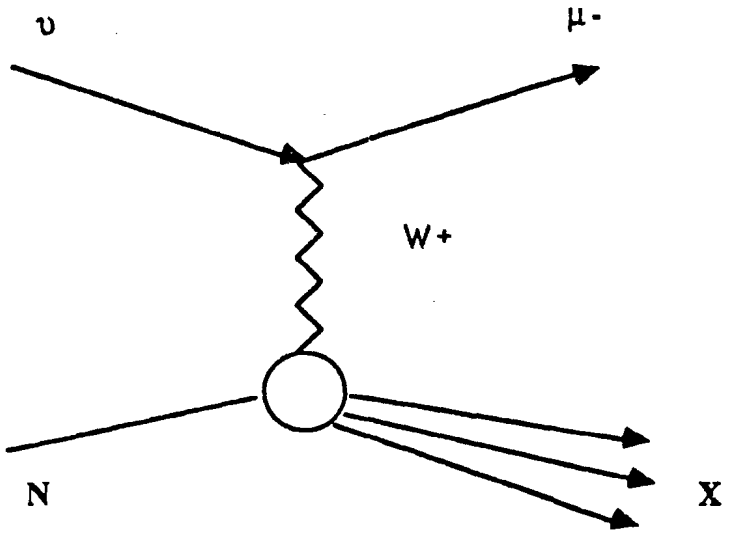

Fig.1.1 Neutrino-nucleon scattering. An incoming muon neutrino scatters off the nucleon N by exchanging the W+ boson. In the final state there are the outgoing muon and the recoil fragments X.

Referring to Fig.1.1 let us define the relevant kinematic variables.

$$s = (P_N + P_\upsilon)^2 = M^2 + 2ME_\upsilon \quad 1.1$$

$$Q^2 = -(P_\upsilon - P_\mu)^2 = 2\,E_\upsilon E_\mu\,(1 - \cos\theta_\mu) \quad 1.2$$

$$\upsilon = E_\upsilon - E_\mu \quad 1.3$$

$$x = Q^2/2M\upsilon \quad 1.4$$

$$y = \upsilon/E_\upsilon \quad 1.5$$

$$W^2 = (P_N - Q)^2 = M^2 + 2M\upsilon - Q^2 \quad 1.6$$

where P_N is the nucleon 4-momentum, P_υ is the neutrino 4-momentum, θ_μ is the angle of the muon relative to the neutrino and M is the nucleon mass. W is the invariant mass of the hadronic system.

A well known feature of weak interactions is parity nonconservation, which is a manifestation of the V-A nature of weak currents. One consequence of that V-A structure is that neutrinos have well defined helicity or spin orientation relative to their direction of motion. Neutrinos are left handed, i.e. their spins are always antiparallel to their direction of motion, and anti-neutrinos are right handed. Consider neutrino scattering off quarks in the center of mass system. For scattering of left handed neutrinos on left handed d quarks, the total angular momentum is zero and the cross section is isotropic. Thus:

$$\frac{d\sigma}{d(\cos\theta^*)} = \frac{G^2 s}{2\pi} , \qquad 1.7$$

where $G = 1.166 \times 10^{-5}$ Gev^{-2} is the Fermi constant, s is defined by Eq.1.1 and θ^* is the angle between the muon and the incident neutrino in the neutrino-nucleon center of mass system.

For particles of opposite helicity, u and υ for example, the total angular momentum is 1 and the cross section of Eq.1.7 is multiplied by the square of angular momentum-one amplitude:

$$\frac{d\sigma}{d(\cos\theta^*)} = \frac{G^2 s}{2\pi} \left(\frac{1 + \cos\theta^*}{2}\right)^2 \qquad 1.8$$

It can be shown that at high energies the center of mass scattering angle θ^* is related to the variable y defined by Eq. 1.5 by the equation $1 - y = (1 + \cos\theta^*)/2$. Therefore Eq.1.8 becomes:

$$\frac{d\sigma}{dy} = \frac{G^2 s}{\pi}(1 - y)^2 \qquad 1.9$$

In the context of the neutrino-nucleon scattering each quark inside the nucleon can be thought of as carrying a fraction x of the total nucleon's momentum P. The probability distribution $f(x)$ of encountering a given type of quark with momentum xP inside the nucleon is not readily calculated in the quark parton model. It depends on the quark's flavor, and , apart from the most minimal versions of the quark -parton model, on Q^2. But f(x) is thought to be independent of the scattering lepton. With this in mind one can modify Eq.1.7 to obtain the cross section for neutrinos scattering off d quarks inside the nucleon:

$$\frac{d\sigma}{dxdy} = \frac{G^2 s}{2\pi} x f(x) \qquad 1.10$$

Let us now show that for massless quarks the momentum fraction x is the same x as defined in Eq. 1.4. The 4-momentum of the massless outgoing quark is -Q + xP. Therefore we have:

$$(-Q + xP)^2 = 0. \qquad 1.11$$

Neglecting the nucleon mass at high energies we have (Eq.1.4) $Q^2 - 2xM\upsilon = 0$, where υ is defined by Eq.1.3. In the case of massive outgoing quark Eq.1.11 becomes $(-Q + xP)^2 = m_q^2$, and the momentum fraction variable x must be modified to become ξ:

$$\xi = \frac{Q^2 + m_q^2}{2M\upsilon} = x + \frac{m_q^2}{2M\upsilon}, \qquad 1.12$$

where we have neglected the small x^2M^2 term. This transformation x --> ξ is known as **slow rescaling**[1.3,1.4] , and ξ is used instead of x to describe the processes involving heavy quark production off light quarks. Of course as with x, ξ is required to satisfy $0 \leq \xi \leq 1$.

1.3 Charged Current Cross Sections.

In its most general form the cross section for neutrino-nucleon scattering can be written in terms of three structure functions F_1, F_2 and F_3 [1.5,1.8], where F_1 and F_2 are analogous to the two form-factors used to describe electromagnetic lepton-nucleon scattering, and F_3 represents the parity violating terms:

$$\frac{d^2\sigma^{\nu(\bar{\nu})}}{dxdy} = \frac{G^2ME}{\pi}\left[\frac{y^2}{2}2xF_1(x,Q^2) + \left(1 - y - \frac{Mxy}{2E}\right)F_2(x,Q^2) \pm (y - y^2/2)\,xF_3(x,Q^2)\right], \qquad 1.13$$

where E is the incoming neutrino energy and M is the nucleon mass.

Let us consider a simple model with four quarks (u,d,c,s). Define the net quark and antiquark distributions, assuming x and Q^2 dependence:

$$q = u + d + s + c \qquad 1.14$$

$$\bar{q} = \bar{u} + \bar{d} + \bar{s} + \bar{c} \qquad 1.15$$

The structure functions F_1,F_2, and F_3 of Eq.1.13 can now be written in terms of the quark distributions of Eq.1.14. For an isoscalar target the structure functions are:

$$F_1 = q + \bar{q} \qquad 1.15$$

$$F_3 = q - \bar{q} \qquad 1.16$$

The Callan - Gross relation gives

$$2xF_1 = F_2 \qquad 1.17$$

The structure functions of Eq.1.15 - 1.17 together with the distributions of Eq.1.13 - 1.14 completely define the neutrino and antineutrino cross sections of Eq.1.13.

1.3 Opposite sign dimuons.

The standard model of opposite sign dimuon production is represented schematically in Fig.1.2. The process involves the production of the charm quark, its hadronization into a charmed particle, most frequently D meson, and its subsequent semileptonic decay.

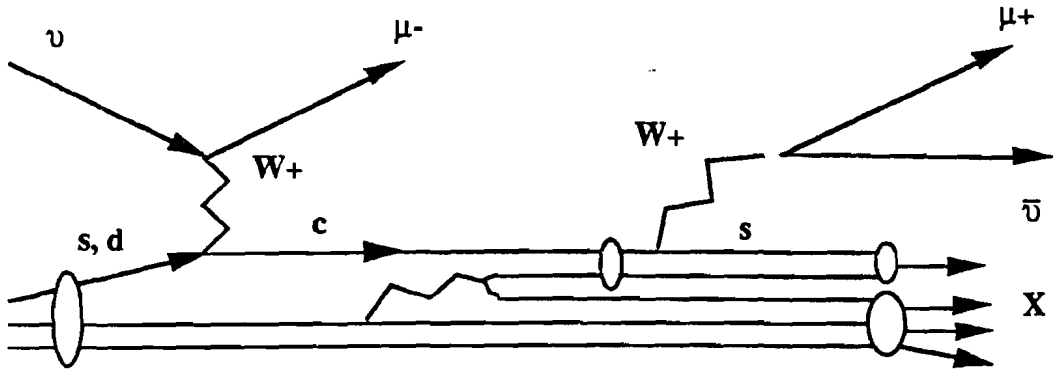

Fig. 1.2 Schematic representation of opposite sign dimuons production by neutrinos

Best estimates of the mass of the c quark are derived from the mass of the lowest bound state of the cc system (J/Ψ particle). These measurements give m_c = 1.5 Gev, thus making it much more massive than either the s or d quarks. Due to the high m_c value, slow

rescaling (Eq. 1.12) becomes a prominent feature of opposite sign dimuon production. In addition to the use of the scaling variable $\xi = x + m_c^2/(2M\upsilon)$, the dimuon production cross section must also include a phase space factor for producing a heavy quark in two-body scattering: $P_{phase} = 1 - m_c^2/2ME_\upsilon\xi$ [1.6]. Let us now write the cross sections for opposite sign dimuon production by neutrinos (Eq. 1.18), and anti-neutrinos (Eq. 1.19) on an isoscalar target as follows:

$$\frac{d^3\sigma^{\upsilon}}{dxdydz} = \frac{G^2ME_\upsilon\xi}{2\pi}\{[u(\xi) + d(\xi)]\,U_{cd}^2 + 2s(\xi)U_{cs}^2\} \times \left(1 - \frac{m_c^2}{2ME_\upsilon\xi}\right) D(z)\,B \qquad 1.18$$

$$\frac{d^3\sigma^{\bar{\upsilon}}}{dxdydz} = \frac{G^2ME_\upsilon\xi}{2\pi}\{[\bar{u}(\xi) + \bar{d}(\xi)]\,U_{cd}^2 + 2\bar{s}(\xi)\,U_{cs}^2\} \times \left(1 - \frac{m_c^2}{2ME_\upsilon\xi}\right) D(z)\,B \qquad 1.19$$

Opposite sign dimuon production by neutrinos occurs on s or d (or u for an isoscalar target) quarks. The distributions u(x) and d(x) in Eq.1.18 represent a sum of both *valence and sea* contributions of up and down quarks; the second term s(x) is purely sea since the nucleon doesn't contain any intrinsic strangeness. In contrast to the neutrino case, the quark distributions in the antineutrino cross section of Eq.1.19 are all sea. U_{cd} and U_{cs} are elements of the Kobayashi-Maskawa matrix that describes the mixing of 6 quarks of different flavors in terms of 15 real mixing angles and 10 complex phases[1.7]. The world average for these constants is $U_{cd} = 0.225$ and $U_{cs} = 0.975$. Therefore quark mixing favors dimuon production off the strange quarks and suppresses the down quark term. In spite of this suppression, however, about the same number of neutrino-induced dimuons are produced off the down quarks as off the strange quarks due to a much larger amount of the

down quarks in the nucleon relative to the strange quarks. For the same reason most of antineutrino production of dimuons is expected to be off the strange sea, since, based on the results of previous experiments $s(x) = \frac{1}{2}\bar{d}(x)$, and $U_{cs}^2 >> U_{cd}^2$.

The function D(z) is the so-called fragmentation function which describes the process of hadronization where a free c quark forms a charm meson. The variable z is the fraction of the charm particle momentum relative to the maximum possible momentum in the W-boson - nucleon center of mass system: $z = p_X / (W^2/4 - M_X^2)^{1/2}$, where M_X and p_X are the charm meson's mass and momentum respectively and W^2 is the invariant mass squared of the hadronic system. D(z) is normalized to unity: $\int_0^1 D(z)dz = 1$. We defer further discussion of the fragmentation function until Chapter IV. And finally, B is the branching ratio for the semileptonic decay of charm mesons into muons $X \rightarrow \mu$ + anything. It is of the order 10%. In all, the opposite sign dimuon cross section is about 1% that of the single muon charged current events for present accelerator energies.

1.4. Strange Sea Content of the Nucleon.

The primary interest in studying opposite sign dimuons lies in the unique opportunity to determine the strange sea content of the nucleon. This quantity, usually denoted κ, is defined as the amount of the strange sea relative to the amount of the up and down sea:

$$\kappa = \frac{2S}{\bar{U} + \bar{D}}, \qquad 1.20$$

where $S = \int_0^1 xs(x)dx$, $\bar{U} = \int_0^1 x\bar{u}(x)dx$ and $\bar{D} = \int_0^1 x\bar{d}(x)dx$. are integrals of the strange, the up and the down sea quark distributions.

The origin and properties of non-valence quarks inside the nucleon can not be explained by the static quark-parton model. To account for them one needs an interacting field theory, such as Quantum Chromodynamics (QCD) [1.8], widely held to be the theory of strong interactions. Without going into details about QCD, let us briefly state the basic concepts here. QCD is a local non-Abelian gauge theory. The gauge group is SU(3) which corresponds to three colors. The quark flavors do not play any significant role in QCD. The eight generators of SU(3) correspond to an octet of gluons - the strong force carriers. As in Quantum Electrodynamics the gluons are spin-1 bosons, but unlike the photons which are neutral, the gluons carry color charge. This difference is due to the non-Abelian nature of QCD and has important consequences.

The simplest process by which non-valence quarks can be created in the nucleon is pair creation by gluons, shown schematically in Fig.1.3.

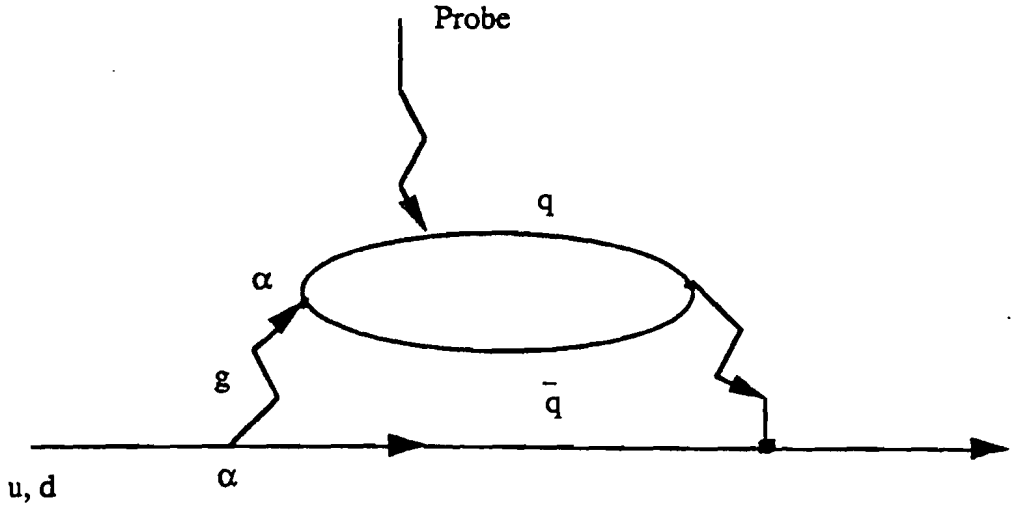

Fig.1.3. Sea quarks pair production by gluons inside the nucleon.

A gluon g emitted by a valence quark dissociates into a virtual quark-antiquark pair which then recombines back to the original configuration. This process can be detected if, for example, a virtual W emitted by a neutrino scatters off one of the virtual quarks. As is evident from Fig.1.3., the amplitude for quark pair production is proportional to the square of the strong interactions coupling constant, which in the first approximation is:

$$\alpha_s = \frac{12\pi}{(33-2n_f)\ln(Q^2/\Lambda^2)}, \qquad 1.21$$

where n_f is the number of light quarks, i.e. quarks with masses much less than Q/2, Q^2 is the 4-momentum-squared of the process (i.e. the 4-momentum squared of the probe), and $\Lambda \approx 200$ MeV is a constant which sets the scale of the Q^2 evolution of α_s.

Since QCD is flavor blind, one would expect all quark flavors to be created in equal proportion. In a model with three quark flavors this is referred to as SU(3) symmetric quark pair production. In a model with six quarks it is known as SU(6) symmetry. This simplified picture does not take into account the differences in quark masses. In the light

quark approximation when $Q^2 >> m_q$, the quark masses do not play any significant role and quark pair production should be SU(3) (or SU(6)) symmetric. In that approximation $\kappa = 1$. At lower Q^2 one expects $\kappa < 1$, since the strange quarks pair production will be suppressed to a certain degree relative to the up and down quarks due to the strange quark's higher mass.

The best estimates of the up, the down, and the strange quark masses are $m_u = m_d \approx 300$ MeV/c^2, $m_s \approx 500$ MeV/c^2, respectively. The mean Q^2 of this experiment is $\langle Q^2 \rangle \approx 25$ (GeV/c)^2. The following question now arises: since $\langle Q^2 \rangle$ is about 50 times larger than m_s, should we expect $\kappa \approx 1$? To answer this question one must know the quark distributions behavior as functions of Q^2. The procedure to follow is to use experimental data from deep inelastic scattering to fix the quark distributions at some value of $Q^2 = Q_0^2$. Evolution to $Q^2 > Q_0^2$ can then be calculated [1.9, 1.10] using the Altarelli-Parisi [1.11] equations. Various parametrizations of the quark structure functions now exist [1.12,1.13]. Fig.1.4 shows a plot due to E.Eichten [1.14] that illustrates Q^2 evolution of the total momentum fraction of the nucleon carried by various quarks and gluons.

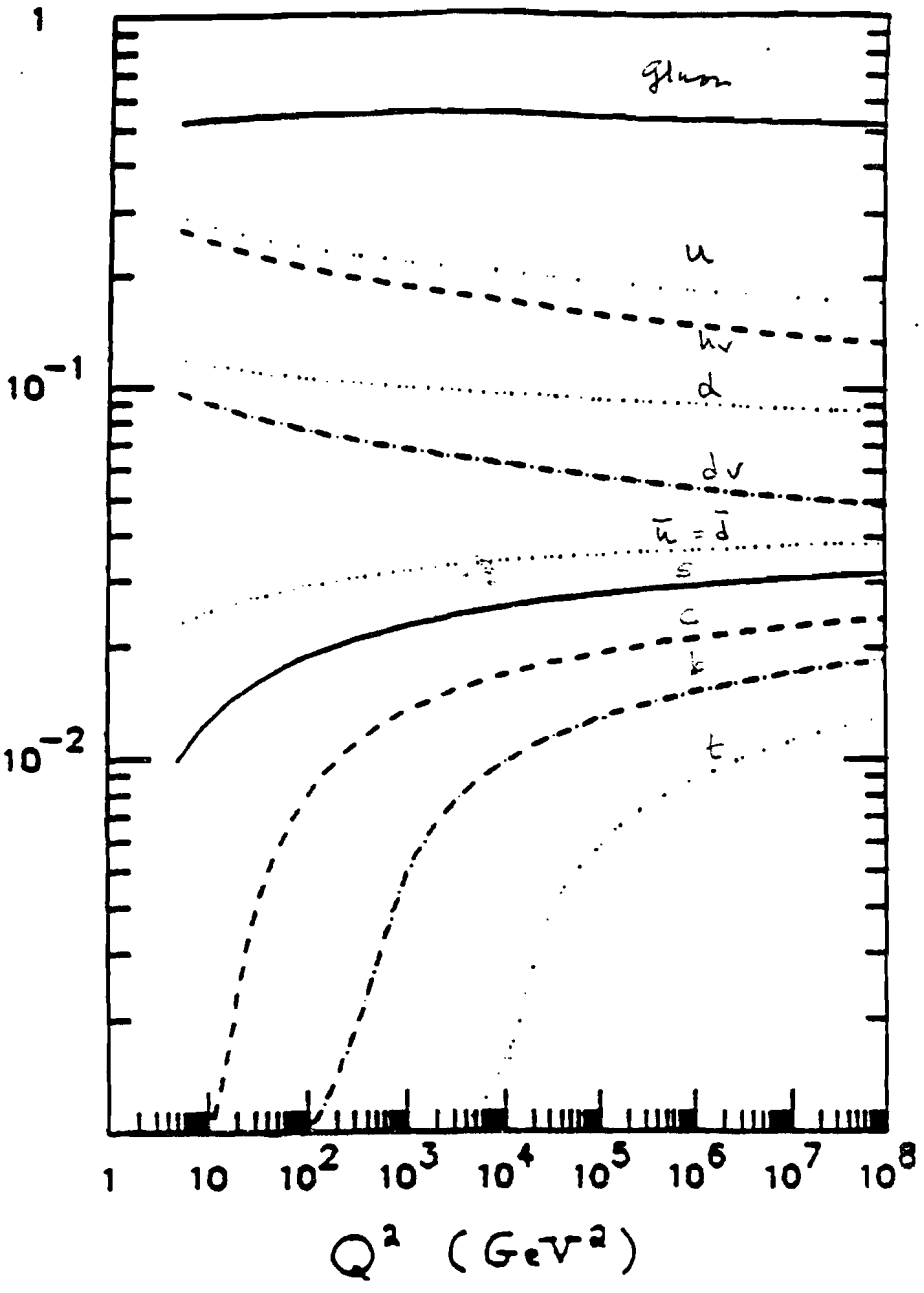

Fig.1.4. The fraction of the total momentum carried by each of the partons of the proton as a function of Q^2. From largest to smallest momentum fraction these partons are: gluon, up quark, up (valence only), down quark, down (valence only), antiup (or antidown) quark, strange quark, charm quark, bottom quark, and top quark.

Knowing the Q^2 dependance of the quark structure functions, it is straightforward to calculate the Q^2 evolution of the strange sea fraction $x(Q^2)$. This evolution, as well as the evolution of the charm, the bottom, and the top sea, is shown in Fig.1.5, which was kindly provided to us by E.Eichten [1.14]. He used the CDHS deep inelastic neutrino scattering data [1.16, 1.17]. The starting point for the strange sea fraction evolution was $x_0 = 0.43$ at $Q_0^2 = 5\ (GeV/c)^2$ [1.13].

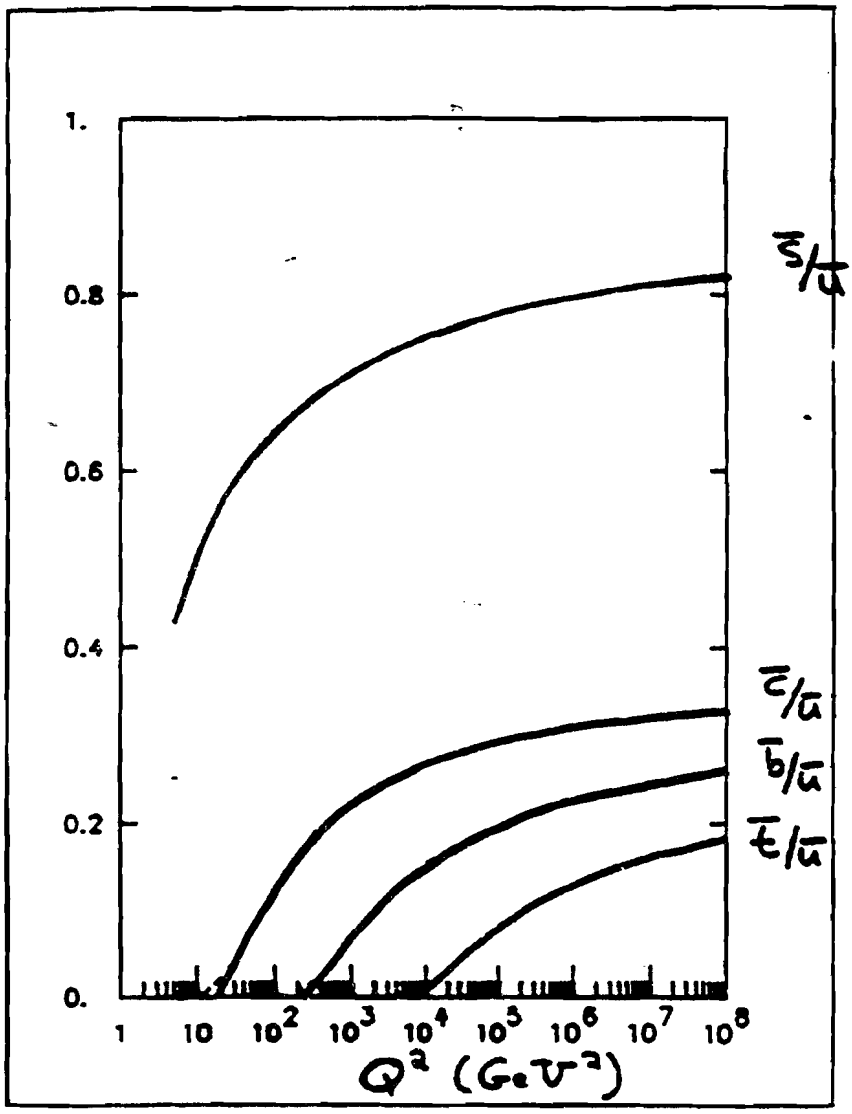

Fig.1.5 Q^2 evolution of the strange sea fraction, the charm sea fraction, the bottom sea fraction and the top sea fraction.

As is evident from Fig.1.5, $x(Q^2)$ evolves slowly over the available range of Q^2. If this picture is right, for this experiment with $\langle Q^2 \rangle \approx 25$ GeV^2 we can expect $x \approx 0.55$ - 0.59.

CHAPTER II.
APPARATUS.

2.1 Neutrino Beam.

The standard method for producing (anti)neutrinos is to allow protons to collide with a stationary target thereby producing pions and kaons which decay into neutrinos and muons. One can control the neutrino type by selecting the electric charge of the secondary pions and kaons. For this experiment, however, there was no sign selection in order to maximize the neutrino flux. The beam used in this experiment is called the quadrupole quadruplet beam because there were four sets of quadrupole magnets focusing the secondary particles after the target [2.1]. The beamline layout is shown in Fig.2.1.

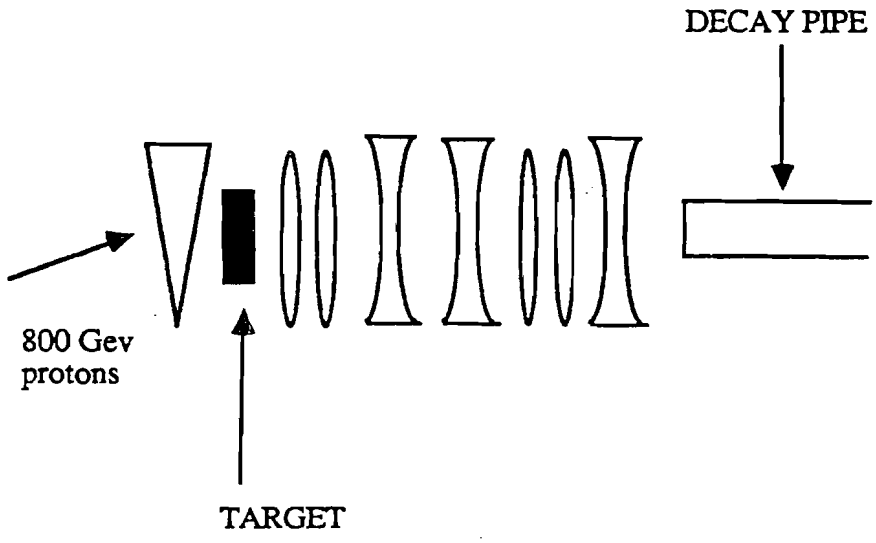

Fig.2.1 Quadruplet neutrino beam layout.

Primary protons accelerated to 800 GeV in the Tevatron entered the neutrino beamline at an upward angle of 13 mrad. The bend was removed by a single dipole magnet, after which

the protons impinged upon target , made of eight pellets of beryllium oxide powder, 14 cm long in all. The emerging secondary particles were collected by four sets of quadrupole magnets, the first 3 sets consisting of two magnets each and the last set consisting of one magnet. Since there were only quadrupoles in the beamline, there was *no charge selection* of the secondary particles.The four sets of magnets formed point-to-parallel optics at the central momentum of 300 GeV/c. That value of central design momentum was chosen to gain the best possible momentum acceptance and to minimize the angular divergence of the beam. Upon exiting the magnets, the secondaries entered the 535 meter long 30 cm diameter decay pipe, where the kaons and the pions decayed, producing neutrinos and antineutrinos. Following the decay pipe there was about 870 meters of iron and earth shielding designed to stop muons and the remaining hadrons.

2.2 Calorimeter.

The Calorimeter components can be divided into two groups: the active and the passive. The active elements detect the presence of charged particles and can be read out for event reconstruction; the passive elements served merely as energy absorbers. The first group included Flash Chambers, Proportional Chambers and Scintillators, the second group consisted of plastic sheets filled with steel shot and sand. The calorimeter was 19 meters long and had a $3.6 \times 3.6\ m^2$ cross section. Some of the calorimeter parameters are listed in Table 2.1.

Table 2.1 Calorimeter parameters.

Radiation length	14cm
Interaction length	90cm
Fiducial mass	9×10^7 g
Density	1.35 g/cm^3
Proton/neutron Ratio	0.964
Critical energy	35 MeV

An overview of the detector with details of the calorimeter construction is shown in Fig.2.2 There were 592 flash chambers, 37 proportional planes and 8 12' × 12' liquid scintillator planes used primarily for triggering on cosmic muons. The calorimeter had a modular construction.Each module had 4 "beams" of 4 flash chambers each, mounted in the sequence U-X-Y-X. Cells in the X chambers ran horizontal, cells in the U and the Y chambers ran 100° and 80° relative to the horizontal plane, respectively. Between the flash chambers there were absorber sheets made of 5cm × 366cm×366cm extruded plastic. They were filled with steel shot or sand. The mixture was chosen to give a 4:1 ratio of interaction length to radiation length which was a reasonable compromise between mass and a good shower angle resolution. The distance between adjacent flash chambers was about 3cm, the proportional planes spacing was about 50 cm and the scintillator spacing was about 250cm.

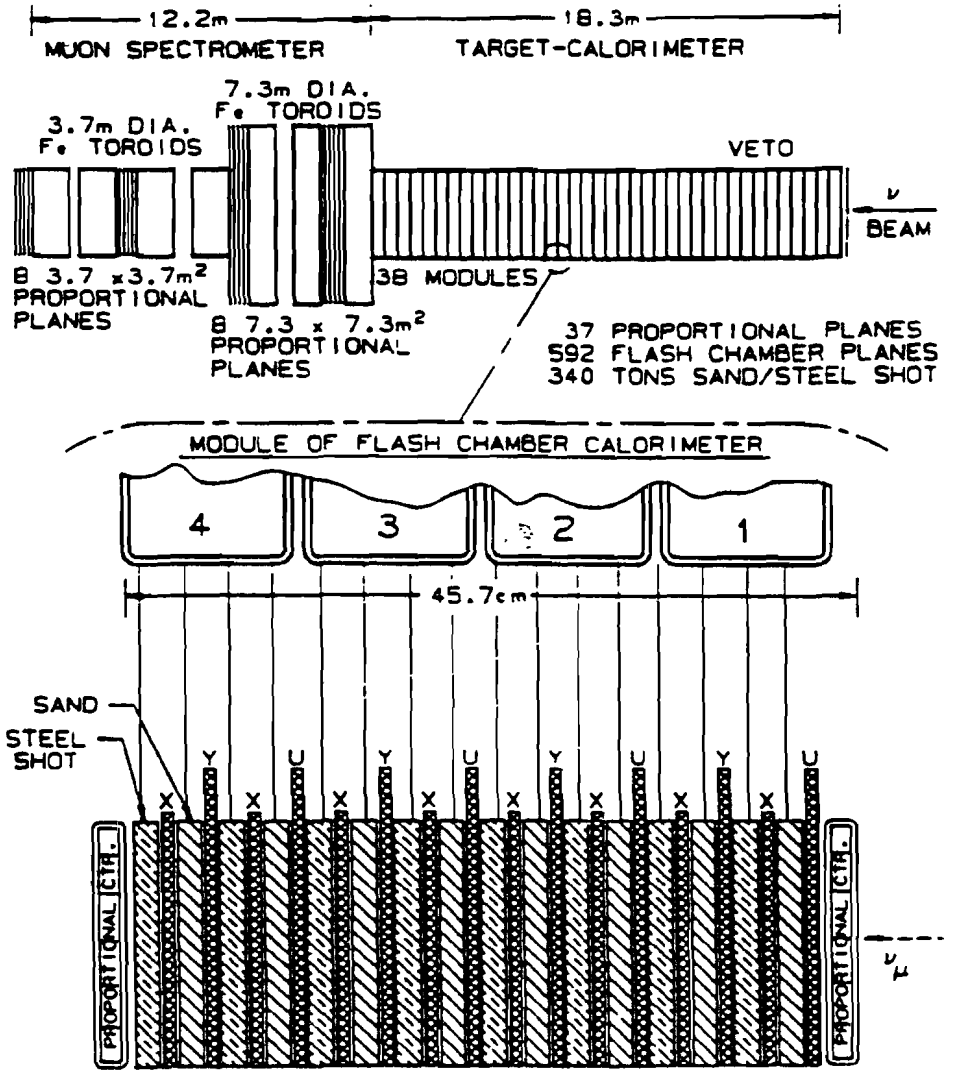

Fig.2.2. An overview of the apparatus with some details of the calorimeter construction.

2.2.1 Flash Chambers.

Flash Chambers (FC) were the main active element of the calorimeter. Because of their numbers and fine sampling, they provide most of the information about interaction in the detector. Their construction is shown in Fig.2.2. The FC were made of 0.58cm × 122cm × 488cm panels of extruded polypropylene, with individual cell size about 4mm × 5mm.

Each FC had three panels held together by mylar tape; 91.5cm × 427cm sheets of aluminum foil were glued to it on both faces of the chamber. There was a single gas supply and exhaust manifold for each polypropylene panel. A mixture of 90% Neon, 10% Helium and 0.2% Argon was flowed through the chambers. Unlike the proportional tubes and the drift chambers, the FC gas was not exhausted into the atmosphere after a single pass, rather it was recycled through a molecular sieve to clean out the impurities of N_2, O_2 , H_2O. The sieve was cooled with liquid nitrogen, so as a result argon was frozen out and reintroduced before being recirculated through the FC's. It was found that a small amount of electronegative gas, such as oxygen and water vapor, reduced the FC's dead time. Therefore a small fraction of the gas was allowed to bypass the filtering to reintroduce oxygen and water into the chambers. The gas composition was monitored by a gas chromatograph and was checked at least once every 8 hours during running.

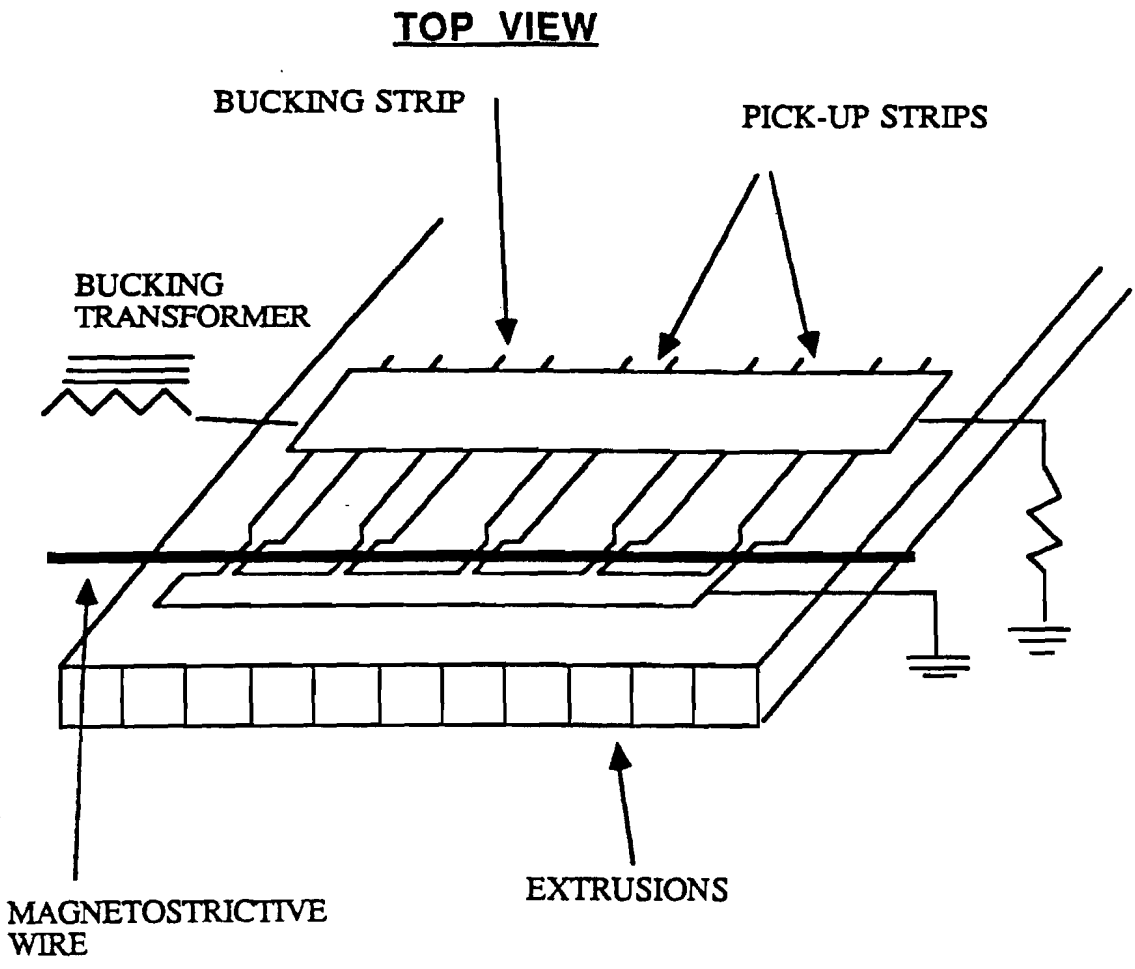

Fig. 2.3 Flash chamber construction.

The FC operation relies on its ability to produce a plasma discharge in FC cells when there is residual ionization left by a passing charged particle. To achieve the plasma formation a 4.5KV pulse was applied to the aluminum foil on one side of the chamber while the other side was held at ground. Most of the pulse's current flowed through the spark gap made of modified Champion marine spark plugs and connected in parallel with the flash chamber. Since the FC's operate in the Geiger regime, it was necessary that the HV pulse had a sufficiently fast rise time, so that the charge inside the cell did not have time to drift to the cell's walls before a plasma could be generated. Typical rise times in this experiment were about 60 ns. Every HV pulse was monitored by an on-line LSI-11 computer. Thyratrons were used as the HV triggering device, each thyratron triggering 80 spark gaps.

The FC readout scheme was as follows. When a plasma was produced in a hit cell it propagated the length of the cell. That changed the capacitance between the aluminum foil on one face of the chamber and the 50cm × 3mm copper strips on the other face, which resulted in a typical current of 0.5A to flow to ground (see Fig.2.3). To further increase the ratio of current for cells with plasma versus empty cells, a 5cm wide strip of aluminum ("bucking " strip) ran over the pick-up strips. A pulse of opposite polarity to the HV pulse was fed to the bucking strip through an inverting transformer. This canceled an unwanted current pick-up when there was no hit cell. The result was currents 10 times larger for cells with plasma than for cells without plasma. Current pick-up was accomplished by the means of a 5mil × 12mil magnetostrictive wire that ran across the pick-up strips. The acoustical wave generated in the wire propagated at the speed of 5000 m/sec and was sensed at each end of the chamber by a magnetic pick-up. To minimize reflections, the ends of the magnetostrictive wire were mechanically terminated. Constant magnetization of the magnetostrictive wire had to be maintained for reliable performance. To achieve the stable operating state, the wire was placed in a 10 mil groove in an aluminum bar and a solenoid was formed by winding a wire around the bar. The solenoid was pulsed every 200 triggers

to remagnetize the magnetostrictive wire. Pick-up amplifiers sent pulses to 1024-bit memory boards. There, as a pulse arrived, a memory address was incremented by a clock, which ran at 2.4 counts per one cell propagation delay. The resulting bit patterns were transferred to a buffer memory and then read out by the PDP-11 computer.

2.2.2 Proportional Chambers.

The main function of the proportional tube chambers (PT) was to provide a signal for the trigger generation; in addition they supplied information about the energy of the shower, which could be used to check the flash chambers especially for high shower densities. The PT were made of 2.5cm × 20cm × 366cm modules of extruded aluminum, each module having 8 cells. 18 modules were assembled into a plane; an input and an output gas manifolds, made of 2.5cm × 2.5cm aluminum, were glued to the edges. A 0.05 mm gold-plated tungsten wire was strung through a cell ending in a nylon bolt, which was glued to the gas manifold. Each wire was connected to the high voltage bus through a 15MΩ resistor. The operating voltage was 1725V. A mixture of 90% Argon and 10% Methane flowed through the planes. This set of operating conditions provided a gas gain of about 1000. To reduce the number of electronic channels, four wires were grouped together, thus reducing the spatial resolution to 10cm.

Each group of 4 wires was connected to an integrating amplifier with a decay time of 100μs. The trigger decision had to be taken very shortly after an event before the ionization in the flash chambers could reach the chambers walls. This Trigger decision was based on the "Fast Out" (FO) signals. The FO signals was formed by taking the difference between the integrating amplifier output and a 250ns tap on the delay line (Fig.2.4).

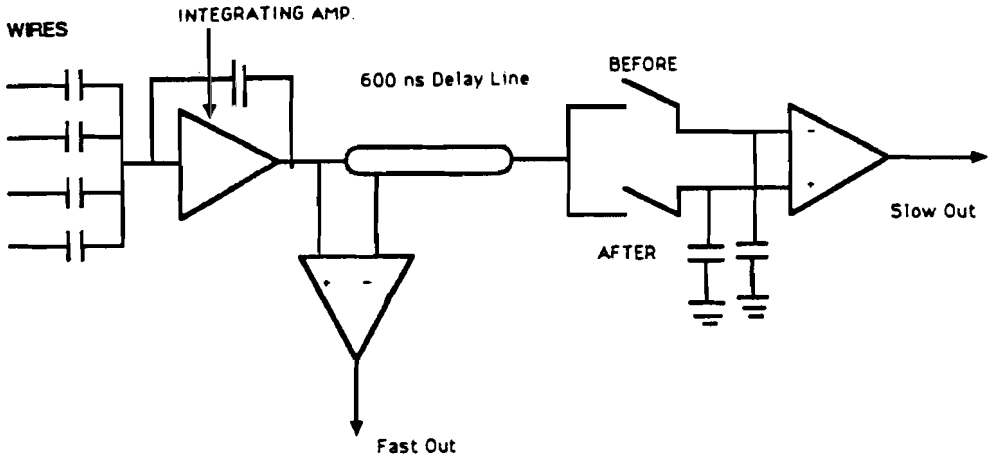

Fig.2.4. PT channel.

The 36 FOs from a plane were then summed to provide an analog signal used in the trigger decisions. After the 600ns delay line the output of the integrating amplifier went through the BEFORE and AFTER switches, which, together with capacitors, formed track-and-hold circuits. The BEFORE switch was opened shortly before an event signal emerged from the delay line 550ns after the event or 100ns after the trigger. The AFTER switch was opened when the event signal has risen - about 400ns later. Then the "Slow-Out" (SO) signal was formed: SO = AFTER - BEFORE which was digitized by 12-bit ADCs. Apart from the FO's, the proportional chambers readout started when the FC noise subsided - about 1ms after the trigger. The complete readout cycle took 1ms. A board, known as the "Electron Logic Board" (ELB), formed "hitbits" by discriminating the FO with externally set thresholds. The hitbits and digitized SO were stored in memory modules and written into the PDP-11 computer.

2.2.4. Calorimeter Drift Planes.

There were 8 12' drift planes in the calorimeter, identical to the toroid 12' planes described below. These planes were used for the alignment purposes to fix the positions of the flash chambers relative to the toroid drift planes. They were also used for the analysis of the test data (see Chapter V), when no flash chamber information was available.

2.3 Muon Spectrometer.

The Spectrometer consisted of magnets, drift planes and scintillator planes.The total iron thickness was about 700 cm and the total length of the spectrometer was approximately 10m. The total energy loss for a muon traversing the spectrometer at normal incidence was 8.1 GeV.

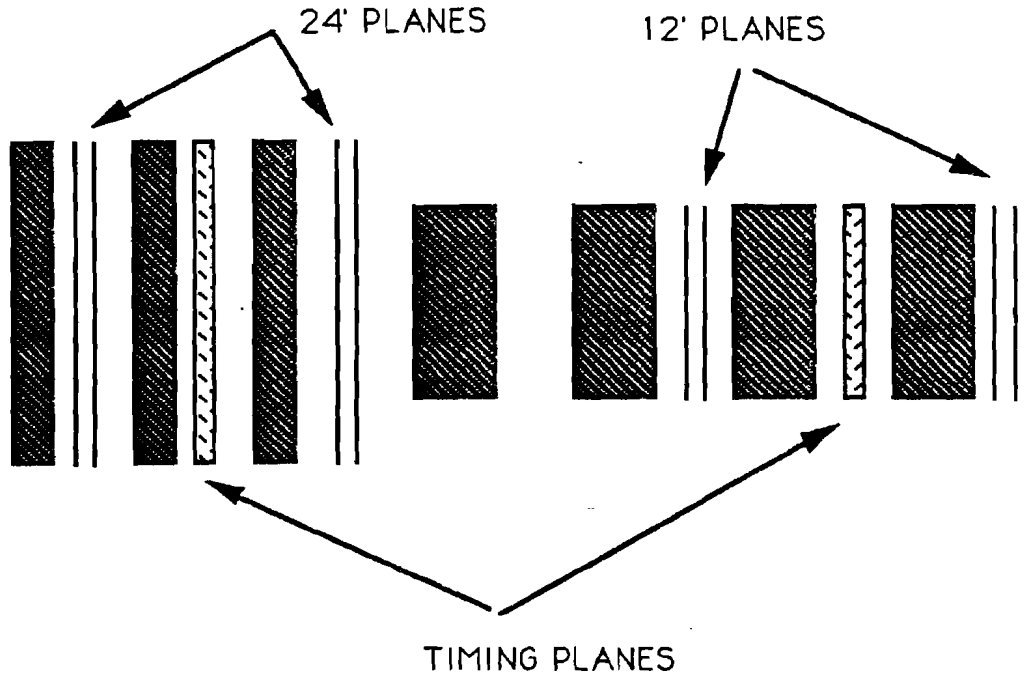

Fig. 2.5. Spectrometer layout.

2.3.1 Magnets.

The magnets had a toroidal geometry and came in two sizes: 24' diameter and 12' diameter. The larger magnets were in the forward section of the spectrometer thereby increasing the acceptance of the device. There were three 24' magnets, each about 2' thick with a 2'-diameter central hole. There were four 12' magnets, 4' thick each with a 1' diameter central hole. Coils were wound through the holes and around the magnets creating a toroidal magnetic field. The magnets were monitored and controlled externally via an EPICS terminal in the control room. The polarity of the magnets was usually set to focus negative muons.

Measurements of the magnetic field were made using Hall probes. For the 12-foot magnets, these measurements were consistent with the field calculation made with the program POISSON. The 24' magnets, however, exhibited a significant discrepancy between calculations and measurement. To determine the 24-foot magnets field fits were performed in which Charged Current data with known energy spectrum were used, and the 24' B-field parameters (parametrized as a 4-th order polynomial) were varied to obtain the best agreement for the energy scale [2.2]. Fig.2.6 shows the field in the 12-foot and the 24-foot magnets.

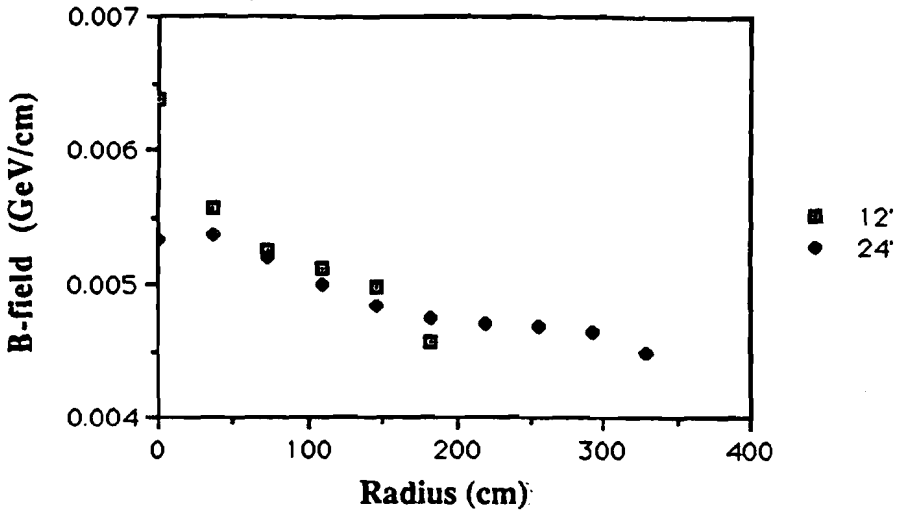

Fig.2.6. Magnetic field in the 12-foot and the 24-foot magnets plotted as functions of the distance from the center of the toroid. The field is in the units of the transverse kick per unit length traveled ((GeV/c)/cm).

2.3.2 Drift Planes.

Like the Proportional Planes, the Drift Planes were made of aluminum extrusions with 2.5cm × 2.5cm cells, but unlike the PT, the drift planes had two layers of cells with a 1/2" offset between front and back faces to eliminate the left-right ambiguity of the drift chambers.(see Fig. 2.7).

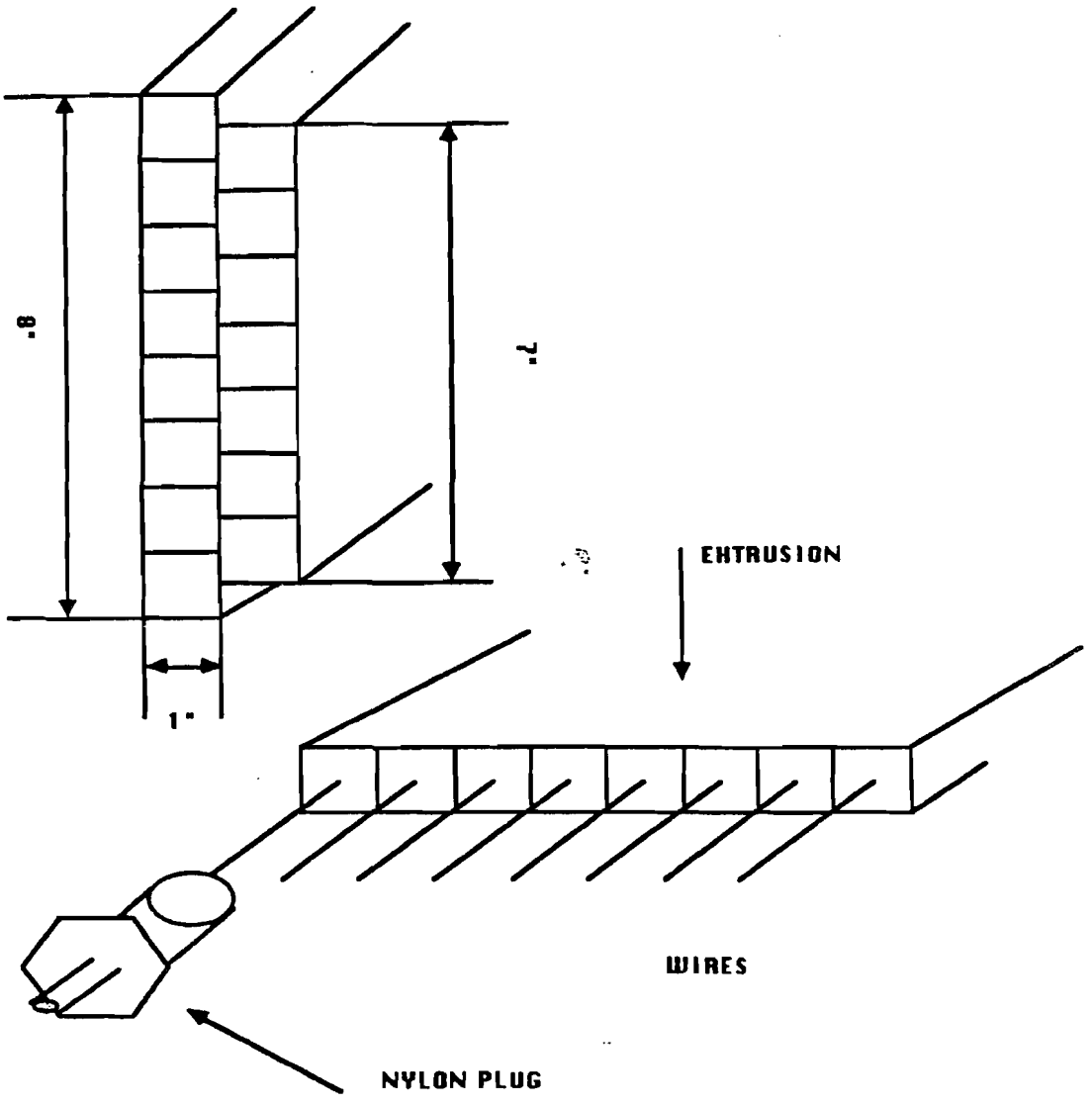

Fig. 2.7 Drift planes extrusions.

A 50 μm gold-plated tungsten wire was strung through each cell with a wire tension of approximately 200g. The wire ended up in a brass pin embedded into a 0.5" nylon bolt, which was epoxied to the extrusion.

A gas mixture of 90% Argon and 10% Ethane was flowed through the planes, at a rate of 1 cubic foot per hour (c.f.h.) for the 12' planes and 2 c.f.h. for 24' planes. The gas flow was monitored with bubble-type flowmeters on the input lines where the input pressure

was maintained at 10 p.s.i. Each 12' plane had one input and output manifold; the 24' planes had separate wing manifolds as shown in Fig. 2.8.

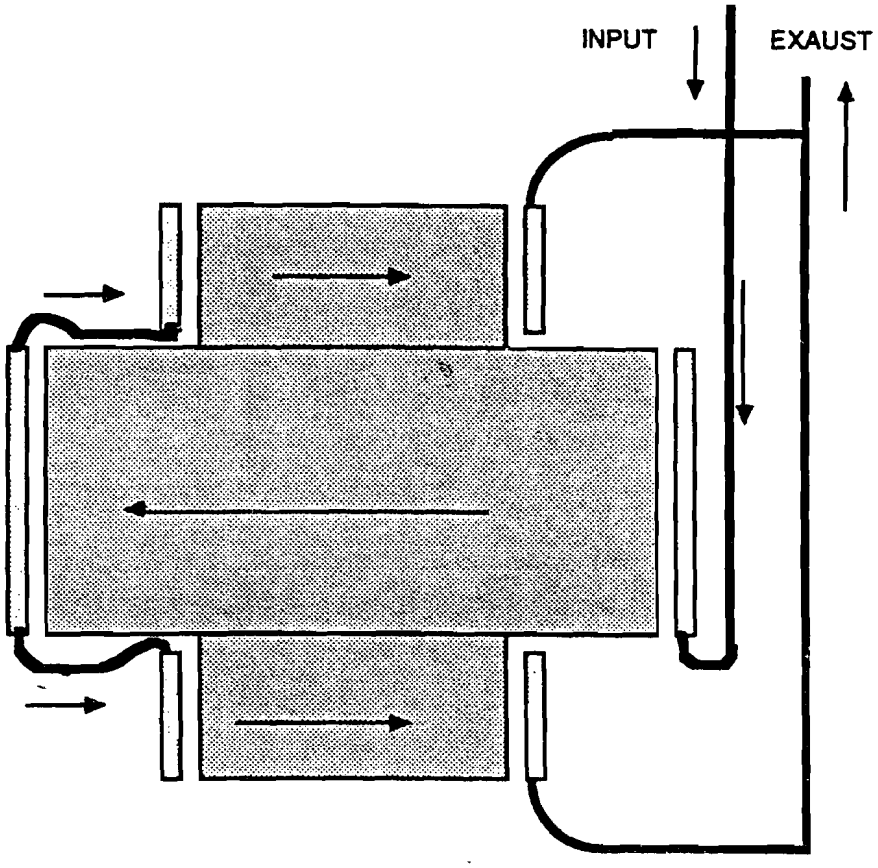

Fig.2.8. 24' planes gas system. Arrows indicate gas flow direction.

The drift chamber operation is based on measuring the electrons' drift time from their production location by a passing charged particle until their reaching the anode wire. From the drift time one can then calculate the particle's distance relative to the wire by integrating the known drift velocity over drift time. The drift velocity depends mostly on the electric field inside the chamber and on the properties of the gas mixture used. The electric field in this case was calculated using electrostatic imaging method with an 13 × 13 grid in each 1" cell. The results are shown in Fig.2.9 The drift velocity came from the CERN program DRIFTDT. Each wire was connected to the high voltage bus via a 10 MΩ resistor.

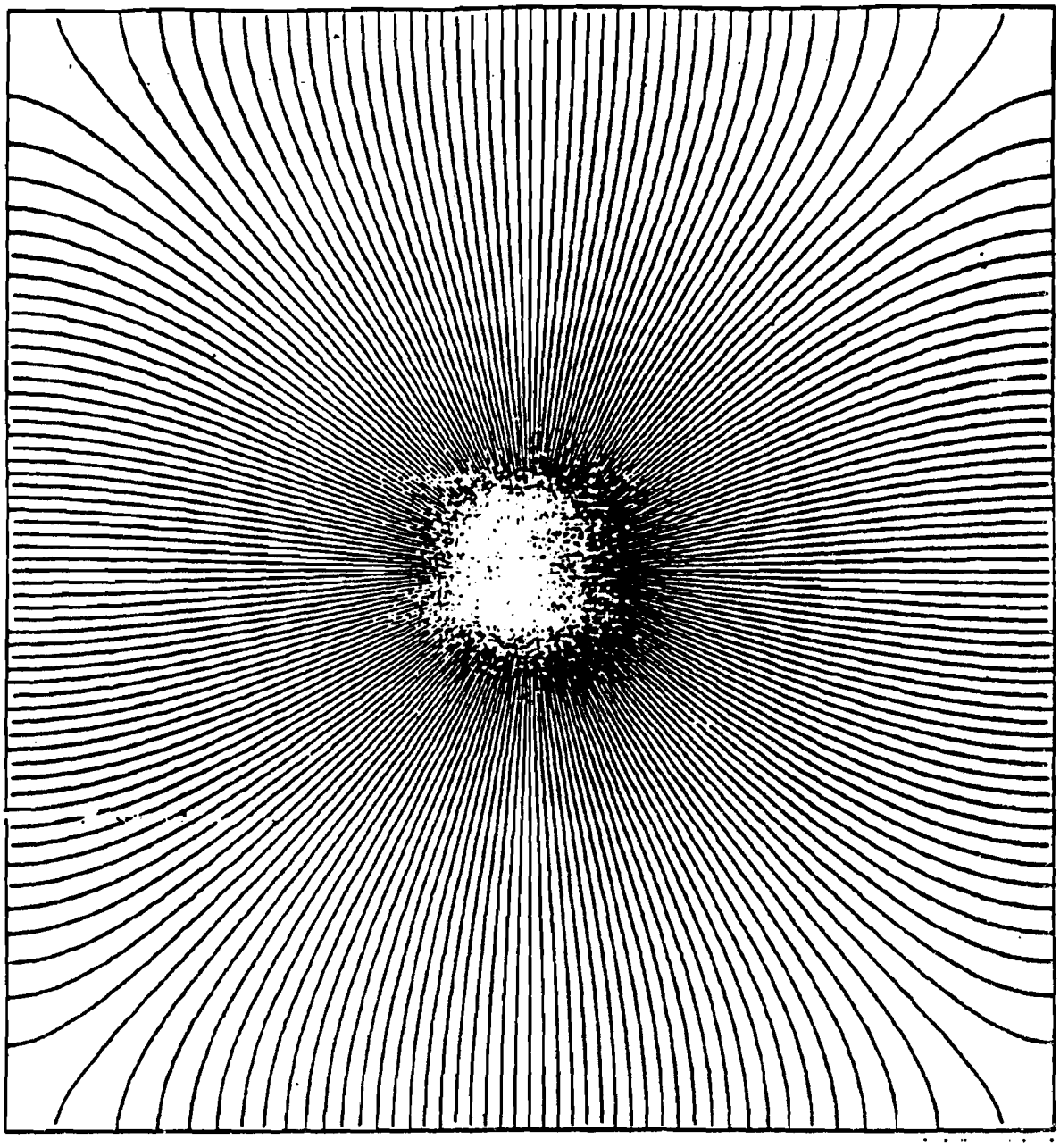

Fig. 2.9. Electric field inside a drift cell.

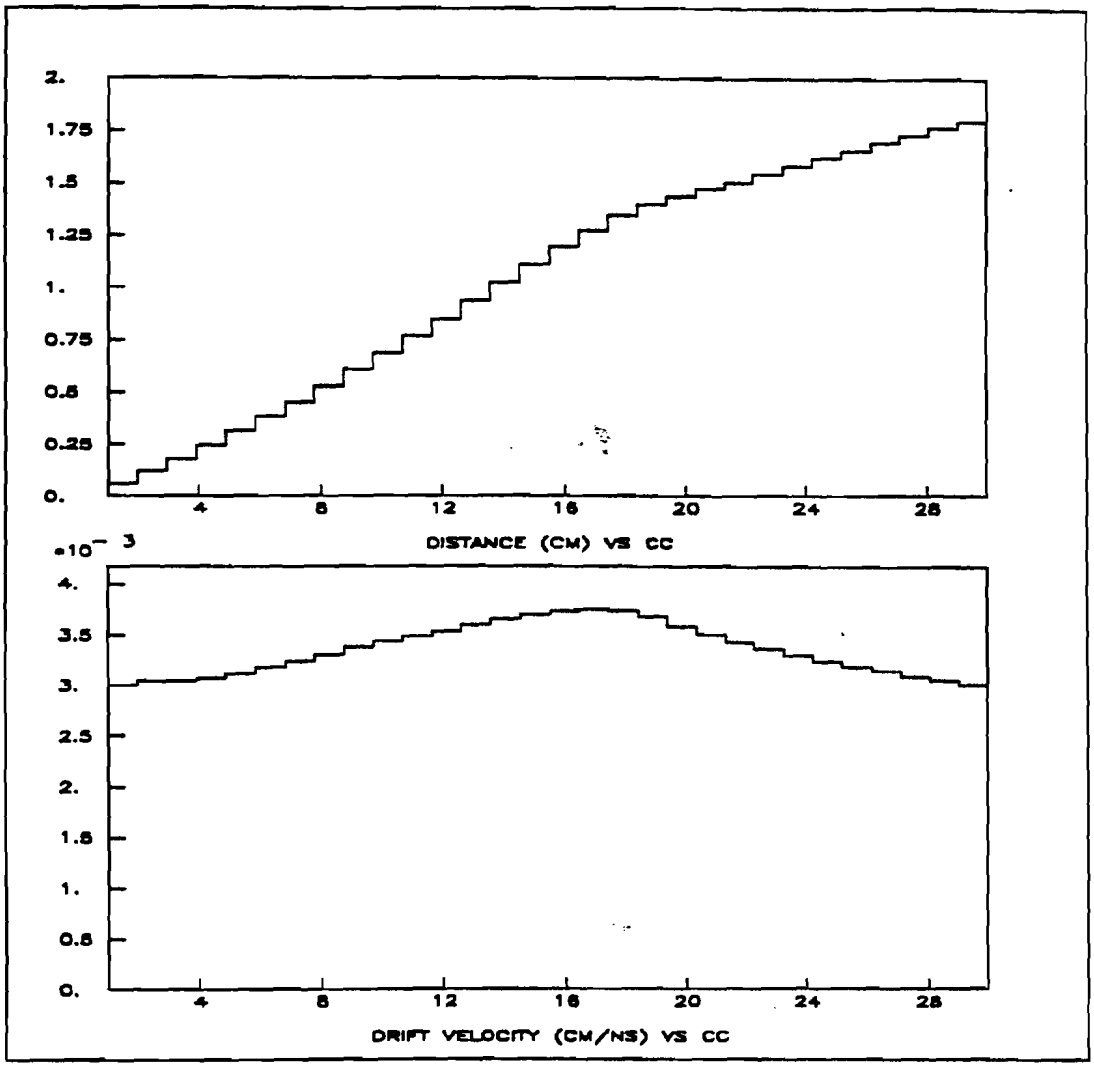

Fig. 2.10. Drift distance in cm (upper plot) and drift velocity in cm/ns (lower plot) as functions of clock counts (each cc = 20 ns).

One of the problems with operating large drift chambers was that the wires become attracted to their own electrostatic image in the walls of drift cells. If a wire gets close to the cell walls an electric discharge occurs causing the wire to bounce back while recharging from the HV power supply and so on. This behavior is known as "wire oscillations". The

24' planes with their extra long wires were more susceptible to this problem than the 12' planes, therefore the 24' planes were run at a lower operating voltage.

2.3.3.Drift Readout.

The task of the Readout System was collecting and storing drift times. The readout system used in this experiment consisted of *TDC cards, Interface cards, Drift Controller, Drift Clock ,and Drift Memory*. The organization of the drift readout system is shown in Fig. 2.11.

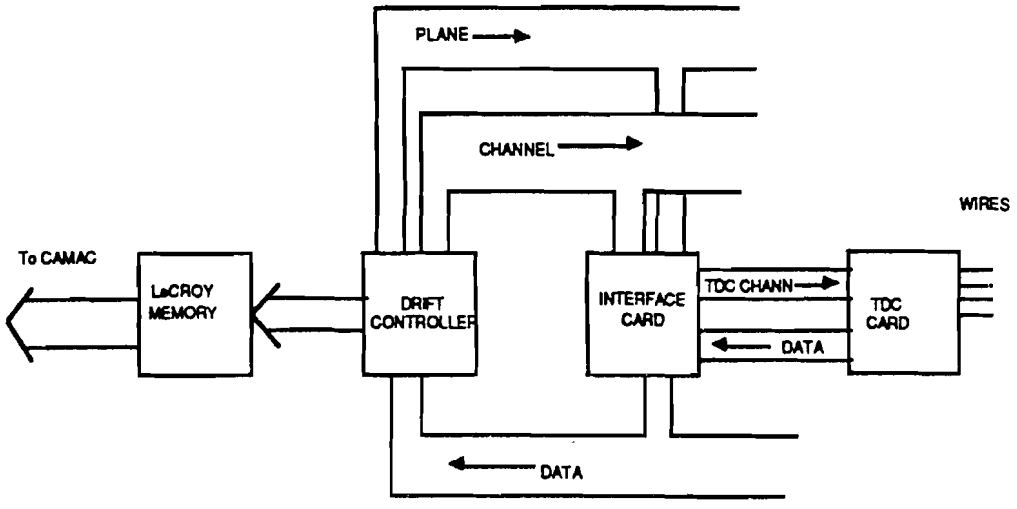

Fig.2.11. Drift readout architecture.

2.3.3.1 Drift Controller.

When the decision was taken to record an event, the controller began interrogating the electronic channels by generating their addresses. The addressing scheme was as follows: each interface card was considered one electronic plane; within an electronic plane wires were numbered 1 through 144. For the 12' chambers electronic planes were equivalent to single wire layer ("face") of the plane, and for the 24' planes there were 2 electronic planes

for each physical "face". All in all, the system had 32 electronic planes (the first 8 were in the Calorimeter) for a total of 4560 instrumented channels. The addresses were transmitted to the planes via two digital buses: one for channel address (1 through 144) and the other one for the plane address. Physically the buses were made of 13-pair flat cables.The planes were daisy-chained with a termination and a pull-up at the end of the chain. There were three such daisy chains: one for the Calorimeter planes, one for the 24' planes and one for the 12' planes. The daisy chains were driven independently by a special fan-out. The data from the planes came via the DATA bus which shared the cable with the PLANE bus; from there it was passed along with the address to the LeCroy memory module for subsequent scanning by CAMAC and storage in the PDP-11 computer.

2.3.3.2 Interface Card.

At the interface card level the numbering scheme changed: whereas the controller addressed all channels on a plane numbered 1 through 144 , the interface card converted that address into a local address which determined which half of a TDC card, containing 8 channels, and which channel of those eight should be addressed. The interface card also generated the Analog Multiplicity signals: AM, AM>0 and AM>1. AM was the combined analog output from a plane's wires. AM>0 and AM>1 were discriminated outputs that came on when at least one or more than one wire was hit respectively.

2.3.3.3 TDC Card.

The TDC cards had 16 electronic channels, each one consisting of an amplifier and a counter. The amplifier features included a pulse sharpening network at the front end and an adjustable threshold which was useful when dealing with noisy wires. The counter was a 6-bit register, so the maximum count was 63. A TDC card was connected to its interface card via a 13-pair flat cable, the length of which varied according to the card's location.

2.3.3.4 Clock.

The entire system was synchronized by a single central clock - a quartz-referenced square wave oscillator. The clock frequency was chosen to be 50 Mhz, so each clock cycle equaled 20ns. Since the clock signal had to be transmitted over relatively long distances, much care was taken to maintain the signal's shape so as to insure proper system synchronization.

2.3.3.5 Operation.

A channel would start counting when a sufficient charge has accumulated on the wire, and it would continue counting until stopped by the STOP signal. The STOP provided the timing reference by marking the time of a particle's passing through the toroids. It was generated by the timing planes - plastic scintillator planes in the toroids, and it arrived at the TDC input delayed by a certain fixed amount. Therefore the measured time was the difference between the actual drift time and the trigger delay time as shown in Fig. 2.12

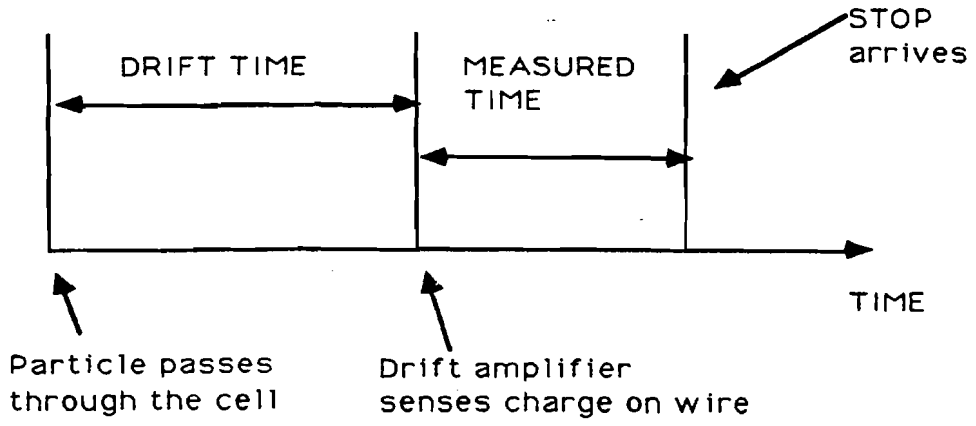

Fig.2.12. Drift Timing.

The STOP signal arrival time (T_{stop}) determination relied on the fact that when a particle passed very close to the wire, the drift time was essentially zero, so the measured time was

equal to T_{stop}. The actual T_{stop} varied from plane to plane and, on a given plane, from TDC card to TDC card because of differences in cable lengths. The necessary small corrections were incorporated into the off-line analysis software to increase the spatial resolution of the device.

2.3.4. Drift Planes Efficiency.

A study of the drift planes efficiency was performed shortly after the 1985 run. We used cosmic muons to provide tracks in the detector. To accumulate high statistics during unattended runs we chose not to use the Flash Chambers, since their use required presence of at least two men according to the safety rules. Instead we used the proportional chambers to fit muon tracks in the calorimeter. The trigger used for this study was similar to the COSMIC trigger (see Chapter III). However, in addition to the calorimeter scintillator planes it also used the toroid back counter in coincidence with them, in order to provide relatively flat muon tracks. This trigger required no energy deposition in the calorimeter. The tracks were then projected into the toroids and hits were counted within certain roads. Since the muon energies were not known, care was taken to properly define the end points of the tracks to avoid possible biases. Fig.2.13 shows a typical event used in the drift efficiency study.

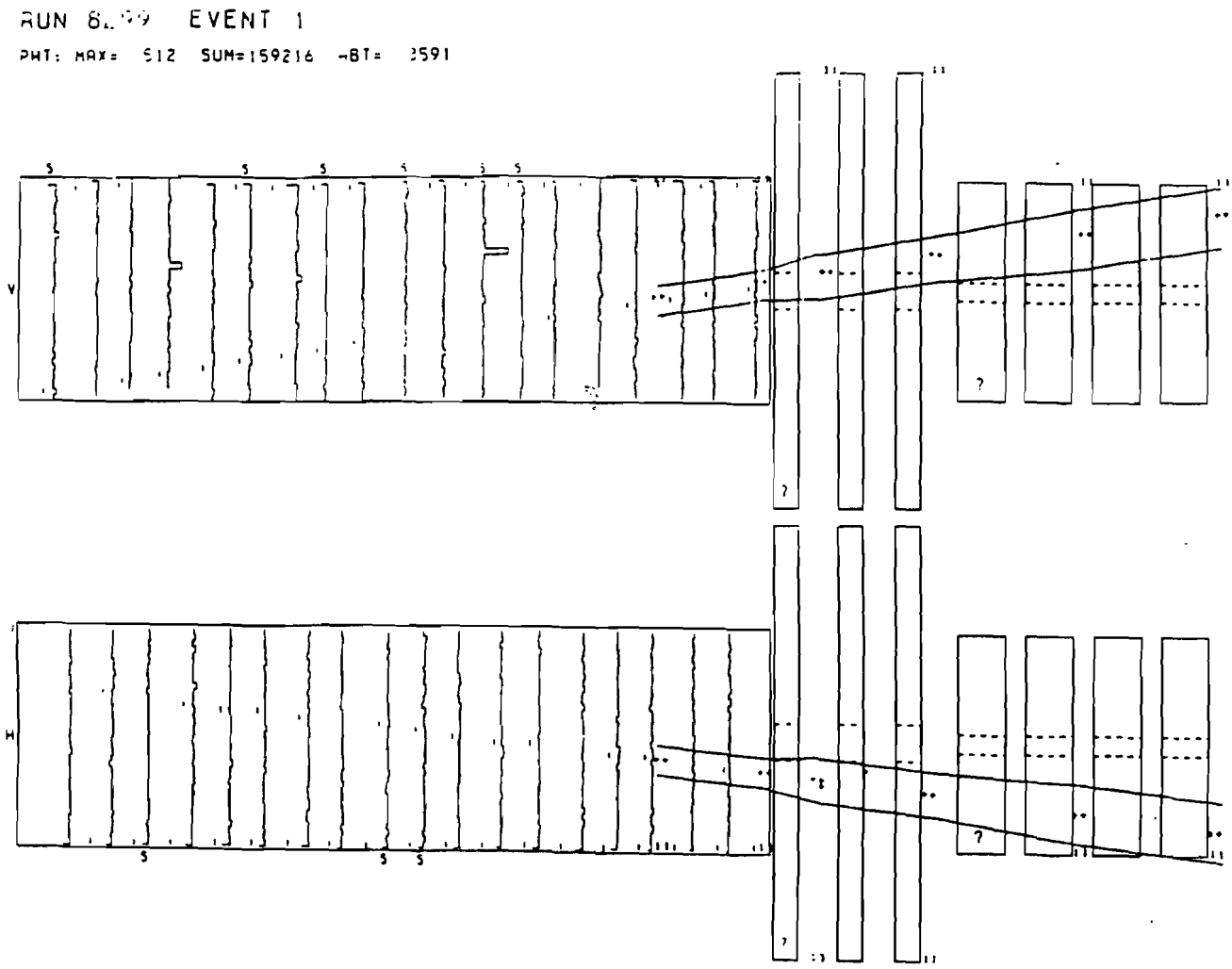

Fig.2.13. A typical cosmic ray event used in the drift planes efficiency study. Hits in the calorimeter and the toroid drift planes are shown as crosses. The smooth lines represent the roads used by the fitting program. Note that the roads are wider in the toroids to accommodate the trajectory bending.

The two parameters most likely to have an effect on the planes efficiency are the operating high voltage (HV) and the gas flow. Fig.2.14 shows the efficiencies of four 12' drift planes as functions of the HV at the normal gas flow of 1 c.f.h. The normal operating HV during the 1985 run for these planes was 1900 volts. Fig.2.15 shows a similar plot for four 24' planes. They were normally operated with HV=1850 volts and the gas flow of 2 c.f.h. The planes appear to be on a plateau under these operating conditions thus allowing for stable operation. The average efficiency of the 12' planes was $\approx$ 92% and for the 24' planes it was $\approx$ 88%.

We found that increasing or decreasing the gas flow by a factor of two did not have a significant effect on most drift planes. From this and the HV studies we conclude that the operating point during the 1985 run was a stable one, and that large variations in efficiency during the course of the run were unlikely.

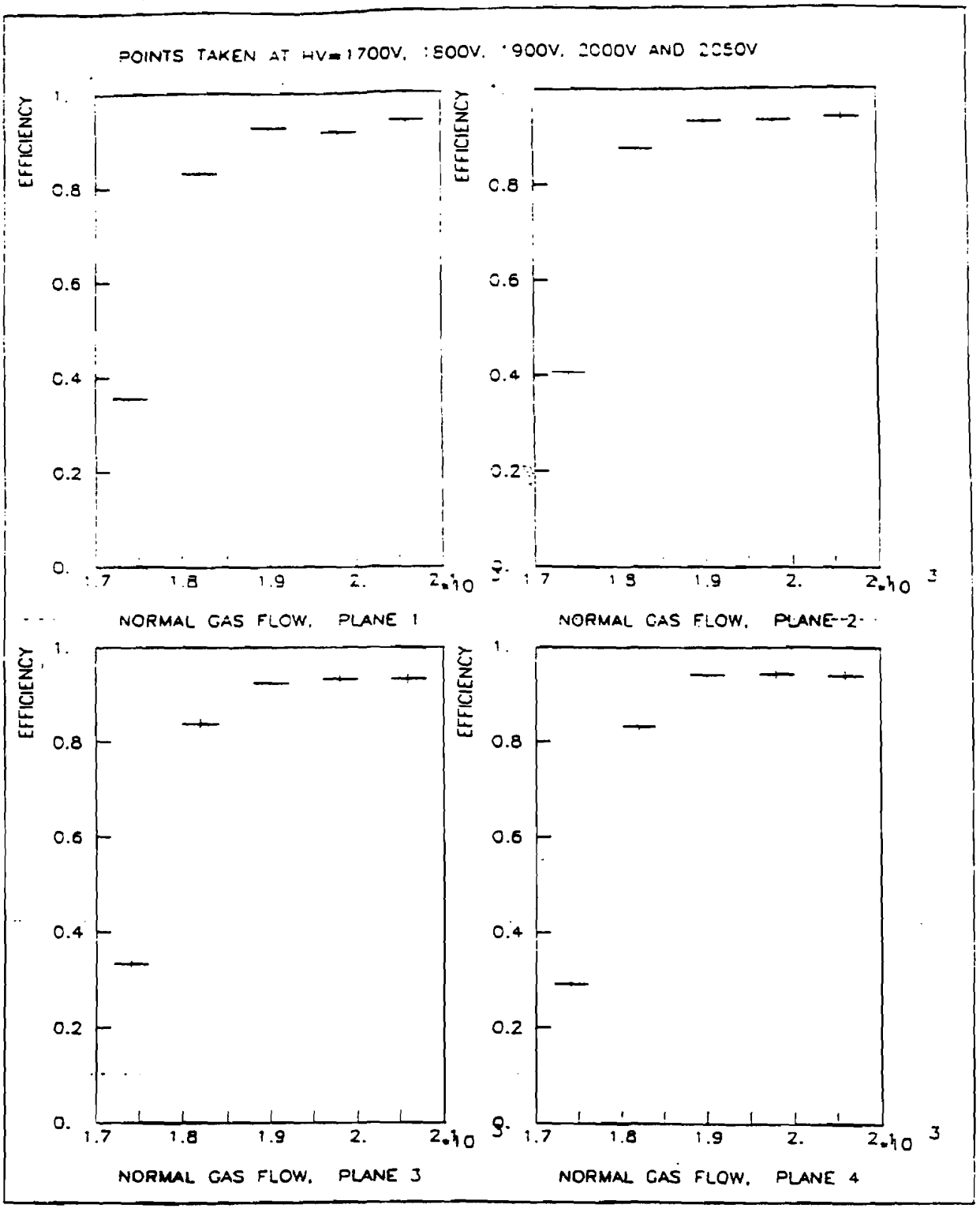

Fig.2.14. 12' drift planes efficiencies as functions of HV at the normal gas flow of 1 c.f.h.

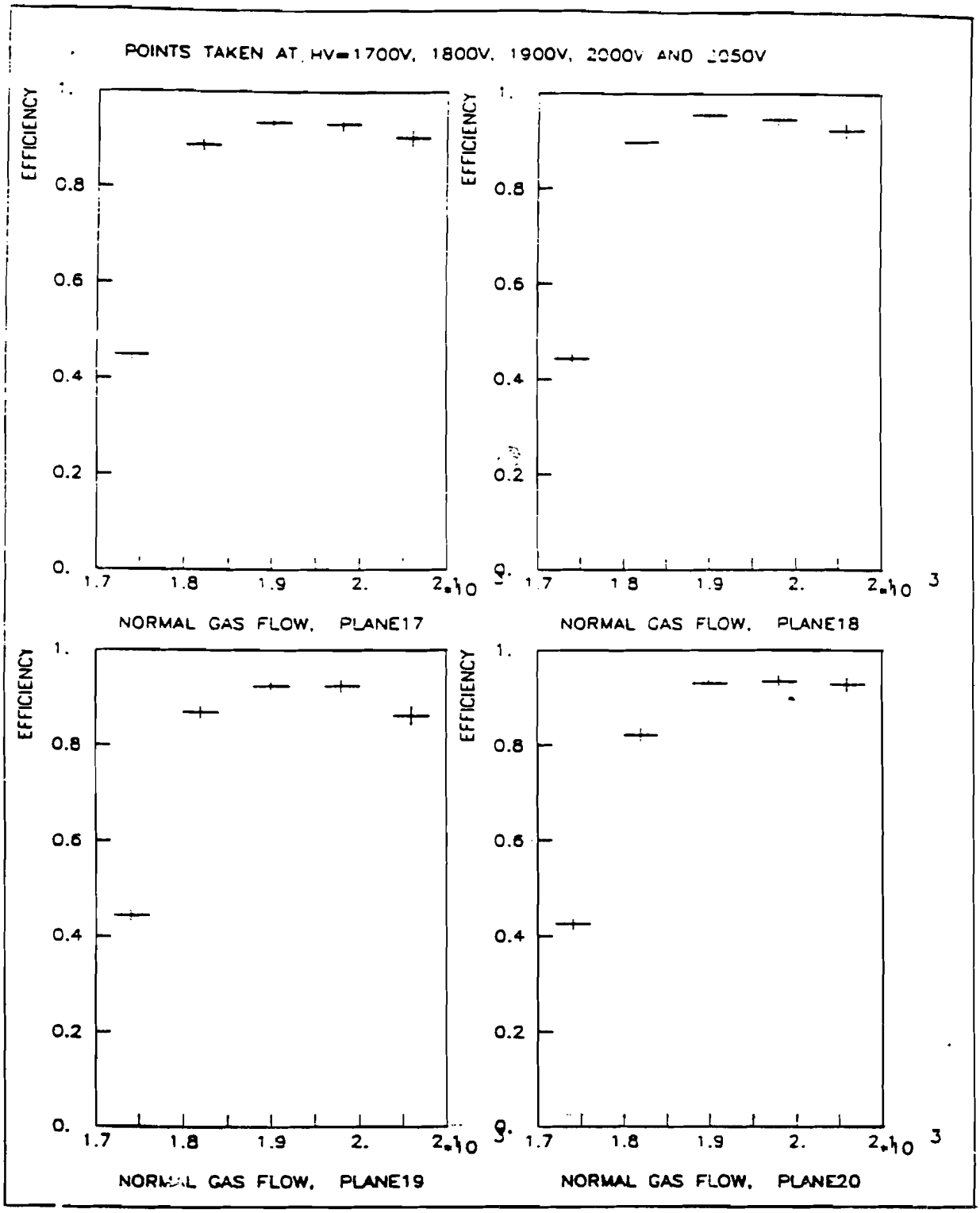

Fig.2.15. 24' drift planes efficiencies as functions of HV at the normal gas flow of 2 c.f.h.

2.4. Alignment and Resolution.

2.4.1. Alignment.

To reconstruct neutrino events accurately it is vitally important to know various detector elements' positions relative to each other. In a large detector, such as ours, the ordinary survey techniques can only provide a starting point for the detector alignment. To do most of the alignment relativistic muons were used to provide reference straight lines.

The first part of the detector to be aligned were the 12' toroid drift planes. Calibration muons taken with the magnets off and degaussed to get rid of residual magnetization were used. The alignment process minimized residuals between the recorded muons positions and straight line fits to their trajectories. Each plane extrusion was aligned separately, since individual extrusions often had position offsets relative to each other. Once the 12' planes were aligned and their positions fixed, the same procedure was repeated for the 24' planes, with the 12' planes providing position reference.

Once the calorimeter drift planes were aligned, they were used as a reference to align the flash chambers using cosmic muons.

The alignment process went through several iterations gradually improving the accuracy of the fits. The final residuals for the drift planes are of the order of 2 mm. The flash chambers residuals are $\approx$ 5mm.

2.4.2. Hadronic Energy and Angle Resolution.

The energy of a hadronic shower in the calorimeter is measured by counting the total number of flash chamber hits. In theory the number of hits in the calorimeter should rise linearly with the shower energy. In practice however, the linearity of the calorimeter response is degraded by several factors, such as the flash chambers inefficiencies and noise, and the saturation of the flash chambers at high hit densities. The flash chambers efficiencies and noise characteristics were studied during the data-taking run using cosmic muons, and run-dependent efficiency and multiplicity tables were produced. To correct for the effects of the flash chambers saturation, a statistical algorithm was used to estimate the number of "effective" particles through a given flash chamber region, and corrections were made to the total number of hits.

To measure the energy resolution of the calorimeter we used a hadron calibration beam with a momentum bite of the order 1%, which is much smaller than the calorimeter energy resolution. The hadron beam is described in more detail in Chapter V. The energy resolution is determined by measuring the width of the reconstructed hadron shower energy distribution. In studying the energy response of the flash chambers for the test data, it was found that it was dependent on the number of events since the last magnetization cycle. The magnetostrictive readout wires were magnetized every 200 events. Apparently, their partial demagnetization was a consequence of reading out many events in the same region, which therefore primarily affected the calibration data. The loss of the readout wires magnetization manifested itself as a drop in the mean number of flash chambers hits for a constant hadron beam energy. To correct for this effect, the flash chambers hit counts for the calibration data were multiplied by a factor F:

$$F = \frac{1 - B\, e^{(-I/N)}}{1 - B}\,, \qquad 2.1$$

where I is the number of events since magnetization, and N and B are constants.

Fig.2.16 shows the plots due to T.Mattison [2.2] of the demagnetization-corrected hadron energy resolution as a function of the calibration beam energy. The energy resolution is fairly constant at energies over 100 GeV and is about 12 - 15%. For the mean hadronic energy of opposite sign dimuon events $\langle E_h \rangle \approx 76$ GeV the energy resolution is of the order 16 - 18%.

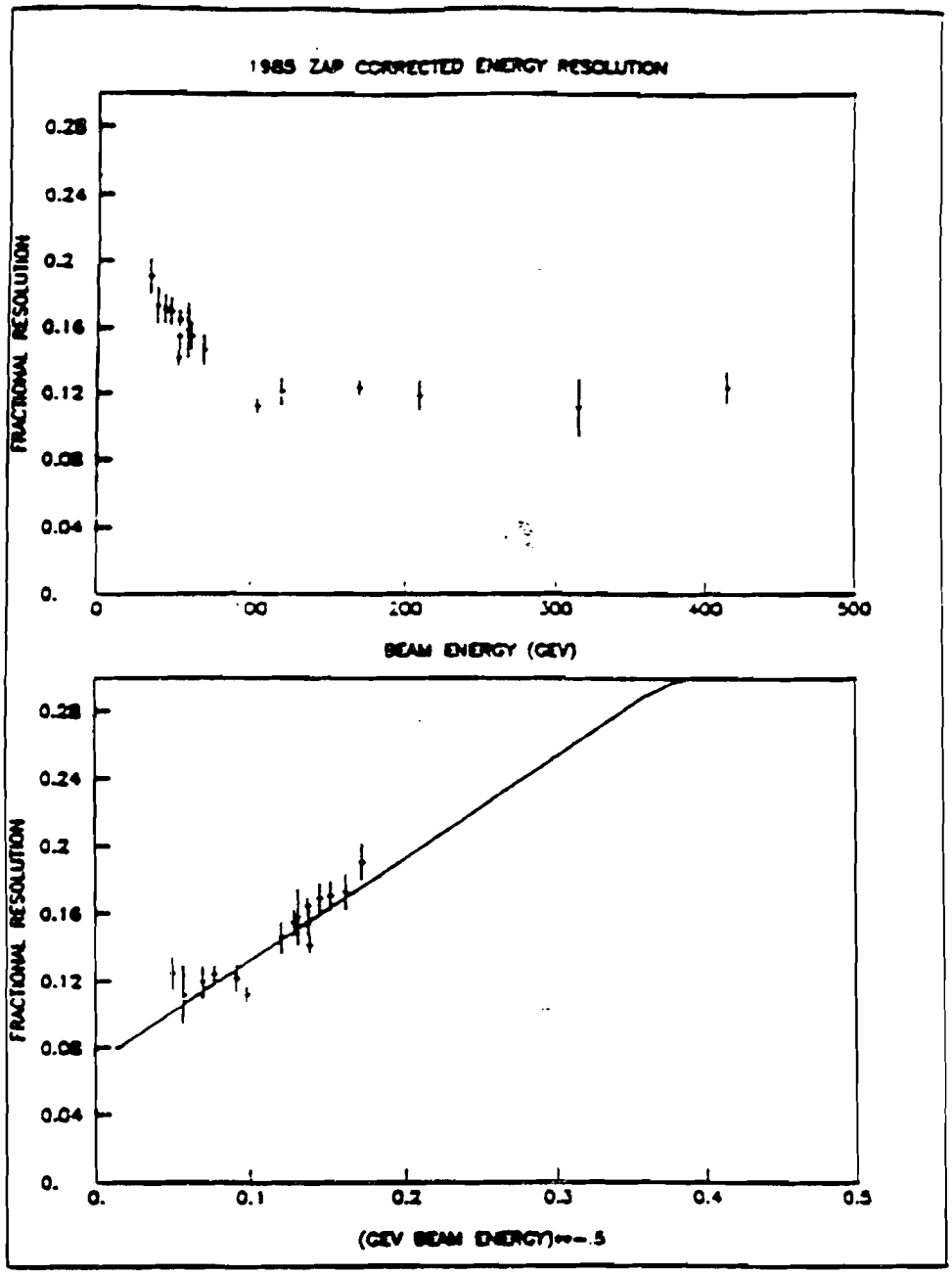

Fig.2.16. Demagnetization-corrected hadronic shower resolution. The upper plot is the fractional shower energy resolution $\sigma(E)/E$ plotted versus the calibration beam energy. The lower plot is $\sigma(E)/E$ plotted versus $1/\sqrt{E}$.

Shower angle resolution can be determined by studying hadronic showers with known angles. We used the hadron test beam data to provide such showers. Of course, the

incident hadron track has to be removed first to make a test beam shower look like a neutrino shower. The inherent uncertainties in the hadron track removal are due to the difficulty in deciding which hits belong to the hadron track and which belong to the shower. The track removal uncertainties translate into uncertainties in the vertex position, to which the shower angle algorithms are very sensitive. The shower angle resolution was worst at low energies being about 40 milliradians at 30 GeV. At high energies the resolution improved to 15 - 20 milliradians at 400 GeV. We used the following representations of the shower angle resolution:

$$\sigma_W(E)/E = 0.011 + 1.064/E\ ,$$
$$\sigma_V(E)/E = 0.0073 + 1.008/E\ , \qquad 2.2$$

where σ_W is the horizontal shower angle resolution, σ_V is the vertical resolution, and E is the hadronic energy in GeV.

2.4.3. Muon Energy Resolution.

Muon energy is determined in the muon spectrometer by measuring the curvature of the muon trajectory. This measurement can not be made arbitrarily accurate however due to the uncertainty introduced by multiple Coulomb scattering in the magnets. The amount of deflection due to scattering ΔX at the rearmost toroid plane can be approximated by the formula $\Delta X \approx \frac{200\ cm}{E_\mu\ (GeV)}$. Given the fact that the spatial resolution of the drift planes is ≈ 2 mm, it is clear that the muon energy resolution is multiple scattering-limited over most of this experiment's energy range.

To determine the muon energy resolution we used a dedicated muon calibration beam. The measurements were taken at four energy points: 50 GeV, 100 GeV, 200 GeV, and 390 GeV. Due to the beamline limitations, our ability to sweep the beam across the detector was very limited. In addition, most of the 390 GeV muons went straight through the hole in the toroidal magnets making them of little use. Another limitation of the calibration data measurement is that we do not have calibration data below 50 GeV, which is again due to the beamline limitations. Fig.2.17 and 2.18 show the fit results for the muon calibration for 50 GeV, 100 GeV, and 200 GeV.

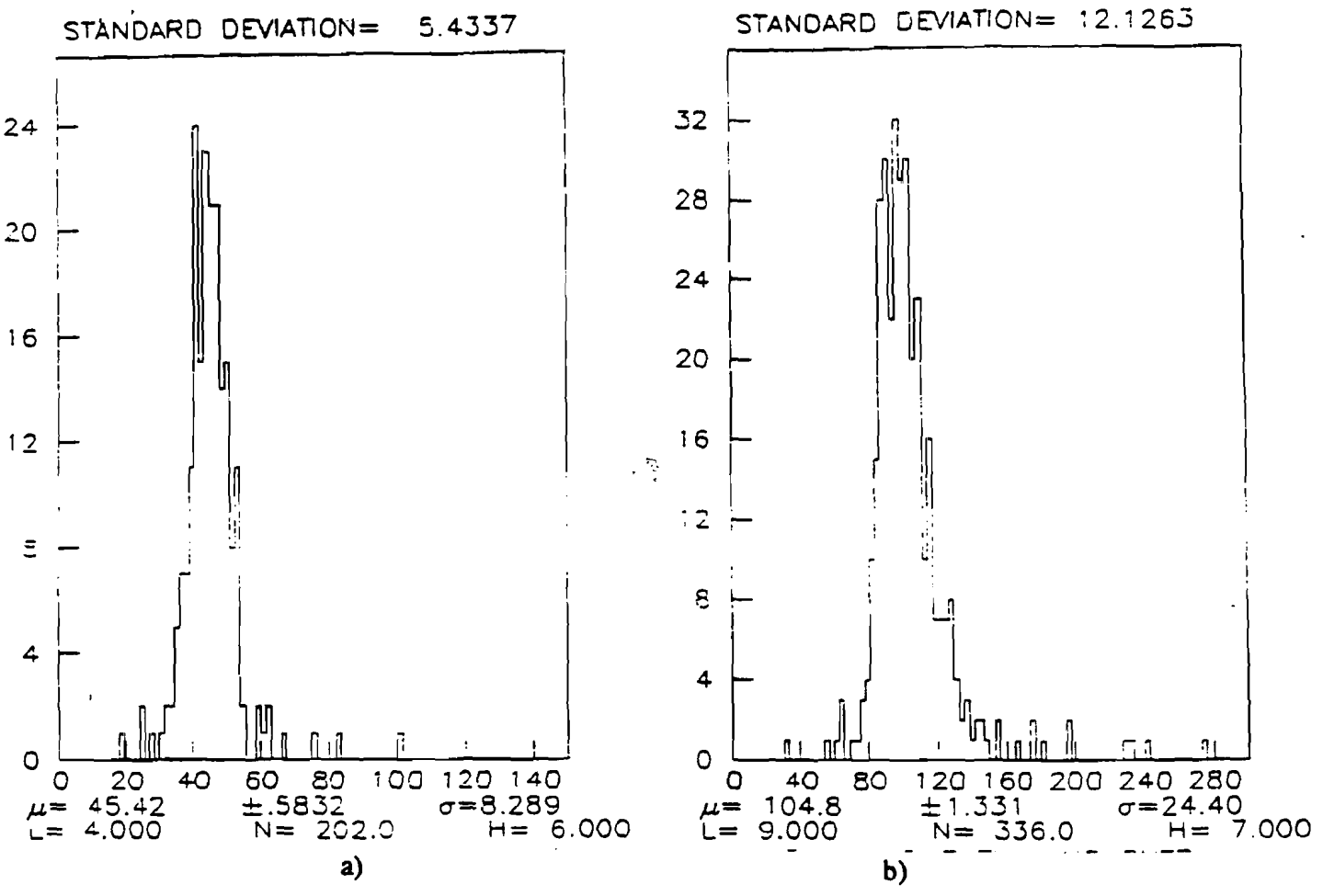

Fig.2.17. Muon calibration fit results for E_{beam} = 50 GeV (a) and E_{beam} = 100 GeV (b). Standard deviation refers to the standard deviation of a gaussian fit to the histograms.

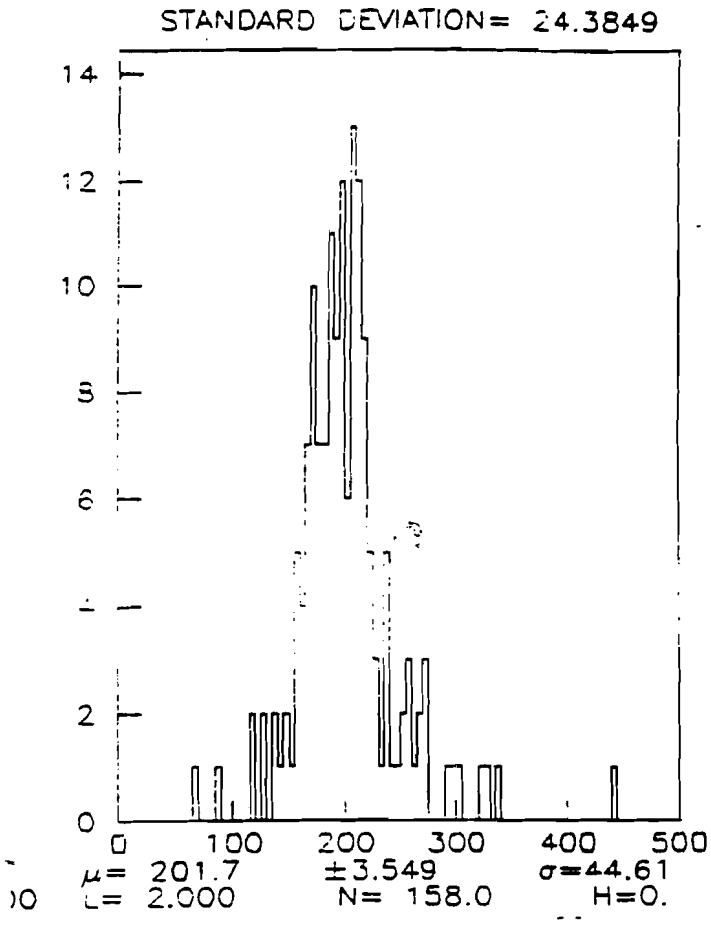

Fig.2.18. Muon calibration fit results for E_{beam} = 200 GeV.

These measurements show that fractional muon momentum resolution $\sigma(E_\mu)/E_\mu$ is essentially flat between 50 GeV and 200 GeV: $\sigma(E_\mu)/E_\mu \approx 12\%$.

To supplement the calibration beam measurements and to extend them to energies below 50 GeV where the bulk of our dimuon data is, we conducted a Monte Carlo study of muon energy resolution. The muons were generated uniformly throughout the calorimeter to make them look like neutrino data, and then propagated through the toroids. The Monte Carlo was made as realistic as possible by incorporating the planes efficiencies, noise hits, energy losses due to various processes, and multiple scattering. The generated events were analyzed by the standard analysis software. The results of this analysis are shown in Fig.2.19.

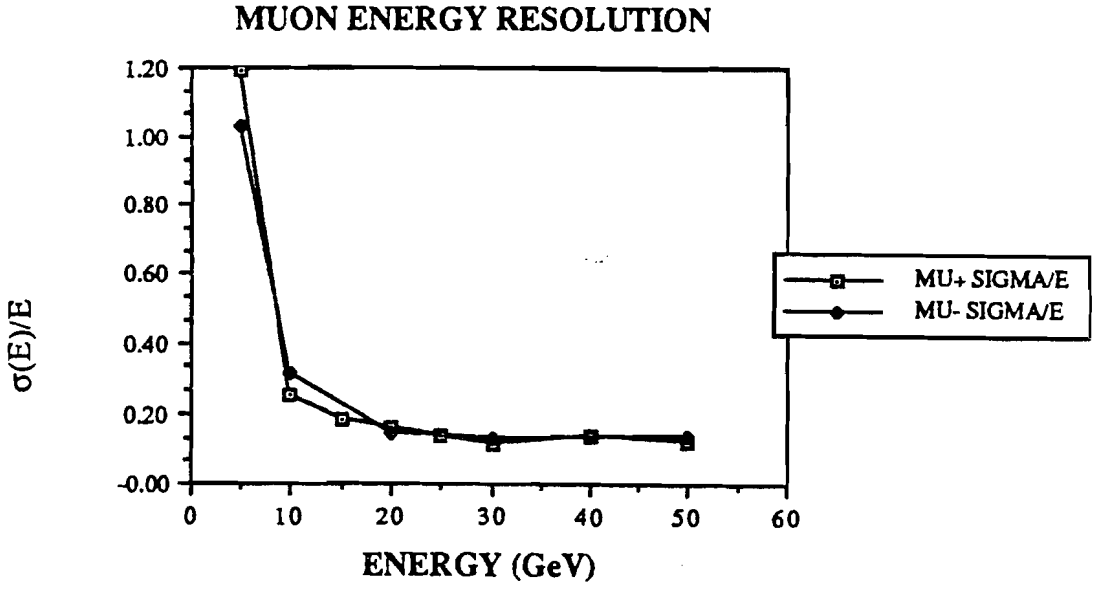

Fig.2.19. Muon energy resolution from the Monte Carlo based study. The vertical axis represents the fractional resolution $\sigma(E_\mu)/E_\mu$, the horizontal axis is muon energy in GeV. The toroids were set to focus negative muons.

Analysis of the Monte Carlo simulation shows that they are consistent with the results obtained from calibration muons at 50 GeV. The energy resolution stays constant down to about 15 GeV. The resolution deteriorates rapidly at muon energies below 10 GeV, where multiple scattering and energy loss make accurate determination of the muon energy more and more difficult.

CHAPTER III.

EVENT SELECTION AND RECONSTRUCTION.

3.1 Introduction.

Neutrino events of interest for this analysis can be characterized as those with one or more muons in the final state. These events had to be filtered from the total neutrino data sample and reconstructed, making them suitable for further analysis. By event reconstruction we mean quantification of an event's topology (i.e. vertex position, particle tracks angles, etc.), as well as other characteristics such as the hadronic shower energy, muon momentum and so on.

Efficient and unbiased event selection is of special importance to this analysis, since the dimuon signal is less than 1% of all Charged Current neutrino events. Hence one must be careful in designing the event selection algorithms for dimuons in order to provide high selectivity needed to filter the dimuon signal out of a much larger sample, and yet ensure that no appreciable number of events are lost in the process.

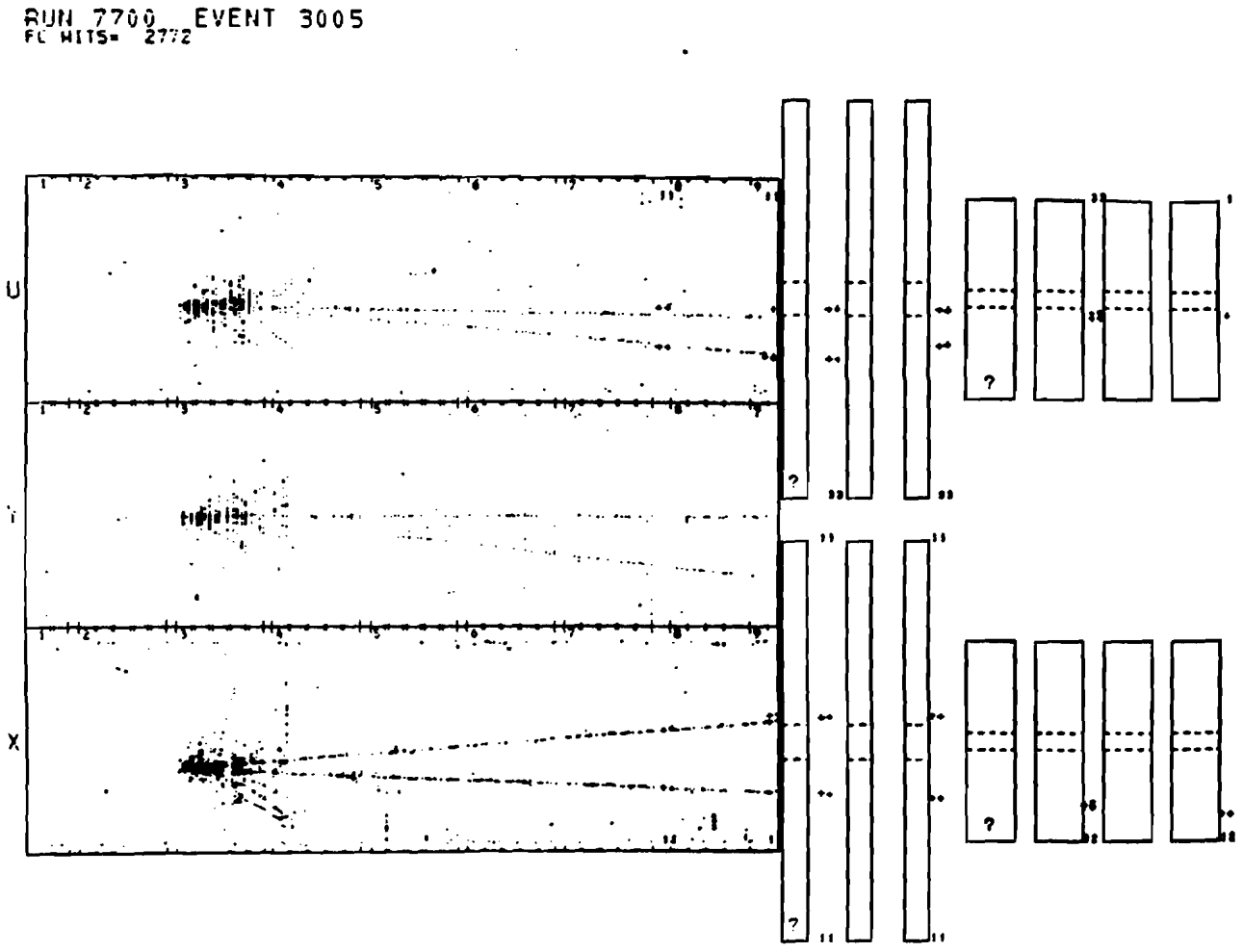

Fig.3.1. A dimuon event in the Lab C detector. Shown are the three views in the flash chambers (X, Y, and U) and the two views in the toroids. The small crosses in the calorimeter and in the toroids represent hits in the calorimeter drift planes and the toroid drift planes, respectively.

3.2 Triggers.

The following triggers were active during the 1985 run: PTH, HiE, QUASI, DIMUON, COSMIC, PEDESTAL and TEST. Of these the first four were neutrino triggers. COSMIC was a cosmic ray trigger which recorded muon tracks in the detector between neutrino

spills. It did not require energy deposition in the calorimeter. PEDESTAL was a special trigger used to determine the proportional tubes pedestal offsets with no tracks present. About 40 events were taken with this trigger in the beginning of each tape. The TEST trigger was dedicated to taking hadron calibration events in between neutrino spills.

3.2.1 PTH, HiE and QUASI Triggers.

The PTH, HiE and QUASI triggers were the primary triggers for Charged Current (CC) neutrino events. They were also responsible for a significant portion of the dimuon data sample. These triggers had the following composition.

$$\text{PTH:} \quad M \bullet \overline{ANTI} \bullet \Sigma\Sigma 75 ,$$

$$\text{HIE:} \quad M \bullet \overline{ANTI} \bullet \Sigma\Sigma 300 ,$$

$$\text{QUASI:} \quad M \bullet \overline{ANTI} \bullet STOP \bullet \overline{\Sigma\Sigma 75} ,$$

where M is the pre-trigger, whose task was to provide an early warning that some energy was deposited in the calorimeter. The M condition went ON when any two proportional planes SUMOUT outputs came ON in coincidence (the coincidence window was 600ns). SUMOUT is a sum of all of a proportional plane's channels, discriminated at 50 mv. This corresponds to a 30% efficiency for a minimum ionizing particle for a single plane. ANTI is the front-of-the detector veto, designed to prevent triggering on charged particles, such as beam muons, arising from neutrino interactions upstream of the detector. It consisted of a scintillator plane, T1 in the front of the detector, and two proportional planes, P4 and P5 in Bay 1. The ANTI composition is $ANTI = T1 \bullet (P4 + P5)$.

The STOP signal was generated upon the coincidence of two plastic scintillator planes, one of which was in the 12' toroids and the other was in the 24' toroids. In addition to

signaling of the presence of a muon in the final state, STOP also provided a timing reference for the drift system.

$\Sigma\Sigma X$ refers to the sum of all proportional planes outputs, discriminated at X mv. Thus $\Sigma\Sigma 75$ required at least 75 mv of total pulse height, $\Sigma\Sigma 300$ required 300mv. $\Sigma\Sigma 75$ threshold of 75mv corresponds to about 5 GeV energy deposition in the calorimeter. As a consequence, the PTH trigger was about 100% efficient above 10GeV. $\Sigma\Sigma 300$ threshold was equivalent to about 100 GeV energy deposition. QUASI was dedicated to quasi elastic events with energy deposition in the calorimeter of less than 5 GeV.

3.2.2 The Dimuon Trigger.

Since the expected dimuon event rate was less than 1% of the charged current event rate, a need was felt for a dedicated dimuon trigger. This trigger was developed early in the 1985 run with the trigger configuration frozen in mid-March of 1985. The trigger was generated upon coincidence of 5 signals:

$$\text{DIMUON} = M_{\text{delayed}} \bullet \overline{\text{ANTI}} \bullet \text{STOP} \bullet \Sigma\Sigma 75 \bullet (\ 2\mu \text{ CONDITION}).$$

M_{delayed} is analogous to the pretrigger for the other neutrino triggers, except that it was delayed by 190ns to accommodate the Dimuon Condition. ANTI, STOP and $\Sigma\Sigma 75$ have been described in the previous sections.

The Dimuon Condition provided indication of multiple muon tracks in the toroids. Since our data acquisition system did not have real-time track fitting capability, the only way to look for multiple muons in the toroids was to look for combinations of multiple hits in the drift planes. Information about the number of hits in a drift plane was provided by the Analog Multiplicity (AM) circuits on the drift interface cards (see Chapter II). Each

interface card had three AM outputs: AM, AM>0 and AM>1. The AM circuits are discriminators that use the combined amplified analog output of all channels on a plane to generate a fixed width (1.5 μs) pulse when the analog output exceeds a preset level. A physical 24' plane corresponds to two "electronic" planes, each having its own interface card. While only AM>1 outputs were used for the 12' planes, both AM>0 and AM>1 outputs were used on the 24-foot planes as shown in Fig.3.2 in order to indicate presence of multiple hits.

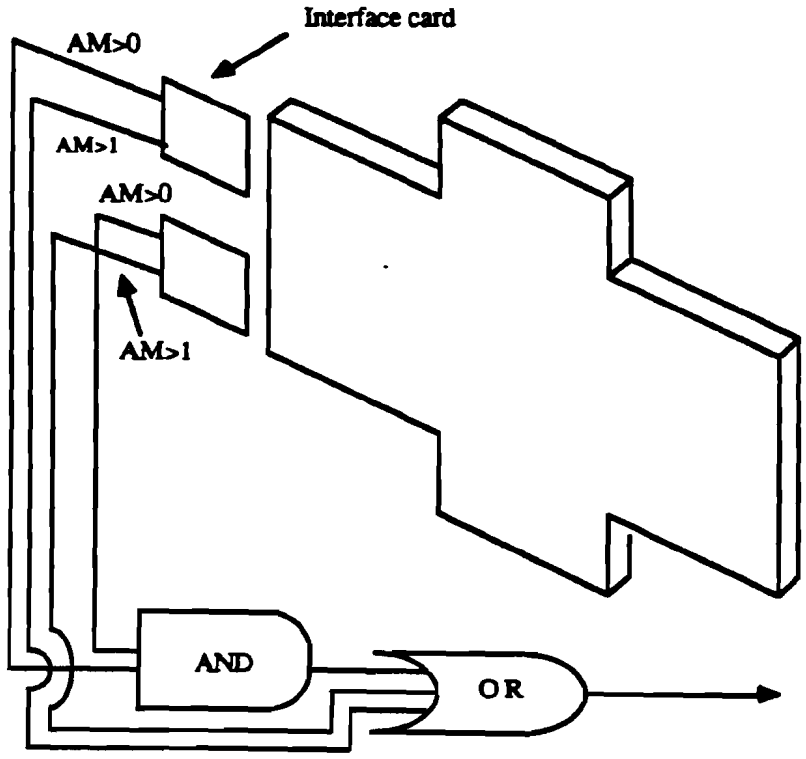

Fig.3.2. Shown is a single 24' plane with two interface cards corresponding to two "electronic" planes attached, and the resulting AM logic.

The Dimuon trigger configuration is shown in Fig.3.3.

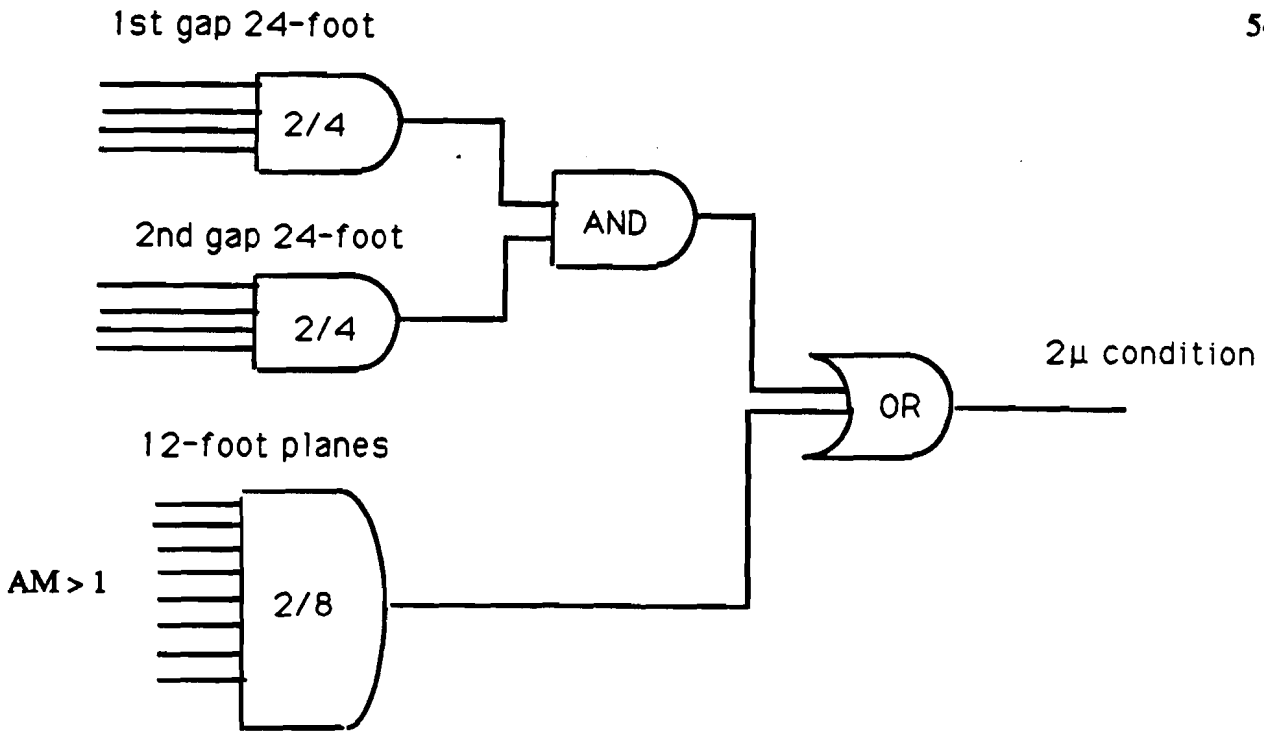

Fig.3.3. Schematic representation of the Dimuon Condition.

As on can see in Fig.3.3, all 12' toroid drift planes are grouped together, whereas the 24' planes are divided into the North and South gaps, each consisting of four planes. Each of the two 24' planes gaps is required to have at least two planes with multiple hits in order to satisfy the dimuon condition. Only two out of eight 12' planes are required to have multiple hits to do the same. The reason for this is that many muons in dimuon events never reach the 12-foot planes because of low energy, so one needs to do most of pattern recognition in the forward portion of the spectrometer, leaving the 12' planes to act more as a safety net.

Because of the size of the detector, the AM signals from the drift planes took a rather long time to reach the central logic rack, where the trigger was formed. Depending on the plane location, these delays varied from 70ns to 140ns. To accommodate the lateness of the Dimuon condition, the M signal was delayed, so that the Dimuon trigger was formed

Dimuon condition, the M signal was delayed, so that the Dimuon trigger was formed **190ns** late relative to other neutrino triggers. This delay has some importance for energy reconstruction in the flash chambers, since they loose ionization rapidly as a function of time elapsed between a particle going through and triggering. It was found that this loss was ≈7.5% and was essentially energy independent. The Dimuon condition efficiency can be calculated as a function of the drift planes efficiency. Despite the average efficiencies of ≈85% for the 12' planes and ≈81% for the 24' planes, the Dimuon condition is found to be nearly 100% efficient.

3.2.3. Triggering Strategy.

The main goal of the 1985 run was the accumulation of rare dimuon events. Therefore it was decided to suppress the minimum bias neutrino trigger, PTH, and to a lesser degree the QUASI trigger, in favor of the Dimuon and the High Energy triggers. To accomplish this, the PTH and QUASI triggers were "prescaled", i.e. only a fraction of events that satisfied these triggers were taken. The prescale factor for the PTH trigger was **11**, which means that every 12th PTH event was actually taken. The prescale factor for the QUASI trigger was **2**. To insure that if there were no rare events in a given neutrino spill, at least some ordinary neutrino events would still be taken, a twofold triggering strategy was adopted. Each neutrino spill was divided into two time intervals, which we call the Beam Gate (BG) and the Tail Gate (TG). During the Beam Gate, which lasted for about 90% of the neutrino spill, the prescaling described above was in effect. If no events were taken during the BG, the prescaling was turned off, so that the detector could still take minimum bias PTH events as well as QUASI events during the TG which was the remainder of the neutrino spill..

3.3. Vertex Reconstruction.

Vertex finding is the first step in the event reconstruction process and is a prerequisite for other steps, such as calorimeter track fitting, shower length and angle determination, etc. The vertex finding program VRTDRV that we used has been described in detail elsewhere[3.1], therefore we give only a brief description here. First, the program made a crude longitudinal shower position estimate using proportional planes. It then made histograms of flash chamber hits in a dynamically adjusted window and fit a straight line to centroids, favoring narrow parts of the shower.

The efficiency of the vertex finding algorithm was measured with full shower Monte Carlo events. It was found that for charged current events the program was essentially 100% efficient for shower energies above 5 GeV. To determine the vertex resolution, VRTDRV results were compared to a visual scan by physicists. Two classes of events were used: hadron calibration events and charged current neutrino events. In both cases the VRTDRV resolution was found to be about 3 cm in the lateral as well as in the logitudinal direction, and roughly independent of the energy of the shower [3.2].

3.4 Calorimeter Track Fitting.

Calorimeter track fitting was performed in two stages, let us call them Coarse Fitting and Fine Fitting. The algorithms involved in both stages had similar logic, the main difference being spatial resolution.

3.4.1. Coarse Fitting.

Starting at the primary neutrino vertex found by VRTDRV, all of the calorimeter downstream of the vertex was divided into 42 angular slices called "bins". The angular sweep of each bin was 0.1 rad. The calorimeter hits were sorted into these bins depending on their position. The program then proceeded to determine the lengths of possible tracks

within each bin. Two factors made this task difficult: flash chamber inefficiency and noise. Variations in the flash chamber efficiency could make portions of tracks disappear, causing the program to think that the track had stopped. Noise hits, on the other hand, could trick the program into finding more "tracks" than there actually were. The algorithm for track length determination that we employed is statistical at heart. It works as follows. On the first pass the program "walks" downstream of the vertex counting the total number of chambers with hits N_{tot} in a given bin. By the time it reaches the end of the detector, the program has calculated the expected number of hit chambers and the error on that number according to the formulae:

$$\sigma^2 = \sum_i [\, \varepsilon_i (1 - \varepsilon_i)] \ , \qquad 3.1$$

where ε_i are the flash chambers efficiencies, and the sum is over all flash chambers.
On the second pass the program starts at the back of the calorimeter and walks upstream , at each step calculating the quantity Y_i:

$$Y_i = \frac{N_i - \langle N_i \rangle}{\sigma_i} , \qquad 3.2$$

where N_i is the number of hit chambers upstream of the current flash chamber, $\langle N_i \rangle$ is the expected number of chambers with hits, and σ_i is the error on $\langle N_i \rangle$. Thus Y_i is the number of standard deviations from the expected number of flash chambers with hits for the track upstream of the current point. This process stopped when Y_i exceeded the maximum $Y_{max} = -5$, meaning that it reached the point where the track ceased being continuous.

In certain situations, namely in cases of tracks with long gaps with no hits, the statistical approach alone tended to make tracks shorter than they actually were. To correct for that the algorithm looked for hits downstream of the newly found end of the track, and, if there were too many, it would start at the other end of the gap. This process could be repeated up to four times, or until there were less than four continuous flash chambers hit outside the track limits. At this point a cut of **400 cm** on track length was applied to cut down on short tracks. Next the program searched for 3-view matches of bins with tracks. For each track the matching was performed by comparing the measured Y slope with the Y slope calculated from the X and U slopes :

$$SLOPE_y = SLOPE_u - 2 * TAN(10) * SLOPE_x \qquad 3.3$$

The maximum allowed slope difference for 3-view matches was 0.2 rad.

3.4.2. Fine Fitting.

This stage of the fitting process used the results of the coarse fitting as a starting point. Now, however, each bin was additionally divided into ten segments with an angular sweep of 0.01 rad each. The fits were performed using the linear least squares method with the road width of 12 clock counts (about 6 cm). An important feature of the fitting algorithm is that it actually does two fits for every track: the downstream weighted fit and the upstream weighted fit. The downstream weighted fits provide the optimal starting point for the subsequent track fits in the toroids, since it emphasizes the hits closest to the toroids. The upstream weighted fits were designed to provide the best measurement of the track's origin, by emphasizing the hits near the vertex. Even though the tracks were fit to a straight line, the flexible weighting scheme allowed for curved tracks. There was also no restriction on crossing a segment's boundary. The track length is determined in the same manner as

described in the previous section. The minimum length requirement for a muon candidate again was 400 cm.

These segment fits often produced more "track candidates" than there were real tracks. Two track candidates were considered discrete if they satisfied certain requirements based on the number of non-shared hits and on the average hit position difference. If the track candidates did not satisfy the discreetness criteria, they were considered the same, and only the best of the pair was retained. The best track was determined as the one with the highest number of hits or the longest one.

In the next step the discrete tracks were 3-view matched. The maximum number of matches per event was 10. The last step in the calorimeter track fitting process was a simultaneous 3-view fit of the 3-view matched tracks.

3.5 Toroid track fitting.

The purpose of toroid track fitting is to determine a charged particle's (usually a muon) momentum by calculating its curvature in the presence of the known magnetic field. This task is complicated by the particle scattering and losing energy while propagating through the magnets. In the case of several particles going through the spectrometer the task of pattern recognition of individual tracks becomes equally important. The toroid track reconstruction strategy adopted for this analysis was two stage. First, preliminary fits were performed using discrete values of momentum as starting points, and simple interpolation/extrapolation was used to cover the momenta between those points. It is at this stage that pattern recognition was accomplished, and drift plane hits to be used for each track were selected. To simplify the fitting process the drift information was not used at this stage thus limiting the spatial resolution to the wire spacing (about 2.5 cm). In the second

stage the final fits were performed, which employed the full covariant error matrix and full available drift information about hit positions.

3.5.1 Coarse fitting and hits selection.

For each calorimeter track a family of trajectories was projected into the toroids at 19 fixed values of inverse momentum 1/p. Next, the program went through the drift planes beginning with the most downstream one. For each plane a group of inverse momenta, corresponding to the trajectories that hit the plane, was found. For each hit in the plane the program then attempted to find a pair of consecutive trajectories which straddled the hit. In case there was no such pair, another pair of trajectories was found, such that one of them came within a road width of the hit. The road width was $10 + 2\ \sigma_{scat}$ (cm), where σ_{scat} is the scattering error at that plane. For a straddling pair of trajectories the program made a linear interpolation in 1/p to find a trajectory that went through the hit, otherwise a linear extrapolation in 1/p was made to do the same. Let us call this calculated extrapolated/interpolated inverse momentum $1/p_0$. The program then proceeded to calculate the trajectory positions at this value $1/p_0$ for all the planes using the same interpolation/extrapolation technique. To gauge the deviation of the current trajectory from the optimum, the program used a simplified χ^2:

$$\chi^2(1/p) = \sum_i W_i\,(Y_i - F_i(1/p))^2\ , \qquad 3.4$$

where Y_i is the (measured) hit position at the i -th plane, $F_i(1/p)$ is the calculated trajectory position at 1/p value of inverse momentum, $W_i = 1/\sigma_i$ is the weight, which includes contributions from both scattering and resolution errors: $\sigma_i = \sigma_i^{scat} + \sigma_i^{res}$. The sum is taken over all drift planes.

Let us define $q_0 = 1/p_0$ and $q = 1/p$. For small $\Delta q = q - q_0$, $\chi^2(q)$ can be calculated in the first order as:

$$\chi^2(q) = \chi^2(q_0) - 2\Delta q \sum_i W_i (Y_i - F_i(q)) \frac{\partial F_i(q)}{\partial q} \qquad 3.5$$

Again Y_i and F_i are the measured and the calculated positions respectively at the i-th plane, and W_i is the weight associated with the scattering error.

Ideally, a fit should use all the hits within its road. In the real world, however, some of the hits may be due to noise, and in the case of multi-muon events, some hits within the same road may belong to different tracks. Because of these complications the program could reject ("zap") hits in order to improve the fit (i.e. minimize its χ^2). If after removal of a hit χ^2 improved by a factor $P_{fact} = 6$, that hit was zapped, after which new $1/p_0$ and χ^2 were calculated.

In addition to being able to fit a track one must also be able to gauge the quality of a fit. χ^2 alone is not enough to do that, since it is relatively easy to make a perfect fit by using just one hit, for example, and a trajectory that goes right through it. To better judge the quality of a fit we used the following quantity:

$$Q = -\log(P_\chi (\chi^2,N) * P_{miss} (N_{miss},N_{hit}) * P_{noise} + Q_{bias}) , \qquad 3.6$$

where $P_\chi(ß,N)$ is the integral of the χ^2 distribution from ß to infinity, or in other words, it is the probability of having χ^2 greater than ß. N is the number of degrees of freedom. $P_{miss}(N_{miss},N_{hit})$ is the probability of missing N_{miss} wire "layers" (drift plane faces) while hitting N_{hit} layers. It is calculated according to the binomial distribution, using the known

(average) drift planes' efficiency. This term is designed to discourage fits to random hits downstream of the spectrometer with no hits used in the upstream planes. P_{noise} is the probability of having noise hits outside the road. And finally, Q_{bias} is a bias term against very soft (less than 3 GeV) fits.

3.5.2. Drift Corrections.

Up to this point we have not used the drift information in order to simplify and speed up the fitting process. At the final stage of the toroid track fitting, however, the full hit position information as recorded by the toroid drift system was used to provide the maximum spatial resolution of about 2mm. Knowing the drift time for a given hit wire is not enough to determine the exact hit position. There is an infinite set of possible positions lying on a circle of radius $R = V_{drift} * T_{drift}$ around the wire, where V_{drift} is the drift speed and T_{drift} is the drift time. It turns out that in order to determine a hit position uniquely, one must have at least one pair of back-to-back hits, i.e. hits in the adjacent layers of a drift plane as shown in Fig.3.4.

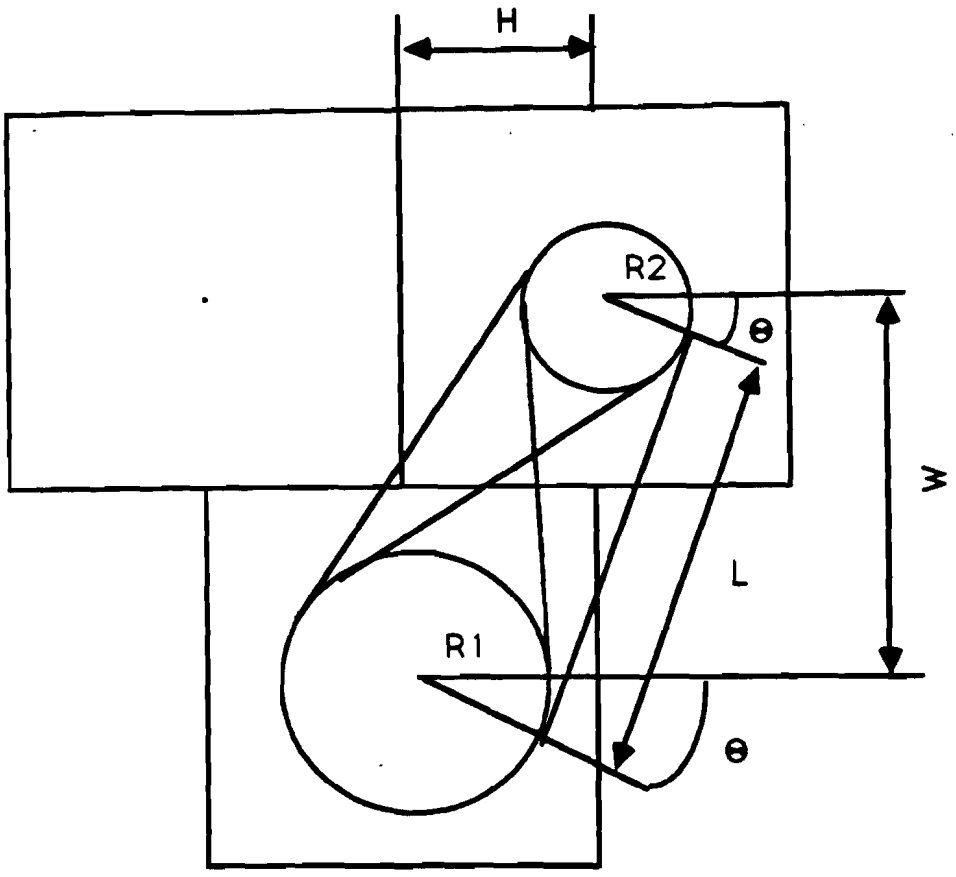

Fig.3.4. Possible slopes for a pair of back to back drift hits.

There are four possible solutions (slopes) for a particle passing through a double layer of drift cells:

$$\cos\vartheta = \frac{-H\,(\pm R_2 - \pm R_1) + \sqrt{W^4 + H^2W^2 - W^2\,(\pm R_2 - \pm R_1)^2}}{H^2 + W^2} \qquad 3.7$$

To determine the true hit position one must compare the four possible slopes with the best estimate, obtained by projecting a muon through the toroids at the value of momentum found in the course of the preliminary fitting. The best match fixes the true hit position.

3.5.3 Final Fits.

In the course of the final fits the full correlated error matrix W_{ij} was used to calculate χ^2:

$$\chi^2 = \sum_{i,j} (Y_i - F_i)\, W_{ij}\, (Y_j - F_j)^T \quad . \qquad 3.8$$

It can be shown that for a particle in a magnetic field propagating in matter, χ^2 is proportional to the square of inverse momentum. Therefore the program fit χ^2 to a parabola in 1/p. Unlike the previous stage, the algorithm was not allowed to add or remove hits from a track. The program started at the best guess for 1/p and calculated χ^2 at 6 points before trying to find the minimum of the parabola. The process was repeated with various step sizes until the best fit was achieved.

3.6 Data Summary Tapes (DST).

Event selection began with splitting off neutrino triggers, i.e. all triggers except test beam events and cosmics. The resulting 56 neutrino tapes contained 61784 events after fiducial cuts. A flow chart of the event selection process is shown in Fig.3.5.

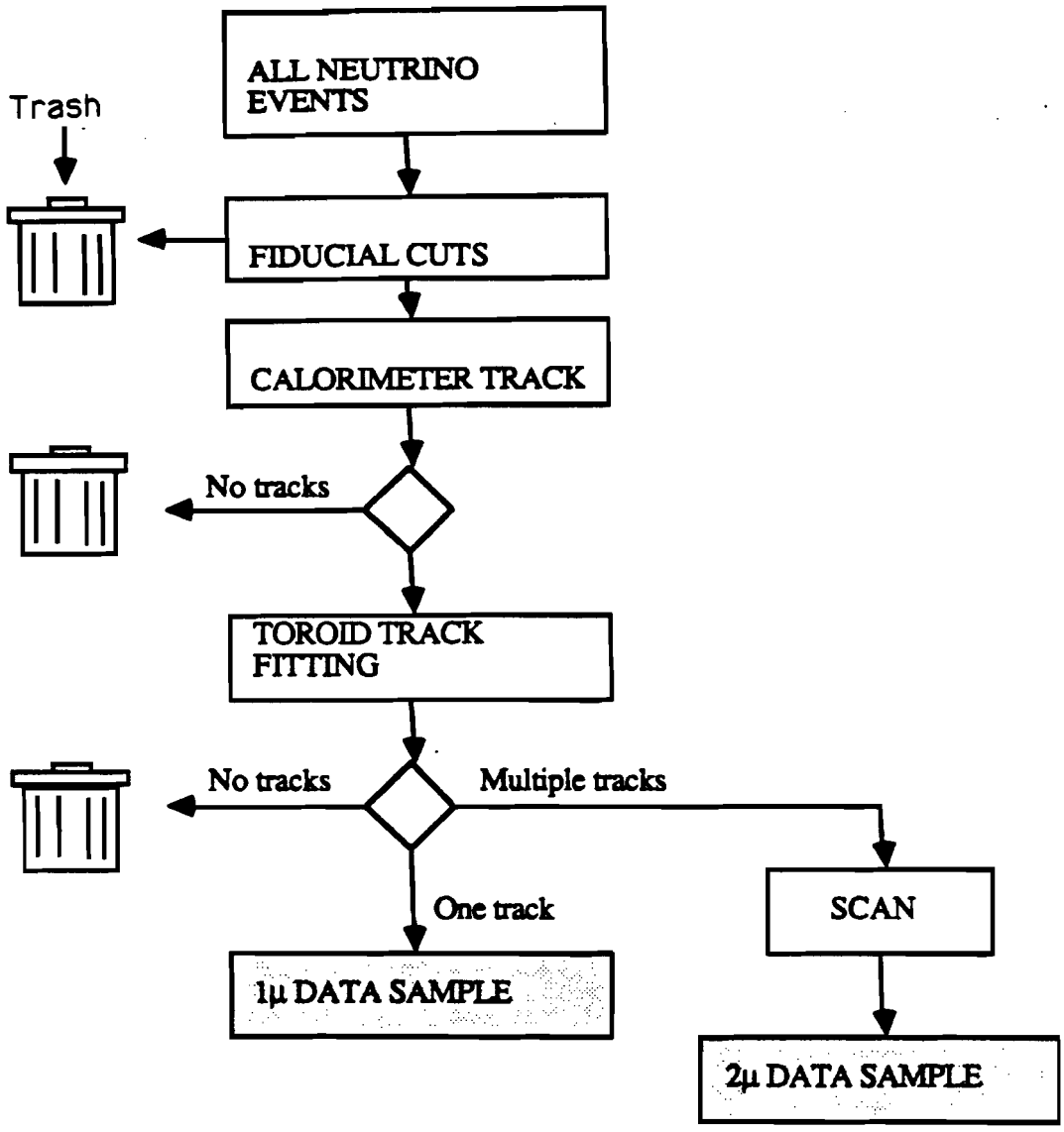

Fig. 3.5. Event selection flow chart.

We used the Fermilab cluster of Cyber's 875 to perform all off-line analysis. Because of the Cyber's memory limitations the full DST cycle required 3 passes. Pass A performed fiducial cuts, vertex reconstruction and calorimeter track fitting. Pass B executed the toroid track fitting. Pass C reconstructed the hadronic shower parameters: energy, length, angles.

The event selection process began with vertex reconstruction followed by the fiducial cuts on the vertex position. The fiducial cuts were designed to ensure the full containment of hadronic showers inside the calorimeter. Laterally the vertex could be no closer than 200 clock counts (about 86 cm) to the calorimeter's edges in each view. Longitudinally the vertex had to be between chambers 41 and 400 (out of a total of 592).

At each stage in the track fitting process events with no muon tracks were discarded. The remaining events were classified as charged current events (one muon track) or dimuon candidates (multiple muon tracks). One important requirement for the toroid tracks was that a good fit had to use at least three hits, not all of them in one view. The hits were also required to be outside of the magnet hole. These requirements were designed to ensure reliability of the fits.

Tables 3.1 and 3.2 show the the statistics of DST Passes A and B for Beam Gate and Tail Gate events. Pass C was essentially 100% efficient, so the numbers for Pass B represent the final numbers of events.

Table 3.1. DST Pass A statistics. Events that passed the fiducial cuts and had at least one calorimete_ muon track.

	Beam Gate	Tail Gate	Total
Events in fiducials	61784	17263	79047
Single muon	47673	14252	61925
Multiple muons	10322	2179	12501

Table 3.2. DST Pass B statistics. Events with at least one toroid track.

	Beam Gate	Tail Gate	Total
Input	57995	16431	74426
Single track	52821	14360	67181
Multiple muons	1133	134	1267

3.5.1.Single Muon Charged Current Events.

Single muon charged current (CC) events were selected solely on the basis of the number of fit toroid muon tracks . Except for the fiducial cuts and the usual fit constraints, the only cut was the minimum shower energy requirement $E_{shower} > 10$ GeV. This cut's purpose was to eliminate the effects of the triggers inefficiency at low hadronic energies. Table 3.2 shows the numbers of CC events for Beam Gate and Tail Gate for different types of trigger. Note that an event could satisfy more than one trigger condition and consequently would have more than one trigger bit set.

Table 3.3. Single μ events after Pass B with $E_{shower} > 10$ GeV, broken down by sign and trigger type.

	Beam Gate	Tail Gate
Total	50539	13631
μ-	44147	11722
μ+	6392	1909
Di-μ	22434	162
HiE	19393	2989
PTH	8155	13272
QUASI	2881	623

3.6. Dimuon Scan.

The final step in the selection of dimuon events was a scan by physicists. The event categories that were rejected at this stage were:

1) trimuon events,

2) out of time events (for example, two superimposed single muon events),

3) events with obvious hardware problems such too much noise, etc.

Out of a total of 1267 dimuon candidates 882 events (803 Beam Gate and 79 Tail Gate) were selected as the final dimuon data sample.

3.7. Event selection efficiency.

Given the weakness of the dimuon signal and the complexity of the associated event selection and reconstruction software, it is important to understand the efficiency of the whole event selection process for both dimuons and single muon charged current events. Perhaps the simplest way to estimate these efficiencies is to compare the results of a visual scan of some unbiased neutrino data sample with the output of the event reconstruction software from the same sample. However, since visual scanning by physicists is very labor intensive, it is difficult to accumulate enough statistics for a good efficiency determination throughout the entire kinematic range of the experiment. In fact, in the case of dimuons there is simply not enough data to do that even if we were to scan our entire neutrino data sample.

We studied the efficiency of the event selection process using Monte Carlo (MC) simulations of charged current events and dimuon events. The physics of both MC's is described in Chapter IV. Our goal was to generate single muon and dimuon "events" in our detector which would be as close as possible to real events, and could be analyzed by the

standard analysis routines. The calorimeter response was simulated by using a full shower MC [3.1] which modeled hadronic shower development and generated hits in the flash chambers, the proportional tubes, etc. The toroid part of the simulation propagated muons through the spectrometer and generated hits in the drift chambers. Such factors as the drift planes efficiencies and noise as well as multiple scattering and energy loss were taken into account. The resulting MC events were then analyzed by the standard DST-maker used on data. Event selection efficiency is determined by comparing the output of a DST pass with its input. For single muon charged current events which passed the fiducial cuts and with $E_\mu > 10$ GeV, the total efficiency is $\approx 95\%$. For dimuon events after fiducial cuts and with $E_\mu > 10$ GeV for both muons, the overall efficiency is $\approx 90\%$. The event selection efficiencies are described in more detail in Appendix A.

CHAPTER IV.
MONTE CARLO

4.1 INTRODUCTION.

Monte Carlo (MC) simulation is used almost universally in modern high energy physics experiments. The reasons for that are manyfold. Experiments are so complex, that even if one were to understand every part quite well, it is still very difficult to fold together characteristics of various pieces of hardware and software in a mathematically coherent way to give an analytical description of the experiment. On a more fundamental level, the physical processes of high energy experiments are inherently probabilistic, so the random nature of the MC technique fits in naturally.

We have used two different kinds of MC simulations in this thesis. The first kind simulated deep inelastic charged current neutrino-nucleon scattering and the second modeled opposite sign dimuon production via creation and subsequent decay of charmed quarks in neutrino-nucleon interactions. The goals of the simulation are to provide estimates of detector acceptances, event selection efficiencies and biases, and to enable comparison of dimuon data with a specific theoretical model. The physics for both MC's was generated in a compact 4-vector form. The simulation of the detector response, however, was performed in two different ways. In what we call the "hybrid" approach, the calorimeter response was simulated by smearing true quantities according to known resolution functions. Muon tracks in the toroids, on the other hand, were simulated in much more detail where individual particles were propagated through the toroids and hits were generated, including noise hits. Multiple scattering and energy loss were also included. The muon spectrometer part of MC events could then be analyzed by the standard muon package.

The main reason for adopting this approach was the prohibitively large amount of time required to generate the needed large number of full shower Monte Carlo events for good comparisons of MC with data. On the other hand, full simulation of toroid tracks preserved all effects of detector acceptances and the muon package quirks. This approach was used for all comparisons of data with MC for both dimuon events and single muon charged current events. The only task for which it was necessary to generate full shower MC events was the study of event selection efficiencies, and so several thousand MC events of that type were generated.

4.2 Beam Files.

4.2.1 Standard Beam Files.

The first step in MC event simulation is to create computer files containing the simulated energies and positions of incoming neutrinos and antineutrinos with the integrated fluxes normalized to the data. Both the neutrino and the antineutrino beam files were created by the Monte Carlo program NUADA [4.1], using a particle production model based on data taken at CERN[4.2]. Fig.4.1 shows neutrino and antineutrino fluxes with 1.2m fiducial radius in the LabC detector for a primary proton energy of 800 GeV.

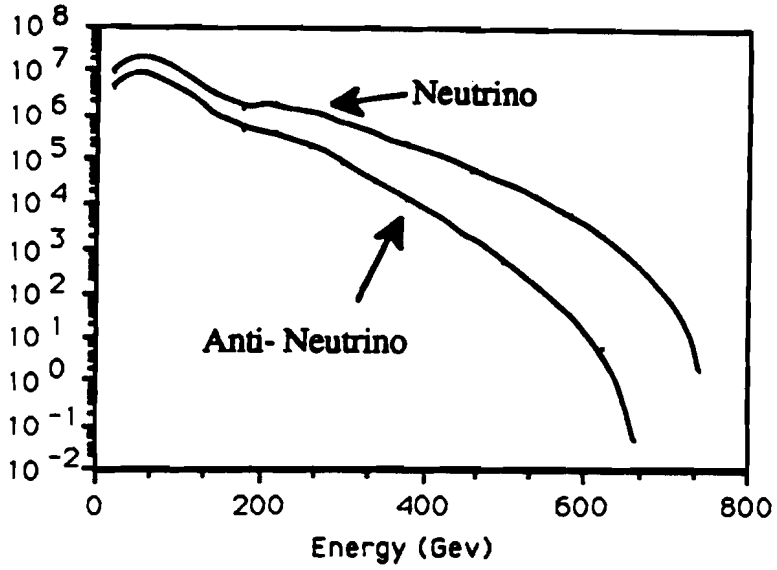

Fig.4.1 Neutrino and antineutrino fluxes in the LabC detector.The units along the vertical axis are $\upsilon/(m^2$ Gev 10^{13} protons)

These beam files were used separately to generate single muon MC events. For the purpose of simulating dimuons, however, it was necessary to create a combined beam file containing both neutrinos and antineutrinos since both were present in the quadruplet beam.

4.2.2. Combined Neutrino + Antineutrino Beam File.

Since there was no secondary charged particle sign selection in the quadruplet beam, both π^+, K^+ and π^-, K^- were present, and therefore antineutrinos constituted a sizable portion of the total beam flux. To determine the ratio of the antineutrino flux to the neutrino flux the following method was adopted. First, all Charged Current events with one muon in the final state were classified as neutrino induced or antineutrino induced, depending on the muon sign. Then single muon MC events of both charge signs were created separately and analyzed in the same manner as the data events. The only acceptance cuts applied to all data

sets, apart from the usual fiducial cuts, were a minimum hadronic energy requirement of 10 GeV, and the three hits in the toroids requirement necessary in order to be able to sign the muon accurately. Since it was difficult to reproduce the results of the trigger prescaling (see Chapter III) that was in effect for the Beam Gate portion of the data, we decided to use only the minimum bias events taken with the PTH trigger. Table 4.1 shows the number of accepted events for the Beam Gate and Tail Gate.

Table 4.1. Events used for antineutrino vs neutrino flux ratio analysis.

	BG events (PTH only)	TG events	Total events
$N_{\mu+}$	1119	1909	3028
$N_{\mu-}$	6937	11722	18659

The purpose of the MC analysis was to determine how many "neutrinos" or "antineutrinos" it took to produce an accepted event. Care was taken to generate neutrino and antineutrino events in exactly the same way, using the same limiting function for the rejection method[4.3]. The MC "flux" count was incremented by one every time a neutrino/antineutrino was read off the beam file in order to generate a Charged Current event. Thus we obtained the following ratios of MC neutrinos/antineutrinos per event with the same cuts as applied to the data:

$$\left.\begin{aligned} R^{\upsilon} &= 7.799 \pm 0.003 \\ R^{\bar{\upsilon}} &= 17.21 \pm 0.08 \end{aligned}\right\} \Rightarrow \frac{S_{\bar{\nu}}}{S_{\nu}} = \frac{R_{\nu}}{R_{\bar{\nu}}} = 0.453 \qquad (4.1)$$

Blair : 0.508 ± 0.035

CCFRS : 0.491 ± 0.012

Let us remark here that the numbers of Eq.4.1 are in arbitrary MC units, and only their ratio has any real significance. To calculate the ratio of the antineutrino to the neutrino flux, one must use the observed numbers of events of both kinds plus the Monte Carlo calculated ratios of (anti)neutrinos per event according to the formula:

$$\frac{\Phi^{\bar{\upsilon}}}{\Phi^{\upsilon}} = \frac{N^{exp}_{\mu+}}{N^{exp}_{\mu-}} \frac{R^{\bar{\upsilon}}}{R^{\upsilon}} = 35.8 \pm 0.7\ \% \ , \qquad 4.2$$

where Φ^{υ} is the integrated neutrino flux, $N^{exp}_{\mu-}$ and $N^{exp}_{\mu+}$ are the numbers of neutrino and antineutrino events, respectively, from Table 4.1. The (anti)neutrinos per event ratios R are given by Eq. 4.1.

4.2.3. Event misclassification corrections.

The method for determining relative fluxes, as described above, has certain inherent errors due to event sign misclassification in both the data and Monte Carlo. Let us first define sign classification efficiencies ß for the Monte Carlo events:

$$\beta_{\mu+} = \frac{N_{\mu+}}{N^{tot}_{\mu+}} \ , \qquad \beta_{\mu-} = \frac{N_{\mu-}}{N^{tot}_{\mu-}} \ , \qquad 4.3$$

where, for example, $N_{\mu+}$ is the number of MC events identified by the event reconstruction program as having a $\mu+$ in the final state, and $N^{tot}_{\mu+}$ is the total number of accepted μ^+ MC events. We now make the assumption that the sign classification efficiencies for the data are the same as for the MC "events". This assumption is entirely reasonable since the sign

assignment depends primarily on track fits in the toroids, and both MC and data analysis use the same software to do the fitting in the toroids. We can now write the following equations for the observed numbers of μ^+ and μ^- events:

$$N^{exp}_{\mu^-} = \beta_{\mu^-} N_{\mu^-} + (1 - \beta_{\mu^+}) N_{\mu^+} \quad , \qquad 4.4$$

$$N^{exp}_{\mu^+} = \beta_{\mu^+} N_{\mu^+} + (1 - \beta_{\mu^-}) N_{\mu^-} \quad ,$$

where $N^{exp}_{\mu^-}$ and $N^{exp}_{\mu^+}$ are the observed numbers of neutrino and antineutrino events, and N_{μ^-} and N_{μ^+} are the true (unknown) numbers of events. Solving this system we get:

$$N_{\mu^-} = \frac{1}{|A|}[\beta_{\mu^+} N^{exp}_{\mu^-} - (1-\beta_{\mu^-}) N^{exp}_{\mu^+}] \quad , \qquad 4.5$$

$$N_{\mu^+} = \frac{1}{|A|}[-(1-\beta_{\mu^+}) N^{exp}_{\mu^-} + \beta_{\mu^-} N^{exp}_{\mu^+}] \quad ,$$

where $|A| = \beta_{\mu^-} \beta_{\mu^+} - (1 - \beta_{\mu^-})(1 - \beta_{\mu^+})$. Therefore the ratio of the true number of antineutrino events to neutrino events is given by:

$$\frac{N_{\mu^+}}{N_{\mu^-}} = \frac{\beta_{\mu^-} N^{exp}_{\mu^+} - (1 - \beta_{\mu^+}) N^{exp}_{\mu^-}}{\beta_{\mu^+} N^{exp}_{\mu^-} - (1 - \beta_{\mu^-}) N^{exp}_{\mu^+}} \qquad 4.6$$

Let us now reevaluate Eq.4.2. From the MC analysis we find $\beta_{\mu^-} = 0.996 \pm 0.009$ and $\beta_{\mu^+} = 0.992 \pm 0.022$. From Table 4.1 we find $N^{exp}_{\mu^-} = 18659$ and $N^{exp}_{\mu^+} = 3028$. Thus the observed ratio is $\frac{N^{exp}_{\mu^+}}{N^{exp}_{\mu^-}} = 0.1623 \pm 0.0032$, and the true ratio as given by Eq.4.6 is $\frac{N_{\mu^+}}{N_{\mu^-}}$ $= 0.155 \pm 0.003$. Applying this corrected ratio to Eq.4.2 we get the flux ratio corrected for events misclassification:

$$\frac{\Phi^{\bar{\nu}}}{\Phi^{\nu}} = 34.2 \pm 0.6\ \% \qquad 4.7$$

Thus correcting for the sign misclassification lowers the flux ratio by about 1.5% compared to the uncorrected ratio of Eq.4.2.

The combined beam file generation was performed using the pure neutrino and pure antineutrino beam files as the input. The program threw a random number and used the ratio of Eq.4.7 to decide which beam file should be referenced. To eliminate possible effects of detector edges, the same lateral vertex position cuts used in the data and the Monte Carlo analysis were applied to the combined beam file generation.

4.3 Quark Distributions.

For the quark distributions we used the parametrization of D.Duke and J.Owens[4.4]. These included both valence and sea distributions as well as the gluon distribution. QCD Q^2-evolution was calculated to leading-log accuracy, and the low limit for the Q^2- evolution was set to 4 $(GeV/c)^2$. The valence quark distributions had the form:

$$x(u_v + d_v) = N_{ud}\, x^{\beta_1} (1 - x)^{\beta_2} (1 + \gamma_{ud} x) \ , \qquad 4.8$$

$$x d_v = N_d\, x^{\beta_3} (1 - x)^{\beta_4} (1 + \gamma_d x) \ , \qquad 4.9$$

where:

$$N_{ud} = \frac{3}{B(\beta_1, \beta_2 + 1)\ [1 + \gamma_{ud}\beta_1/(\beta_1 + \beta_2 + 1)]} \ ,$$

$$N_d = \frac{1}{B(\beta_3, \beta_4 + 1)\ [1 + \gamma_d \beta_3/(\beta_3 + \beta_4 + 1)]} \ ,$$

and B(a,b) is the beta function.

The gluon and sea distributions are parametrized as:

$$xq(x) = Ax^a (1-x)^b (1+ \alpha_1 x + \beta_1 x^2 + \gamma_1 x^3) , \qquad 4.10$$

$$xG(x) = Ax^c (1-x)^d (1+ \alpha_2 x + \beta_2 x^2 + \gamma_2 x^3) . \qquad 4.11$$

All the parameters in Eq. 4.8 - 4.11 are defined as functions of $s = \ln[(\ln Q^2/\Lambda^2)/(\ln(Q_0^2/\Lambda^2)]$, where $Q_0^2 = 4$ (GeV/c)^2 and $\Lambda = 0.4$ GeV/c. Fig.4.2 show the valence u and d quark distributions as well as the sea distribution at different values of Q^2 for the parametrization above.

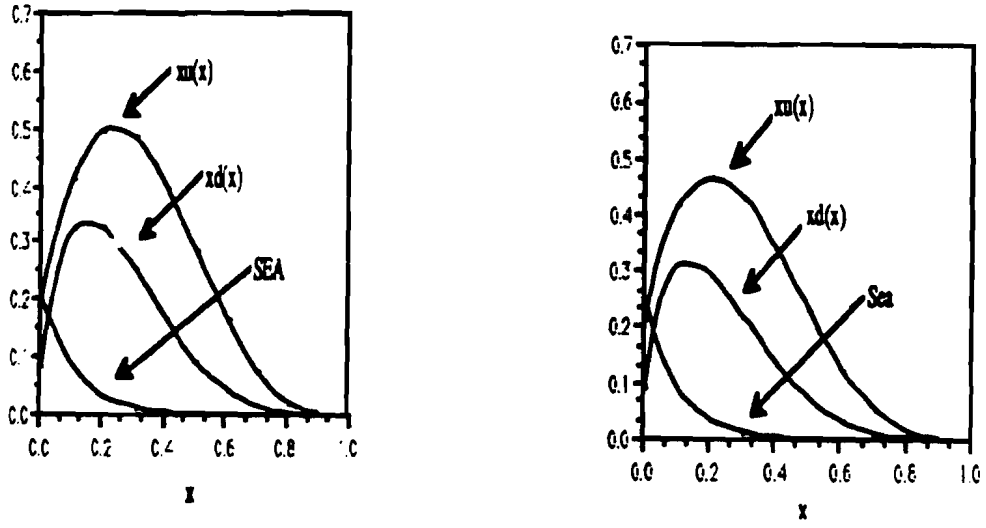

Fig.4.2 The quark distributions. The figure on the left shows the valence and the sea distributions at $Q^2 = 5$ (GeV/c)^2. The figure on the right shows the same distributions at $Q^2 = 20$ (GeV/c)^2.

4.4. Single Muon Charged Current Monte Carlo.

Even though the main focus of this thesis is on the opposite sign dimuons, we still need an accurate charged current deep inelastic scattering Monte Carlo simulation. There are several reasons for that. First, the charged current MC is needed together with a dimuon MC to calculate the opposite sign dimuon rates relative to single muon charged current (CC) events. According to the standard model of dimuon production (see Chapter I), this rate should exhibit the suppression of dimuon production at low neutrino energies as a result of the slow rescaling. Comparing a CC MC with data also allows us to check and gain understanding of many aspects of the experiment important for the dimuon analysis, such as resolution smearing, energy scales etc..

The Charged Current MC was generated using the hybrid approach described in Section 4.1. The calorimeter portion of the simulation was performed in a 4-vector form while muon tracks in the toroids were simulated in as much detail as possible. The quark distributions of Section 4.3 were used. We also performed radiative corrections[4.5] for deep inelastic scattering. We excluded the top and the bottom quarks from the simulation due to their negligible contributions at present energies. Quark mixing was taken into account by using the Kobayashi - Maskawa matrix. Slow rescaling in the production of the heavy charm quark (Eq.1.11) was also included. To make the analysis of MC events as close to that of real CC data as possible, the same software was used to reconstruct muon tracks in the toroids for MC events as for data. For comparisons of data with Monte Carlo the, following cuts were imposed on both:

1) vertex position between chambers 41 and 400;

2) lateral vertex position no closer than 200 clock counts (about 48 cm) from the edges;

3) number of fit muon tracks = 1;

4) shower energy $E_h > 10$ Gev;

5) muon energy $E_\mu > 10$ Gev;

6) to avoid any biases due to prescaling (see Chapter III) only data events with PTH trigger bit ON were used (this was irrelevant for the MC).
We would like to emphasize that no sign selection was made, therefore both neutrino and antineutrino CC events were analyzed together. This is done primarily in order to make the CC analysis consistent with the analysis of the dimuon data.

As we mentioned before, the only difference between the analysis of the data and the MC was that the MC events did not go through the calorimeter track fitting process. Therefore we applied a correction to the MC events to account for the calorimeter track finding package efficiency, based on the study of that efficiency described in Chapter III. In particular, all MC events with $E_\mu < 20$ GeV were weighted by the efficiency factor $\varepsilon = 0.7174$.

The comparisons of data with MC are shown in Fig.4.3 through Fig.4.10 in the form of the standard comparison plots designed by T. Mattison [4.6]. The upper left corner graph in each plot shows the data with the Monte Carlo superimposed. The smooth line represents MC, the points with errors represent data. The upper right corner graph is the same except that it uses log scale. The lower left corner graph is the data - MC difference and the lower right graph is the ratio of data to MC.

Fig.4.3 and 4.4 show the lateral vertex position distributions. Independent studies of neutrino and antineutrino CC data established that the neutrino and antineutrino components of the quadruplet beam had different spatial distributions. The difference between the centroids was about 36 cm horizontally and about 14 cm vertically. The fact that the distributions in Fig.4.3 and 4.4 agree very well confirms that the combined beam file used for this analysis accurately reproduces the spatial properties of the both components of the quadruplet beam. Fig.4.5 through 4.7 check the energy scale of the experiment, where

Fig.4.5 shows the energy distribution of hadronic showers, whereas Fig.4.6 shows the muon energy distribution, and Fig.4.7 shows the total visible energy distribution.

Finally Fig.4.8 through 4.10 show the kinematic quantities x,y and Q^2 of CC events.

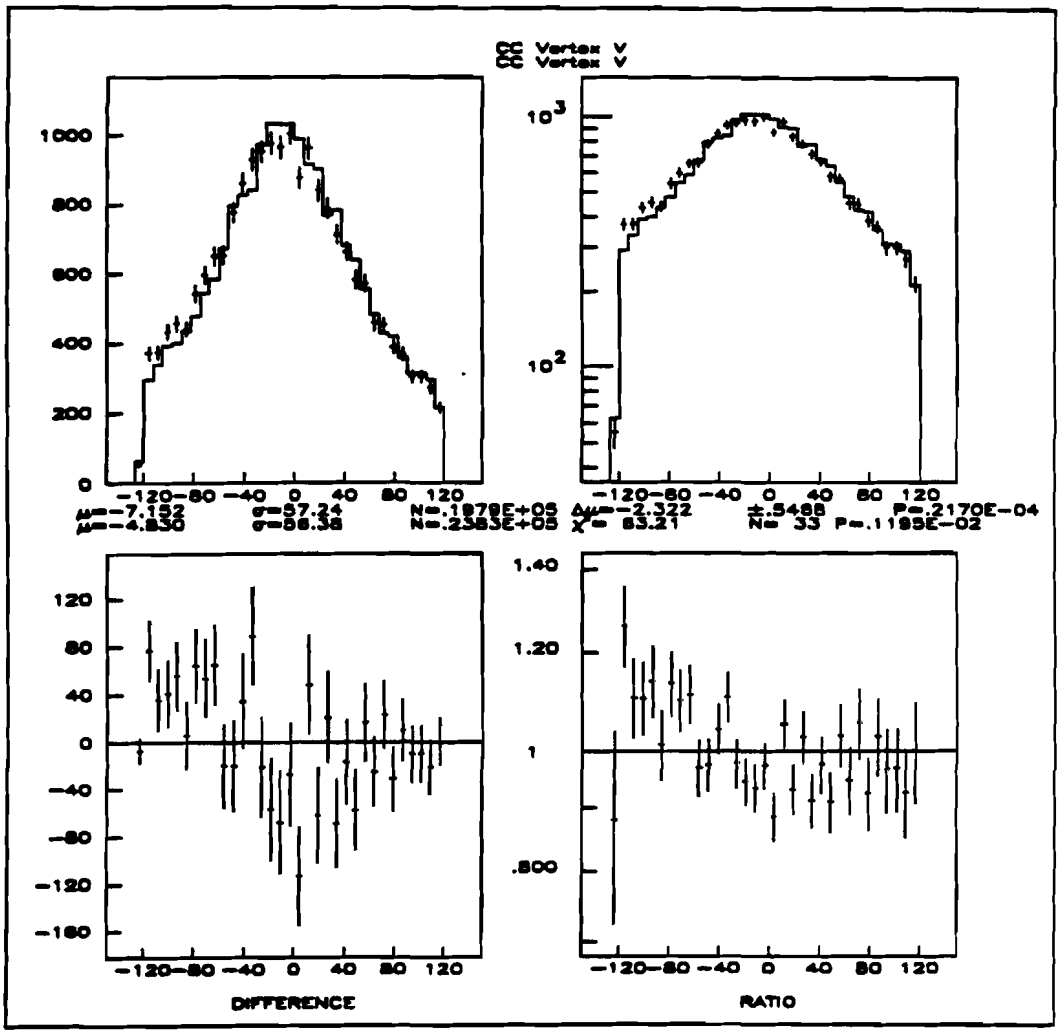

Fig.4.3.Comparison of vertical position of (anti)neutrino vertices in CC events with Monte Carlo.

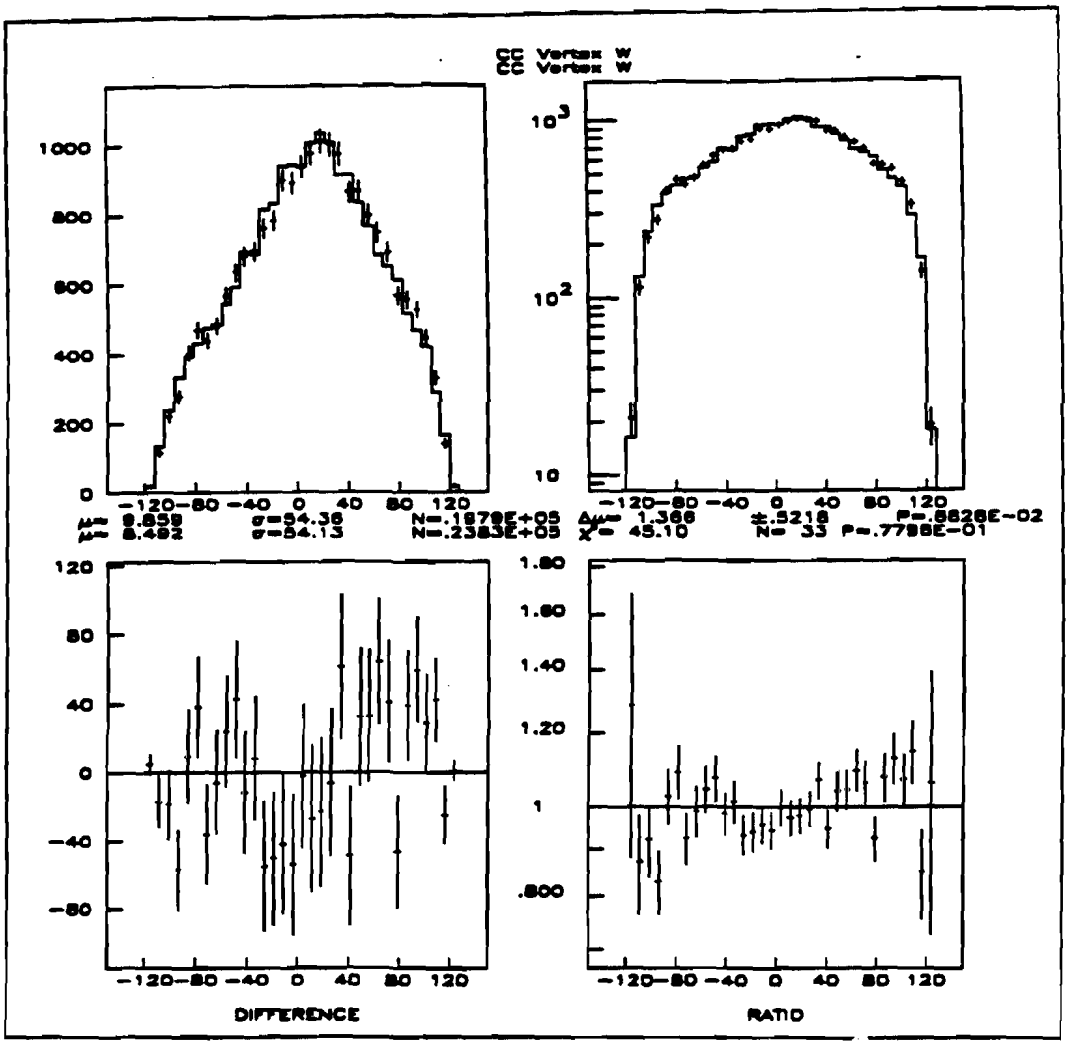

Fig.4.4.Comparison of horizontal position of (anti)neutrino vertices in CC events with Monte Carlo.

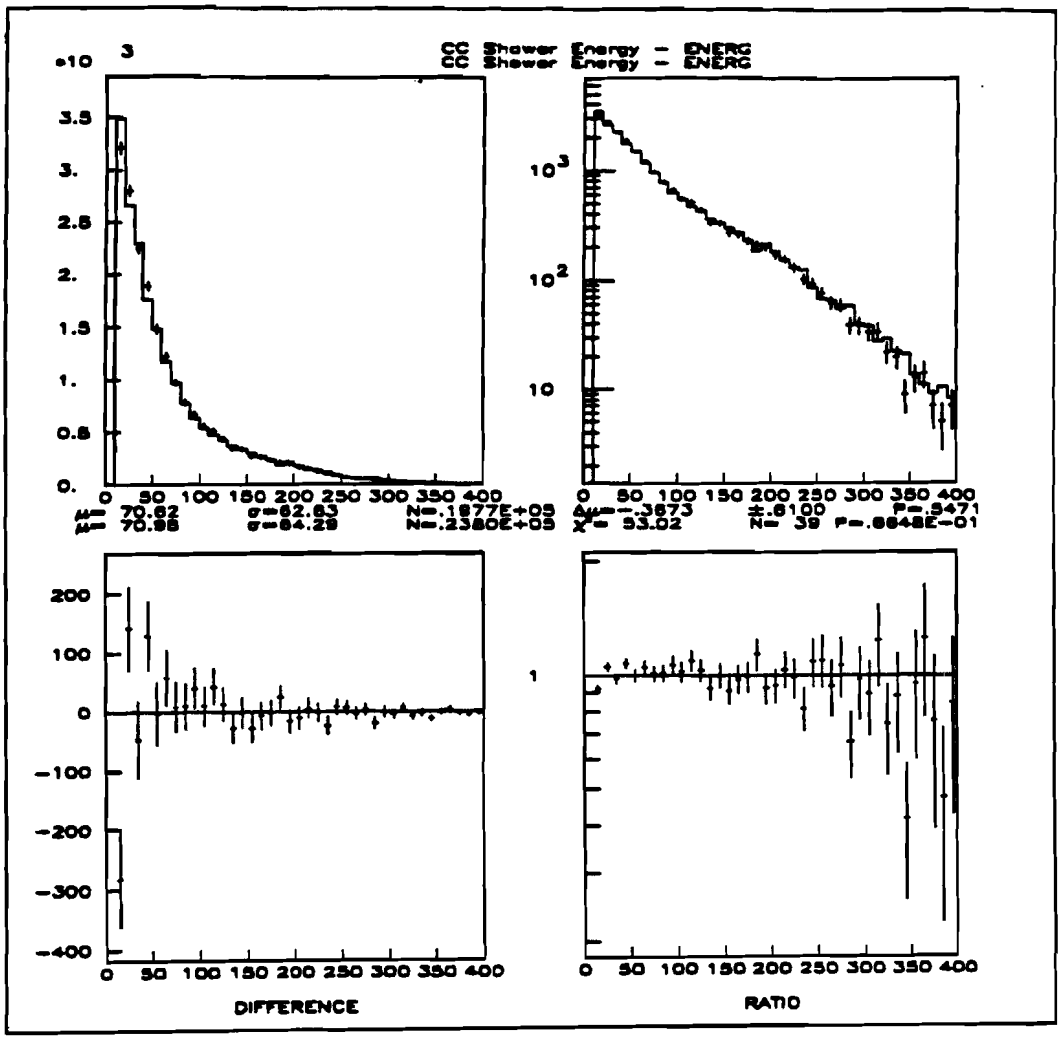

Fig.4.5.Comparison of hadronic shower energy of CC events with Monte Carlo.

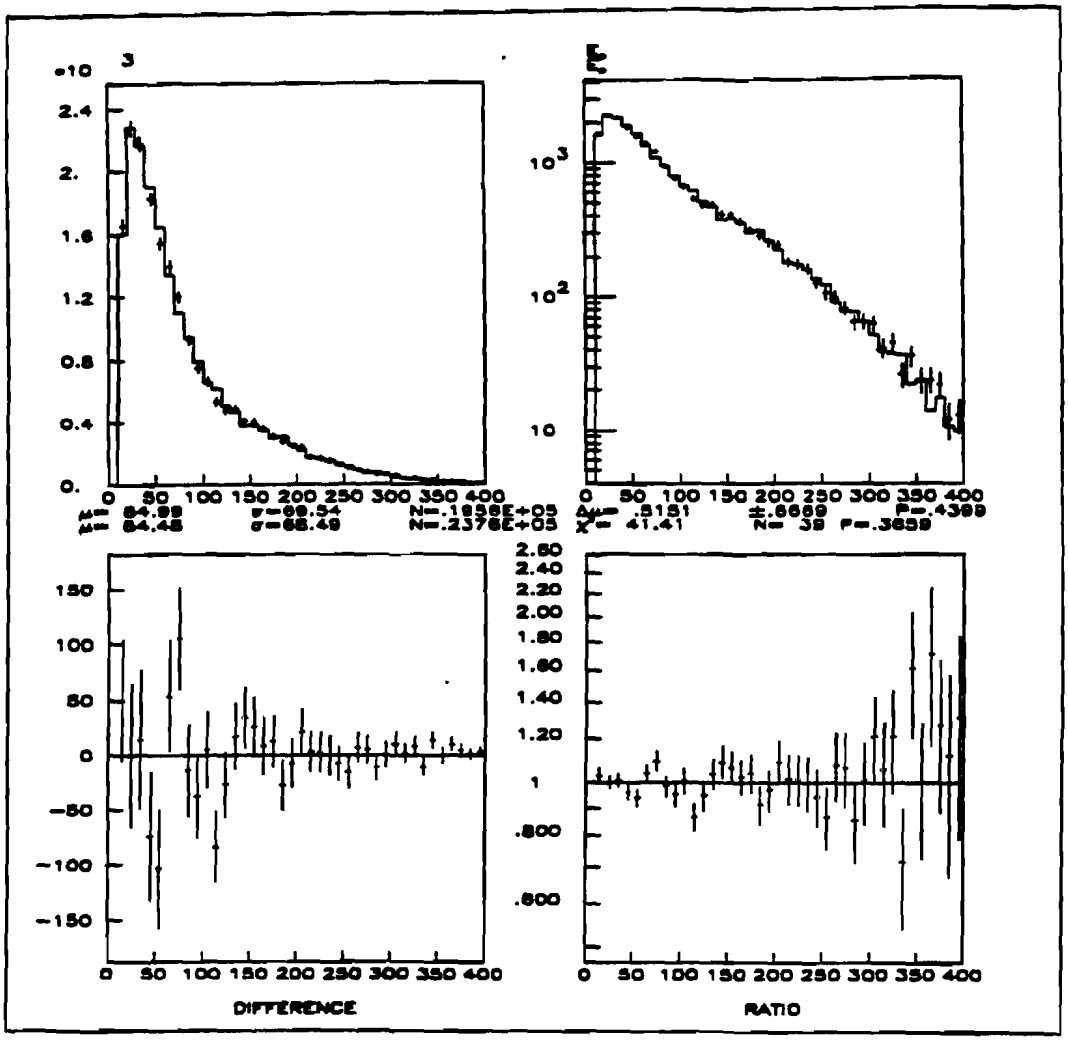

Fig.4.6.Comparison of the muon energy in CC events with Monte Carlo.

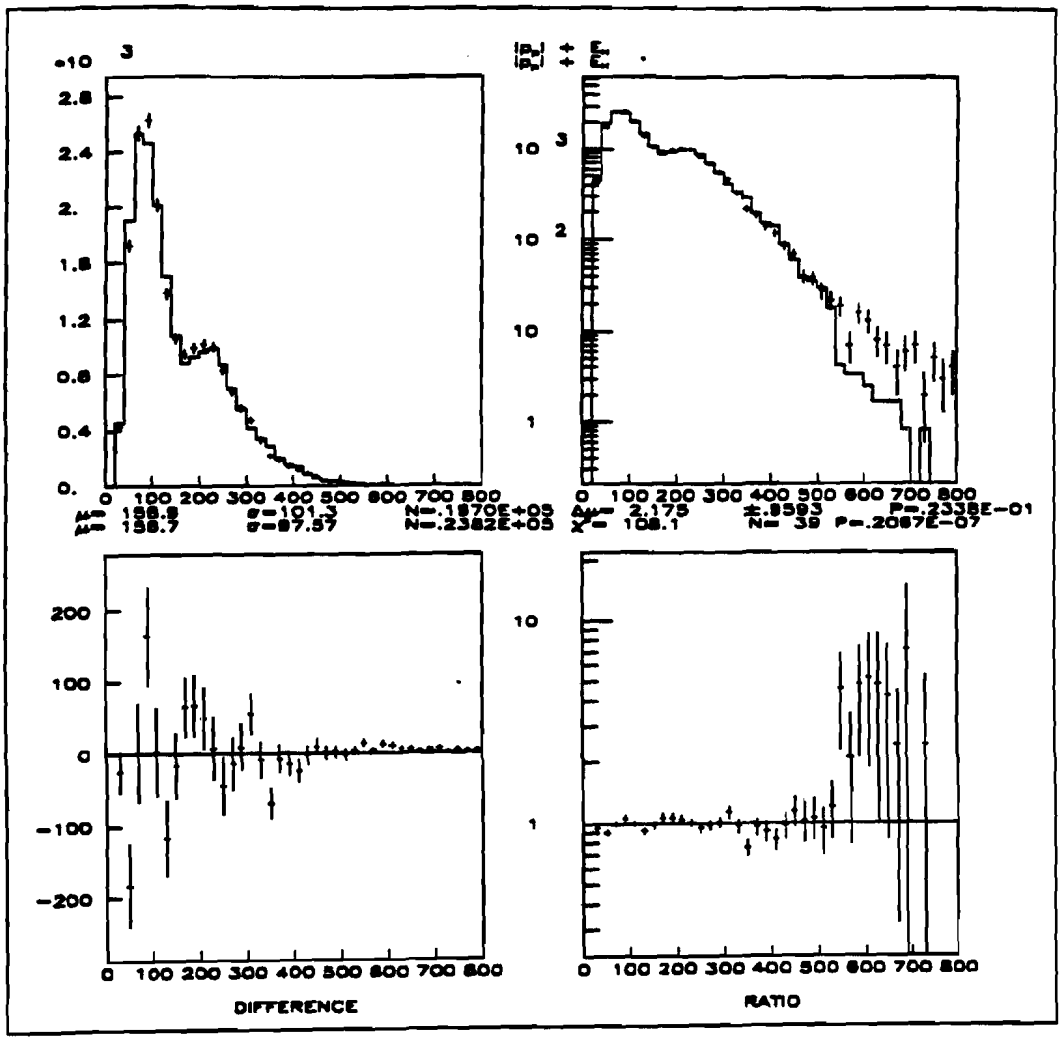

Fig.4.7.Comparison of the total visible energy of CC events with Monte Carlo.

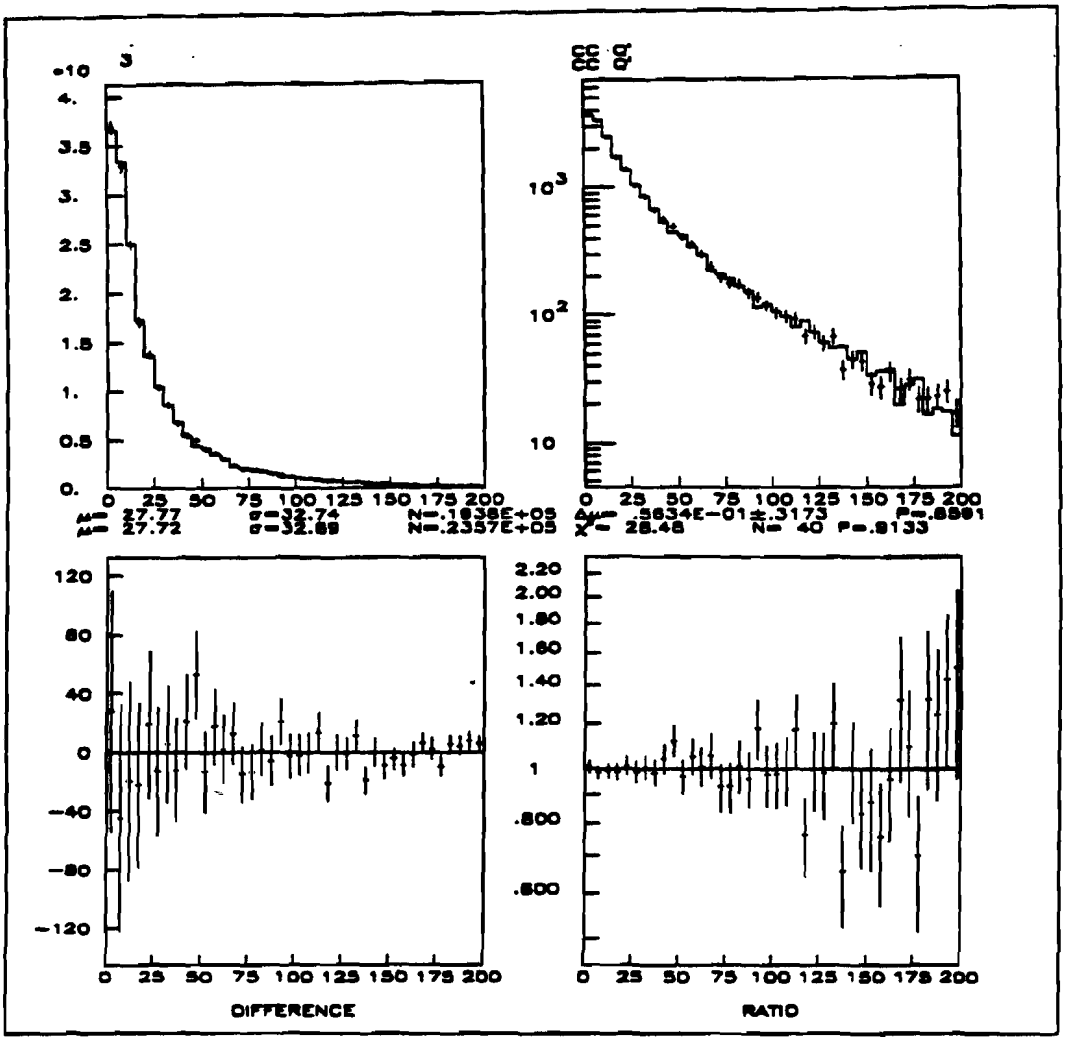

Fig.4.8.Comparison of the Q^2 distribution in CC events with Monte Carlo.

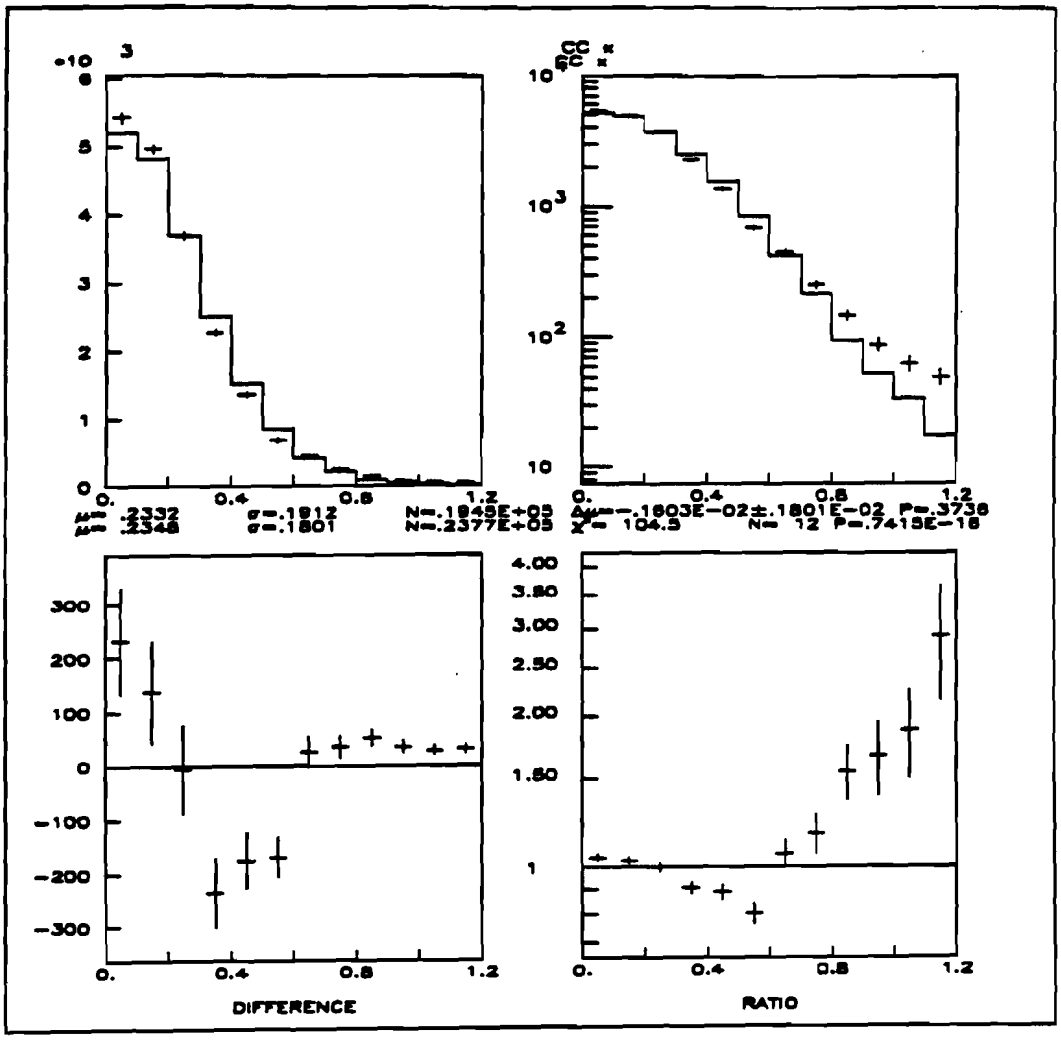

Fig.4.9.Comparison of the $x_{visible}$ distribution in CC events with Monte Carlo.

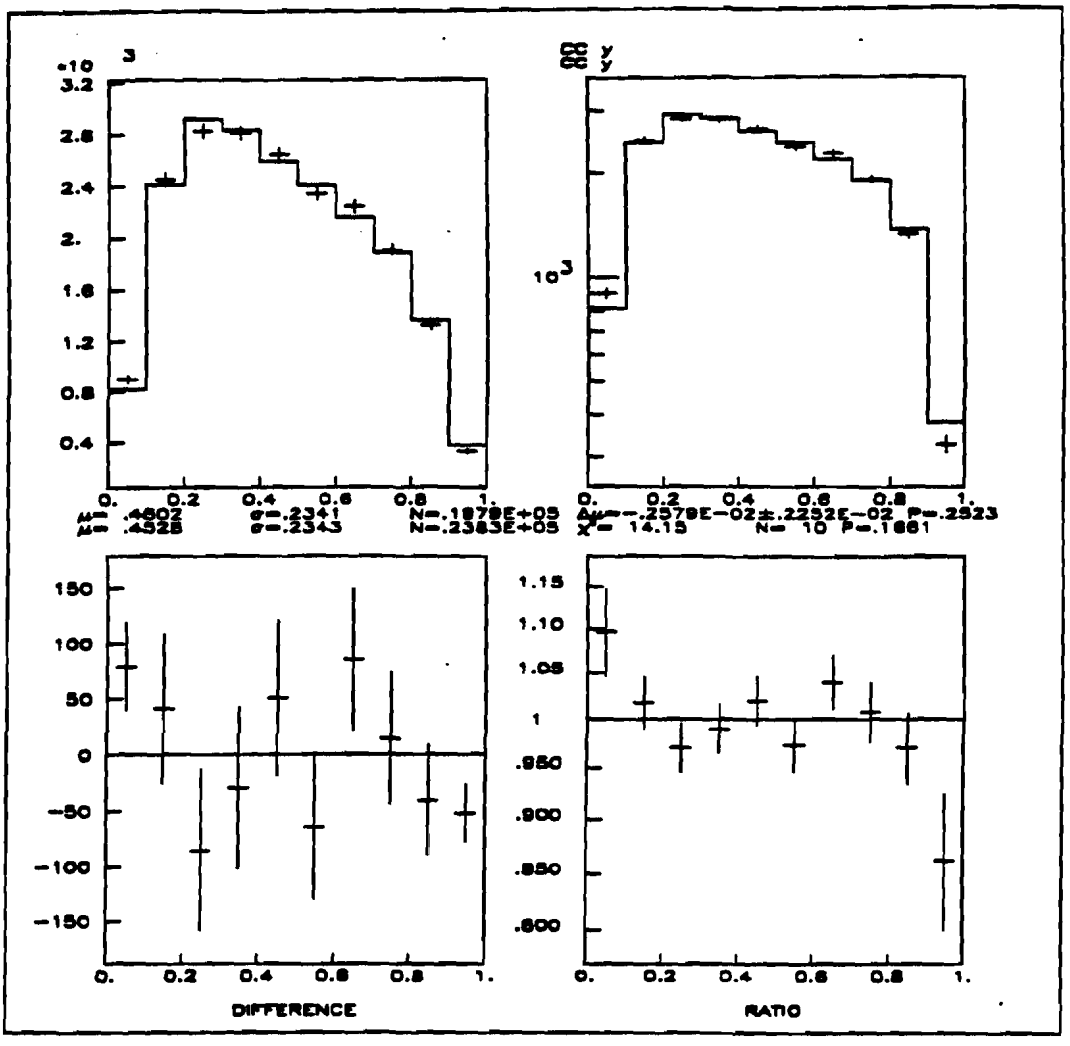

Fig.4.10.Comparison of the $y_{visible}$ distribution in CC events with Monte Carlo.

4.5. Opposite Sign Dimuons Monte Carlo.

4.5.1. Quark Distributions and the Strange Sea Fraction.

The cross section for opposite sign dimuon production is given by Eq.1.18 for neutrinos and by Eq.1.19 for antineutrinos. The up and the down quark distributions in Eq.1.18 include contributions from both valence and sea quarks. The explicit parametrizations of these distributions are given in Section 4.3. The strange sea is assumed to have the same x-distribution as the up and the down sea and its amount relative to the up and down sea is usually described by parameter κ (Eq.1.20). It is assumed (see Chapter I) that $u_{sea} = d_{sea} = \bar{u}_{sea} = \bar{d}_{sea}$. The value of κ used for MC generation was $\kappa = 0.42$. These assumptions are tested in our data analysis.

4.5.2 Charm quark fragmentation.

Since quarks can not exist in free form, the charm quark produced in reaction shown in Fig.1.2 has to rapidly "fragment" to form a hadron, most typically the D meson. From a theoretical standpoint the description of this process is within the realm of Quantum Chromodynamics (QCD). However, since the process is highly non-perturbative, due to the small values of Q^2 involved, one's ability to calculate the quantitative properties of the fragmentation is very limited. It is necessary therefore to resort to phenomenological descriptions of quark fragmentation. Several such models exist, the most popular being the one due to Petersen [4.7]. In his model the heavy quark fragmentation function is of the form:

$$D(z) = \frac{1}{z\left(1 - \frac{1}{z} - \frac{\varepsilon}{(1-z)}\right)^2}, \qquad 4.12$$

where $z = p/p_{max}$, with p being the charmed meson's momentum after fragmentation, and p_{max} is the maximum possible charmed meson momentum. Note that all quantities are defined in the W-boson - nucleon center of mass system. Thus for a charmed meson of mass M:

$$p_{max} = \sqrt{W^2/4 - M^2}\,, \qquad 4.13$$

where W is the invariant mass of the final-state hadronic system defined by Eq.1.6.

The only free parameter in this model, ε, is best determined by studying charm fragmentation in e^+e^- reactions [4.8]. The results from ARGUS collaboration, that have energy range compatible with this experiment, indicate $\varepsilon = 0.19 \pm 0.03$. That value of ε was used in the Monte Carlo generation. Fig 4.11 shows the Petersen fragmentation function for $\varepsilon = 0.19 \pm 20\%$.

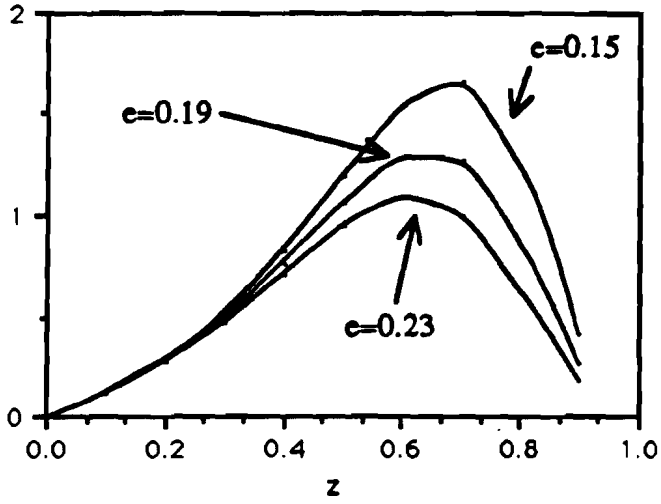

Fig.4.11 The Petersen fragmentation function. shown for three different values of ε. Note that D(z) in this figure is not normalized.

One of the features of quark fragmentation is that the resulting hadron(s) emerge with some transverse momentum relative to the direction of motion of the parent quark. The origin of this transverse momentum is again thought to lie with QCD, although no reliable calculations exist. Most experiments [4.9] use p_t distributions of the form $\frac{dN}{dp_t} \sim \exp(-a\, p_t^{\beta})$.

We used a = 1.1 and ß = 2, i.e. :

$$\frac{dN}{dp_t} = \exp(-1.1\, p_t^2). \qquad 4.15$$

4.5.3 D-meson Decays.

The immediate source of the second muon in opposite sign dimuon production is semileptonic decays of the D^0 and $D^{\pm}$ mesons. These decays have been studied extensively by several groups. The latest results from MARK III collaboration [4.10] are shown in Table 4.2

Table 4.2. Decay modes and branching ratios of D^0 and $D^{\pm}$ mesons. For each mode the first error is statistical, the second one is systematic.

Decay Mode	Branching Ratio
$D^0 \rightarrow K^- \mu^+ \upsilon_\mu$	$4.1 \pm 0.7 \pm 1.2\%$
$D^+ \rightarrow \bar{K}^0 \mu^+ \upsilon_\mu$	$10.2 \pm 2.1 \pm 3.6\%$
$D^0 \rightarrow \bar{K}^0 \pi^- \mu^+ \upsilon_\mu$	$2.7 \pm 1.1 \pm 1.6\%$

To simulate the decays of Table 4.2 we used the matrix element for three body semileptonic decays calculated by V.Barger and R.J.N.Phillips [4.11]. In the zero lepton mass approximation the matrix element is:

$$|M|^2 = -2\,(p_\mu\, p_\upsilon)\, W_1 + [2\,(p_\mu\, p)(p_\upsilon\, p)/m_D^2 + (p_\mu\, p_\upsilon)]\, W_2 + [(p_\mu\, q)(p_\upsilon\, p)/m_D^2 - (p_\mu\, p)\,(p_\upsilon\, q)/m_D^2]\, W_3\,, \qquad 4.16$$

where p_μ and p_υ are the muon and the neutrino 4-momenta respectively, p is the 4-momentum of the hadronic system, $q = -(p_\mu - p_\upsilon)$ is the 4-momentum transfer, m_D is the mass of the D-meson, and finally W_1, W_2 and W_3 are decay structure functions depending only on q^2 and $p \cdot q$.

The D decay modes can be classified into two groups: the scalar decays and the vector decays. The modes $D^0 \rightarrow K^- \mu^+ \upsilon_\mu$ and $D^+ \rightarrow K^0 \mu^+ \upsilon_\mu$ represent the scalar decays since $K^\pm$ and K^0 are pseudoscalar particles. For these reactions we have W_2 = constant and $W_1 = W_3 = 0$.

The third mode $D^0 \rightarrow K^0 \pi^- \mu^+ \upsilon_\mu$ can be either a scalar or a vector decay depending on the spin of the $K^0\pi^\pm$ system (S-wave or P-wave states). The S-wave decay is treated similarly to the first two modes. For the P-wave decay we have $W_1 = W_2 = 1$ and $W_3 = 0$. We assumed the P-wave state of the $K^0\pi^\pm$ system can be approximated by the K^* (892) resonance[4.10]. The actual decay then becomes a chain $D \rightarrow K^*\mu^+\upsilon_\mu$, $K^* \rightarrow K^0\pi$. To account for the resonant nature of K^* the matrix element above must be multiplied by the Breit-Wigner function:

$$f = \frac{1}{1 + (4/\Gamma^2)\,(M - M^*)^2}\,, \qquad 4.17$$

where Γ = 51.1 MeV is the full width of the K^* with M^* = 892 MeV, and M is the mass of the $K^0\pi^\pm$ system for a given event.

The rest of the dimuon Monte Carlo simulation is straightforward. The initial deep inelastic scattering resulting in the production of the c quark is performed in the lab system. The c quark fragmentation into the D meson is simulated in the W-boson - nucleon center of mass system. The semileptonic decays of the D meson are done in the D rest system, thus requiring subsequent boosts back first to the W-boson - nucleon c.m. system, and then to the original lab system.

We defer the discussion of the results of this simulation until Chapter VI where we will compare them with data.

CHAPTER V.
BACKGROUND.

5.1 Introduction.

According to the Standard Model of electroweak interactions, the expected rate of opposite sign dimuons due to charm quark production, followed by its hadronization and the subsequent semi-leptonic decay of a charmed particle, is less than 1% of the rate of single muon Charged Current events. Because of the smallness of the prompt opposite sign dimuon signal, it is important to fully understand the alternative (non charm production-related) processes that can produce two oppositely charged muons in the final state. The most important of such processes is leptonic decays of π's and K's in (anti)neutrino induced hadronic showers. We used a Monte Carlo (MC) simulation to model these processes. The Monte Carlo had two distinct parts: the primary decay simulation and the secondary decay simulation, explained in detail in sections 5.3 and 5.4, respectively. To model particle production in neutrino showers, both parts relied on the Lund Monte Carlo, which has by now become a standard tool in high energy physics research.

In this chapter we intend to establish that our like-sign dimuon data are fully consistent with their origin being leptonic decays of π's and K's. We will use the like sign data together with the results of the background MC simulation to predict the opposite sign dimuon background. The total background comes to about 24% of our opposite sign dimuon signal.

5.2 The Lund Model.

Since the Lund model has been extensively described elsewhere [5.1], we will only give a brief summary here. The basic concept of the Lund model is that of string fragmentation.

Let us consider an e^+e^- --> quark + antiquark process in the center of mass system, for example. After the e^+ and e^- interact there is a quark and an antiquark, moving in the opposite directions. The strong field between them forms a colour flux tube, the main feature of which is that the potential between the quarks rises linearly with distance. The energy density in the flux tube is about 1 GeV/fm. The relativistically invariant description of the flux tube is given in terms of the massless relativistic string with no transverse momentum. As the quark and the antiquark are moving further and further apart, a break in the string occurs, creating two new ends corresponding to a new quark-antiquark pair. The process of breaking up continues until there is no energy left, forming quark pairs which become mesons. Once the string break-up is complete, the Lund Monte Carlo program will allow unstable mesons to decay using known branching ratios into "stable" particles, by which we mean particles that could be detected - μ, K, π etc. For this analysis we used the Lund program "LEPTO", the version of the Lund MC specifically formulated for deep-inelastic lepton-nucleon scattering utilizing first order QCD corrections. The incoming (anti)neutrino energy and momentum, which LEPTO uses as an input, were supplied by a separate beam MC program described in Chapter IV. We used the Lund MC with the default parameters as specified in [5.1].

Experimental data on hadron production show a logarithmic dependence of hadron multiplicities, $\langle n \rangle$, on W^2 - the hadronic mass squared of the event. The relation is $\langle n \rangle = a + b \ln W^2$, where a and b are constants. This result is demonstrated in Figures 5.1 through 5.4, which are "super scatterplots" of $\pi^{\pm}$ and $K^{\pm}$ multiplicities versus $\ln(W^2)$ for neutrino "events" in the Lund MC simulation. The lower right corner plots are conventional scatter plots of multiplicities (vertical axis) versus $\ln(W^2)$ (horizontal axis). The upper right corner plots show mean multiplicities as functions of $\ln(W^2)$ (labeled mean Y vs X), where the logarithmic behavior of $\langle n \rangle$ is easily seen. The straight lines of these plots are linear

fits to <n>. The two small plots in the upper left corner are the X and Y projection (top and bottom respectively), and finally the lower left corner plot is mean $\ln(W^2)$ vs <n>.

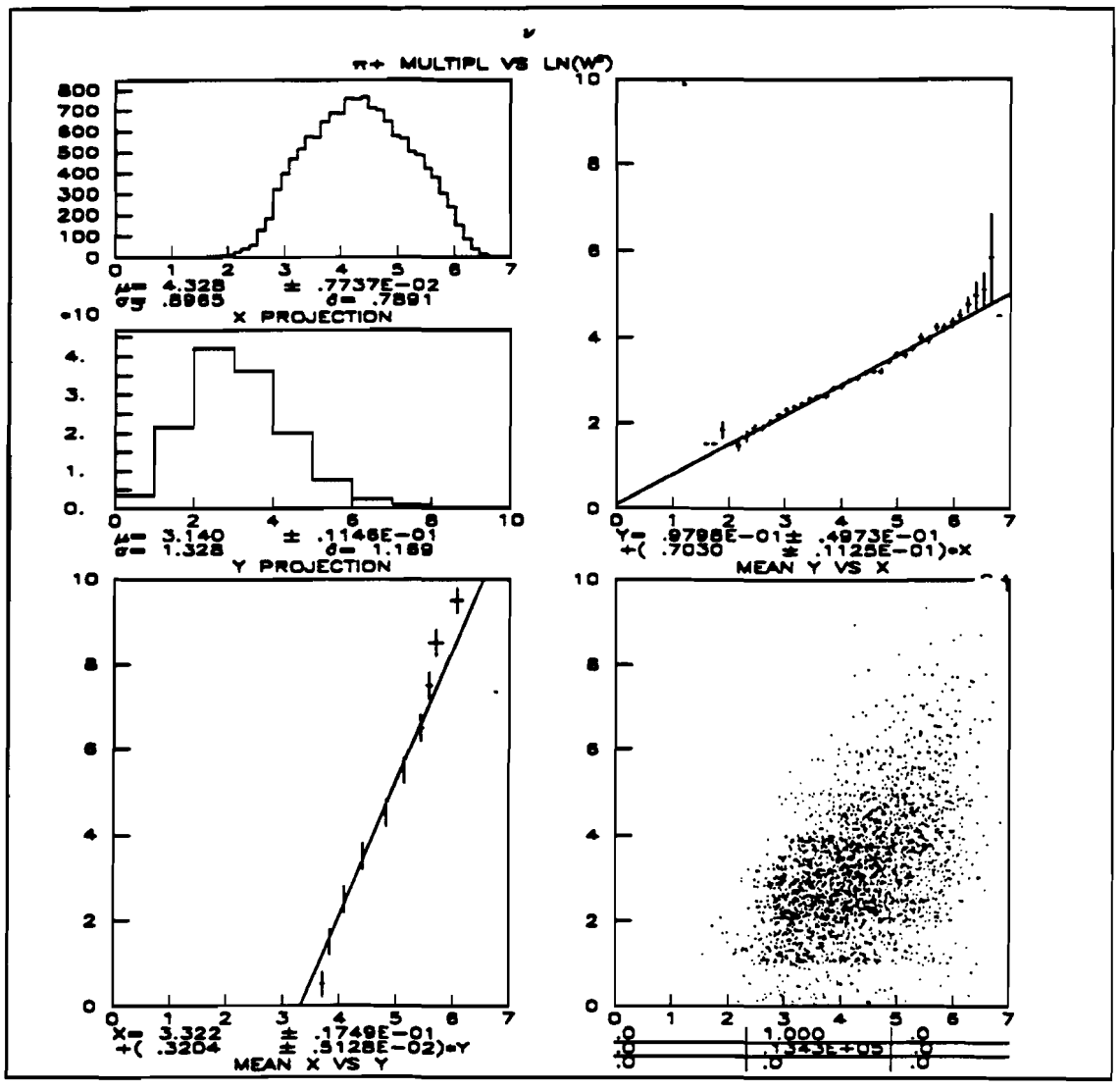

Fig.5.1. Super scatter plots of π^+ multiplicities in neutrino-induced showers versus $\ln(W^2)$. W is in GeV/c^2.

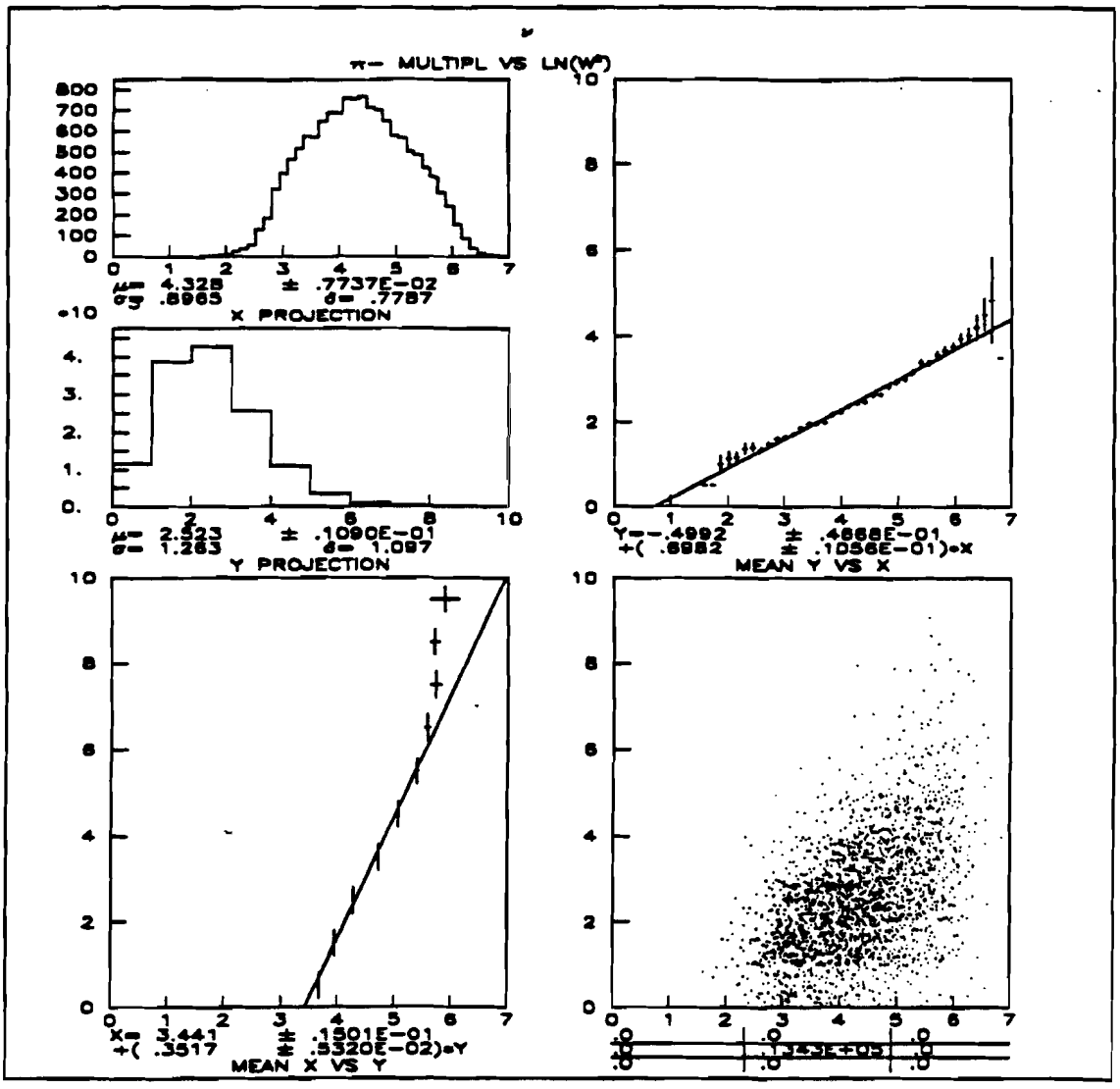

Fig.5.2. Super scatter plots of π^- multiplicities in neutrino-induced showers versus $\ln(W^2)$. W is in GeV/c^2.

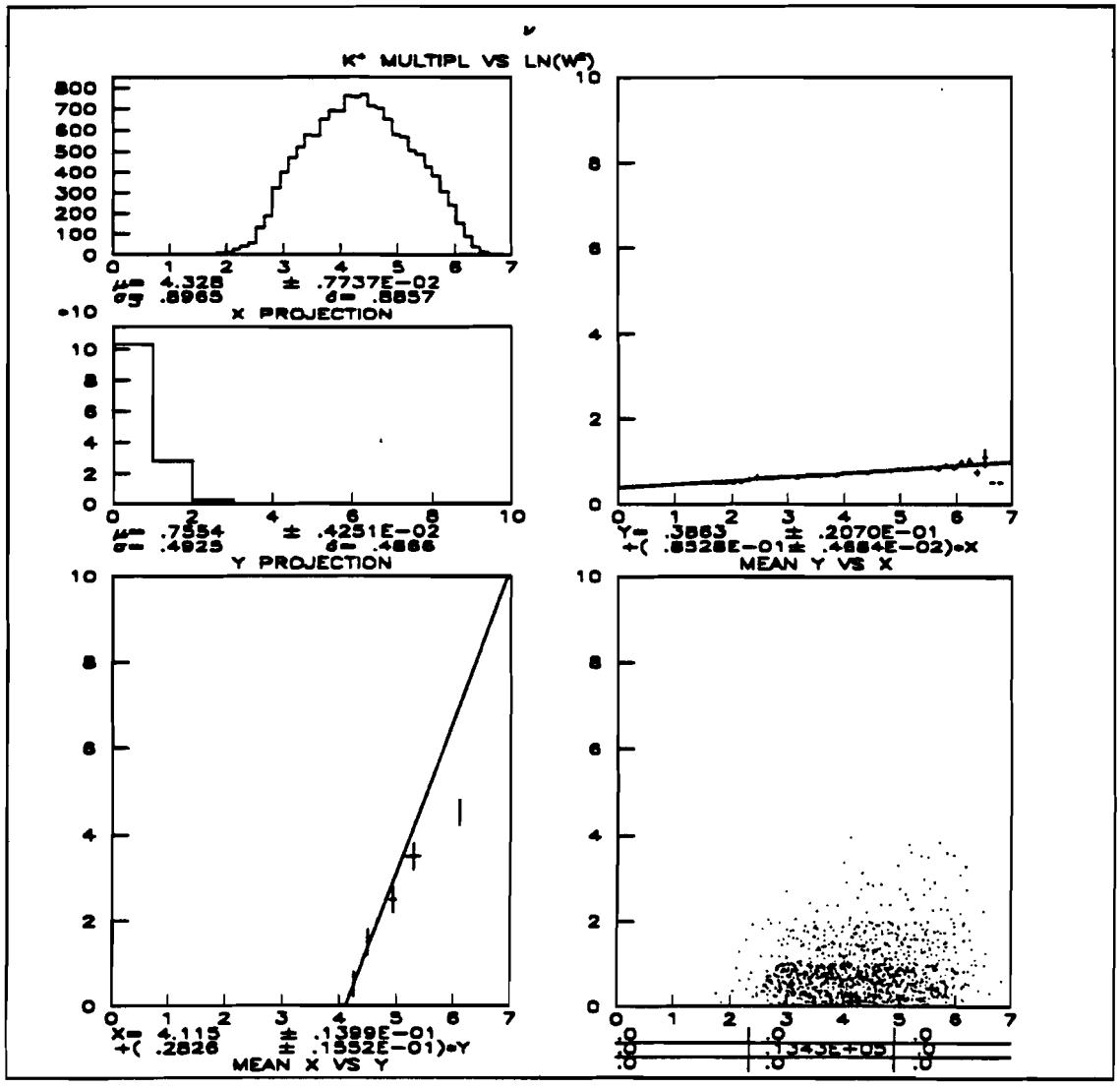

Fig.5.3. Super scatter plots of K^+ multiplicities in neutrino-induced showers versus $\ln(W^2)$. W is in GeV/c^2.

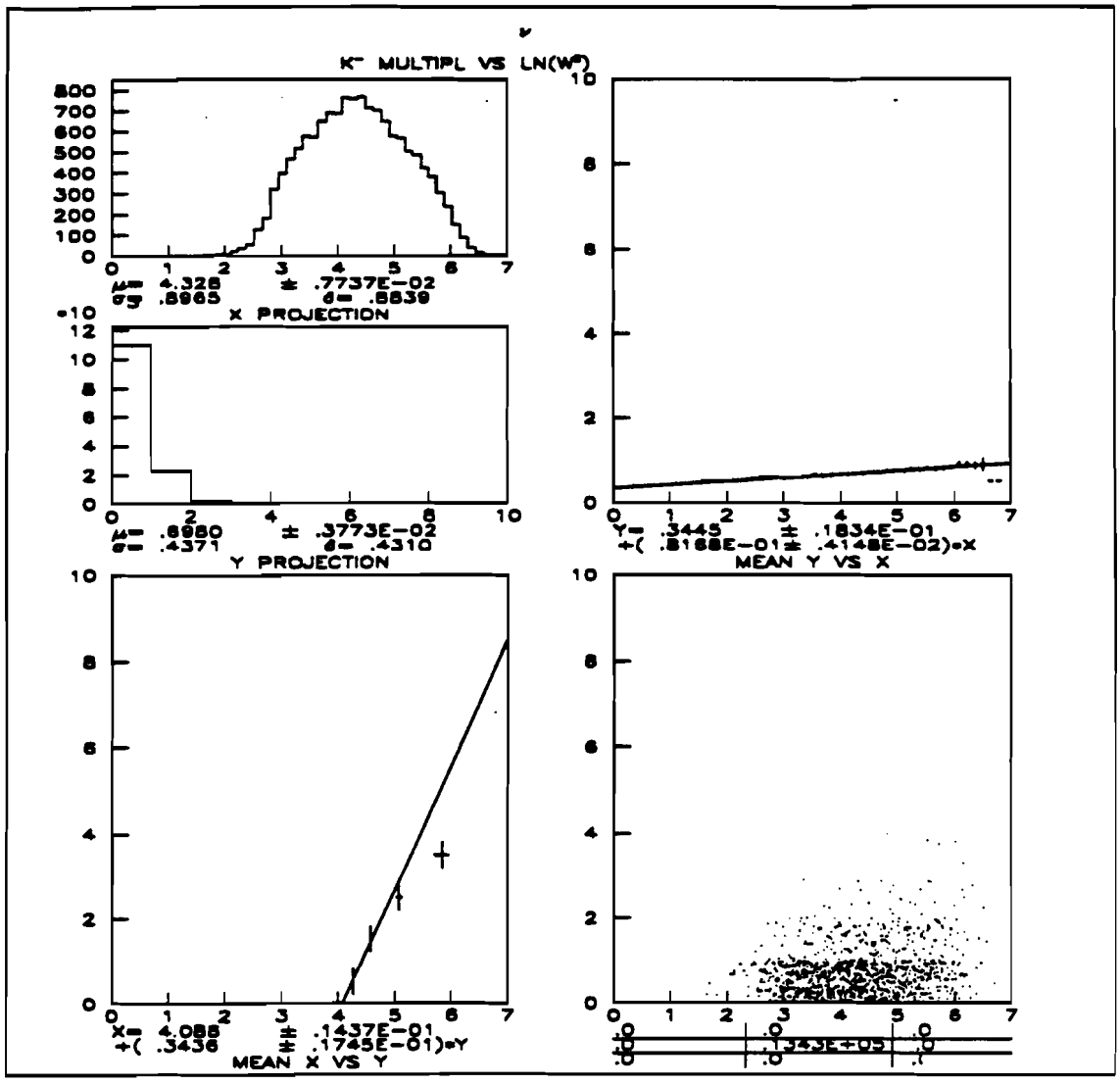

Fig.5.4. Super scatter plots of K^- multiplicities in neutrino-induced showers versus $\ln(W^2)$. W is in GeV/c^2.

5.3 Primary decays.

Muon-producing decays of first-generation hadrons, created at the primary neutrino vertex as a result of quark / jet fragmentation as shown in Fig.5.5, are called "primary" decays.

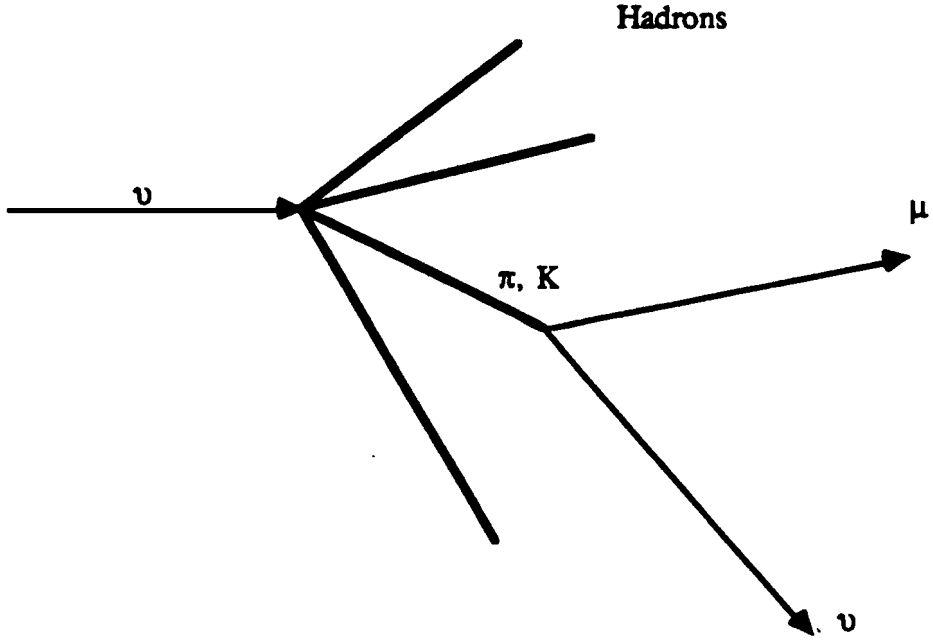

Fig.5.5. Schematic representation of primary muon production via decays of first generation π's or K's.

The differential probability for a particle to decay after it has traveled a distance L in the detector is:

$$\frac{dP(L)}{dL} = \frac{1}{\lambda_D} \exp[-L\,(\frac{1}{\lambda_D} + \frac{1}{\lambda_I})]\,, \qquad 5.1$$

where λ_D is the decay length and λ_I is the interaction length.

The decay length is defined as $\lambda_D = \gamma\beta c\tau \approx \frac{E}{m} c\tau$, where $\beta = v/c$, $\gamma = (1-\beta^2)^{-1/2}$, τ is the particle's life time in its rest frame, and E and m are its energy and mass, respectively. For the average $\pi^{\pm}$ with an energy of 5 GeV, we find $\lambda_D \approx 2.8 \times 10^4$ cm. For the average $K^{\pm}$ with an energy of 8.3 GeV, $\lambda_D \approx 6.2 \times 10^3$ cm.

The interaction length λ_I is defined as $\lambda_I = \frac{A}{\sigma \rho N_A}$, where A is the atomic number of the media, σ is the absorption cross section per nuclei, ρ is the absorber density, and N_A is Avogadro's number. For the Lab C detector A = 20.2, ρ = 1.35 g/cm^3. To determine inelastic cross sections for $\pi^{\pm}$'s and $K^{\pm}$'s in the Lab C detector, we used the results obtained for aluminum [5.2],[5.3] which has the atomic number closest to that of our calorimeter material. For kaons, the absorption cross section has no energy dependence between 0.1 and 100 GeV and its value is σ_K = 310 mb. For pions, the cross section can be parametrized as $\sigma_\pi = 455.3\ e^{(-0.019\ E_\pi)}$ mb for $E_\pi < 14$ GeV, and σ_π = 340 mb for E_π > 14 GeV. With these parameters, the average interaction length for a kaon is ≈ 75 cm and for a pion it is ≈ 120 cm. Since $\lambda_D >> \lambda_I$, Eq.5.1. can be written as

$$\frac{dP(L)}{dL} = \frac{1}{\lambda_D} \exp(-\frac{L}{\lambda_I}) \qquad 5.2$$

Thus the total integrated decay probability from L=0 to L>>λ_I is typically $P = \lambda_I/\lambda_D \approx 3.5\times10^{-3}$ for a 5 GeV $\pi^{\pm}$, and $\approx 1.2 \times 10^{-2}$ for an 8 GeV $K^{\pm}$ without taking into account the branching ratios.

Most primary decay muons come from $\pi^{\pm}$ and $K^{\pm}$ decays. Other muon-producing decays, such as decays of K_L's, K_S's and others, were investigated and found to have a negligible effect. In the case of $K^{\pm}$'s, both the "direct" mode $K^{\pm} \rightarrow \mu^{\pm} + \upsilon$ and the "indirect" mode

$K^{\pm} \rightarrow \pi^{\pm} + \pi^0$, with $\pi^{\pm}$ subsequently decaying $\pi^{\pm} \rightarrow \mu^{\pm} + \upsilon$, were simulated. Fig. 5.6 - 5.7 show Lund energy spectra for $\pi^{\pm}$ and $K^{\pm}$ in neutrino-induced showers. The distributions are normalized to the same number of incident neutrinos. For comparison Fig.5.8 - 5.9 show the same $\pi^{\pm}$ and $K^{\pm}$ spectra for antineutrino events.

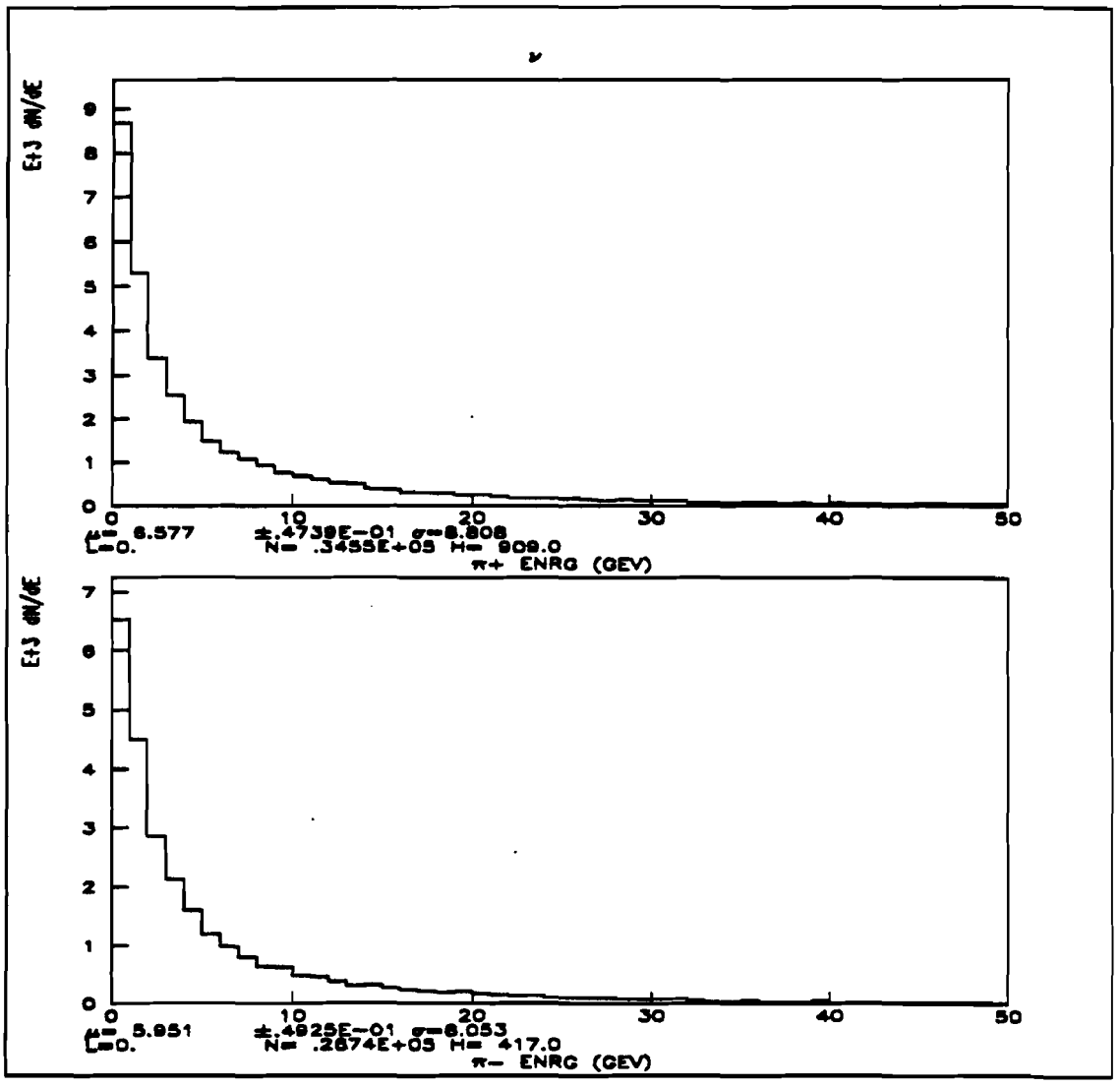

Fig.5.6. Lund energy spectra for π^+ (upper plot) and π^- (lower plot) in neutrino-induced showers. The distributions are normalized to the same number of incident neutrinos.

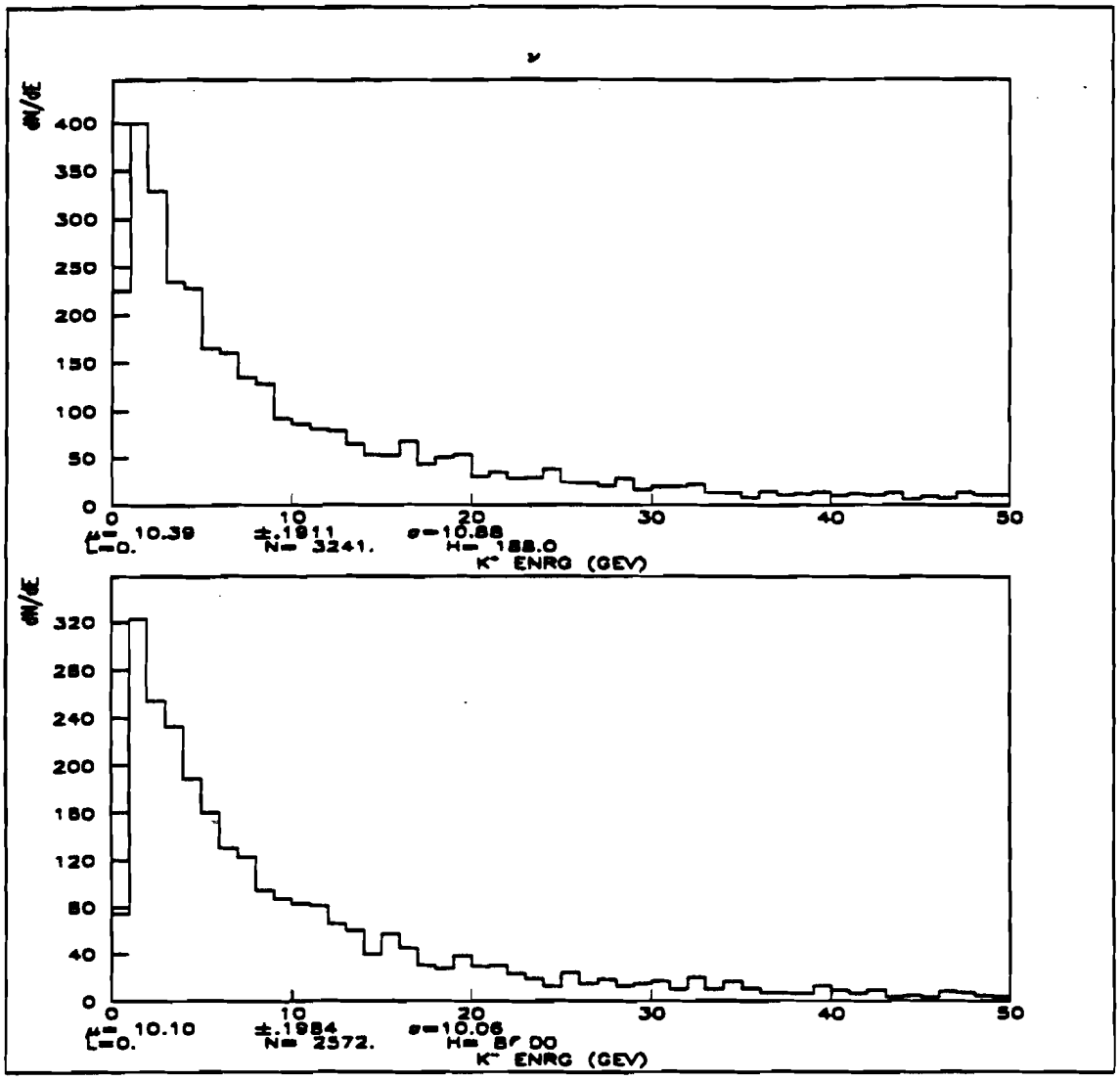

Fig.5.7. Lund energy spectra for K^+ (upper plot) and K^- (lower plot) in neutrino-induced showers. The distributions are normalized to the same number of incident neutrinos.

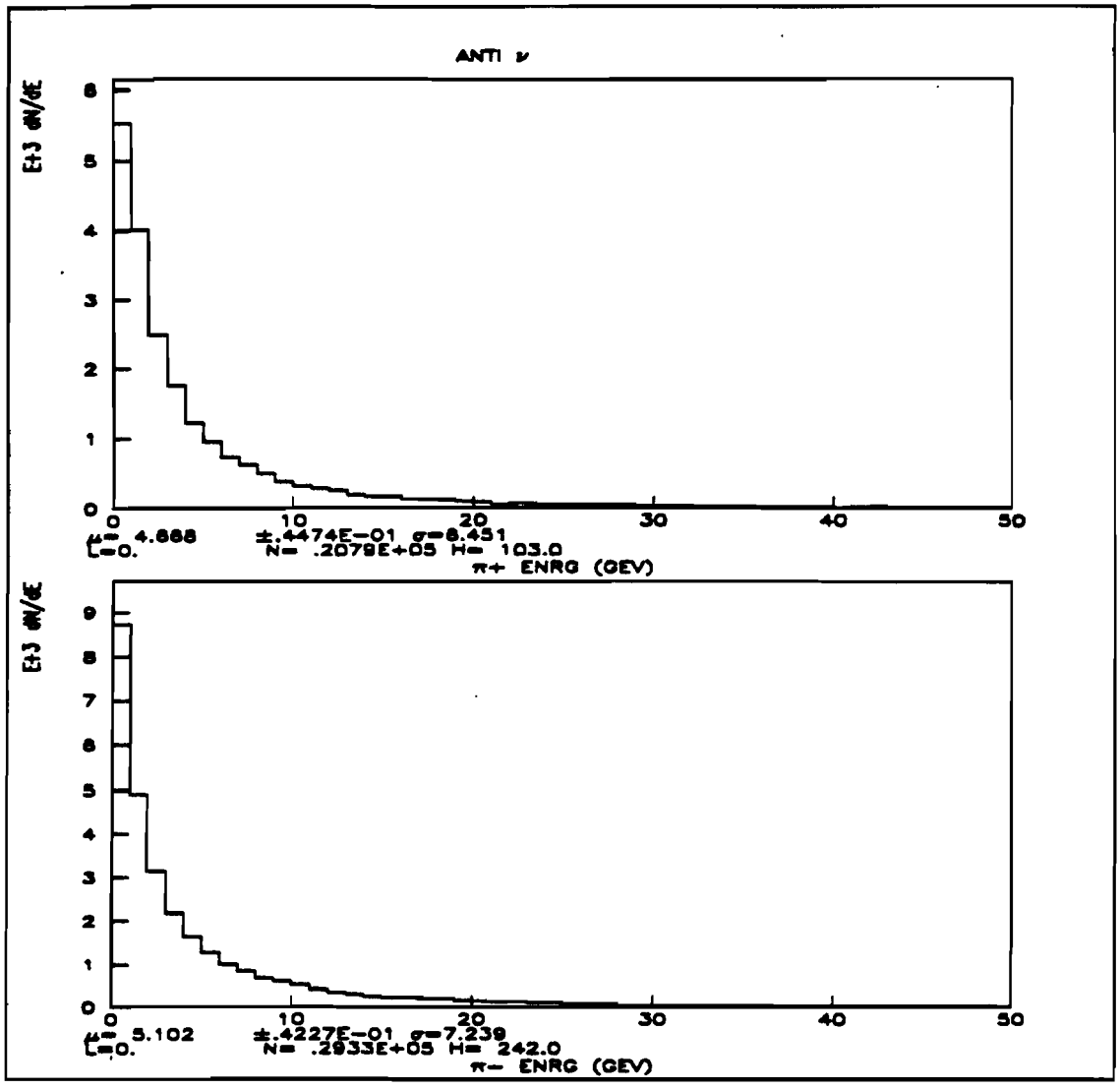

Fig.5.8. Lund energy spectra for π^+ (upper plot) and π^- (lower plot) in antineutrino-induced showers. The distributions are normalized to the same number of incident antineutrinos.

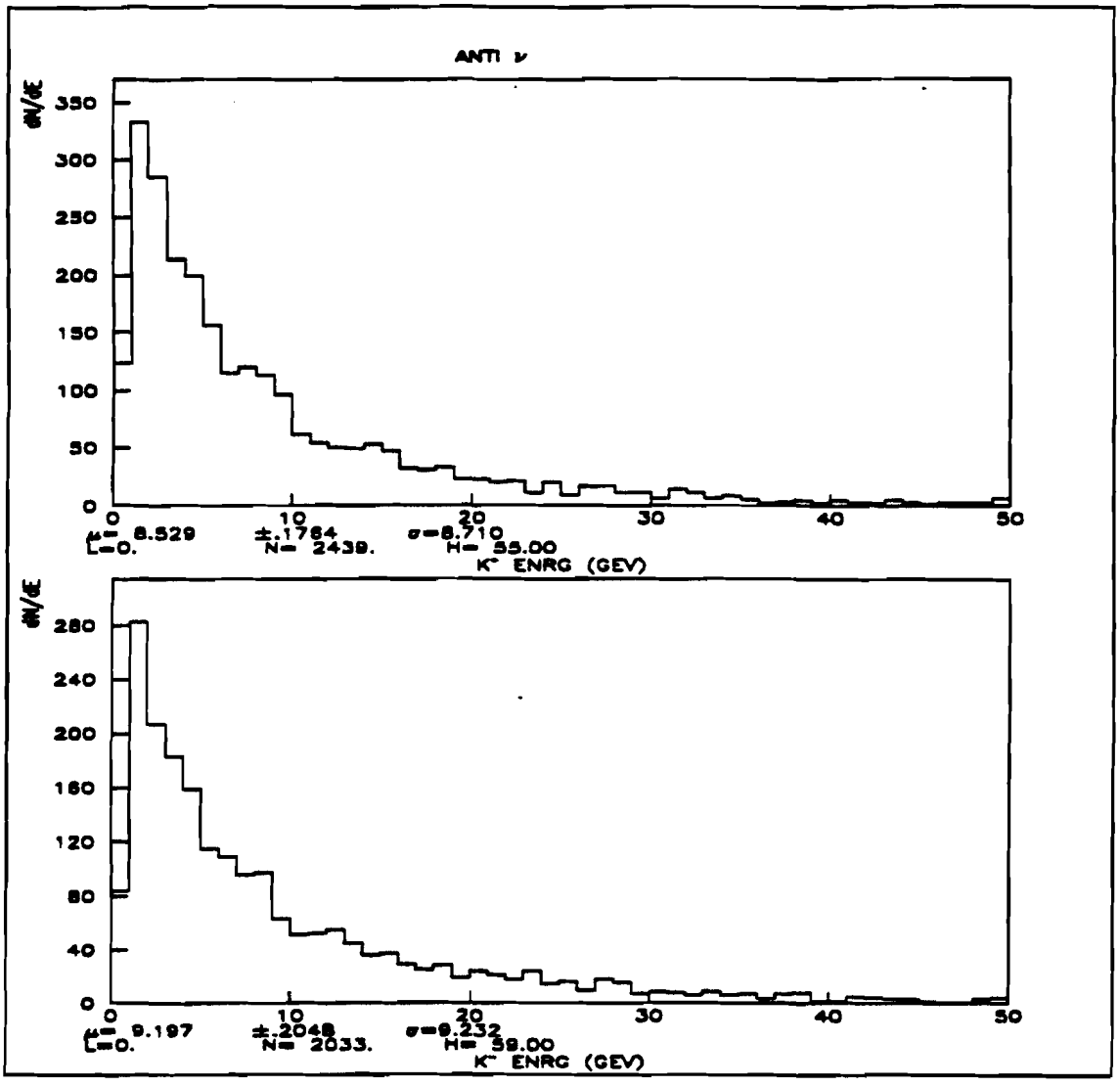

Fig.5.9. Lund energy spectra for K^+ (upper plot) and K^- (lower plot) in antineutrino-induced showers. The distributions are normalized to the same number of incident antineutrinos.

To compute the total primary decay background we have treated each $\pi^{\pm}$ and $K^{\pm}$ in the hadronic shower as a decay candidate. There are two mathematically correct ways to determine the decay point and the decay probability for each particle. The first method is to generate the decay track length uniformly from 0 to ∞. The decay probability then is the integral $P(L) = \int_0^L \frac{dP(\eta)}{d\eta} d\eta$, where L is the decay length and $P(\eta)$ is given by Eq.5.1. This method is very inefficient, however, since most decays will occur outside of the detector and would be automatically rejected. We chose instead to generate the decay track length to match the probability distribution of Eq.5.1 according to the formula :

$$L = -\frac{\lambda_D \lambda_I}{\lambda_D + \lambda_I} \ln(1 - \xi) , \qquad 5.3$$

where λ_I and λ_D are the interaction and the decay lengths respectively, and ξ is the random number distributed uniformly between 0 and 1. To compute the decay probability one now must integrate the probability distribution of Eq.5.1 from 0 to the detector boundaries. Thus for an infinite detector this probability would simply be $P = \lambda_I/(\lambda_I + \lambda_D)$. For a finite detector the probability becomes:

$$P = \frac{\lambda_I}{\lambda_I + \lambda_D} (1 - e^{-\alpha L_{max}}) , \qquad 5.4$$

where $\alpha = \frac{\lambda_I + \lambda_D}{\lambda_I \lambda_D}$, and L_{max} is the maximum decay length in the detector available for a given particle. Only decays occurring inside the detector were accepted. For each decay probability P_i, the program then threw a random number ξ_i evenly distributed between 0

and 1. If ξ_i was less than P_i the decay was selected for further processing. The muons resulting from the selected decays were then propagated through the calorimeter and the toroids. This was done in much the same way as for the other MC simulations described in Chapter IV. Since muon propagation in the calorimeter and the toroids and the subsequent event reconstruction all required considerable amount of computer time, we could not afford to consider those events that didn't have any decay muons in them. That reduced the amount of computer time needed to generate sufficient numbers of decay events to a reasonable amount, but it also raised the question of the decay rate normalization.

To make the results of the MC calculations useful for comparison with data, we had to normalize the decay events to single muon Charged Current (CC) events. To accomplish this task limited numbers (several thousands) of neutrino and antineutrino single muon CC events were used to calculate the cumulative single-muon event acceptance defined as $\beta = \frac{N_{1\mu}}{N_{cc}}$, where $N_{1\mu}$ is the number of reconstructed CC events that passed all of the cuts described below and N_{cc} is the total number of generated CC events. The values of β for neutrinos and antineutrinos are $\beta_1 = 0.4319$, $\beta_2 = 0.3874$, respectively. To calculate the primary decay rates we then used the following formula:

$$R = \frac{N_{2\mu}}{\beta N_{cc}}, \qquad 5.5$$

where $N_{2\mu}$ is the number of reconstructed accepted dimuon decay events; N_{cc} is the number of Charged Current events generated to obtain $N_{2\mu}$.

The same cuts were used in the analysis of the MC dimuon decay events as in the analysis of the data. These cuts were:

1) the fiducial cuts; 2) the minimal shower energy cut $E_{shower} \geq 10$ GeV; 3) the muon energy cut $E_{\mu 1,\mu 2} \geq 10$ GeV; and 4) the toroid hole cut described in Chapter III.

Table 5.1 shows a summary of the primary decay rates relative to single-muon CC events with the cuts described above.

Table 5.1 Primary background rates for neutrino and antineutrino events per accepted single muon CC event. The errors are statistical

Neutrinos		Antineutrinos	
$\mu^-\mu^-$	$(4.34 \pm 0.14)\times10^{-4}$	$\mu^+\mu^+$	$(3.15 \pm 0.12)\times10^{-4}$
$\mu^-\mu^+$	$(5.82 \pm 0.17)\times10^{-4}$	$\mu^+\mu^-$	$(4.21 \pm 0.14)\times10^{-4}$

The results of the primary decay simulation are shown in Fig.5.10 through Fig.5.15. Fig.5.10 shows energy spectra for negative like-sign muons in neutrino events. Fig.5.11 shows energy spectra for opposite sign muons in neutrino events. Fig. 5.12 - 5.13 are analogous to Fig.5.10 - 5.11 except that they show the spectra for antineutrino events. Fig.5.14 shows the primary $\mu^-\mu^-$ and $\mu^-\mu^+$ decay rates for neutrino events plotted as functions of the visible hadronic shower energy. Fig. 5.15 shows the primary $\mu^+\mu^+$ and $\mu^+\mu^-$ rates for antineutrino events as functions of the shower energy.

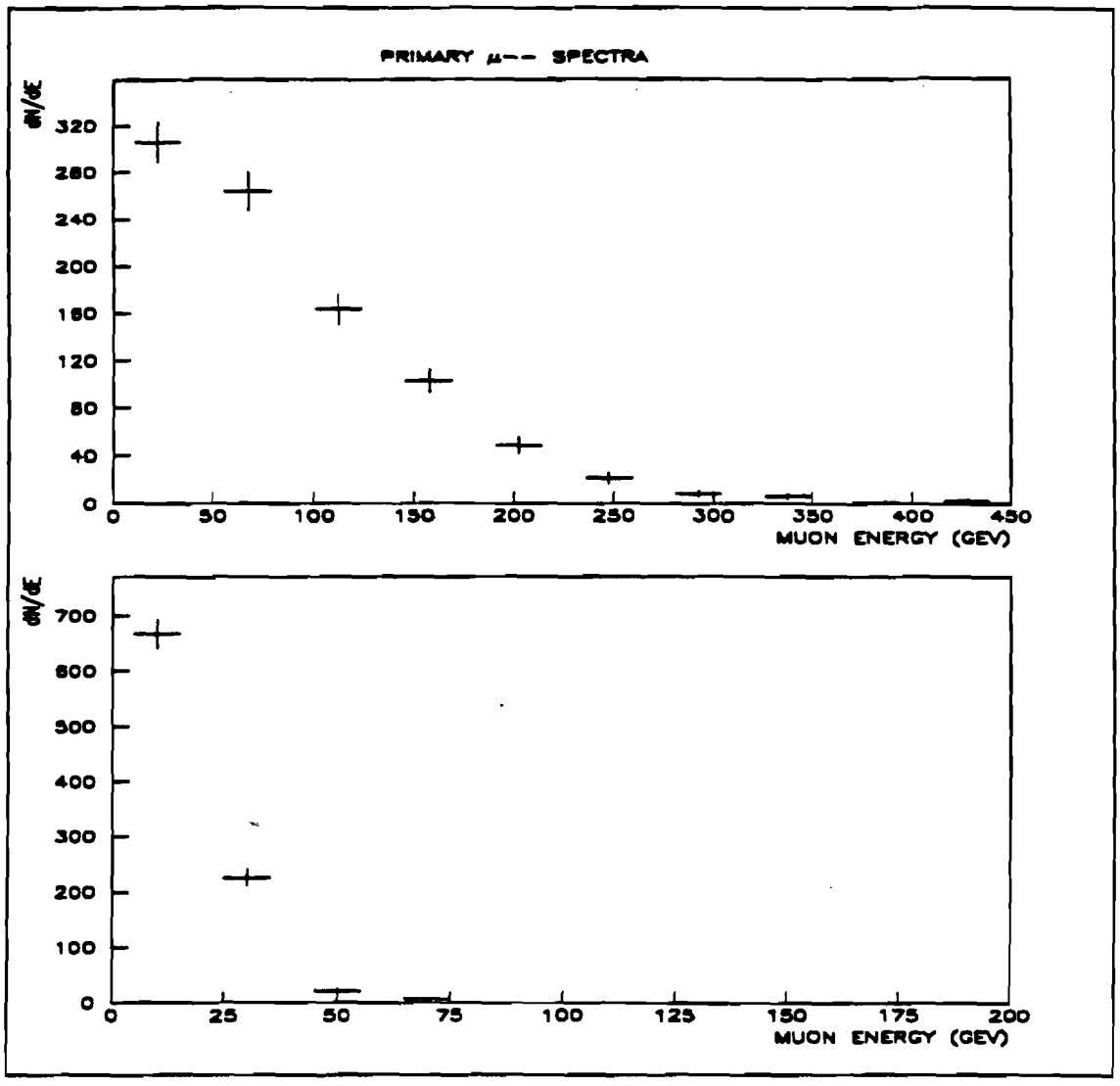

Fig.5.10 Muon energy spectra for neutrino-induced $\mu^-\mu^-$ primary decay events. The upper plot represents the leading (highest energy) muon, the lower plot represents the second muon.

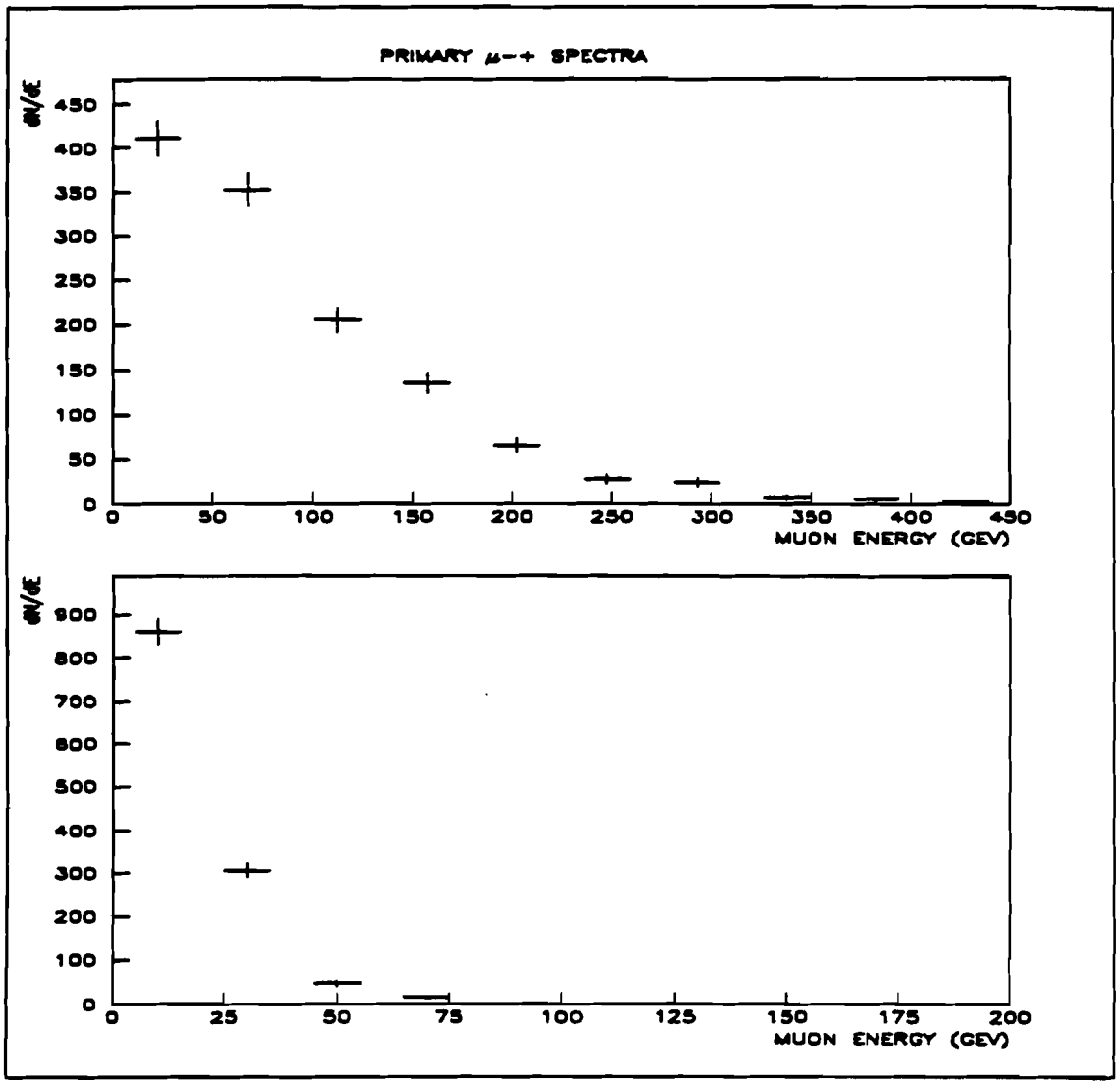

Fig.5.11 Muon energy spectra for neutrino-induced $\mu^-\mu^+$ primary decay events. The upper plot represents the leading muon, the lower plot is for the second muon.

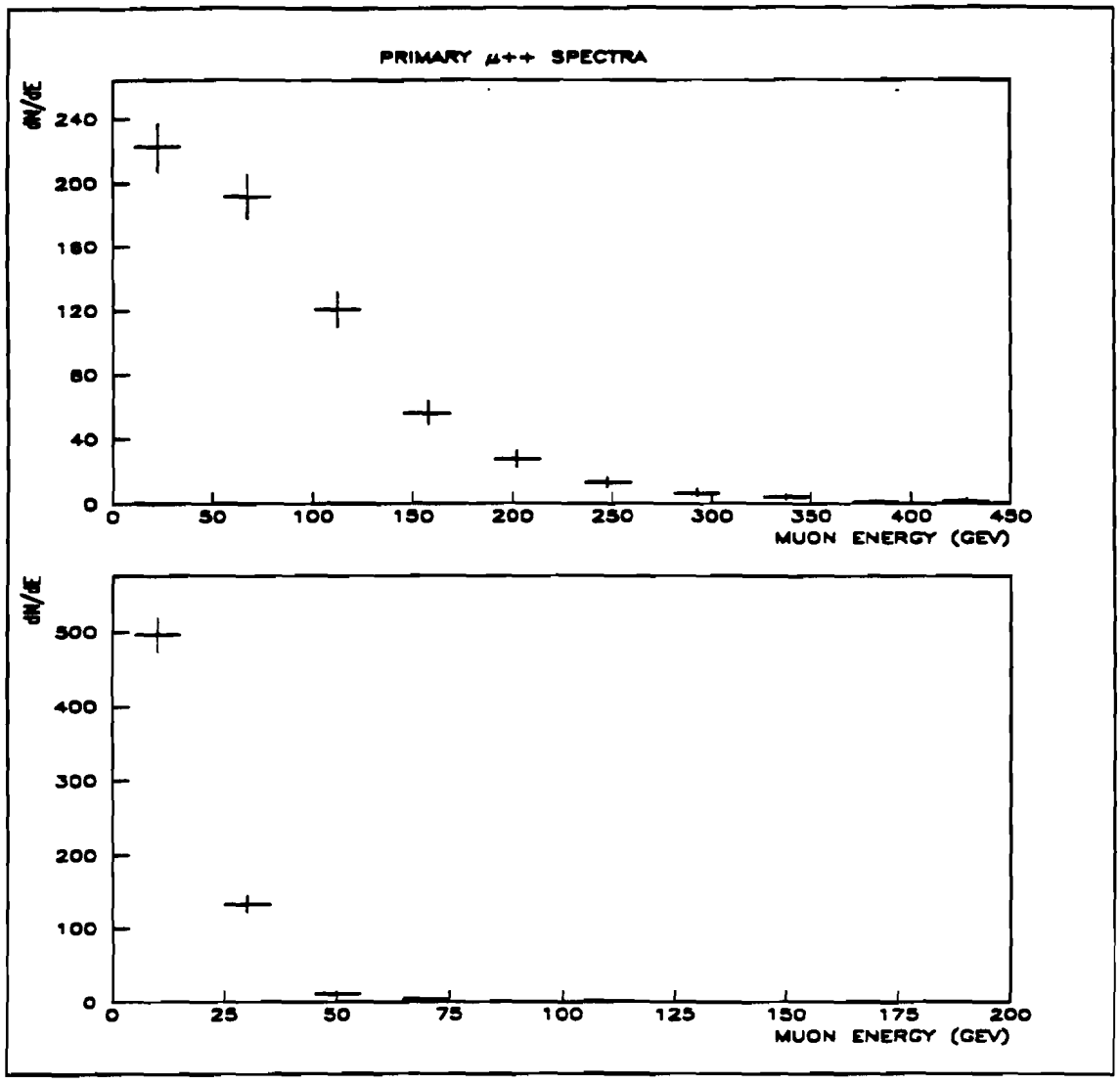

Fig.5.12 Muon energy spectra for antineutrino-induced $\mu^+\mu^+$ primary decay events. The upper plot represents the leading muon, the lower plot represents the second muon.

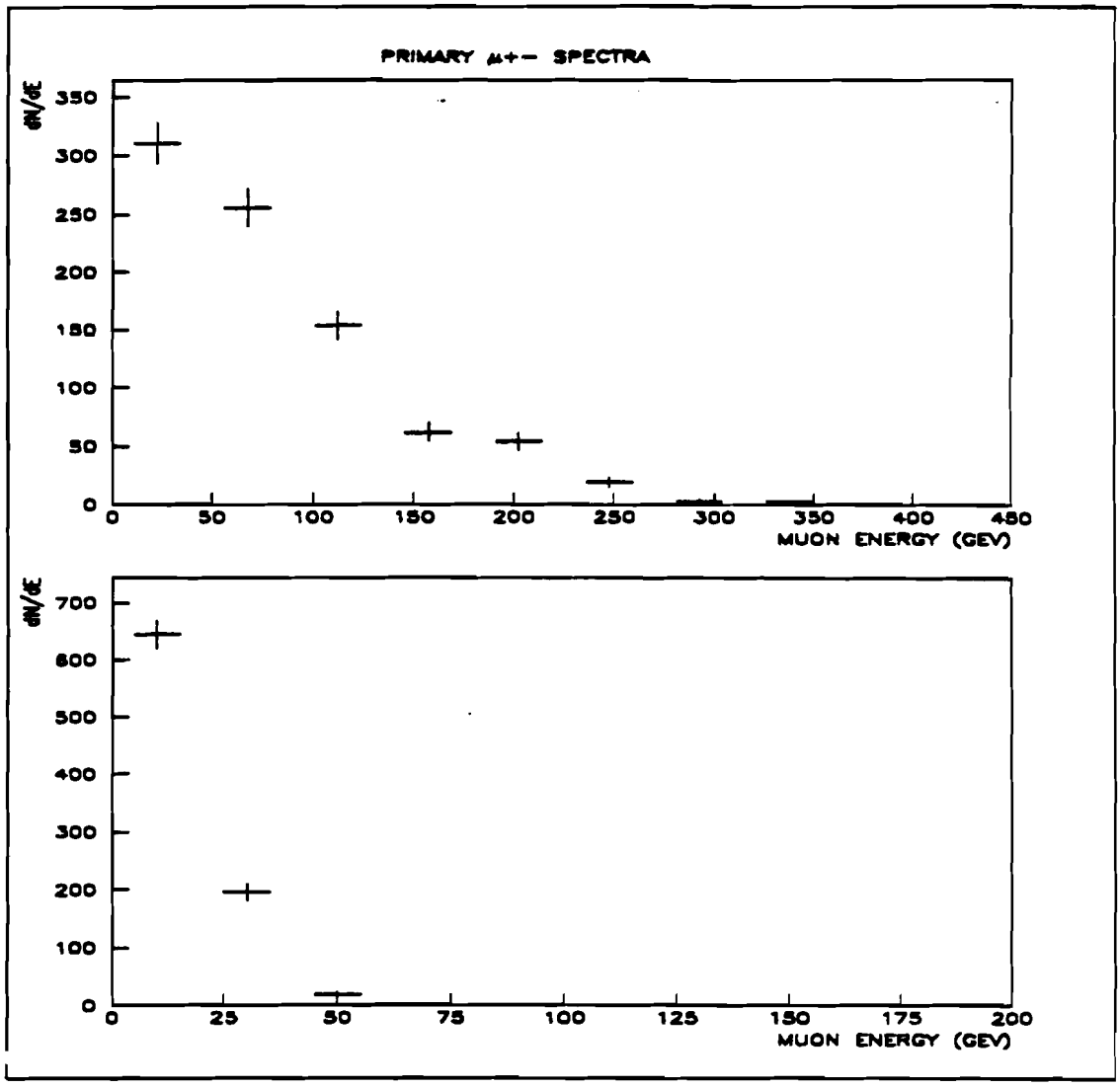

Fig.5.13 Muon energy spectra for antineutrino-induced $\mu^+\mu^-$ primary decay events. The upper plot represents the leading muon, the lower plot represents the second muon.

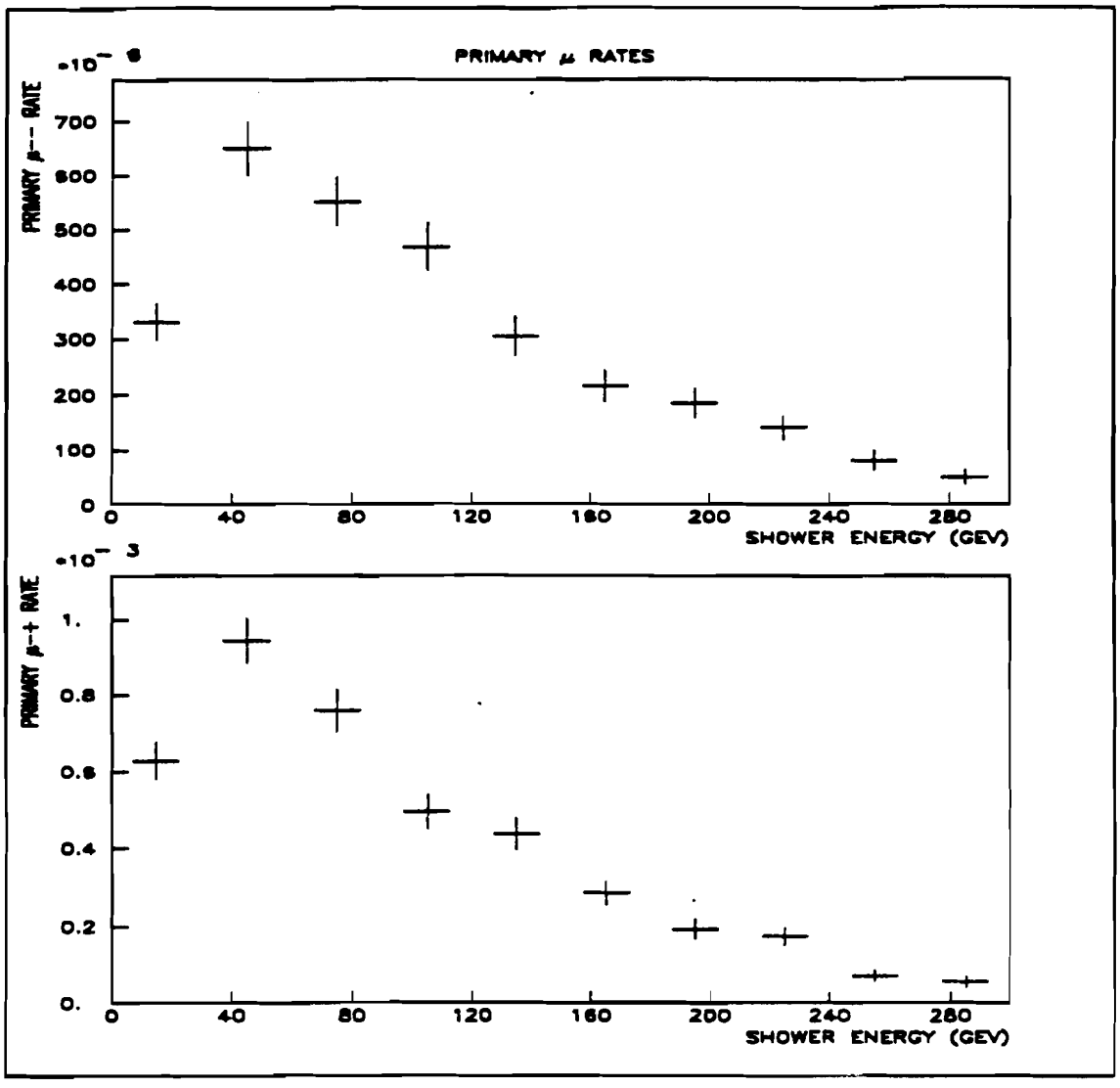

Fig.5.14 Background rates for $\mu^-\mu^-$ (upper plot) and $\mu^-\mu^+$ (lower plot) events resulting from primary decays in neutrino-induced showers plotted versus hadronic shower energy. The rates are in the units of 10^{-6} (normalized per accepted CC MC event).

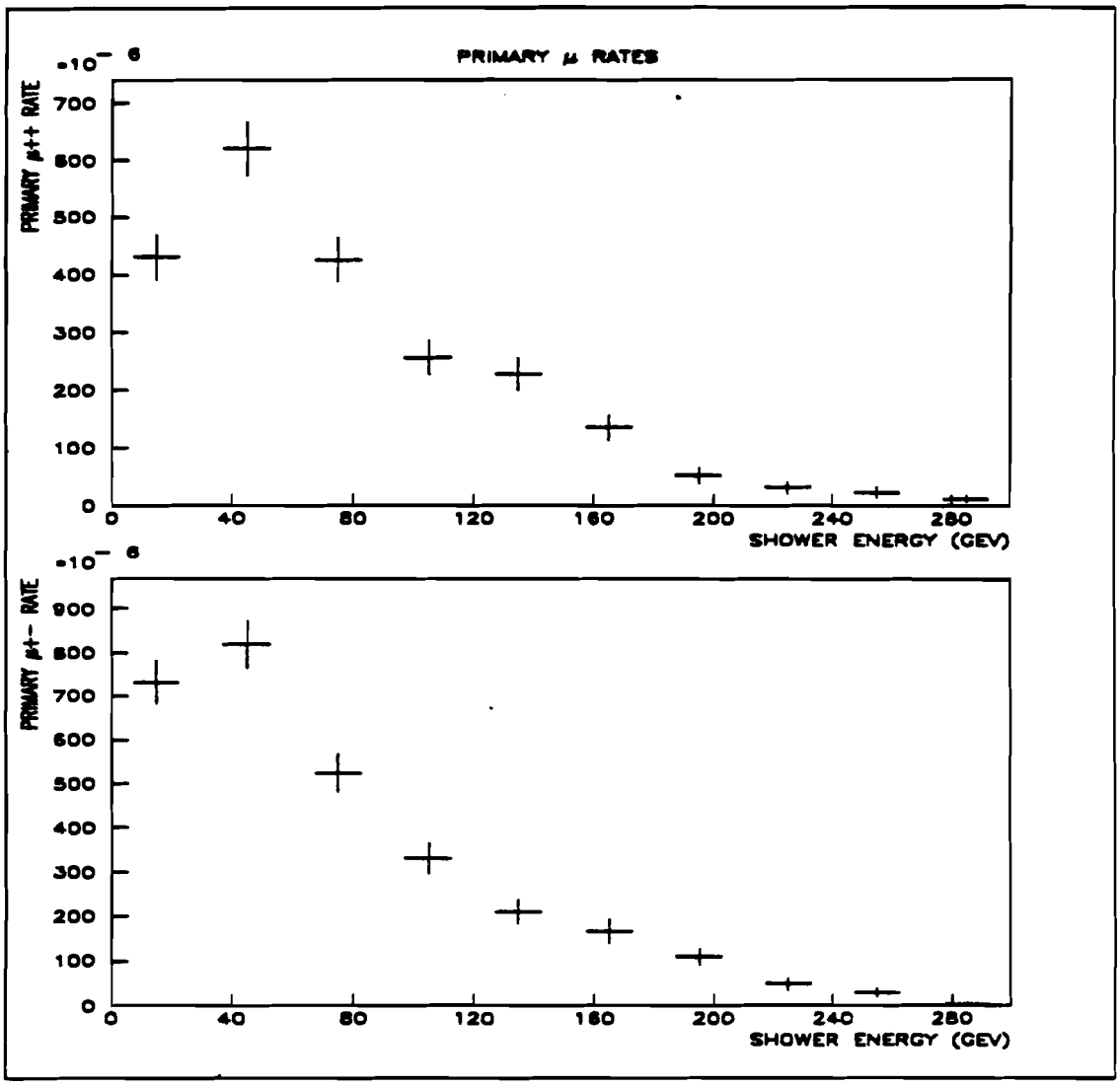

Fig.5.15 Background rates for $\mu^+\mu^+$ (upper plot) and $\mu^+\mu^-$ (lower plot) events resulting from primary decays in antineutrino-induced showers plotted versus hadronic shower energy. The rates are in the units of 10^{-6} (normalized per accepted CC MC event).

5.4 Secondary Decays.

If a primary hadron interacts before it decays it produces more hadrons, which in turn may either interact or decay. We shall call "secondary decays" those decays of the higher generation hadrons. The process is shown in Fig.5.16.

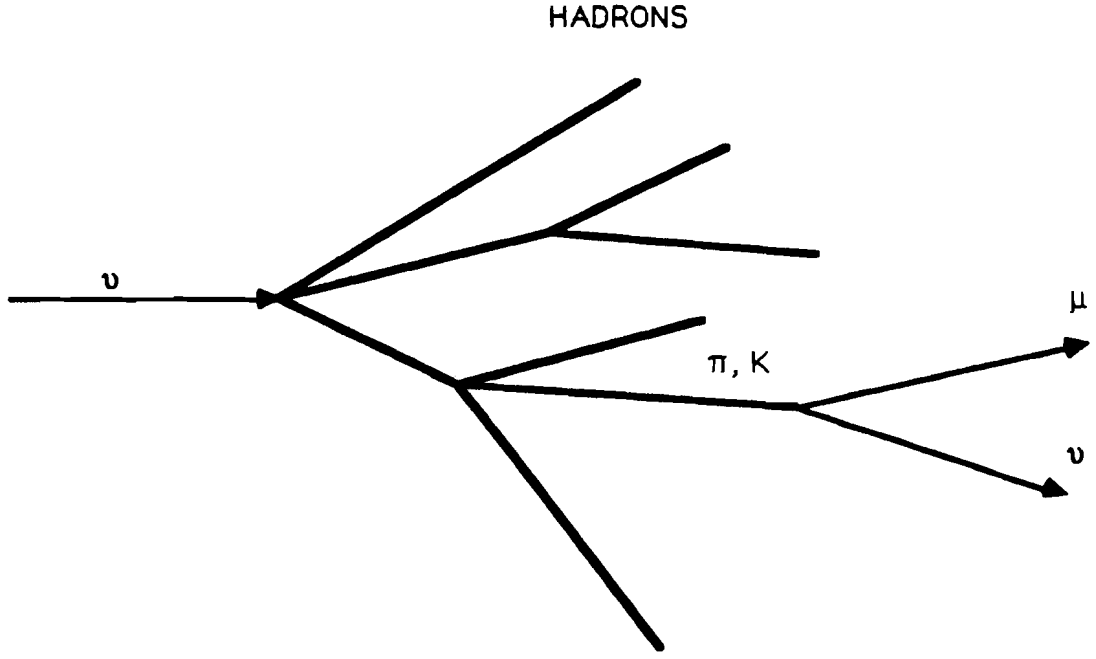

Fig.5.16. Schematic representation of secondary muon production via decays of higher-generation π's or K's.

The simulation of the secondary decays using Monte Carlo methods is difficult because of multiple generations of hadrons and large numbers of particles involved. The approach adopted by this analysis has been to study hadron-induced showers using a dedicated hadron test beam. The secondary decay rates from hadron-induced showers of the test beam data were then applied to simulate the secondary decays in (anti)neutrino-induced showers.This allowed us to reliably determine the secondary decay rate in our detector without having to use the results of other experiments, obtained under different conditions,

or investing a considerable effort into developing and running sophisticated shower Monte Carlo simulations, which may have large systematic errors of their own.

5.4.1 Test Beam.

The test beam layout is shown in Fig.5.17. Hadrons were produced by allowing the 800 GeV protons to collide with an aluminum target. The energy of the hadrons was controlled by two sets of dipole bending magnets. Downstream of the target the beam trajectory was determined by four trigger counters. The beam entered the Lab C detector in the horizontal plane at an angle of **69 mrad** relative to the detector axis. The momentum bite was calculated to be $\Delta p/p \approx 3\%$ full width at half maximum.

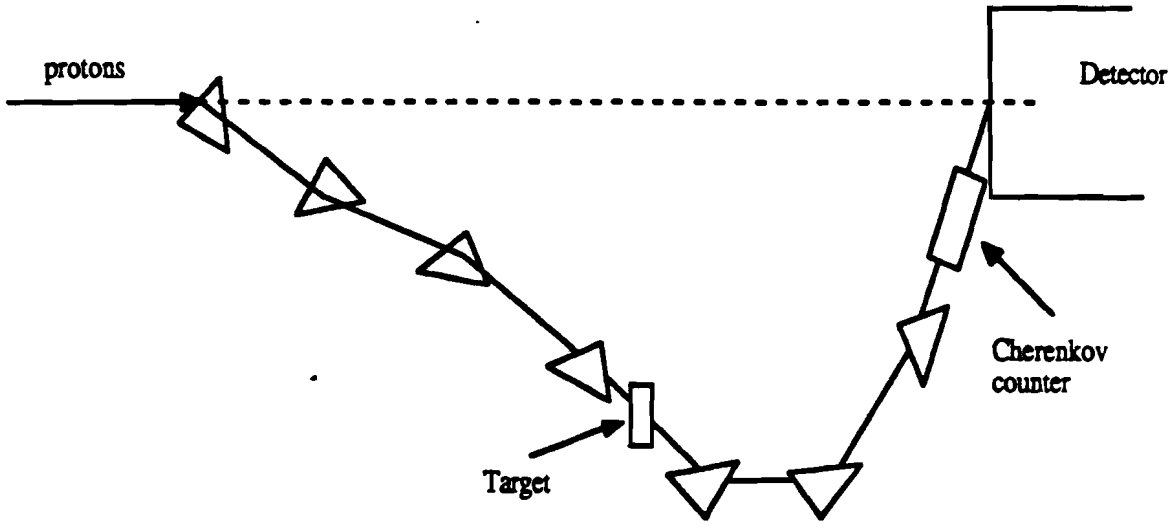

Fig.5.17 Schematic diagram of the test beam layout. Triangles represent dipole magnets. The lateral scale has been expanded

A threshold gas Cherenkov counter was installed in the beamline just upstream of the detector. It was used primarily to determine the beam particle composition, shown in

Table 5.2. For beam energies of up to 100 GeV the test beam particle composition is roughly equal to that of Lund-generated neutrino showers.

Table 5.2. Particle composition of the test beam. The particle fractions are calculated according to a model due to A.Malensek [5.10].

Beam energy [GeV]	π [%]	K [%]	p [%]
33.8	86	9	5
52.5	83	9	8
104.1	76	8	17
209.2	60	6	34
315.8	39	4	57
415.4	20	3	77

5.4.2 Test Events Selection and Reconstruction.

There were two distinct types of test events recorded in the 1985 run: flashing (FL) and non-flashing (NF) events. For NF events only the proportional tube and drift tube information was recorded. The FL events were either deep events with shower vertex beyond Bay 4, or events with the STOP counter hit. Since the NF events were low bias test events in which the flash chambers were not pulsed, the data rate for NF events was about an order of magnitude higher than that for FL events. This allowed a large sample of NF events to be accumulated for the decay rate measurement. Therefore the decay rate analysis concentrated mainly on using NF events. To analyze these events we used the Calorimeter Proportional Tubes (PT) information to find and fit calorimeter muon tracks and to identify

hadron showers. The calorimeter drift planes were used to improve the spatial resolution of the track fits and to help identify muons. Events with muon tracks were then passed on to the toroid muon fitting package for analysis. The program performance was verified by a visual scanning of a fraction of the selected events by physicists.

The information used at the proportional plane level were the HITBIT and the SUMOUT[5.4] signals. The HITBIT signal was the latched output of a PT plane amplifier. As a reminder, each PT amplifier was connected to 4 wires, therefore the spatial resolution of the PT chambers was about $\frac{10cm}{\sqrt{12}}$. The drift planes' resolution was 2.5cm if no drift timing information was available as in the case of no back-to-back hits. The resolution was close to 1.5mm for the case of back-to-back hits with drift timing information available. A HITBIT went ON when the amplifier pulse height was greater than 20 mV at trigger time, which corresponded to the average efficiency for muons of about 85-90%. The SUMOUT was the fast analog signal from each PT plane, discriminated at 35 mV and latched at trigger time with the average efficiency for muons of about 30%. Another piece of information available at each plane was the Analog Multiplicity (AM) signal, which was latched if at least two channels were above the threshold at trigger time.

The first step in the pattern recognition process was to identify each PT plane as being in a NEUTRAL state (no HITBITs ON), a TRACK state (one HITBIT ON or SUMOUT latch with no HITBIT ON) or a SHOWER state (either more than one HITBIT ON or AM latch ON). Thus classified, the planes were then grouped into segments of contiguous planes of the same type. Tracks were formed by the concatenation of track segments, allowing for missing hits or small bremsstrahlung showers along the path. A least squares fit was then performed to obtain a first pass trajectory.

At this point in the analysis the events were checked for consistency with the TEST VETO condition which required no latch activity in the first two PT planes. The TEST VETO was designed to eliminate straight-through muons and hadronic showers originating outside the detector. TEST VETO failures amounted to about 10% of the events. The remaining events were classified into three general categories: JUNK, MUON and SHOWER.

The JUNK condition simply indicated an inconsistency between HITBITs and SUMOUTs downstream of the second plane. The MUON classification was based on the fact that muons generate about one HITBIT per PT plane while traversing many planes, whereas hadronic showers usually generate several HITBITs per planes but in far fewer planes. This made it possible to devise a 2-dimensional cut in the space of TOTAL HITBITs versus number of planes with more than one HITBIT as shown on Fig.5.18. Since the discrimination is most difficult at lower energies, the cut was tuned at the lowest available energy of 35 GeV.

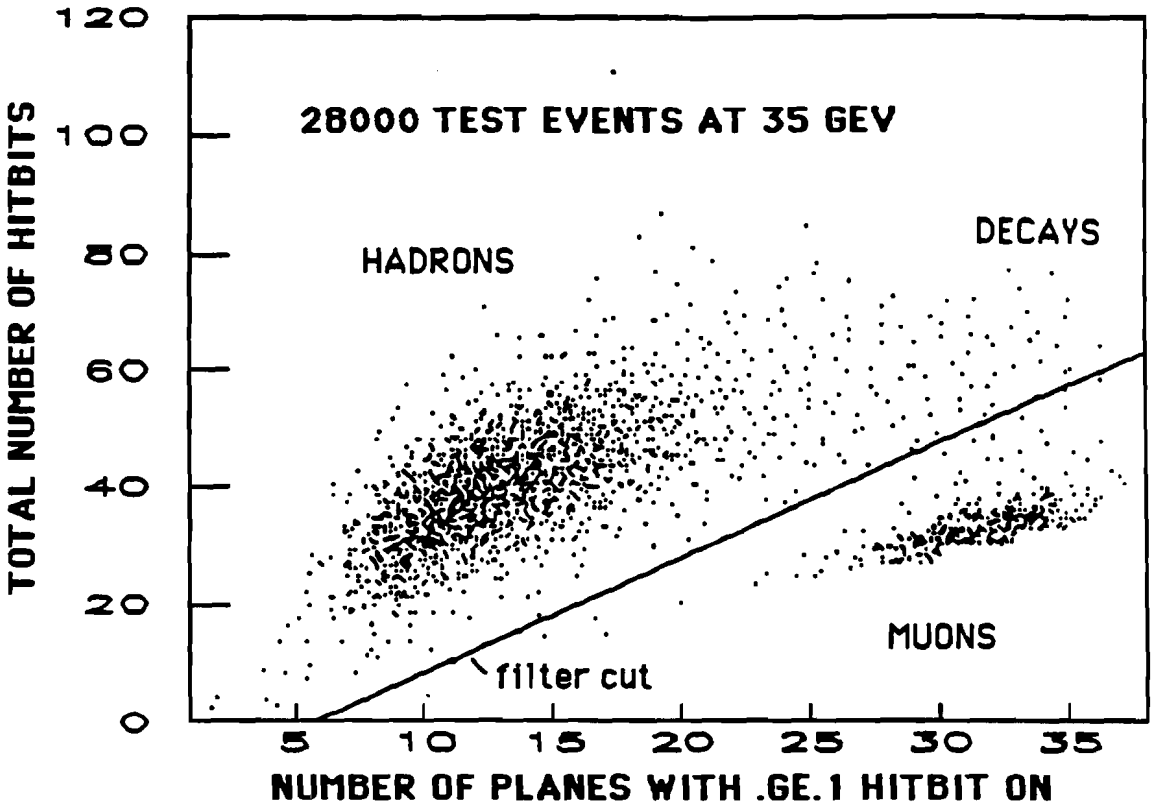

Fig. 5.18 Scatter plot of total number of HITBITS versus number of planes with more than one HITBIT ON. The straight line represents the cut separating hadron showers from muons.

The events satisfying the SHOWER condition were the most important ones for the decay analysis. Here the program looked for a particular decay topology: a hadronic shower of some minimum length followed by a muon track of some minimum length. Specifically, the single decay muon class (designated DK1MU) required a shower segment of at least 4 contiguous planes long, followed by a track of at least 6 planes long with at least 2 hits in each view to determine the track direction. To eliminate long hadron tracks, a requirement was made that there be no more than one "shower" plane in the last five planes of the track. At this point a second pass fit was made to all MUON and SHOWER events. Its most

important feature was the use of the calorimeter drift planes to improve the accuracy of the fits, taking advantage of the drift planes' 1.5 mm resolution. Finally, we required each muon track to have at least 3 drift planes hits outside the magnet hole and in both views. This is the same requirement that we applied to the rest of the data. Table 5.3 shows the numbers of accepted decay events for different test beam energy settings and various muon momentum cuts.

Table 5.3. Shown are the numbers of accepted decay events for different test beam settings and muon momentum cuts as well as the total number of test events (no muon required) for each beam setting.

P_μ cut	Beam energy (Gev)			
(± GeV/c)	35	50	100	150
Total number of events	85435	95467	57682	54077
> +4	53	78	119	178
< -4	18	62	89	127
> +8	42	70	99	155
< -8	14	50	63	108
> +10	31	57	83	134
< -10	10	41	57	87
> +15	12	15	29	56
< -15	2	7	20	40

Fig 5.19. and 5.20 show decay rates for positive and negative muons with different momentum cuts, calculated as ratios of the number of accepted decay muons versus the total number of events for each test beam energy setting.

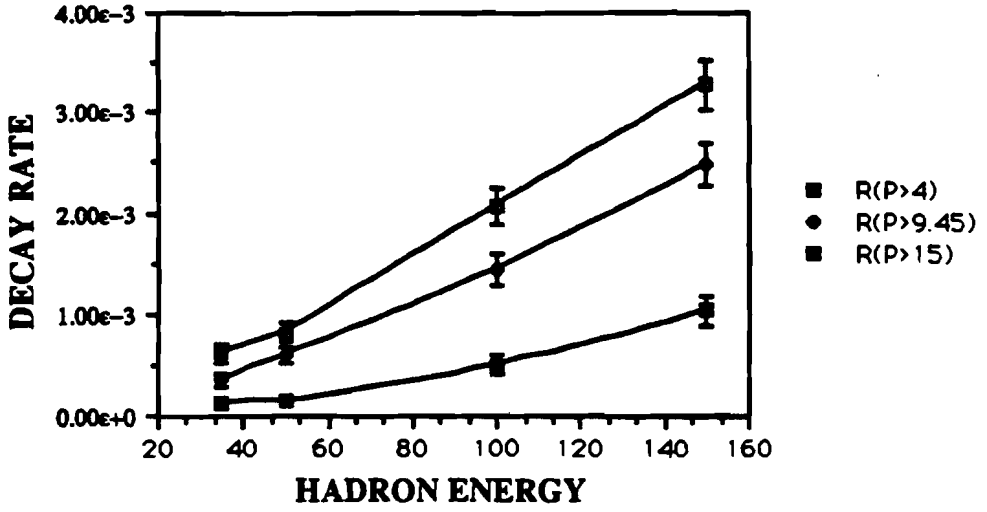

Fig.5.19 Positive decay muon rates for three muon momentum cuts as a function of hadron energy

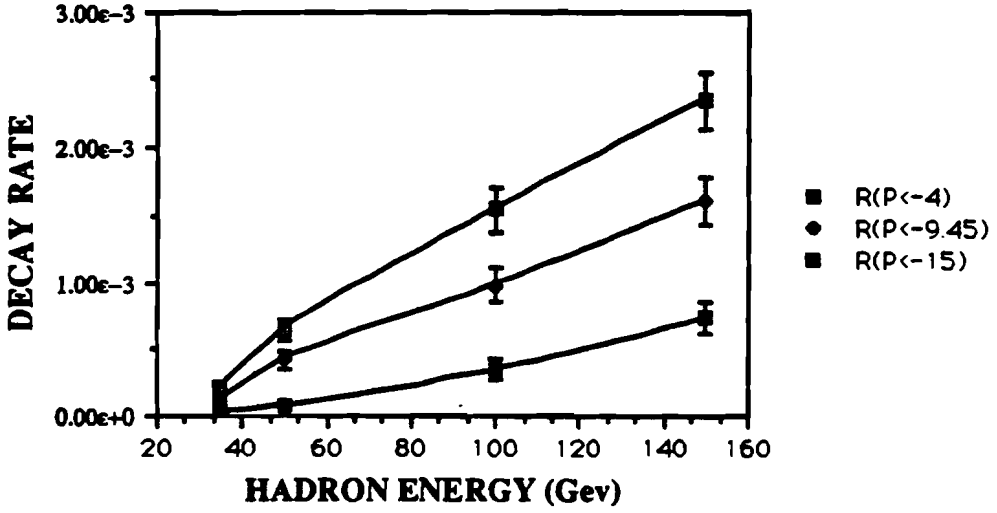

Fig.5.20 Negative decay muon rates for three muon momentum cuts as a function of hadron energy

Overall as one can see from Fig.5.19 and 5.20, increasing the muon cut from 4 GeV/c to 10 GeV/c decreases the secondary decay rates by about a factor of 2.

To parametrize the measured decay rates we used a simple first-order function of the following form:

$$R = \alpha\,(E_h - p_{cut})\,,\ E_h > p_{cut} \qquad 5.5$$
$$R = 0\,,\ E_h < p_{cut}\,,$$

where E_h is the hadron energy, p_{cut} is the muon momentum cut , and α is a constant. For p_{cut} = 10 GeV/c the rates for the μ^+ and μ^- decays respectively are:

$$R^+ = (1.73 \pm 0.07)\times 10^{-5}\,(E_h - 10)$$
$$R^- = (1.13 \pm 0.05)\times 10^{-5}\,(E_h - 10) \qquad 5.6$$

5.4.3. Acceptances.

One must be careful in applying the decay rates of Eq. 5.6 to the neutrino data. First, there is the question of the decay muon sign. Since the test beam consisted of positive hadrons, it is not surprising to find that the μ^+ rate is higher than the μ^- rate. It is natural to assume, however, that there exists a charge symmetry: i.e. for a negative test beam the ratio R^-/R^+ would be equal to R^+/R^- for a positive beam. Thus in the decay simulation for a given hadron in a neutrino shower, we determined the sign of the decay muon based on the hadron's sign and the ratio R^+/R^- .

Another important consideration is the decay muon's experimental acceptances. The requirement of the TEST VETO virtually eliminated test events in Bay 1 in the detector, and resulted in most showers beginning in Bay 2 (about 80 cm from the front of the detector). This longitudinal vertex distribution of test beam events stands in contrast to the longitudinal distribution of neutrino vertices which was essentially uniform and extended all the way from the front of the detector to Bay 8. This difference in the longitudinal vertex

distribution could in principle reduce the test events' acceptance relative to the dimuon data. Given the fact that the test beam was centered laterally, it is straightforward to calculate the maximum slope for a decay muon originating in the front of the detector just past the TEST VETO requirements to hit the 24' toroids: $\theta_{max} = \pm 0.21$ rad. Fig.5.21 - 5.24 show slope distributions of the decay muons with a muon momentum cut of 4 GeV/c at four test beam energy settings: 35, 50, 100 and 150 GeV. Several features of the decay data are evident. First, whereas the vertical slopes are centered at 0 radians, the horizontal slopes are centered at about 69 mrad which is consistent with the test beam geometry as described in Section 5.4.1. The second conclusion is that even with this relatively low muon momentum cut there is no visible cutoff due to acceptance limitations.

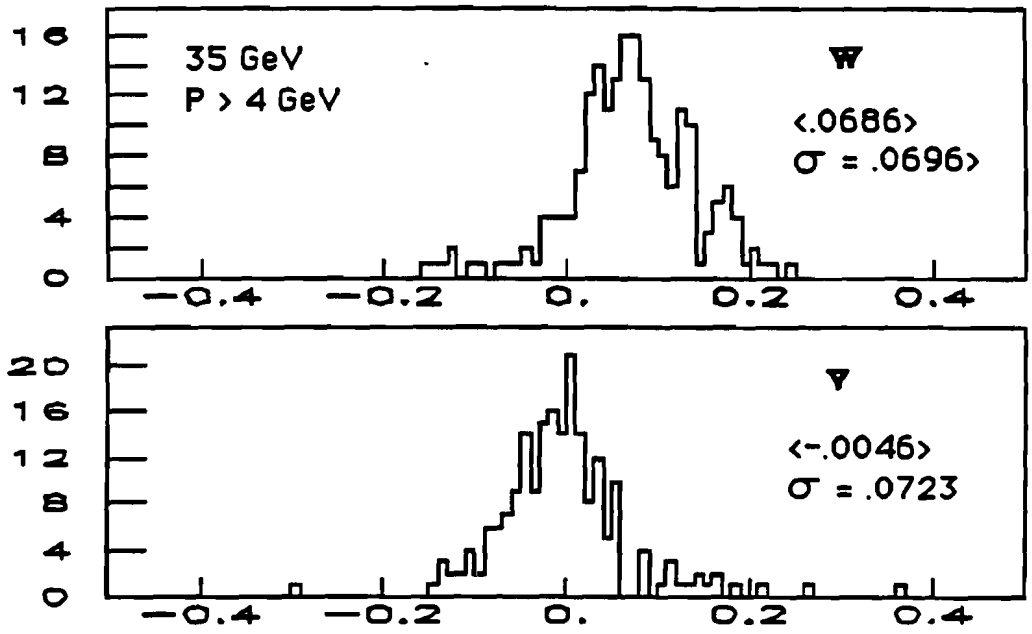

Fig.5.21 Horizontal (upper plot) and vertical (lower plot) slopes of decay muons with $p_\mu > 4$ GeV/c at $E_{beam} = 35$ GeV

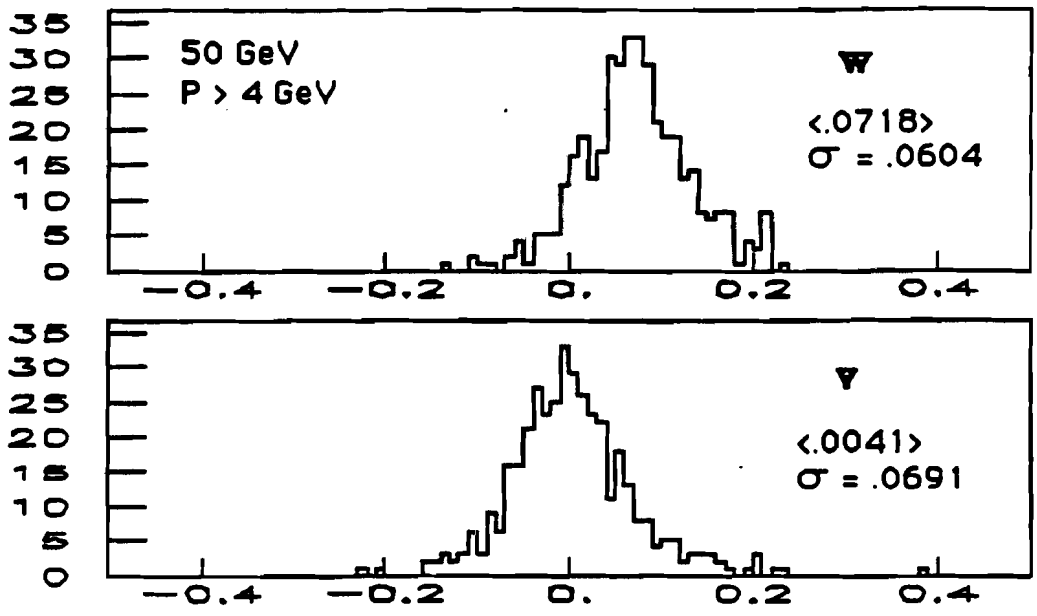

Fig.5.22 Horizontal (upper plot) and vertical (lower plot) slopes of decay muons with $p_\mu > 4$ GeV/c at $E_{beam} = 50$ GeV

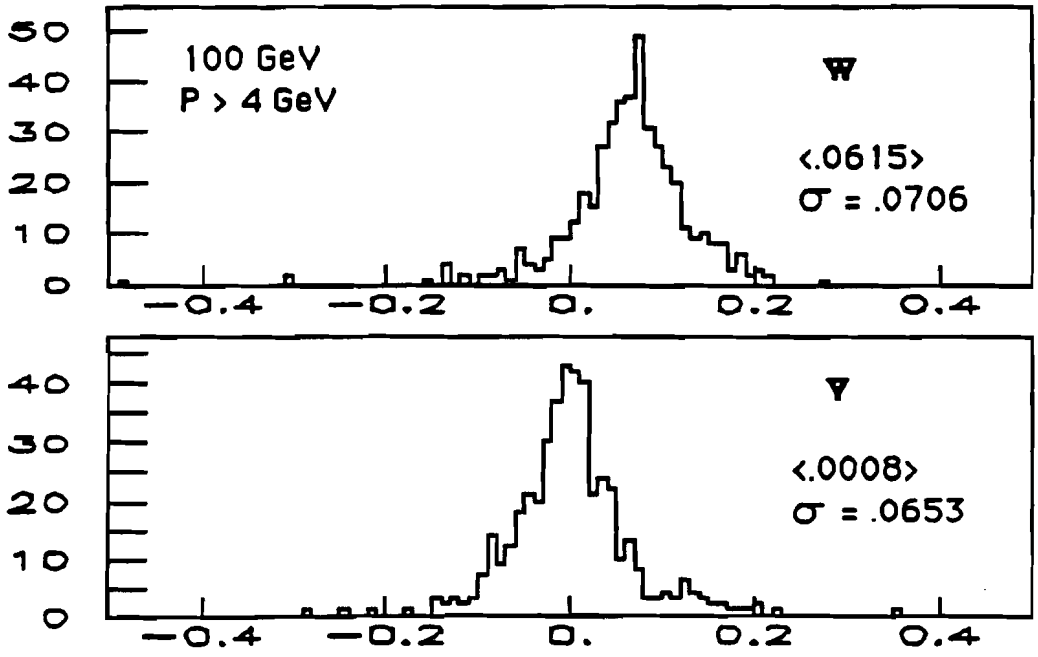

Fig.5.23 Horizontal (upper plot) and vertical (lower plot) slopes of decay muons with $p_\mu > 4$ GeV/c at $E_{beam} =$ 100 GeV

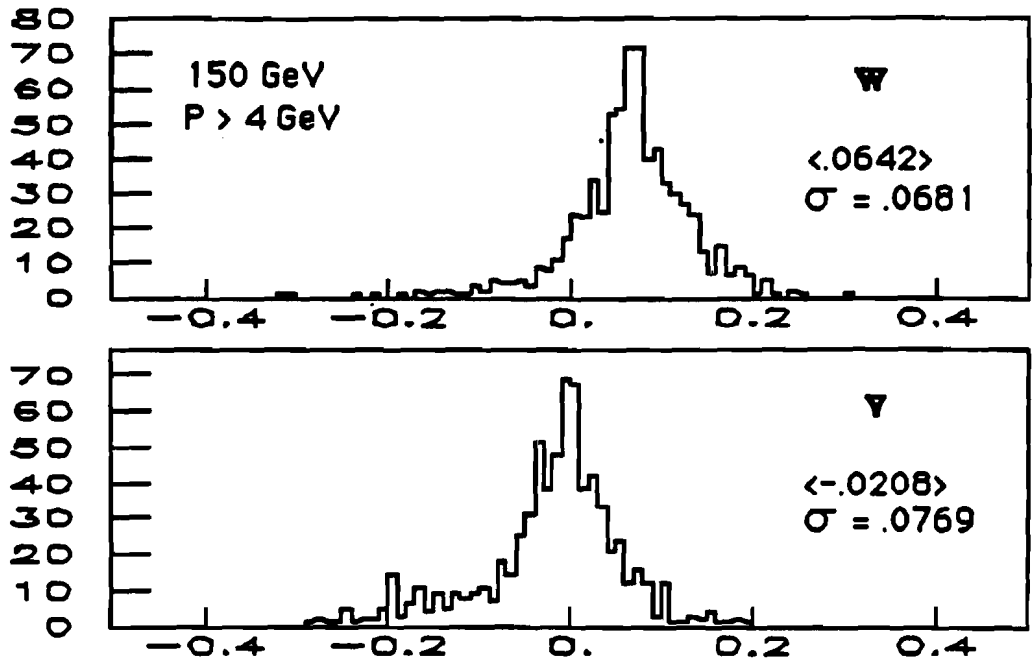

Fig.5.24 Horizontal (upper plot) and vertical (lower plot) slopes of decay muons with $p_\mu > 4$ GeV/c at $E_{beam} = 150$ GeV

This absence of acceptance limitations becomes even more evident in Fig.5.25 a) - c) which show slopes for the decay muons with $p_\mu > 9.45$ GeV/c for three test beam energy settings. So far we have ignored the fact that the test beam was centered laterally whereas the neutrino events were distributed within the approximate fiducial radius of 110 cm. Taking these differences into account reduces the maximum acceptance angle to about $\theta_{max} = \pm$ **0.135 radians.** Fig.5.25 a) - c) show that even these more stringent acceptance criteria are satisfied at $p_\mu > 9.45$ GeV/c. A potential source for higher acceptance losses for decay muons in neutrino showers relative to the test data is due to the fact that the test beam was centered laterally in the detector, whereas the neutrino showers had broad lateral distributions (see Chapter V). This possibility was investigated via a Monte Carlo calculation in which the test data showers were distributed throughout the detector according to the neutrino data distributions. The acceptance losses proved to be negligible. Hence the test beam decay muons are a good estimate of the secondary decay background.

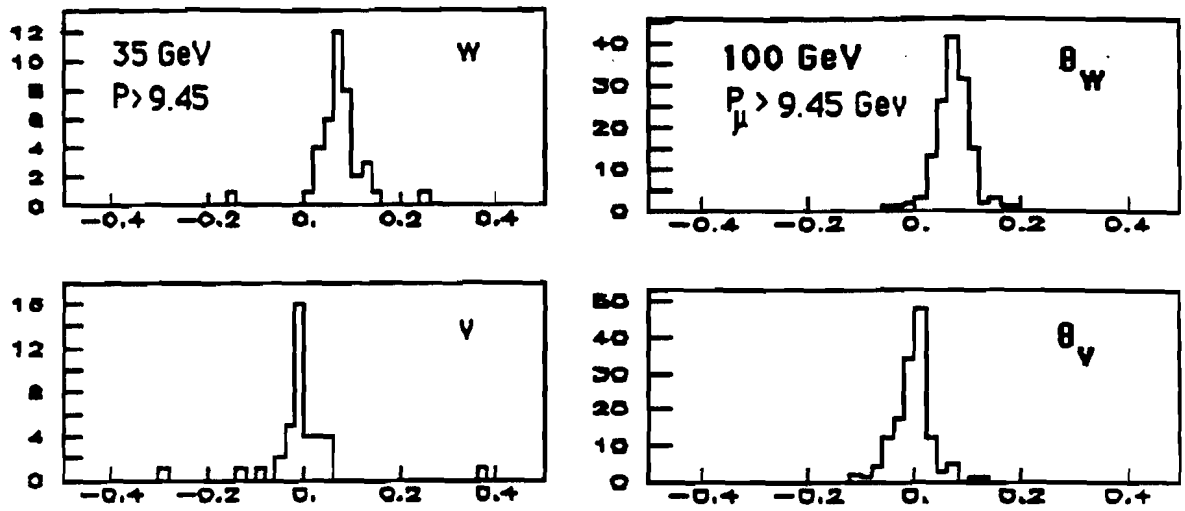

a) b)

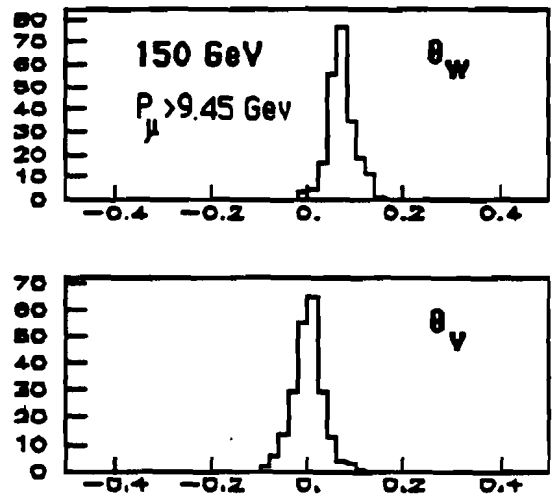

c)

Fig. 5.25 Horizontal and vertical slopes of decay muons with p_μ > 9.45 GeV/c at E_{beam} = 35 GeV (a),E_{beam} = 100 GeV (b) and E_{beam} = 150 GeV (c).

5.4.4. The Secondary Decay Simulation.

The secondary decay simulation differed from that of the primary decay in that we did not produce complete MC "events", which could then be analyzed using the standard analysis routines. Instead, the secondary decay simulation computed the decay rates that could be plotted as functions of such variables as W^2, or shower energy, for example. We would like to emphasize, however, that since these decay rates are based on experimental results, they already have in them the effects of the experimental acceptances and resolutions.

To determine the secondary decay rate one needs to calculate the probabilities of producing a decay muon from every available hadron in the shower using Eq.5.6. As in the simulation of primary decays, we used LEPTO to generate (anti)neutrino-induced hadronic showers. Our test beam consisted mainly of pions especially at low energies (see Table 5.2) plus some kaons and protons. Generally speaking, the percentages of K's and p's were higher in neutrino showers than in the test beam, and neutrons were also present. To obtain the muon yields for kaon- , proton- , and neutron-induced showers relative to the muon yields of pion-induced showers, we followed the calculation done by K. Lang [5.5]. The relative muon yields averaged over energy were 1.8 for kaons, 0.8 for protons and 0.775 for neutrons. Taking the relative muon yields into account increases the secondary rates calculated with equal muon yields for all hadrons by 5% for $\mu^-\mu^+$, and 6% for $\mu^-\mu^-$. The total rates change by 1.5% and 1.3% , respectively. A summary of the secondary decay rates is shown in Table 5.4. The rates are calculated as the ratio of the secondary decay events versus the accepted single-muon CC events.

Table 5.4. Summary of the secondary decay rates for neutrino and antineutrino events. The rates are calculated as the numbers of the decay events per accepted CC MC event. The errors are statistical.

	Neutrinos	Antineutrinos
$\mu^-\mu^-$	$(1.57 \pm .01)\times10^{-4}$	
$\mu^+\mu^+$		$(8.6 \pm 0.08)\times10^{-5}$
$\mu^-\mu^+$	$(2.05 \pm .01)\times10^{-4}$	$(9.71 \pm 0.08)\times10^{-5}$

As Table 5.4 shows, antineutrino opposite sign rates are about 44% of the neutrino rates, assuming equal fluxes of neutrinos and antineutrinos. Given the fact that the antineutrino flux is about 30% of the neutrino flux in the quadruplet beam, the opposite sign background rate due to antineutrinos is about 14% of the neutrino rate. Overall the secondary opposite sign background rate due to both neutrinos and antineutrinos is about 30% of the primary decay rate (see Table 5.1). Fig.5.26 - 5.27 show secondary decay rates for neutrinos and antineutrinos respectively with E_μ>10 GeV as functions of shower energy. The rates are calculated as the ratios of the numbers of the accepted decay events divided by the numbers of the accepted charged current events with E_μ> 10 GeV.

To get some insight into the energy behavior of the decay rates, let us make a simple estimate. The total decay probability for a particle can be approximated as $P \sim \lambda_I/\lambda_D$, where λ_I is the interaction length and λ_D is the decay length. Assuming λ_I is constant and using $\lambda_D = \gamma\beta c\tau \approx \frac{E}{m} c\tau$, we get $P \sim 1/E$, where E is the particle's energy. Then the secondary decay rate is $R \sim \langle n \rangle \langle 1/E_h \rangle$, where $\langle n \rangle$ is the average hadron multiplicity per event, and $\langle 1/E_h \rangle$ is the average inverse energy of a hadron. One can write $\langle 1/E_h \rangle = \langle n/E_{shower} \rangle$. Making the approximation $\langle 1/E_h \rangle \approx \langle n \rangle/E_{shower}$, we can write the decay

rate as R ~ $\langle n \rangle^2 / E_{shower}$. As was mentioned earlier $\langle n \rangle$ rises logarithmically with W^2. At low E_{shower}, $\langle n \rangle^2$ rises faster than E_{shower}, and so the decay rate also rises. Then $\langle n \rangle$ begins to slow down stopping the rise in R. At still higher E_{shower} $\langle n \rangle$ becomes almost constant thus causing R to go down.

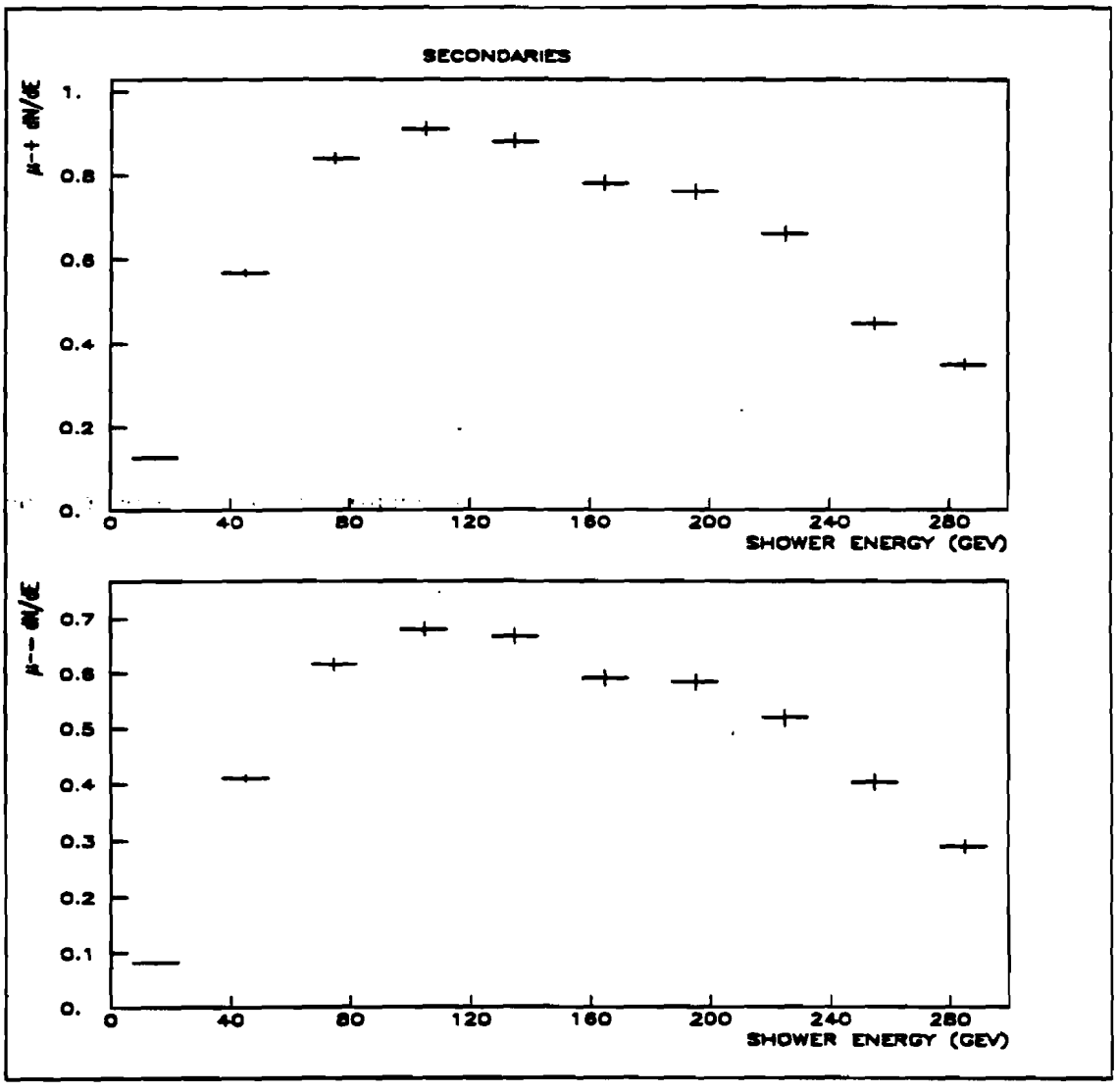

Fig.5.26 Secondary decay rates for neutrino-induced showers as functions of the shower energy. The upper plot represents the $\mu^-\mu^+$ rate, and the lower plot represents the $\mu^-\mu^-$ rate. The rates are in the units of 10^{-6} (normalized per accepted CC MC event).

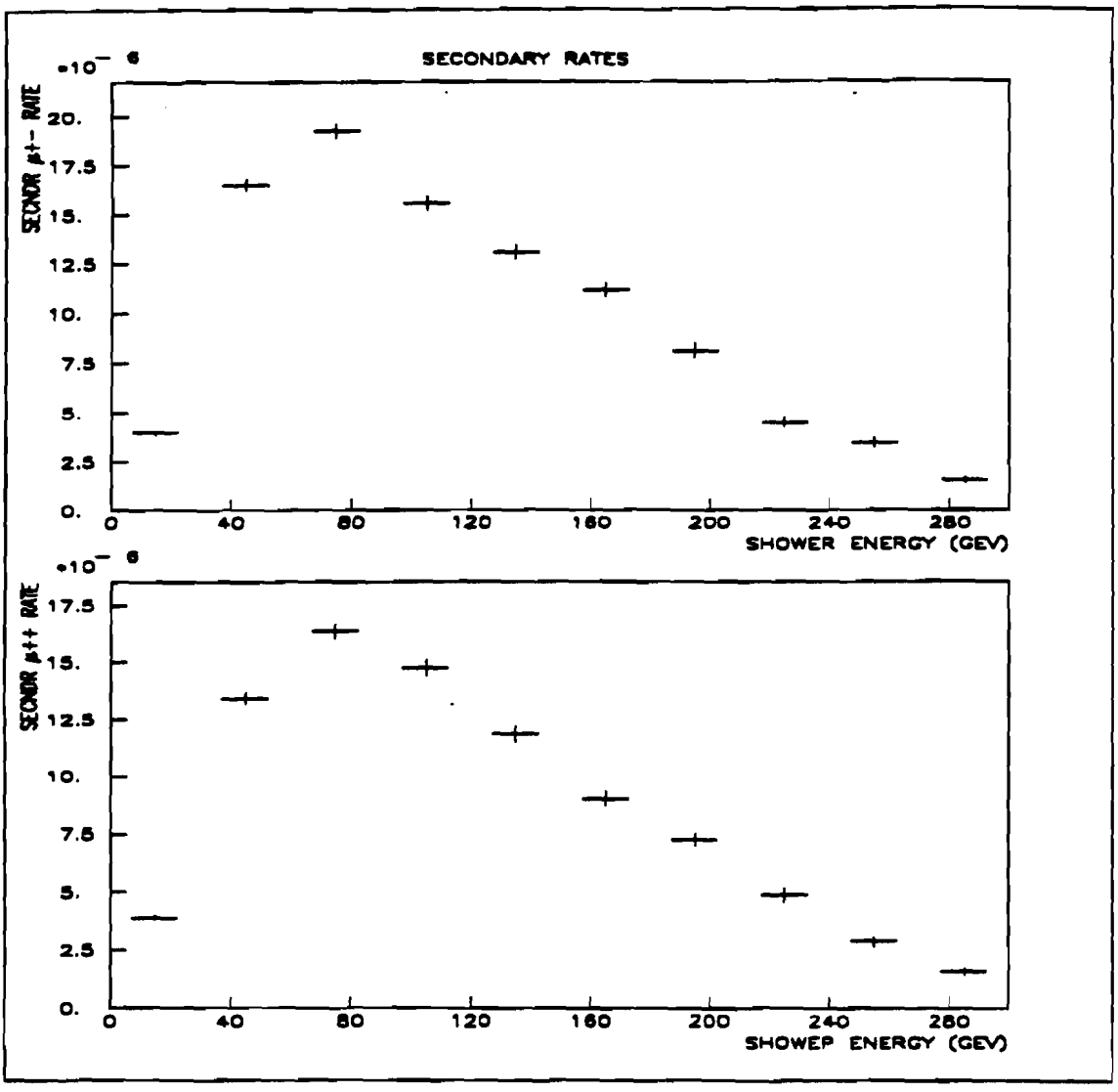

Fig.5.27 Secondary decay rates for antineutrino-induced showers as functions of the shower energy. The upper plot represents the $\mu^+\mu^-$ rate, and the lower plot represents the $\mu^+\mu^+$ rate.The rates are in the units of 10^{-6} (normalized per accepted CC MC event).

5.5 Results and comparison with data.

To calculate the total decay rates we added the primary and the secondary decay rates to obtain Fig.5.28 - 5.29 for neutrinos and antineutrinos, respectively. All rates are normalized per accepted charged current event with $E_\mu > 10$ GeV.

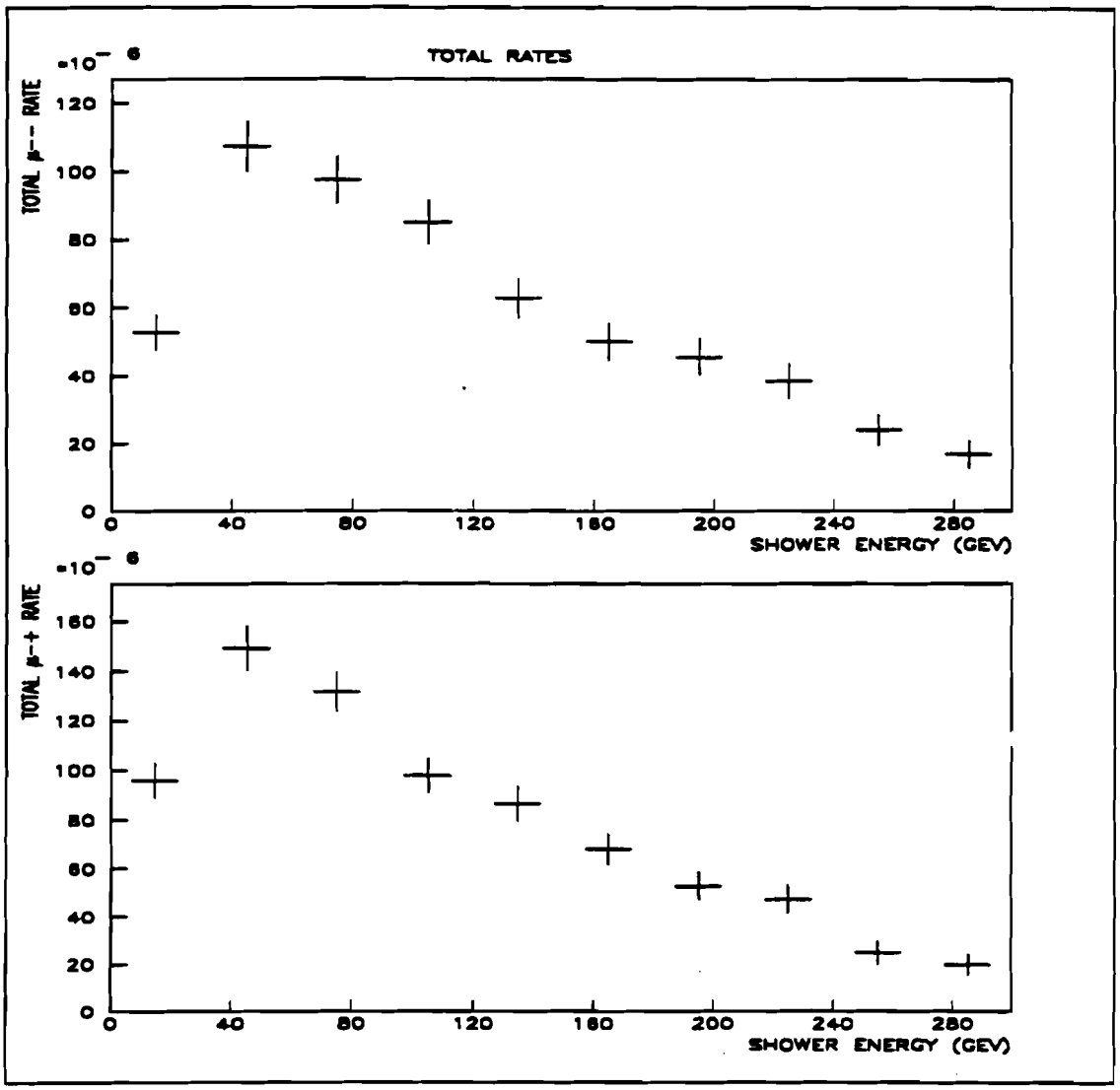

Fig.5.28. Total rate for neutrino $\mu^-\mu^-$ (upper plot) and $\mu^-\mu^+$ (lower plot) background events as a function of shower energy. The vertical scale is in the units of 10^{-6} (normalized per accepted CC MC event).

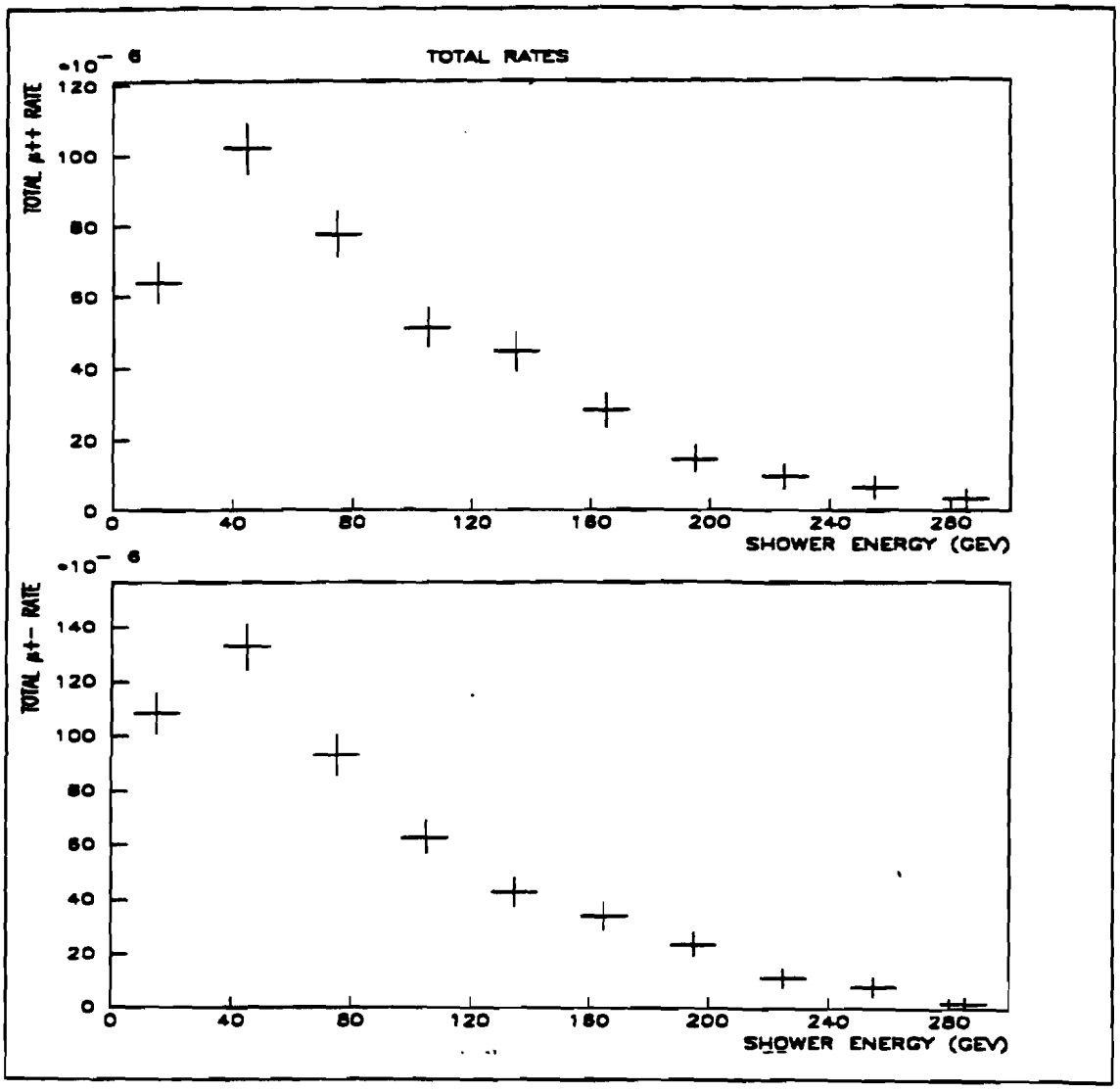

Fig.5.29. Total decay rate for antineutrino $\mu^+\mu^+$ (upper plot) and $\mu^+\mu^-$ (lower plot) events as a function of shower energy.The vertical scale is in the units of 10^{-6}.

A summary of total MC background rates is shown in Table 5.5.

Table 5.5. Monte Carlo calculated total background rates for a pure neutrino, a pure antineutrino beams. The rates are normalized per accepted CC MC event. The errors are statistical.

	Neutrino	Antineutrino
$\mu^-\mu^-$	$(5.91 \pm 0.14)\times10^{-4}$	
$\mu^-\mu^+$	$(7.87 \pm 0.17)\times10^{-4}$	$(5.18 \pm 0.14)\times10^{-4}$
$\mu^+\mu^+$		$(4.01 \pm 0.12)\times10^{-4}$

It has been speculated for a long time that like-sign dimuon events have their origin in leptonic hadron decays in neutrino showers [5.6],[5.7]. The recent extensive investigation of the subject by the CCFR collaboration [5.8], [5.9] supports this point of view. They accumulated 101 $\mu^-\mu^-$ events and 15 $\mu^+\mu^+$ events with $P_\mu > 9$ GeV/c for both muons. Of these events they calculate that 76.9 ± 9.4 $\mu^-\mu^-$ events and 7.9 ± 1.5 $\mu^+\mu^+$ events come from hadron decay background. Also taking into account overlays and trimuons, the total background becomes 82.5 ± 9.7 for $\mu^-\mu^-$ events and 8.6 ± 1.6 for $\mu^+\mu^+$ events, which is consistent with the total like-sign dimuon signal.

Our experiment has accumulated 57 $\mu^-\mu^-$ and 8 $\mu^+\mu^+$ events with $E_\mu > 10$ GeV as well as the other cuts applied to the dimuon data sample as described in Chapter III. The like-sign dimuon rates calculated in the usual manner as the ratio of the accepted like-sign events to the accepted CC events are shown in Table 5.6. It is evident from comparing Tables 5.5 and 5.6 that the data rates for both $\mu^-\mu^-$ and $\mu^+\mu^+$ events are in good agreement with the Monte Carlo calculated background rates. This result therefore confirms the notion that like sign dimuon events come from leptonic hadron decays in (anti)neutrino showers.

In addition to a good agreement between the total MC decay rates and data, it is important to establish that the energy dependence of the MC decay rates corresponds to that of data. Due to the data statistics limitations the only meaningful comparison available is for the negative like sign dimuons. Fig.5.30 shows the data and MC negative like sign rates plotted as functions of the shower energy.

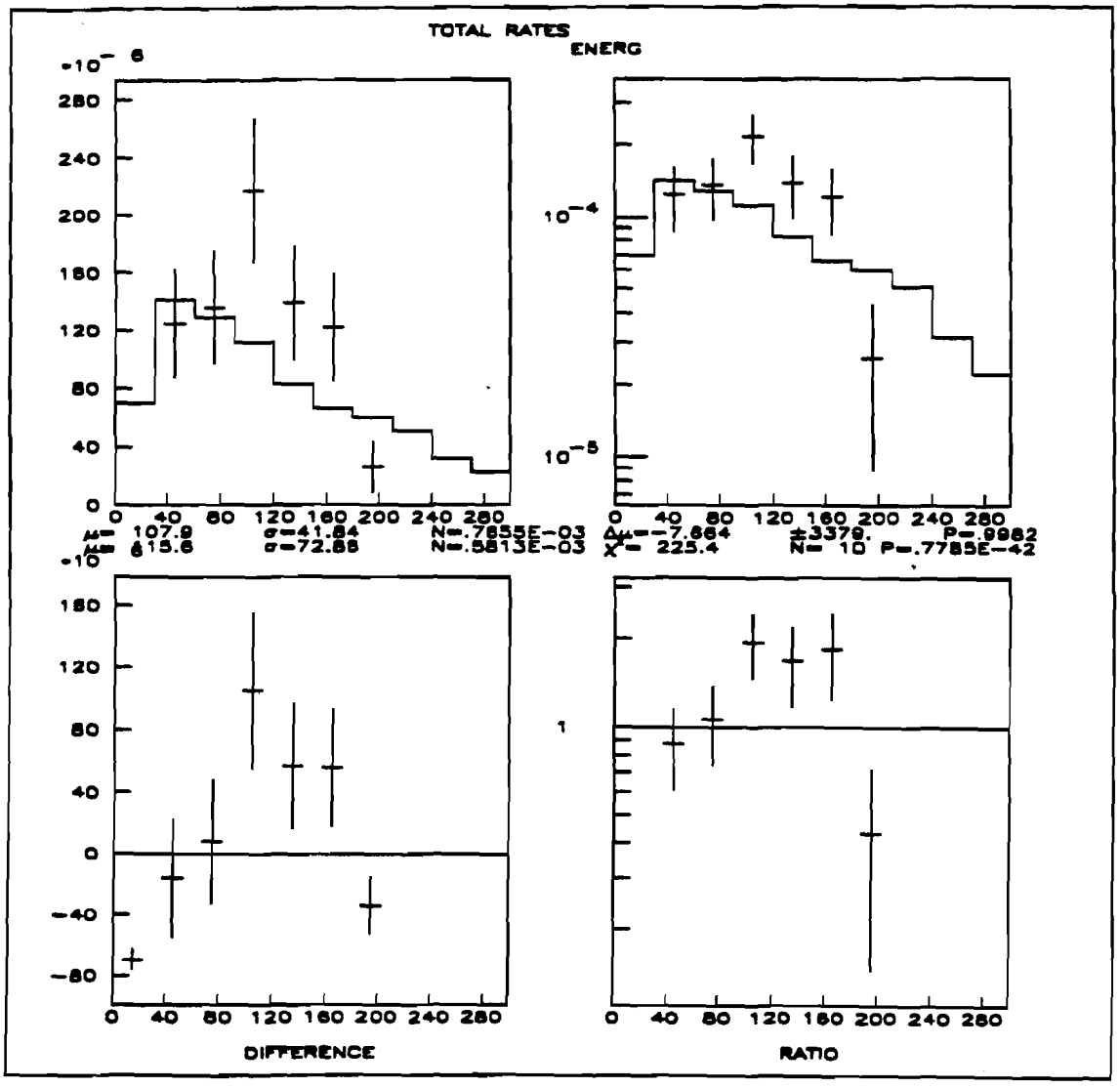

Fig.5.30. Data (points with errors) and Monte Carlo (smooth line) $\mu^-\mu^-$ rates. The rates are in the units of 10^{-6} (normalized per accepted CC MC event).

To perform the background subtraction for the opposite sign dimuon analysis we use the like-sign events thereby accounting for all the experimental efficiencies, resolutions, etc. Table 5.7 shows the ratio of opposite-sign to like-sign dimuon rates for positive and negative like-sign events for 10 bins in hadronic shower energy. As we explain in Chapter VI we use the numbers from Table 5.7 to predict the numbers of opposite sign background events per each like sign event.

Table 5.6. Like sign data sample and event rates. The rates are normalized per accepted CC MC event. The errors are statistical only.

	$\mu^-\mu^-$		$\mu^+\mu^+$	
	# events	Rate	# events	Rate
Beam Gate	49	$(6.12\pm 0.89)\times10^{-4}$	7	$(5.72 \pm 2.16)\times10^{-4}$
Tail Gate	8	$(7.48 \pm 2.64)\times10^{-4}$	1	$(5.9 \pm 5.9)\times10^{-4}$
Total	57	$(6.52 \pm 0.86)\times10^{-4}$	8	$(5.76 \pm 2.03)\times10^{-4}$

Table 5.7. Monte Carlo calculated ratios of opposite sign vs like sign event rates for negative and positive like sign events. The errors are statistical

E_{shower} (Gev)	R^{-+}/R^{--}	R^{-+}/R^{++}
0 - 30	1.819 ± 0.219	1.693 ± 0.191
30 - 60	1.390 ± 0.122	1.302 ± 0.122
60 - 90	1.349 ± 0.125	1.199 ± 0.134
90 - 120	1.149 ± 0.120	1.230± 0.178
120 - 150	1.377 ± 0.166	0.962 ± 0.166
150 - 180	1.356 ± 0.190	1.217 ± 0.265
180 - 210	1.155 ± 0.182	1.655 ± 0.541
210 - 240	1.228 ± 0.216	1.200 ± 0.580
240 - 270	1.041 ± 0.270	--------
270 - 300	1.179 ± 0.376	--------

Knowing these ratios allows one to calculate the amount of opposite sign background based on the known number of the like sign events as a function of E_{shower}. The background subtraction procedure is described in detail in Chapter VI. We would like to emphasize that possible biases due to incompleteness of the MC model are minimized by using the relative numbers only.

A few remarks are in order. In our analysis we assumed that the knowledge of the E_{shower} behavior of the decay rates is enough to perform the background subtraction accurately. In other words, we assume that the decay rates are not strongly correlated with other

kinematic variables such as x_{vis} ,y_{vis} ,etc. We feel that this assumption is entirely reasonable because the decay rates for individual hadrons depend only on their energy and the shower energy is simply the sum of these energies.

5.6. Systematic errors on the background calculation.

We investigated several sources of systematic errors for the background calculation. These sources and the corresponding errors are listed below.

1. The strangeness suppression parameter λ in the Lund Monte Carlo. It is defined as $\lambda = P(s)/P(u)$, where P(s) is the probability of strange quark pair production, and P(u) is the probability of u (or d) quark pair production. The Lund default value that we used is $\lambda = 0.3$. We varied λ from 0.2 to 0.4 with the total decay range changing by ±9.5%.

2. A ±10% uncertainty in the secondary decay rate parametrization leads to ±4% systematic error on the total decay rate.

3. An estimated ±2% uncertainty in the interaction and decay lengths for pions and kaons results in ±0.8% systematic error on the decay rate.

The above systematic errors taken in quadrature result in a total estimated systematic error on the decay rate of ±10.3%.

CHAPTER VI.
RESULTS.

6.1 Introduction.

Detailed understanding of opposite sign dimuons production offers opportunities for determining several important parameters, relevant not just to dimuons, but in a broader context of the quark-parton model. The most important of these parameters is the amount of strange sea inside the nucleon x, which we discussed in Chapter I. Opposite sign dimuons offer the unique opportunity for determining this quantity. It is of particular interest to compare the amount of strange sea for this experiment with earlier results obtained at lower Q^2. This gives us an opportunity to compare the QCD-based predictions about x evolution with data.

There are other parameters in the standard charm production model of opposite sign dimuons that can be determined from opposite sign dimuons. They are the semileptonic branching ratio B, the elements U_{cd} and U_{cs} of the Kobayashi-Maskawa matrix, and finally, the mass of the charm quark. We think that our measurements of these quantities complement results of other experiments in an independent way.

6.2 Background Subtraction.

To subtract the background due to muonic decays in hadron showers, we used the like-sign dimuon events together with the MC calculation of the background, described in Chapter 5. As we showed in Chapter V, our MC calculation, as well as other experiments' independent analysis, indicate that essentialy all like-sign events come from hadron decays in neutrino showers. The background MC calculation provides us with a means of predicting the number of opposite sign background events per each like-sign event. To

simulate the opposite sign background events, the like sign events' entries into all histograms were weighted by the "transfer" coefficients of Table 5.7, depending on the hadronic shower energy of the event. The resulting like-sign dimuon distributions were then subtracted from the corresponding opposite sign distributions.

A summary of the final dimuon data sample is shown in Table 6.1. Events are grouped according to trigger type (Beam Gate or Tail Gate) and muon sign ($\mu^-\mu^+$, $\mu^-\mu^-$ or $\mu^+\mu^+$) The cuts applied to the dimuon data sample are the same cuts that we applied throughout this analysis. They were:

1) the fiducial cuts;

2) $E_{shower} > 10$ GeV;

3) $E_{\mu 1,\mu 2} > 10$ GeV;

4) the toroid magnet hole cut.

Table 6.1. Summary of the final dimuon data sample.

	Beam Gate	Tail Gate	Total
$\mu^-\mu^+$	346	47	393
$\mu^-\mu^-$	49	8	57
$\mu^+\mu^+$	7	1	8
Weighted $\mu^-\mu^-$	68.12	10.40	78.52
Weighted $\mu^+\mu^+$	13.10	1.30	14.4
$\mu^-\mu^+$ after background subtr.	264.78	35.30	300.1

The total calculated background is **92.9** events or **23.7%** of the opposite sign dimuon data sample. The total number of opposite sign dimuons after background subtraction is **300.1**

events. To illustrate the effects of the decay background on the opposite sign dimuons, we show distributions of three quantities before and after the background subtraction. Fig.6.1 shows the leading muon's energy, Fig.6.2 shows the second muon energy, and Fig.6.3 shows the $x_{visible}$ distribution.

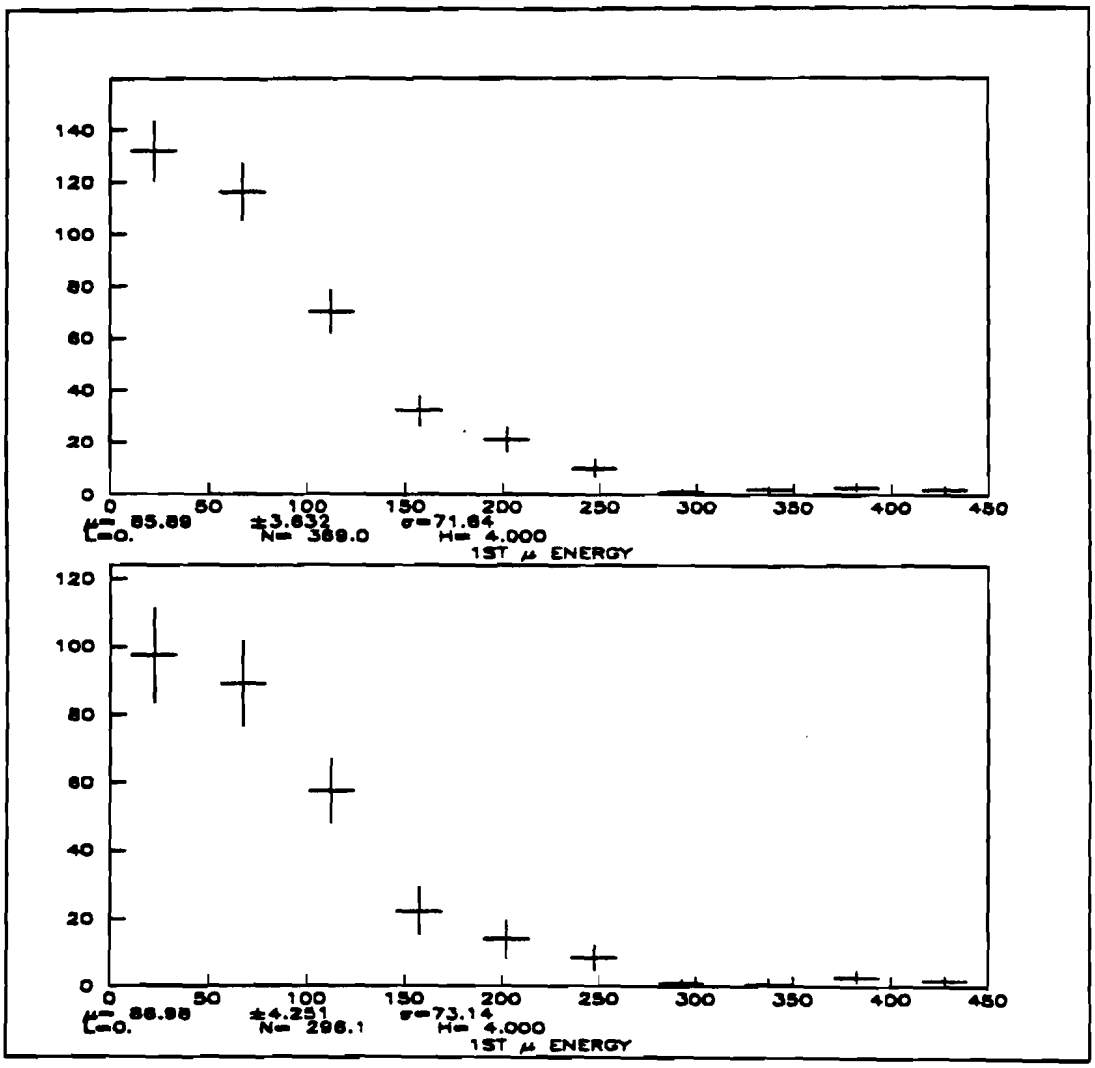

Fig.6.1. The leading muon energy before (upper plot) and after (lower plot) the background subtraction.

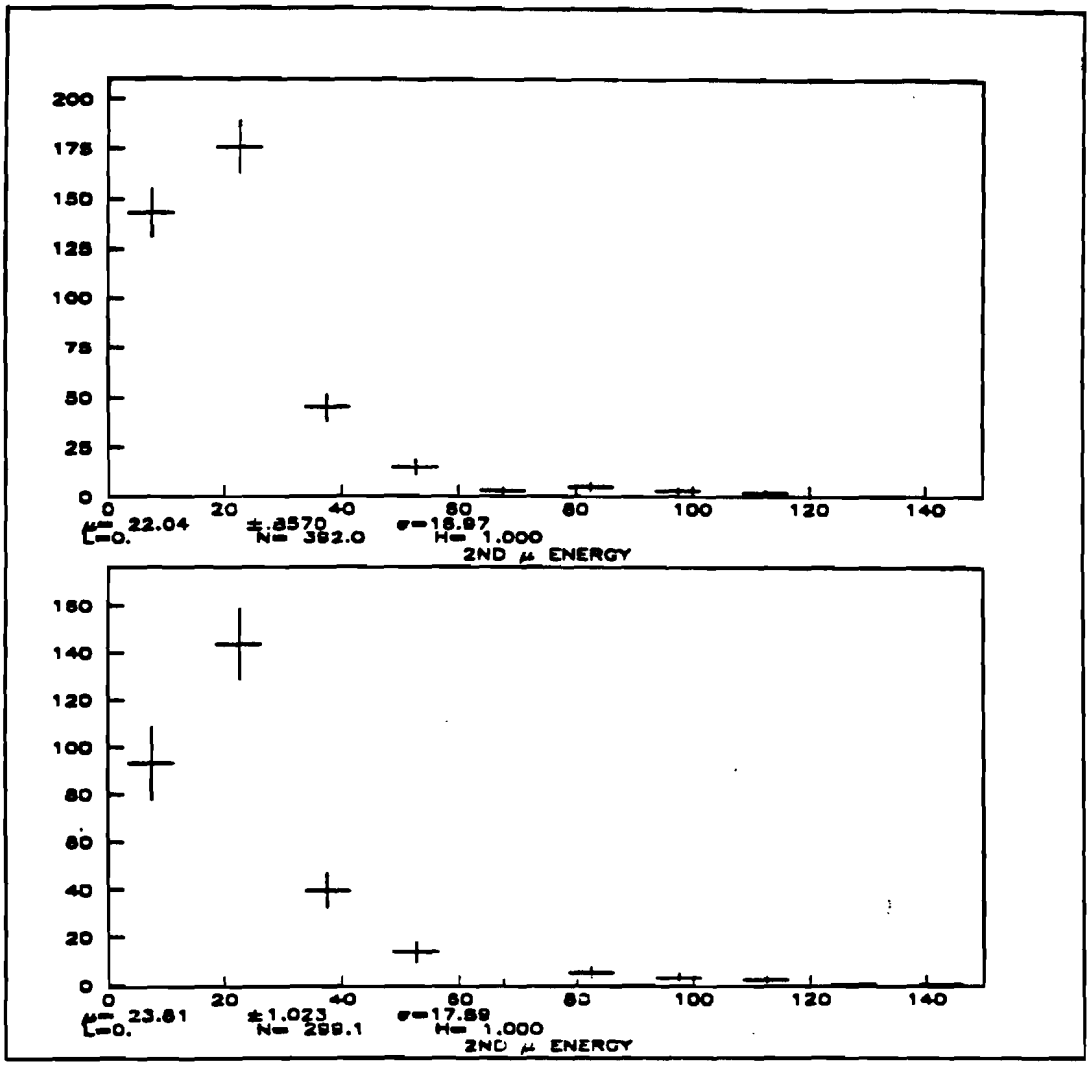

Fig.6.2. The second muon energy before (upper plot) and after (lower plot) the background subtraction.

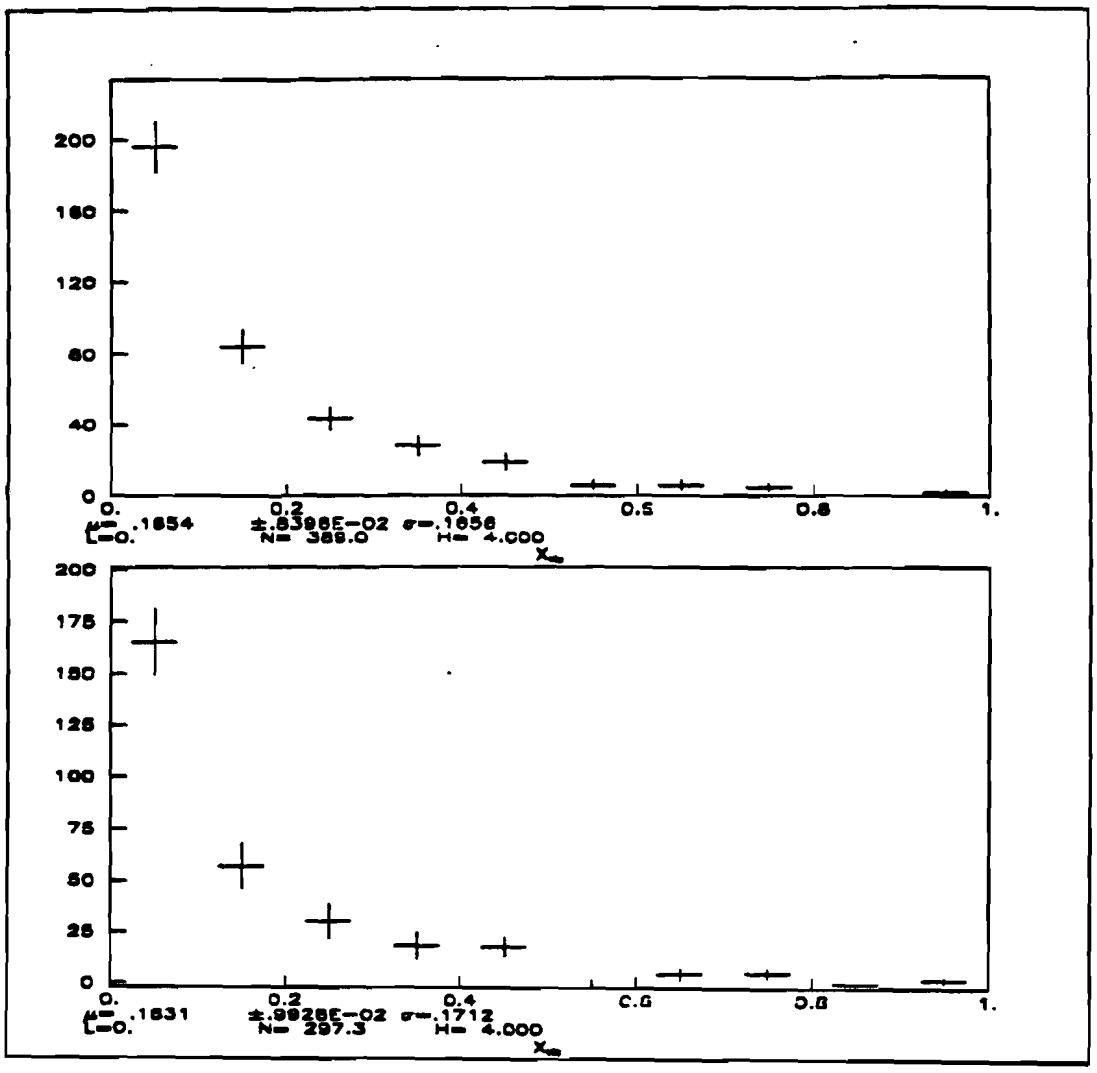

Fig.6.3. $X_{visible}$ before (upper plot) and after (lower plot) the background subtraction.

The method of background subtraction described above is not very sensitive to the systematic errors on the decay rates calculated in Chapter V, Section 6.6. The reason for this is that uncertainties in the parameters of our background Monte Carlo affect both the opposite sign and the like sign decay rates in the same manner. Therefore their ratios, which are what we use for the background subtraction, stay nearly constant. However,

since we use the like sign dimuons to estimate the background, the statistical limitations of the like sign data sample translate into a systematic error on the final result. We estimate the average statistical error on the bin contents for the like sign dimuons to be ±30.4% for bin-by-bin background subtraction. In addition one has to consider the systematic error arising from the statistical uncertainties in the calculation of the transfer coefficients of Table 5.7. We estimate that error to be ±12% on the average. The two systematic errors taken in quadrature result in the total systematic error on the background of ± 32.7%.

6.3 Strange Sea Content of the Nucleon.

First, let us recall that the strange sea content of the nucleon κ is defined as the ratio of the amount of the strange sea over the sum of the up and the down sea:

$$\kappa = \frac{2S}{\bar{U} + \bar{D}}, \qquad 6.1$$

where $S = \int_0^1 xs(x)dx$, $\bar{U} = \int_0^1 x\bar{u}(x)dx$, and $\bar{D} = \int_0^1 x\bar{d}(x)dx$.

Since the sea quarks are created in pairs (see Chapter I), one may safely assume that $u_{sea}(x) = \bar{u}_{sea}(x)$ and $d_{sea}(x) = \bar{d}_{sea}(x)$. Let us define $\Xi(x) = u_{sea}(x) = d_{sea}(x)$. Then the strange sea structure function can be written as $s(x) = \bar{s}(x) = \kappa\Xi(x)$. The neutrino and antineutrino dimuon cross sections of Eq.1.18 and 1.19 can now be written as follows:

$$\frac{d^3\sigma^{\upsilon}}{dxdydz} = \frac{G^2 M E_{\upsilon} \xi}{2\pi} \{[u(\xi) + d(\xi)]\, U_{cd}^2 + 2\Xi(\xi)\,(U_{cd}^2 + \kappa U_{cs}^2)\} \times (1 - \frac{m_c^2}{2ME_{\upsilon}\xi})\, D(z)\, B \qquad 6.2$$

$$\frac{d^3\sigma^{\bar{\upsilon}}}{dxdydz} = \frac{G^2 M E_{\upsilon} \xi}{2\pi} 2\Xi(\xi)\,(U_{cd}^2 + 2\kappa U_{cs}^2)\,(1 - \frac{m_c^2}{2ME_{\upsilon}\xi})\, D(z)\, B \qquad 6.3$$

where G is the Fermi constant, M is the nucleon mass, E_{υ} is the neutrino energy, u(x) and d(x) are the valence quarks distributions, $\Xi(x)$ is the sea distribution, m_c is the charm quark mass, U_{cs} and U_{cd} are elements of the Kobayashi-Maskawa matrix, ξ is the slow-rescaled variable, D(z) is the fragmentation function, and B is the charm meson semileptonic branching ratio.

To determine κ we compared the data and the MC $x_{visible}$ distributions by forming a χ^2 between the two. The best fit of the Monte Carlo to data is found by minimizing the χ^2. $X_{visible}$ is the experimental analog of the slow rescaling variable ξ of Eq.6.2 and 6.3:

$$x_{visible} = \frac{Q^2_{visible}}{2M_p(E_{shower} + E_{\mu 2})}, \qquad 6.4$$

$$Q^2_{visible} = 4E_{vis}E_{\mu 1}\sin^2(\theta/2), \qquad 6.5$$

where $E_{\mu 1}$ and $E_{\mu 2}$ are the 1st and the 2nd muons energies respectively, E_{vis} is the total visible energy of the event, and θ is the angle between the neutrino and the 1st muon. We define the 1st muon as the highest energy muon.

It is convenient to view the fitting process as a motion in the fit parameters space along the χ^2 surface, until the global minimum (if it exists) is reached. Generally speaking, each point in the parameter space corresponds to a set of MC events generated with the parameters' values corresponding to that point. In practice, generating a new set of MC events for every change of the fit parameters is, of course, unfeasible. Therefore we used one set of MC events, produced at some initial point λ_0 in the parameter space, and applied corrections to these events as the fit moved away from λ_0. In particular, each MC event entry into the appropriate x_{vis} histogram was weighted according to Eq.6.5:

$$W = \frac{\sigma^{\nu(\bar{\nu})}(\xi, Q^2, \lambda)}{\sigma^{\nu(\bar{\nu})}(\xi, Q^2, \lambda_0)} \quad , \qquad 6.6$$

where σ is the neutrino or antineutrino cross section of Eq.6.2 or 6.3 depending on the event type, λ_0 is the initial point in the parameter space at which the Monte Carlo was generated, and λ is the current position in the parameter space.

We chose not to separate the antineutrino-induced from neutrino induced dimuons in contrast to other dimuon analyses[6.1, 6.2] for the following reasons. The usual method for separating neutrino and antineutrino dimuon events is to discriminate on the basis of the transverse momentum p_t of the muons with respect to the hadronic shower. Since the muon with the lowest p_t is expected to come from the charm particle decay, its sign will determine the sign of the neutrino. This method, however, relies on detailed MC simulation of hadronic shower development in order to reproduce precisely not only the physics of the process, but also the experimental resolutions, inefficiencies, etc. This elaborate simulation is likely to introduce some systematic errors into the analysis, and these errors are often hard to calculate. By combining the neutrino and antineutrino dimuon events in our

analysis, we avoided making any cuts based on intricate details of hadron shower topology and relied instead on finding out the precise ratio of antineutrino to neutrino fluxes in the quadruplet neutrino beam. This we could accomplish by a rather simple analysis of Charged Current single muon events, and as we showed in Chapter IV, the results show very good agreement with data. Fig.6.4 shows x_{vis} distributions for both neutrino and antineutrino MC dimuon events after the cuts. It is calculated that the antineutrino content in our dimuon data sample is 19.2%.

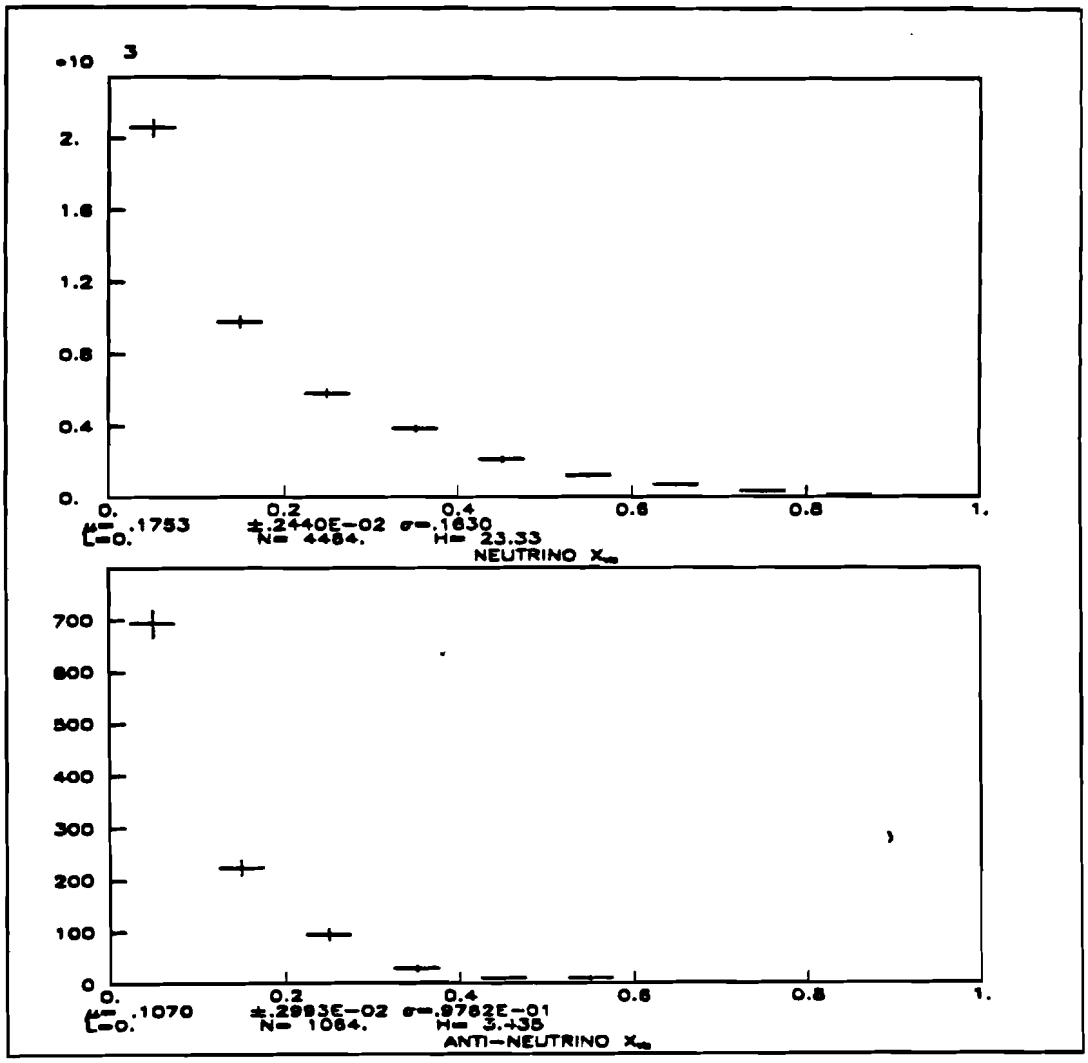

Fig.6.4. MC x_{vis} distributions for neutrino (upper plot) and antineutrino (lower plot) events. Both distributions are normalized to the same number of charged current events.

We have performed three different types of fits using the x_{vis} distribution. The fits differ by the number of parameters we varied along with χ. The first type is a single-parameter fit for χ alone, the second type is a two parameter fit for B and χ. The last type is a 3-parameter fit for χ, U_{cd} and U_{cs}.

χ^2 minimization for all the fits in this chapter was performed using the MINUIT function minimization package [6.3]. The data x_{vis} distribution were in the form of a 10-bin histogram. Table 6.2 shows the contents of the data x_{vis} distribution before background subtraction, background x_{vis} contents, and x_{vis} after background subtraction.

Table 6.2. Contents of the data x_{vis} histogram before and after background subtraction.

x_{vis}	Opposite sign	Background	After subtraction
0 to 0.1	196	30.77	165.23
0.1 to 0.2	84	27.06	56.94
0.2 to 0.3	43	13.18	29.82
0.3 to 0.4	28	9.66	18.34
0.4 to 0.5	19	1.38	17.62
0.5 to 0.6	6	8.25	-2.25
0.6 to 0.7	6	1.38	4.623
0.7 to 0.8	5	0	5
0.8 to 0.9	0	0	0.
0.9 to 1.0	2	0	2

The low population of bins 6 through 10 is consistent with with 0. Therefore only the first five bins were used in the fits. The number of degrees of freedom for the fits can be calculated according to the following formula: $N_f = N_{bin} - N_{param}$, where N_f is the number

of degrees of freedom, N_{bin} is the number of bins, and N_{param} is the number of fit parameters.

The dimuon MC used in the fits was of the hybrid type described earlier (Chapter IV). It was generated with the following parameters: $\kappa = 0.42$, $U_{cd} = 0.225$, $U_{cs} = 0.972$. Since we wanted to investigate the sensitivity of our results to the changes in m_c, three sets of MC events were produced with m_c = 1.0 GeV/c^2, 1.5 GeV/c^2, and 2.0 GeV/c^2. The semileptonic branching ratio B was not a parameter in the MC generation, since it enters the cross sections of Eq.6.2 and 6.3 as an overall normalization factor. Therefore we introduced the desired branching ratio at the fitting stage simply by normalizing the MC events to a predetermined number.

Since the fits described in the next three sections used both the shape and the normalization information of the x_{vis} distributions, the Monte Carlo "data" had to be properly normalized to the expected number of dimuon events which we calculated according to the following formula:

$$N_{expected} = N_{cc} \frac{R_{2\mu}}{R_{1\mu}} B \,, \qquad 6.7$$

where $N_{expected}$ is the expected number of opposite sign dimuon events at the initial values of the MC parameters, $R_{2\mu}$ is the number of accepted dimuon MC events after the cuts per unit of MC "flux", $R_{1\mu}$ is similar to $R_{2\mu}$ except that it is calculated for single muon charged current MC events, B is the semileptonic branching ratio. N_{cc} is the total number of data charged current events calculated as follows:

$$N_{cc} = N_{cc}^{BG}(PTH) * 12 + N_{cc}^{TG}(PTH) \,, \qquad 6.8$$

where $N_{cc}^{BG}(PTH)$ is the number of minimum bias Beam Gate PTH events, and $N_{cc}^{TG}(PTH)$ is the number of Tail Gate PTH events. Because of the trigger prescaling during the Beam Gate, $N_{cc}^{BG}(PTH)$ has to be multiplied by the prescale factor of 12 to obtain the total number of minimum bias charged current BG events. There was no prescaling during the Tail Gate (see Chapter III and Section 6.4).

To validate the fitting algorithm we fit two statistically independent sets of Monte Carlo events against each other, using one as "data" and the other as "theory". The fit returned the original values of the MC parameters within small statistical errors, thus confirming the soundness of the algorithm. We also performed consistency checks by varying the starting points of the fits described below to make sure that the results do not depend on the initial conditions.

6.3.1. Single Parameter Fits for χ.

Changing χ results in changes in both the shape of the x_{vis} distribution and its normalization. Another parameter that has strong influence on the x_{vis} normalization is the semileptonic branching ratio B, which enters the dimuon cross sections of Eq.6.2 and 6.3 as an overall multiplicative factor. It is then expected that B and χ should be strongly negatively correlated. To investigate the B-dependence of χ we performed a series of one-parameter fits for χ at several fixed values of B in the interval from 0.06 to 0.11. The results are shown in Table 6.3 and Fig.6.5 and 6.6.

Table 6.3. Results of the single-parameter fits for the strange sea content κ at m_c = 1.5 GeV/c^2. The errors are statistical.

B	κ	χ^2
0.06	0.89 ± 0.09	4.65
0.07	0.72 ± 0.08	4.16
0.08	0.60 ± 0.07	3.92
0.084	0.56 ± 0.06	3.90
0.085	0.55 ± 0.06	3.90
0.090	0.51 ± 0.06	3.94
0.10	0.43 ± 0.05	4.21
0.11	0.37 ± 0.05	4.74

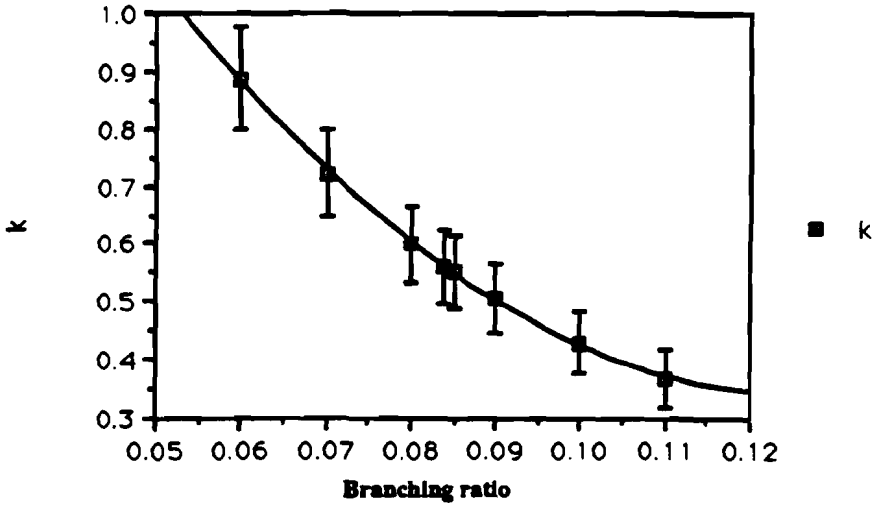

Fig.6.5. Strange sea fraction k as a function of the semileptonic branching ratio B at m_c = 1.5 GeV/c^2. The errors are statistical.

As expected $\varkappa$ decreases when B increases. A second order polynomial fit for $\varkappa(B)$ gives the following result:

$$\varkappa(B) = 2.308 - 31.168\ B + 123.36\ B^2 \qquad 6.9$$

Fig.6.6 shows the minimum χ^2 of the fits as a function of the branching ratio.

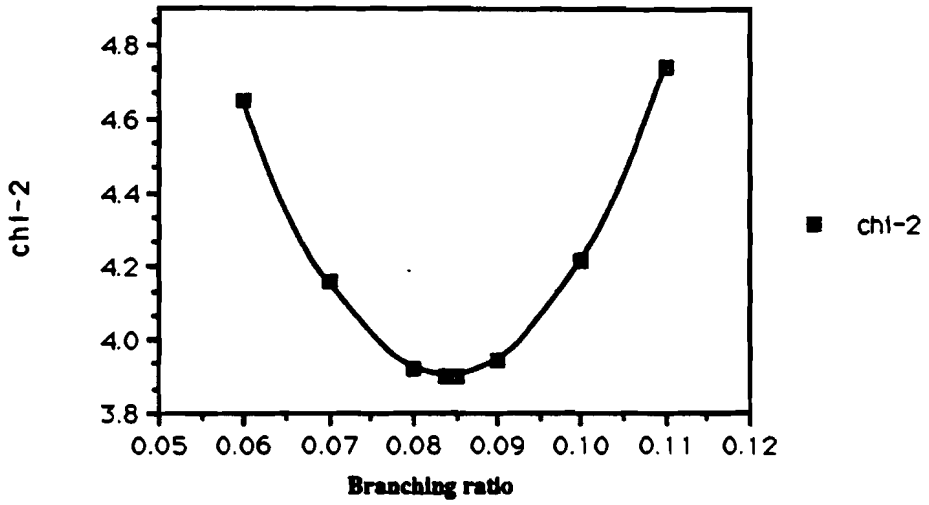

Fig.6.6. Minimum χ^2 of the 1-parameter fits for $\varkappa$ as a function of the branching ratio. M_c = 1.5 GeV/c^2.

The $\chi^2(B)$ curve shows a minimum at B_0 = **0.084**. The minimum χ^2 is **3.9** for 4 degrees of freedom. This B_0 corresponds to the following value of $\varkappa$:

$$\varkappa = 0.56 \pm 0.06 \pm 0.07, \qquad 6.10$$

where the first error is statistical, and the second error is due to 32.7% uncertainty in the background. A comparison of the data x_{vis} versus MC for the above values of x and B is shown in Fig.6.7 in the form of the standard comparison plot.

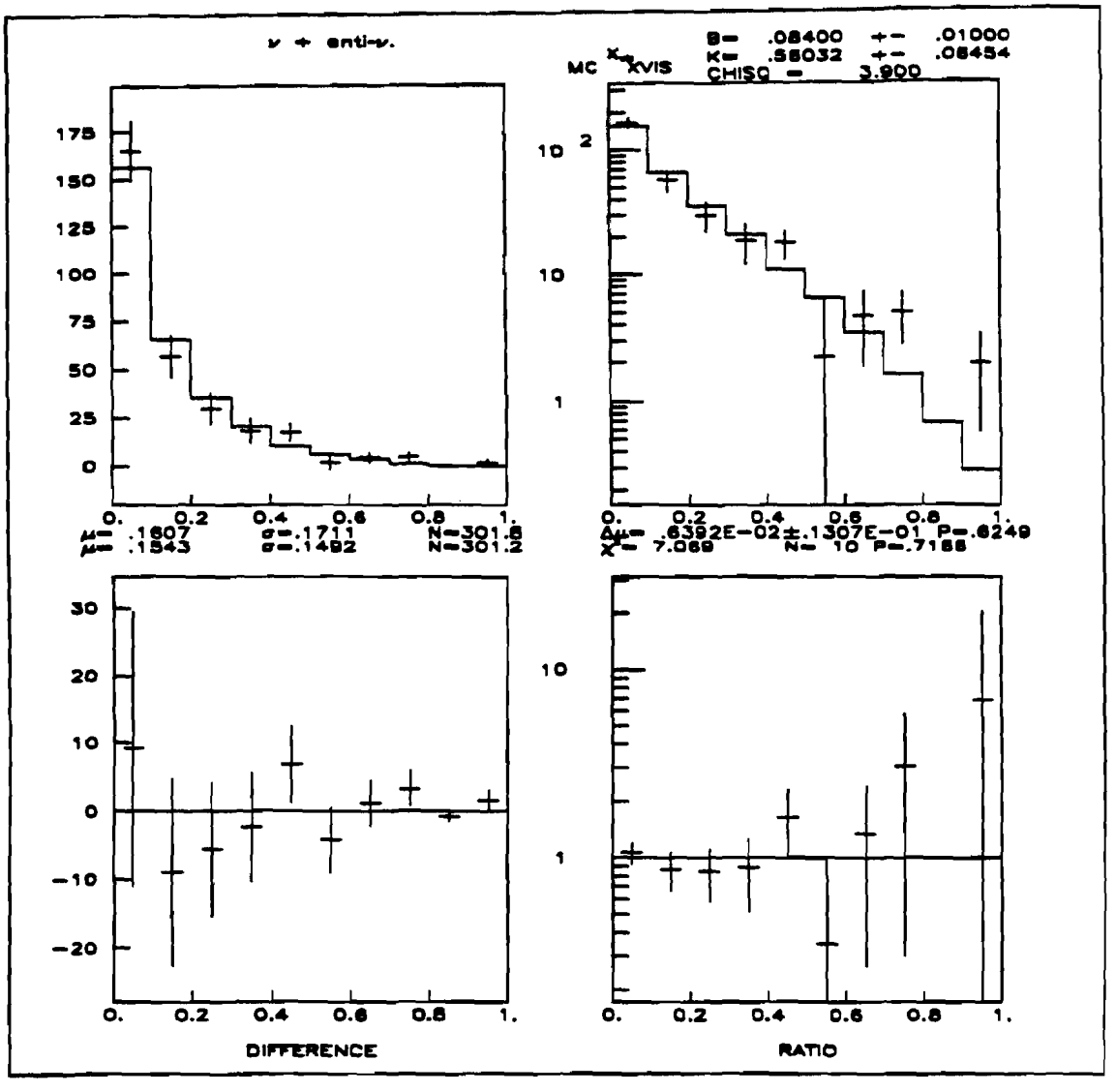

Fig.6.7. The best fit of MC to the data at B = 0.084 and m_c = 1.5 GeV/c^2. Points with errors represent data, the smooth line is Monte Carlo.

To determine sensitivity of our results to changes in the charm quark mass m_c, we repeated the fits at m_c = 1.0 GeV/c^2 and m_c = 2.0 GeV/c^2 with the branching ratio fixed at B = 0.084. The results are summarized in Table 6.4.

Table 6.4. Summary of the 1-parameter fits for κ at B = 0.084, performed for three values of the charm quark mass. In all cases the first error is statistical, and the second one is the systematic error due to 32.7% uncertainty in background.

m_c (GeV/c^2)	κ	χ^2
1.0	$0.54 \pm 0.06 \pm 0.07$	4.24
1.5	$0.56 \pm 0.06 \pm 0.07$	3.90
2.0	$0.70 \pm 0.08 \pm {}^{+0.09}_{-0.08}$	3.7

As Table 6.3 shows, changing m_c from 1 GeV/c^2 to 1.5 GeV/c^2 does not result in any statistically significant change in κ, whereas increasing m_c from 1.5 to 2 GeV/c^2 changes κ by + 27%. This highly nonlinear behavior of κ as a function of m_c may indicate some complicated thresholds in the dimuon production process, which perhaps are not fully accounted for by the usual slow rescaling formalism. We must point out here that the question of the mass of the charm quark is still an open one. It is possible that the value m_c = 1.5 GeV/c^2 derived from studies of the bound states of the cc system, is not directly applicable to this analysis.

One of the most interesting questions about the strange sea fraction of the nucleon is the question of its evolution as a function of Q^2. In order to investigate this aspect of κ, our dimuon data sample was divided into three bins in Q^2: $Q^2 < 10$ GeV^2, $10 < Q^2 < 40$ GeV^2, and $Q^2 > 40$ GeV^2. The first two bins had approximately equal numbers of events. The third bin contained about a factor 1.5 fewer events than the first two. We performed single

parameter fits for κ for each of the three bins of Q^2. The branching ratio of B = 0.084 was used for all of these fits, since it is unlikely that B depends on Q^2. We used only one value of the charm quark mass m_c = 1.5 GeV/c^2. The fitting procedure was identical to that used for other single parameter fits in this section. The results are summarized in Table 6.5.

Table 6.5. Q^2 dependence of κ for B = 0.084 and m_c = 1.5 GeV/c^2. For each κ the first error is statistical, and the second error is due to 32.7% uncertainty in background.

Q^2 (GeV^2)	κ	χ^2
$Q^2 < 10$	$0.53 \pm 0.07 \pm 0.02$	2.21
$10 < Q^2 < 40$	$0.50 \pm 0.10\ ^{+0.07}_{-0.08}$	2.66
$Q^2 > 40$	$0.58 \pm 0.23 \pm 0.14$	3.73

The results in Table 6.5 are consistent with κ staying constant over the available range of Q^2. This is not surprising since, as we discussed in Chapter I, the QCD evolution of κ as a function of Q^2 is logarithmic in nature, and hence very slow.

6.3.2. Two Parameter Fits for B and κ.

For these fits we allowed both B and κ to vary freely. As was shown in the previous section, B and κ are highly correlated. Therefore when determining them both simultaneously, one can expect larger errors than when fitting for only one of these parameters. To illustrate this point, Fig.6.8 shows the 2-dimensional χ^2 surface for a simultaneous fit for B and κ at m_c = 1.5 GeV/c^2.

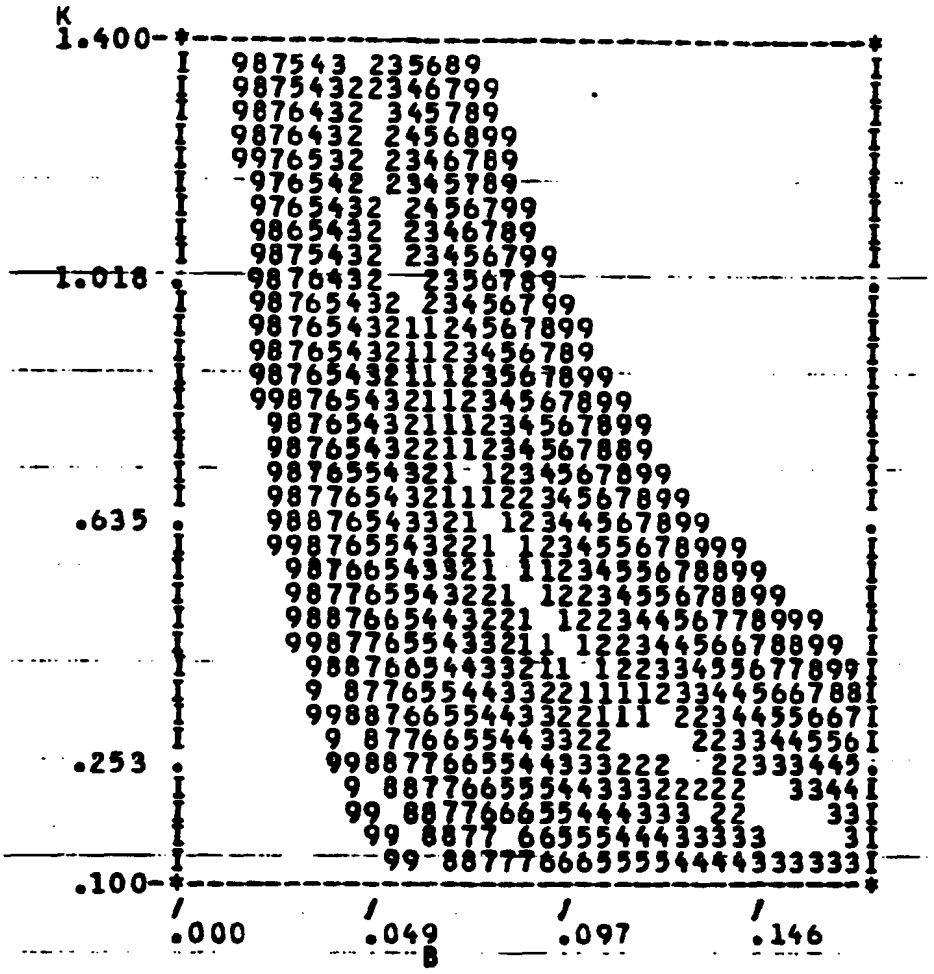

Fig.6.8. χ^2 surface for a simultaneous fit for B and κ at m_c = 1.5 GeV/c^2. The branching ratio B is plotted along the horizontal axis, and κ is plotted along the vertical axis.

As we see B and κ are indeed negatively correlated. In fact, the correlation coefficient for B and κ is -0.974. The minimum χ^2 of this fit is χ^2_{min} = 3.71 for five degrees of freedom. At χ^2_{min} the best values of B and κ are B = 0.084 ±0.03 and κ = 0.56 ± 0.27, where the errors are statistical. Table 6.5 lists the values of χ^2 corresponding to the first six contours of Fig.6.6.

Table 6.6. χ^2 values corresponding to the contours of Fig.6.6.

Contour	χ^2
1	4.71
2	7.71
3	12.71
4	19.71
5	28.71
6	39.71

In Fig.6.9 we show a comparison of the data x_{vis} distribution with the MC for the fit described above.

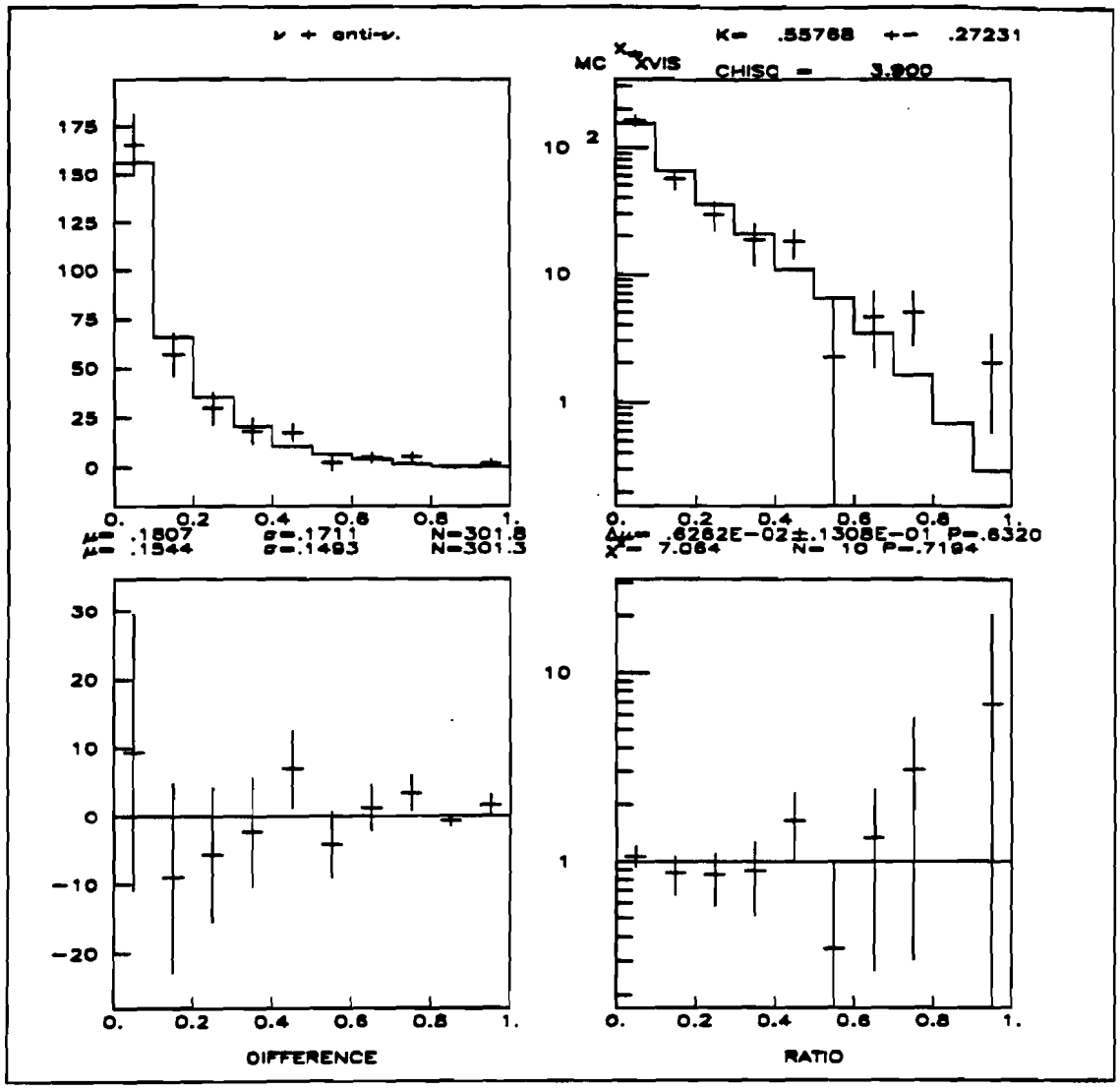

Fig.6.9. A comparison plot of data x_{vis} vs MC for a 2-parameter fit for B and K at m_c = 1.5 GeV/c^2.

As in the previous section we repeated the fits at three values of m_c: 1 GeV/c^2, 1.5 GeV/c^2, and 2.0 GeV/c^2. The results are shown in Table 6.7.

Table 6.7. The results of 2-parameter fits for B and χ for three values of m_c. The first error is statistical, the second error is due to 32.7% uncertainty in background.

m_c (GeV/c^2)	χ	B	χ^2
1.0	$0.57 \pm 0.28 \,^{+0.08}_{-0.06}$	$0.082 \pm 0.027 \,^{+0.015}_{-0.013}$	4.23
1.5	$0.56 \pm 0.27 \,^{+0.08}_{-0.06}$	$0.084 \pm 0.028 \pm 0.014$	3.90
2.0	$0.50 \pm 0.29 \,^{+0.08}_{-0.06}$	$0.12 \pm 0.04 \pm 0.02$	3.55

In summary, the results of the two parameter fits for B and χ are consistent with the results of the previous section obtained at the fixed B of 0.084. We do not see any appreciable change in χ as a function of m_c , although the fit errors are much larger than those of the previous section.

6.3.3. Three Parameter Fits for χ, U_{cd}, and U_{cs}.

From the cross section of Eq.6.2 it is seen that the elements U_{cd} and U_{cs} of the Kobayashi-Maskawa matrix together with χ determine the relative strengths of the valence and sea contributions to the opposite sign dimuon cross section for neutrinos. We performed simultaneous fits for χ, U_{cd} and U_{cs} to check sensitivity of χ to changes in U_{cd} and U_{cs}, and as an independent measurement of these two elements of the Kobayashi-Maskawa matrix. The fit method used is the same as for the fits in the previous sections of this chapter. The semileptonic branching ratio was set at B = 0.084. The starting values of the fit parameters were as follows: χ = 0.42, U_{cd} = 0.225, U_{cs} = 0.972. The results are shown in Table 6.8.

Table 6.8. Results of three parameter fits for κ, U_{cd}, U_{cs} for three values of the charm quark mass at B = 0.084. For all quantities the first error is statistical, the second error corresponds to 32.7% background uncertainty.

m_c (GeV/c^2)	1.0	1.5	2.0
κ	$0.55 \pm 0.07 \,^{+0.02}_{-0.03}$	$0.56 \pm 0.07 \,^{+0.0}_{-0.07}$	$0.65 \pm 0.08 \,^{+0.02}_{-0.06}$
U_{cd}	$0.222 \pm 0.037 \,^{+0.018}_{-0.020}$	$0.225 \pm 0.038 \pm 0.019$	$0.242 \pm 0.041 \,^{+0.019}_{-0.021}$
U_{cs}	$0.975 \pm 0.061 \,^{+0.008}_{-0.000}$	$0.973 \pm 0.061 \,^{+0.036}_{+0.019}$	$0.981 \pm 0.064 \,^{+0.024}_{+0.005}$
χ^2	4.23	3.90	3.55

It interesting to note that simultaneous fits for κ, U_{cd} and U_{cs} allow a more precise determination of κ than two parameter fits for B and κ. We attribute this to the fact that κ is less strongly correlated with U_{cd} and U_{cs} than it is with B (the correlation coefficient for B and κ is -0.974). To illustrate this point we reproduce a typical correlation matrix for the 3-parameter fits (m_c = 1.5 GeV/c^2):

Table.6.9. Correlation matrix for a simultaneous fit for κ, U_{cd}, U_{cs} at m_c = 1.5 GeV/c^2.

	κ	U_{cd}	U_{cs}
κ	--	- 0.605	0.153
U_{cd}	- 0.605	--	-0.613
U_{cs}	0.153	- 0.613	--

Finally, Fig.6.10 shows a 3-parameter fit to x_{vis} at m_c = 1.5 GeV/c^2.

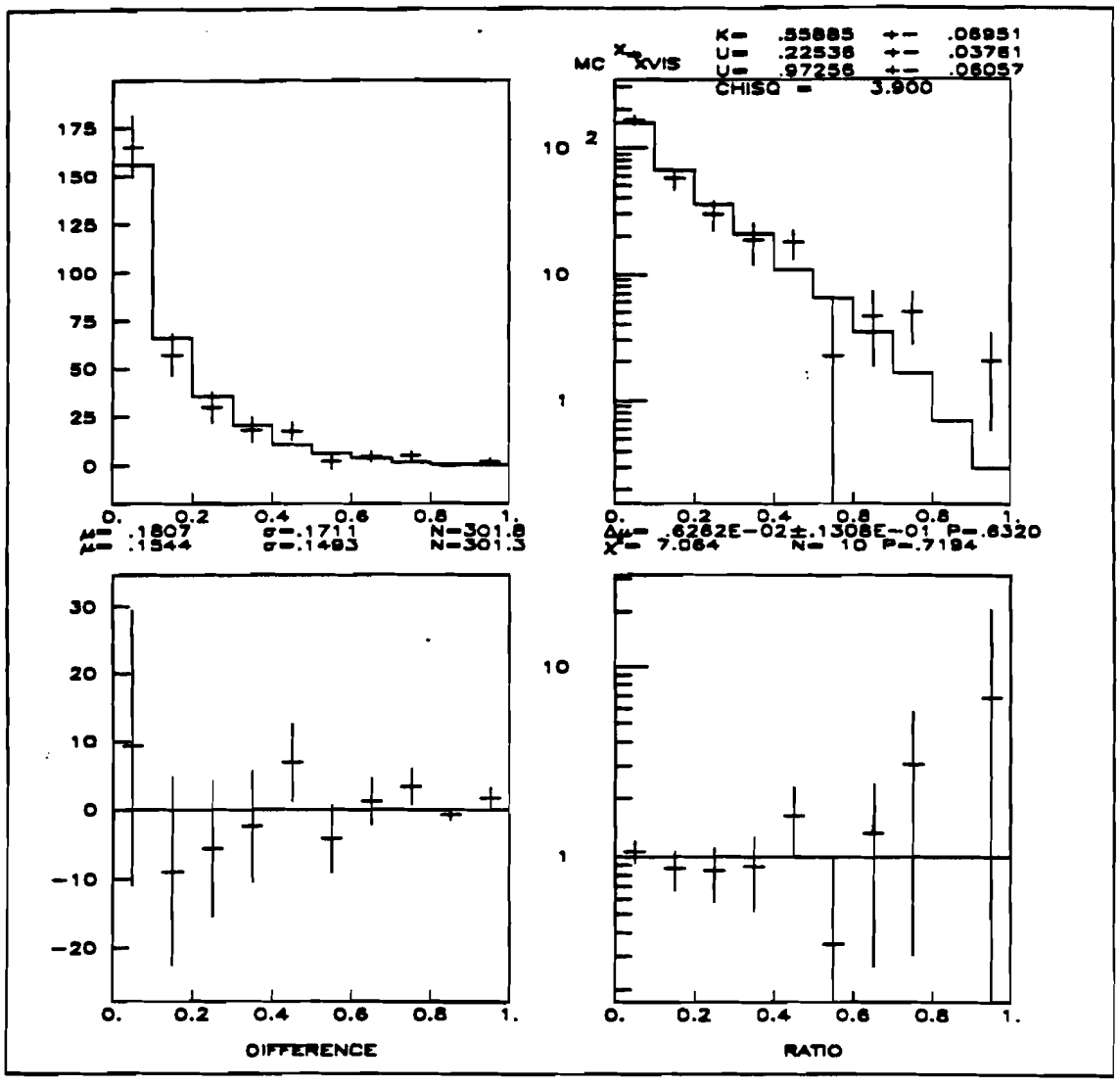

Fig.6.10. A simultaneous fir for x, U_{cd}, U_{cs} at B = 0.084 and m_c = 1.5 GeV/c^2. The points with errors represent data, the smooth line is the Monte Carlo.

6.4. Opposite Sign Dimuon Rates and the Mass of the Charm Quark.

To calculate the dimuon rates we divide the number of the accepted dimuon events by the number of the accepted single muon charged current events, with the same cuts applied to both the dimuon and the single muon data samples. Care must be taken of the trigger prescaling (see Chapter III). Since our trigger prescaling allowed only one out of twelve minimum bias charged current events to be taken during the Beam Gate (BG) cycle, we calculated the BG dimuon rate in the following way:

$$R_{BG}(2\mu/1\mu) = \frac{N_{2\mu}}{N_{1\mu}(PTH) * 12}. \qquad 6.10$$

The Tail Gate (TG) dimuon rate is simply:

$$R_{TG}(2\mu/1\mu) = \frac{N_{2\mu}}{N_{1\mu}(PTH)} \qquad 6.11$$

where $N_{2\mu}$ is the number of the accepted dimuon events, $N_{1\mu}$ is the number of single muon charged current events. Both the dimuon and the single muon charged current events were subject to the same energy and fiducial cuts, described previously in this chapter.

Table 6.10 lists the numbers of the opposite sign dimuons after background subtraction in 10 bins of $E_{visible}$. Table 6.11 lists the combined background subtracted BG + TG dimuon rates as a function of E_{vis}.

Table.6.10. Opposite sign dimuons with $E_{\mu 1,2} > 10$ GeV before and after the background subtraction. The errors shown are the systematic errors due to 32.7% background uncertainty.

$E_{visible}$ (GeV)	Before background subtraction	After Background subtraction
0 - 50	5	5 ± 0
50 - 100	57	44.7 ± 4
100 - 150	88	79.9 ± 2.6
150 - 200	71	47.5 ± 7.7
200 - 250	66	47.8 ± 5.9
250 - 300	48	29.0 ± 6.2
300 - 350	25	18.5 ± 2.1
350 - 400	15	11.1 ± 1.3
400 - 450	7	7 ± 0.
450 - 500	3	1.8 ± 0.4

Table 6.11. Background subtracted opposite sign dimuon rates. The first error is statistical, the second error is due to 32.7% background uncertainty.

$E_{visible}$ (GeV)	$R(2\mu/1\mu)$
0 - 50	$(8.80 \pm 3.94 \pm 0.) \times 10^{-4}$
50 - 100	$(1.39 \pm 0.21 \pm 0.13) \times 10^{-3}$
100 - 150	$(4.01 \pm 0.45 \pm 0.14) \times 10^{-3}$
150 - 200	$(3.86 \pm 0.56 \pm 0.63) \times 10^{-3}$
200 - 250	$(3.76 \pm 0.54 \pm 0.47) \times 10^{-3}$
250 - 300	$(3.33 \pm 0.62 \pm 0.72) \times 10^{-3}$
300 - 350	$(4.07 \pm 0.95 \pm 0.47) \times 10^{-3}$
350 - 400	$(4.62 \pm 1.39 \pm 0.54) \times 10^{-3}$
400 - 450	$(5.76 \pm 2.17 \pm 0.) \times 10^{-3}$
450 - 500	$(3.59 \pm 2.68 \pm 0.78) \times 10^{-3}$

Fig.6.11 shows the total background corrected dimuon rate. The suppression of the dimuon rate at low energies ($E_{visible} < 100$ GeV) is attributed to the effects of slow rescaling (see Chapter I). In other words, production of the massive charm quark imposes a kinematic threshold on the reaction, and the phase space factor of Eq.1.20 and 1.21 causes the dimuon cross sections to rise with the neutrino energy. At higher energies ($E_{vis} > 100$ GeV) the dimuon rate stays essentially constant, which is also in accordance with the charm model of opposite sign dimuons production.

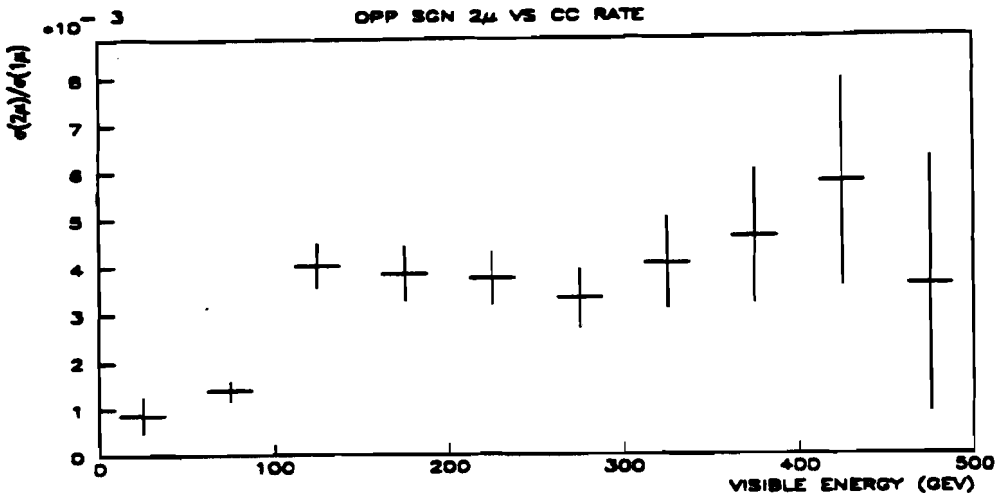

Fig.6.11. Background corrected opposite sign dimuon rate as a function of E_{vis} - the total visible energy in GeV. The errors are statistical.

Since, the rise of the opposite sign dimuon rate at high energies is due to the slow rescaling mechanism, we used these data to extract information about the mass of the charm quark. Of all the parameters in the cross sections of Eq.6.2 and 6.3 we chose to concentrate on just two: the mass of the charm quark m_c, and the semileptonic branching ratio B, in order to keep the fit errors to a minimum.

In the first series of fits we kept the branching ratio fixed at the previously determined value of $B_0 = 0.084$. The strange sea fraction κ was 0.56 in accordance with the results of the previous sections. The starting value of m_c was 1.0 GeV/c^2, and the fit χ^2 had 9 degrees of freedom. The fit gave the following result:

$$m_c = 1.91 \pm 0.28^{+0.45}_{-0.55} \ (\text{GeV}/c^2) \qquad 6.12$$

$$\chi^2 = 17.6$$

where the first error is statistical and the second one is due to 32.7% background uncertainty. Fig.6.12 shows the comparison of the data dimuon rate with the MC at the m_c of Eq.6.11.

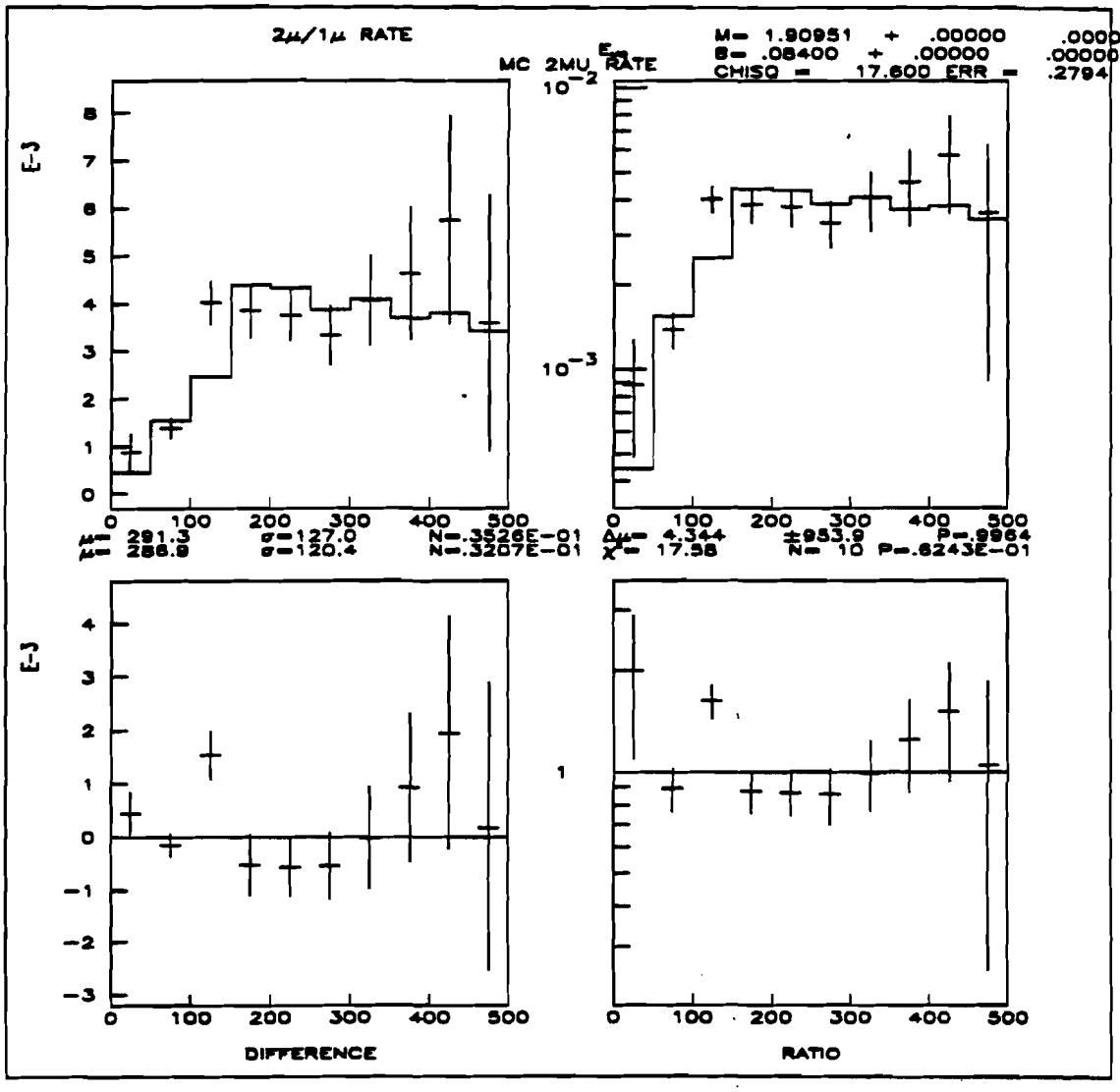

Fig.6.12. The data opposite sign dimuon rate versus MC at m_c = 1.91 GeV/c^2. Points with errors represent data, the smooth line is the Monte Carlo.

The next fit was just like the previous one, except that both m_c and B were allowed to vary freely. The results are as follows:

$$m_c = 1.49 \pm 0.92^{+0.35}_{-0.88}\ (GeV/c^2) \qquad 6.13$$

$$B = 0.077 \pm 0.012 \pm 0.015$$

$$\chi^2 = 17.3$$

As before, the first errors are statistical, the second ones are due to 32.7% background uncertainty. The results of the two parameter fit for B and m_c are illustrated by Fig.6.13.

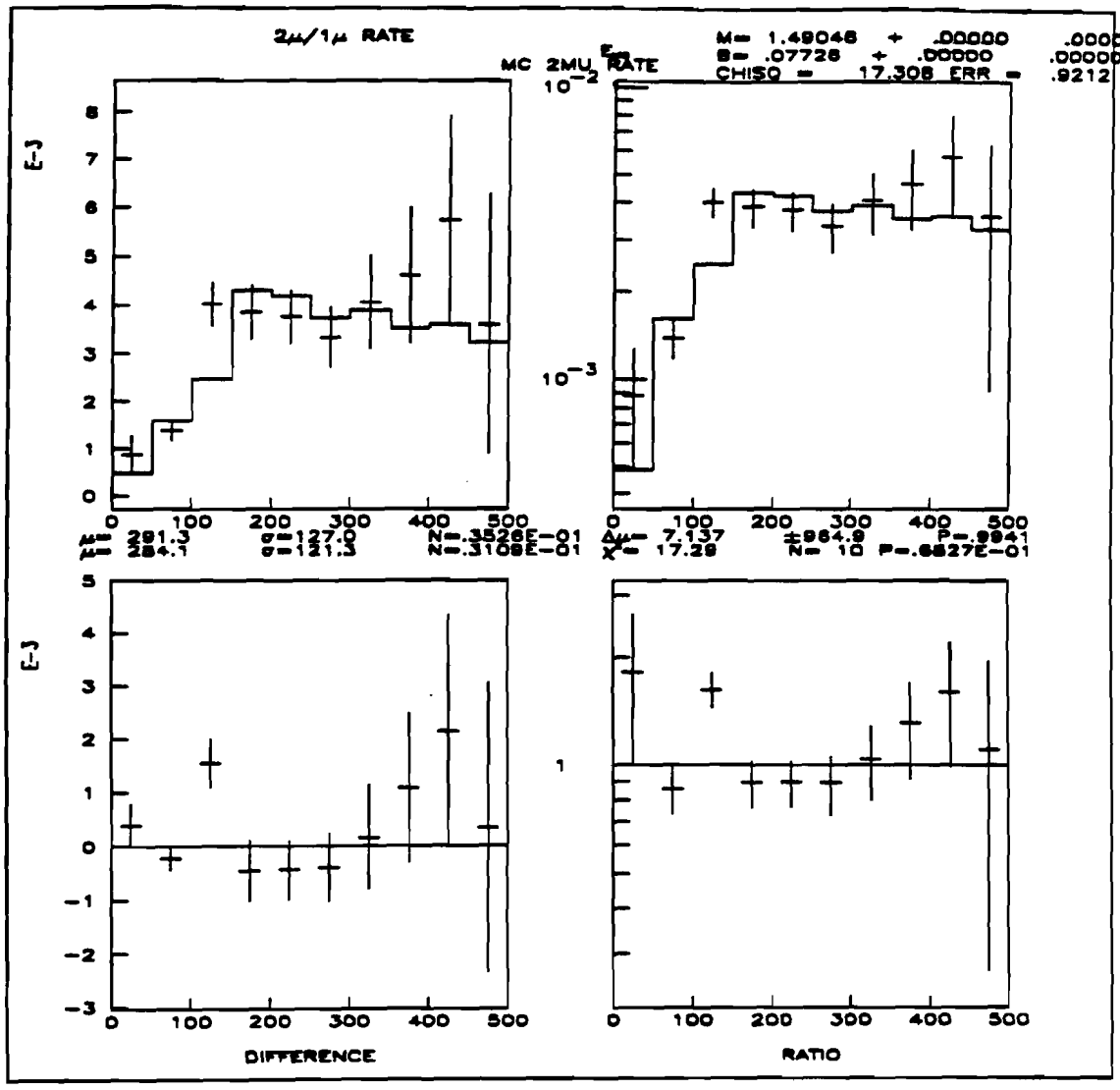

Fig.6.13. The data opposite sign dimuon rate versus MC at m_c = 1.49 GeV/c^2 and B = 0.077. Points with errors represent data, the smooth line is the Monte Carlo.

To summarize: the results of this section are consistent with the standard charm production model of the opposite sign dimuons, including the slow rescaling mechanism. The canonical value of the charm mass m_c = 1.5 GeV/c^2 is well within our fit errors. The result for the semileptonic branching ratio B is also consistent with the results of the previous sections obtained with a different method.

6.5. Kinematic Properties of the Opposite Sign Dimuons.

In this sections we compare various kinematic distributions of our opposite sign dimuon data sample with the Monte Carlo. The goal is to conduct an extensive check of the various kinematic aspects of the standard charm model of opposite sign dimuons. The data sample in this section is the same background corrected data sample used throughout this chapter, with the cuts specified in Section 6.2. The Monte Carlo used here has been described before (see Chapter IV). Its parameters were as follows: $\chi = 0.56$, $m_c = 1.5$ GeV/c^2, $U_{cd} = 0.225$, $U_{cs} = 0.972$. The MC events were subject to the same cuts as the data.

Here are definitions of some kinematic quantities not previously defined:

$$E_{visible} = E_{shower} + E_{\mu 1} + E_{\mu 2} \qquad 6.14$$

$$E_{hadron} = E_{shower} + E_{\mu 2} \qquad 6.15$$

$$Y_{visible} = E_{hadron} / E_{visible} \qquad 6.16$$

$$W_{visible} = (2M_N E_{hadron} + M_N^2 - Q^2_{visible})^{1/2} \qquad 6.15$$

$$m_{12} = [\, (E_{\mu 1} + E_{\mu 2})^2 - (p_{\mu 1} + p_{\mu 2})^2 \,]^{1/2} \qquad 6.18$$

$$Z_{exp} = \frac{E_{\mu 2}}{E_{\mu 2} + E_{shower}} \qquad 6.19$$

where $E_{\mu 1}$ and $E_{\mu 2}$ are the energies respectively of the leading (the highest energy) muon and the second muon, M_N is the nucleon mass, $Q^2_{visible}$ is defined by Eq.6.5, m_{12} is the invariant mass of the muon pair, and Z_{exp} is the experimental fragmentation variable.

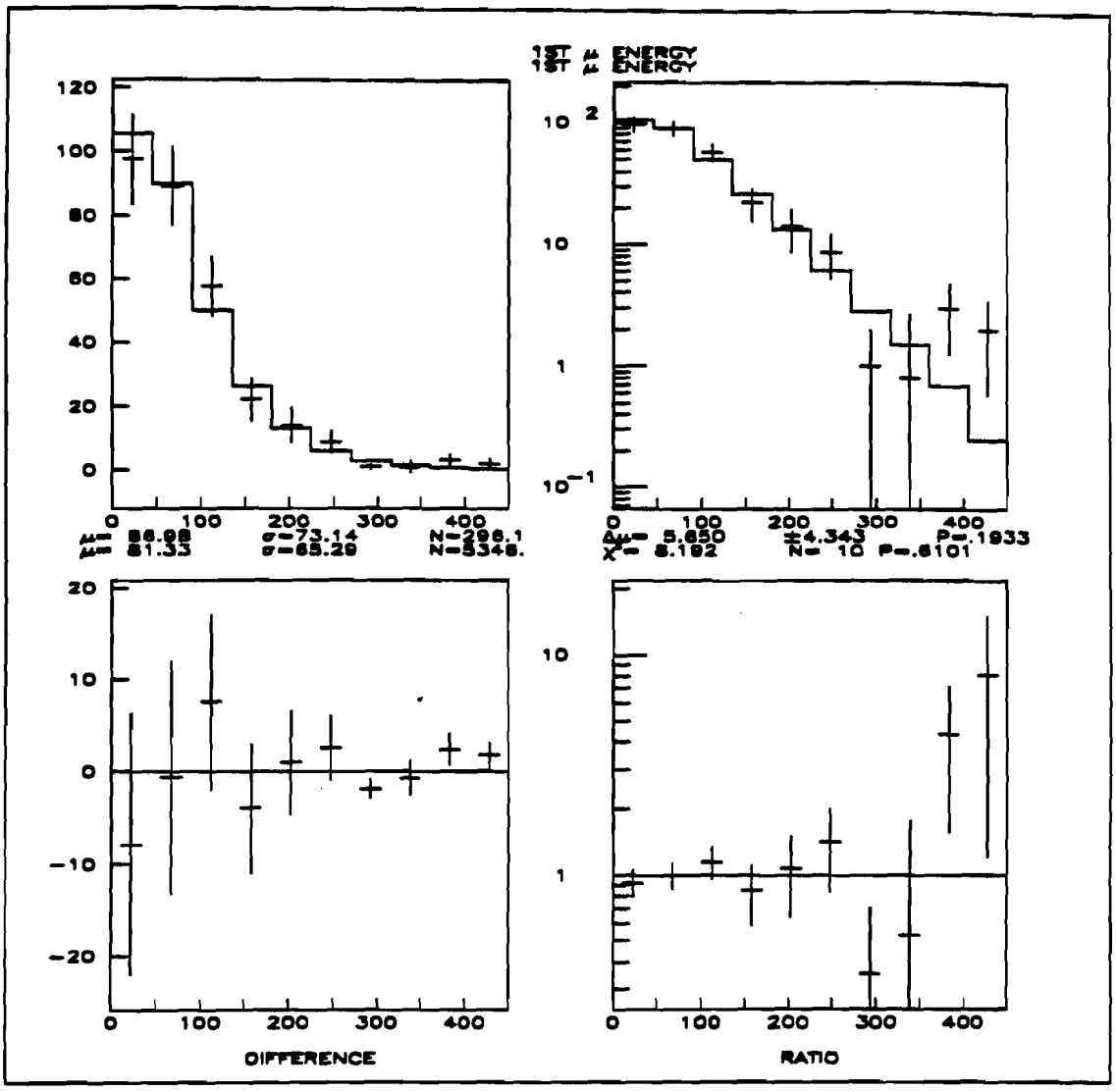

Fig.6.14. Leading muon energy in GeV. Points with errors represent data, the smooth line is the MC. $\chi^2 = 8.2$ for 10 degrees of freedom.

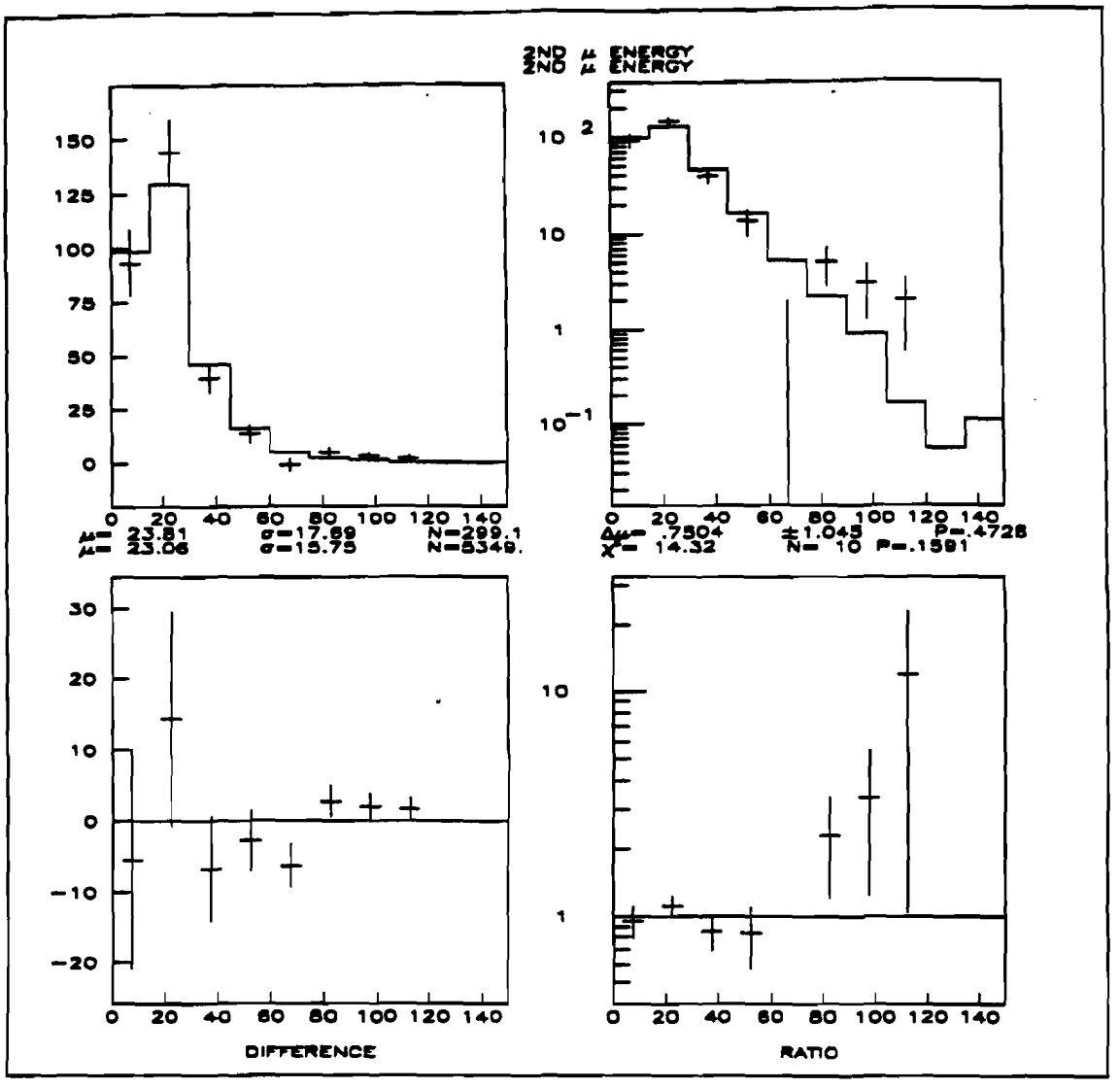

Fig.6.15. Second muon energy in GeV. Points with errors represent data, the smooth line is the MC. $\chi^2 = 14.3$ for 10 degrees of freedom.

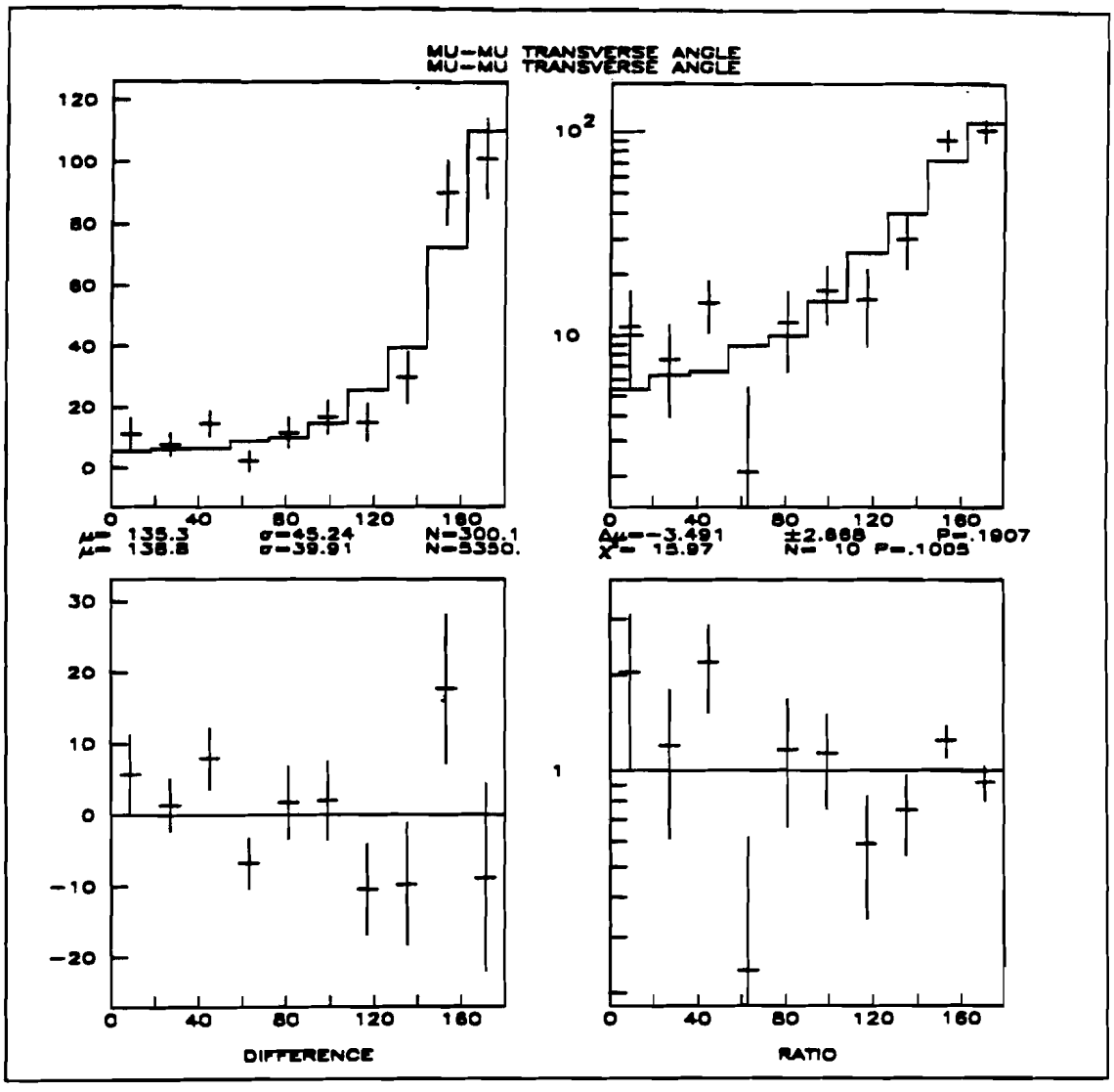

Fig.6.16. Angle between the muons in the plane perpendicular to the beam neutrino direction. Points with errors represent data, the smooth line is the MC. $\chi^2 = 16$ for 10 degrees of freedom.

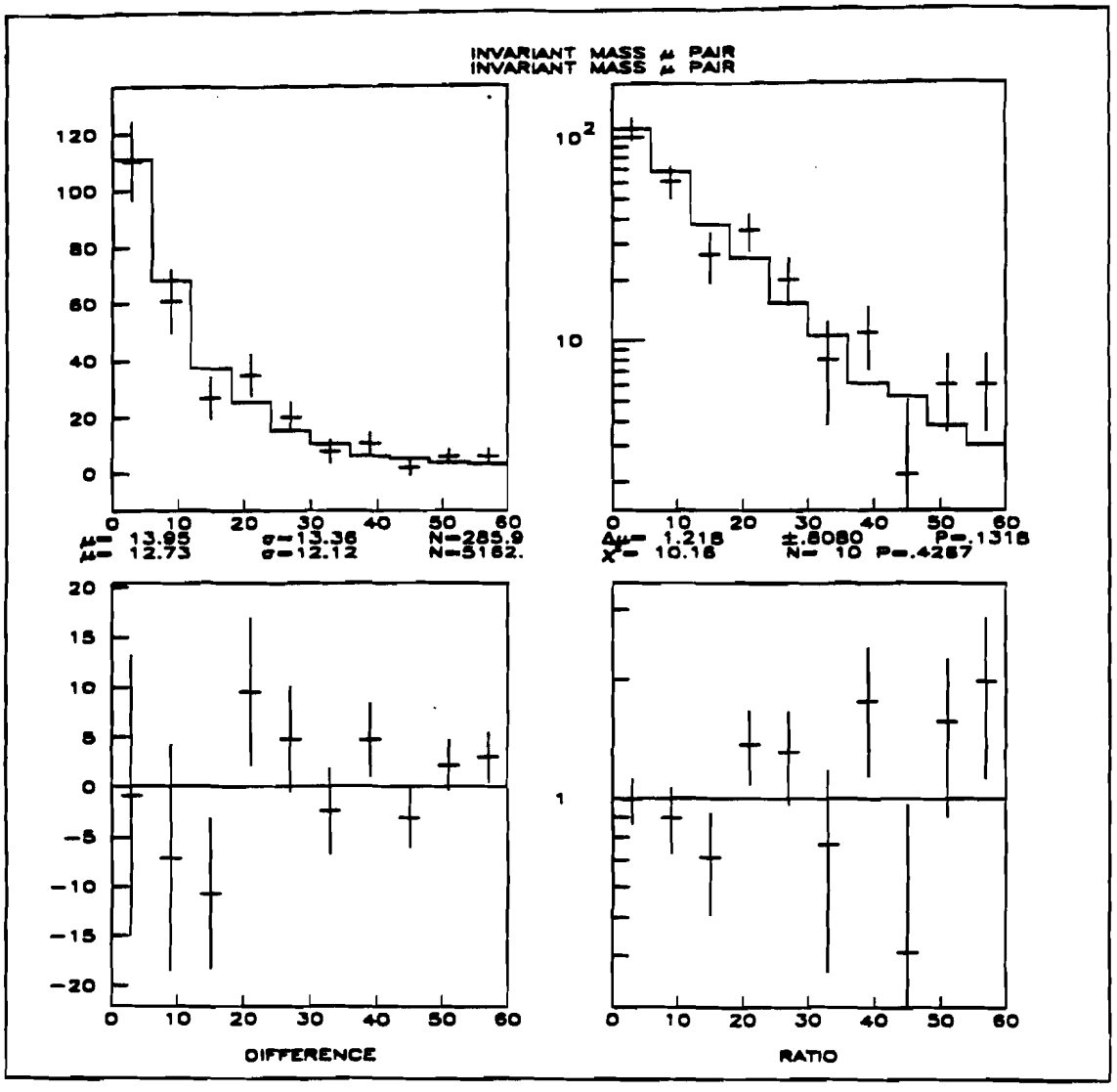

Fig.6.17. Square of the invariant mass of the muon pair in $(GeV/c^2)^2$. Points with errors represent data, the smooth line is the MC. $\chi^2 = 10.2$ for 10 degrees of freedom.

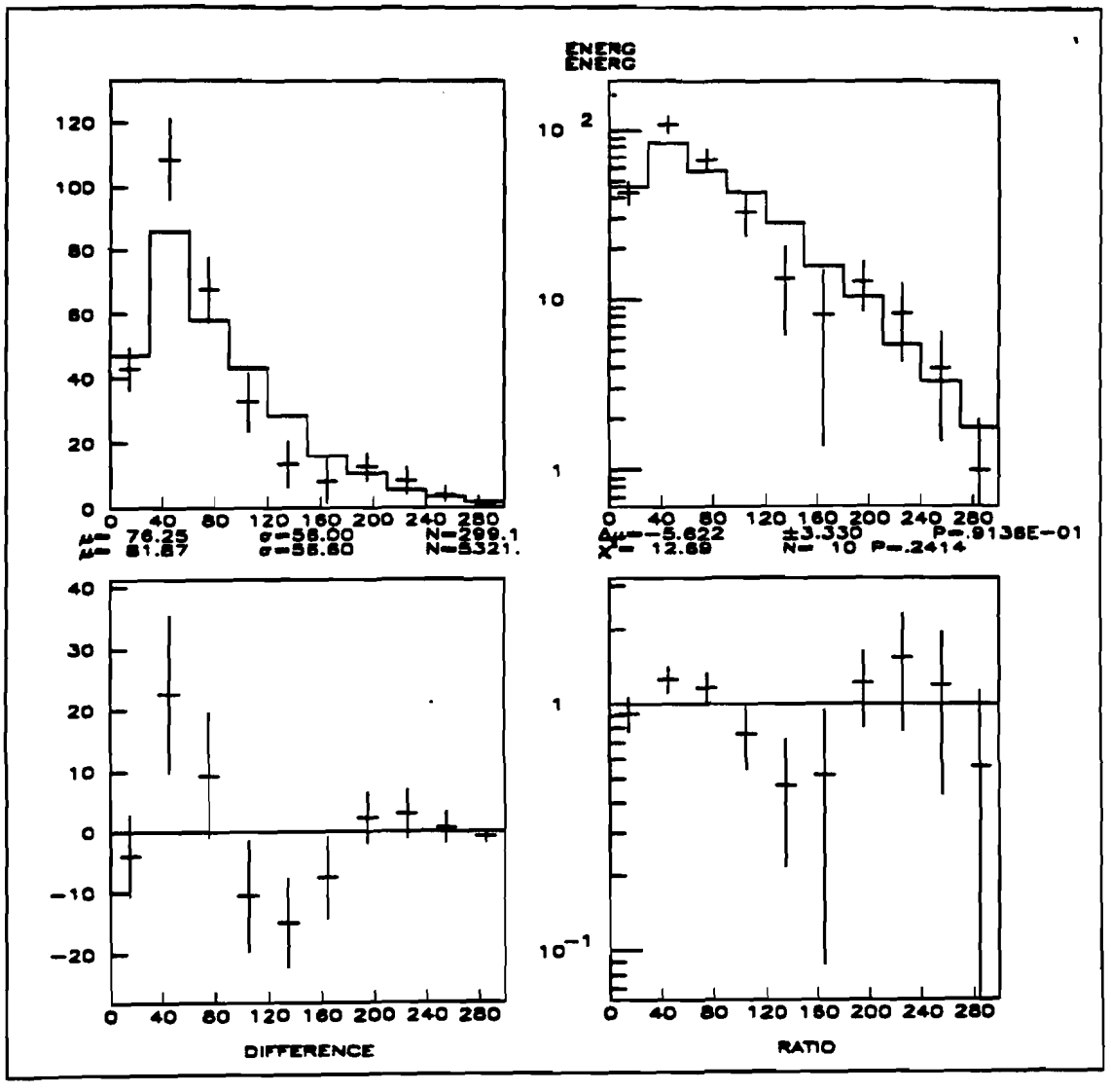

Fig.6.18 Hadronic shower energy in GeV. Points with errors represent data, the smooth line is the MC. $\chi^2 = 12.6$ for 10 degrees of freedom.

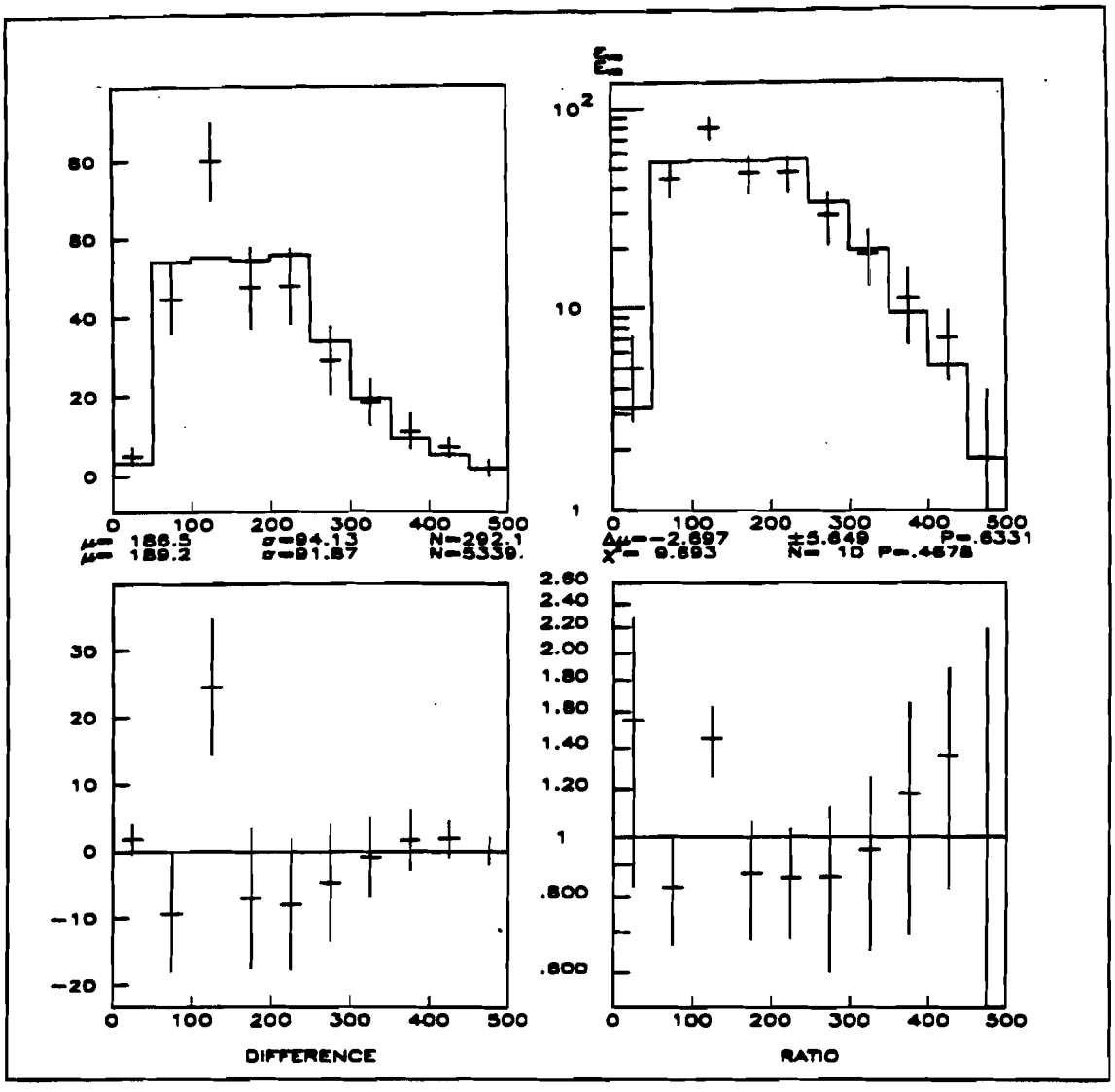

Fig.6.19. Total visible energy in GeV. Points with errors represent data, the smooth line is the MC. χ^2 = 9.6 for 10 degrees of freedom.

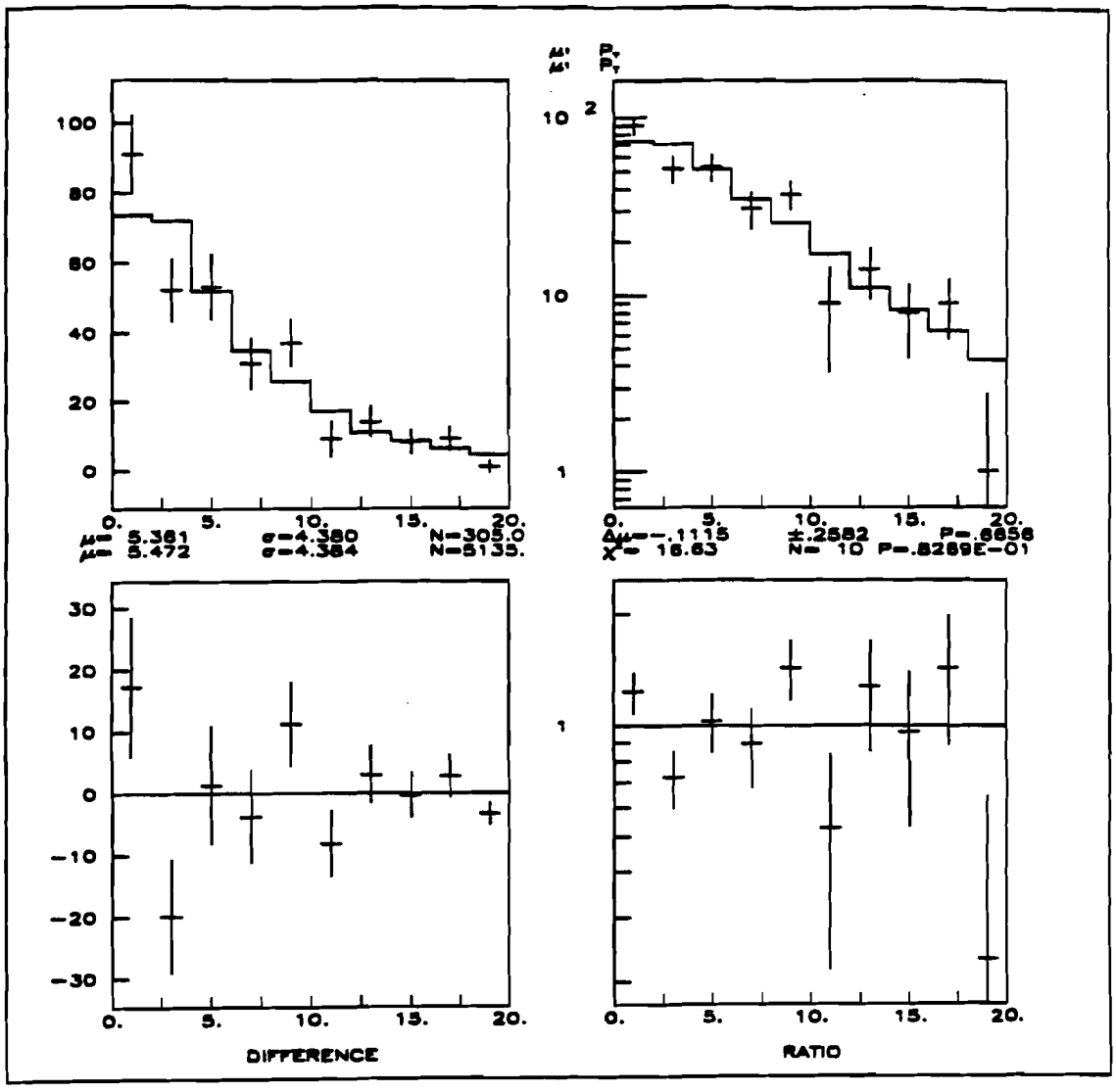

Fig.6.20 Transverse momentum in GeV/c of the leading muon with respect to the shower. Points with errors represent data, the smooth line is the MC. χ^2 = 16.6 for 10 degrees of freedom.

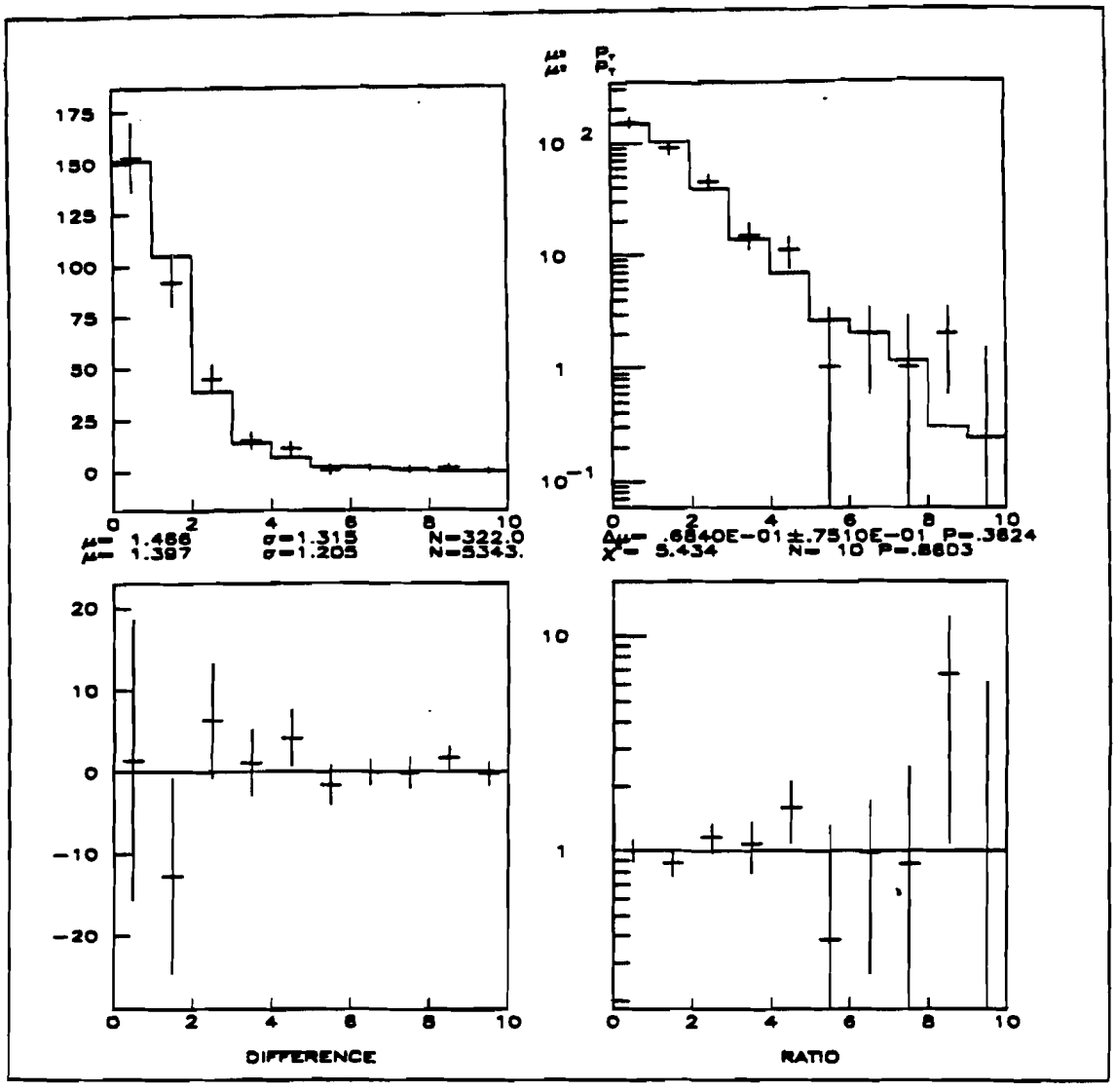

Fig.6.21 Transverse momentum in GeV/c of the second muon with respect to the shower. Points with errors represent data, the smooth line is the MC. χ^2 5.4 for 10 degrees of freedom.

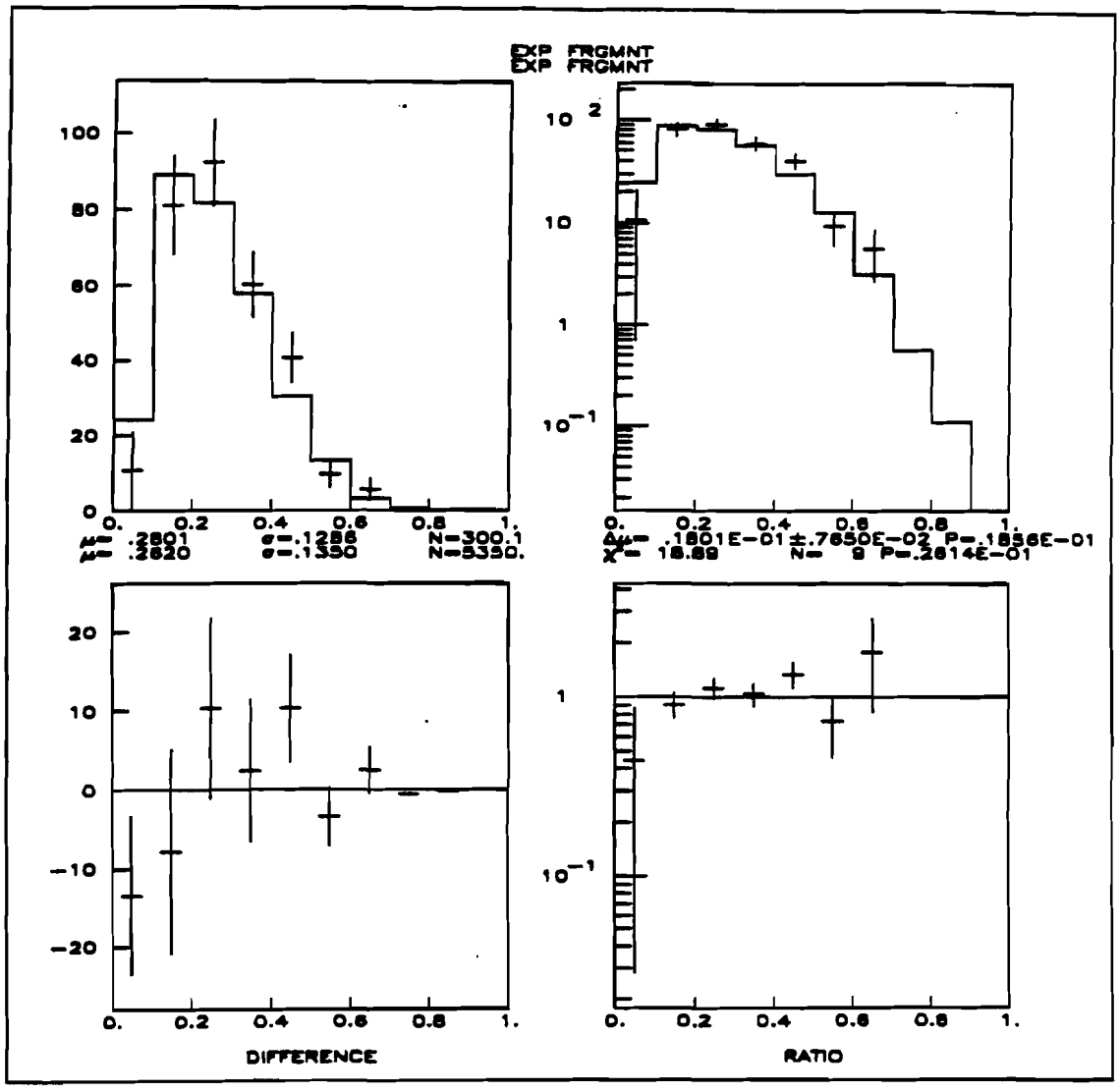

Fig.6.22 Experimental fragmentation function. Points with errors represent data, the smooth line is the MC. $\chi^2 = 18.9$ for 9 degrees of freedom.

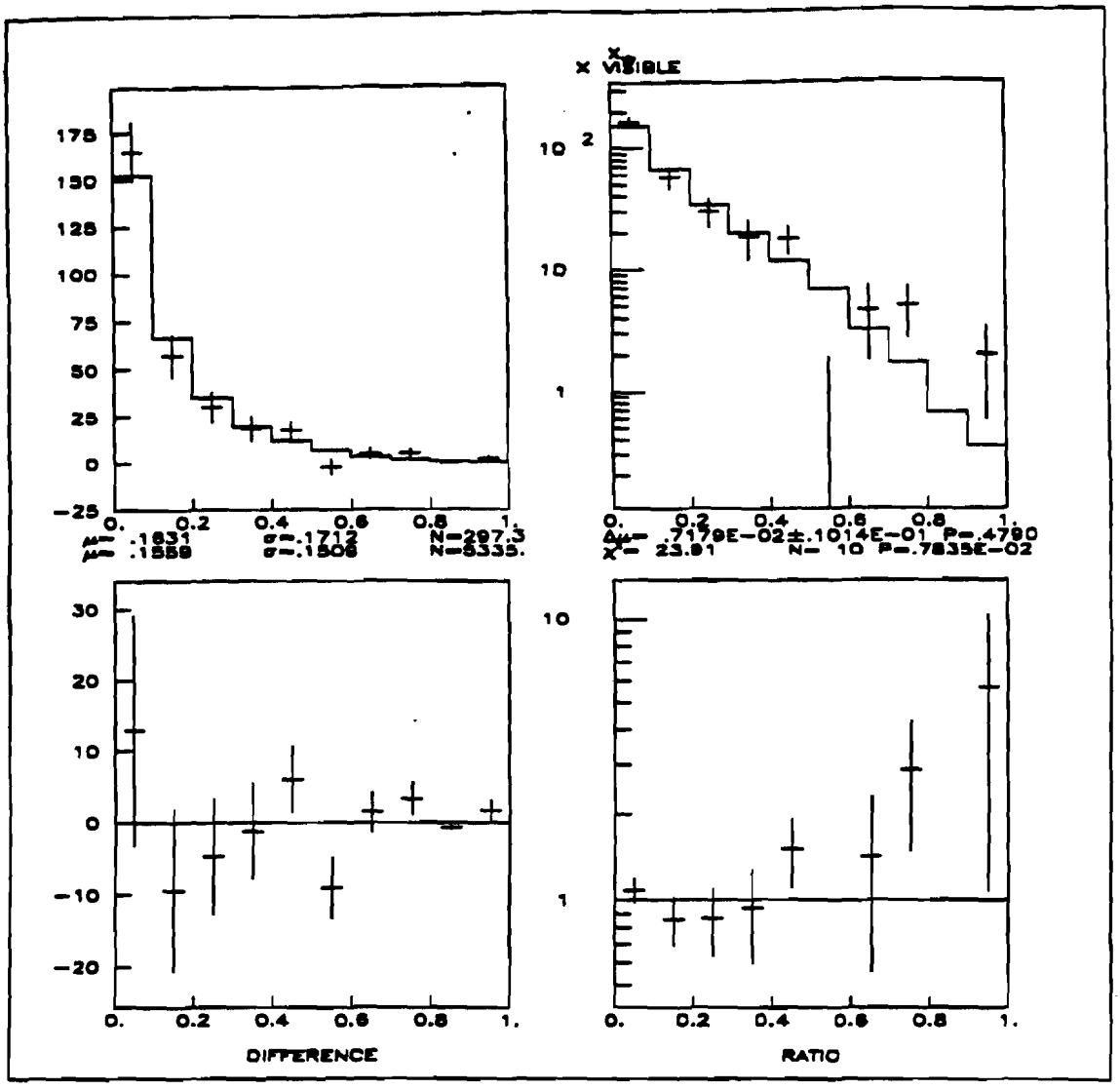

Fig.6.23 $X_{visible}$. Points with errors represent data, the smooth line is the MC. $\chi^2 = 23.9$ for 10 degrees of freedom.

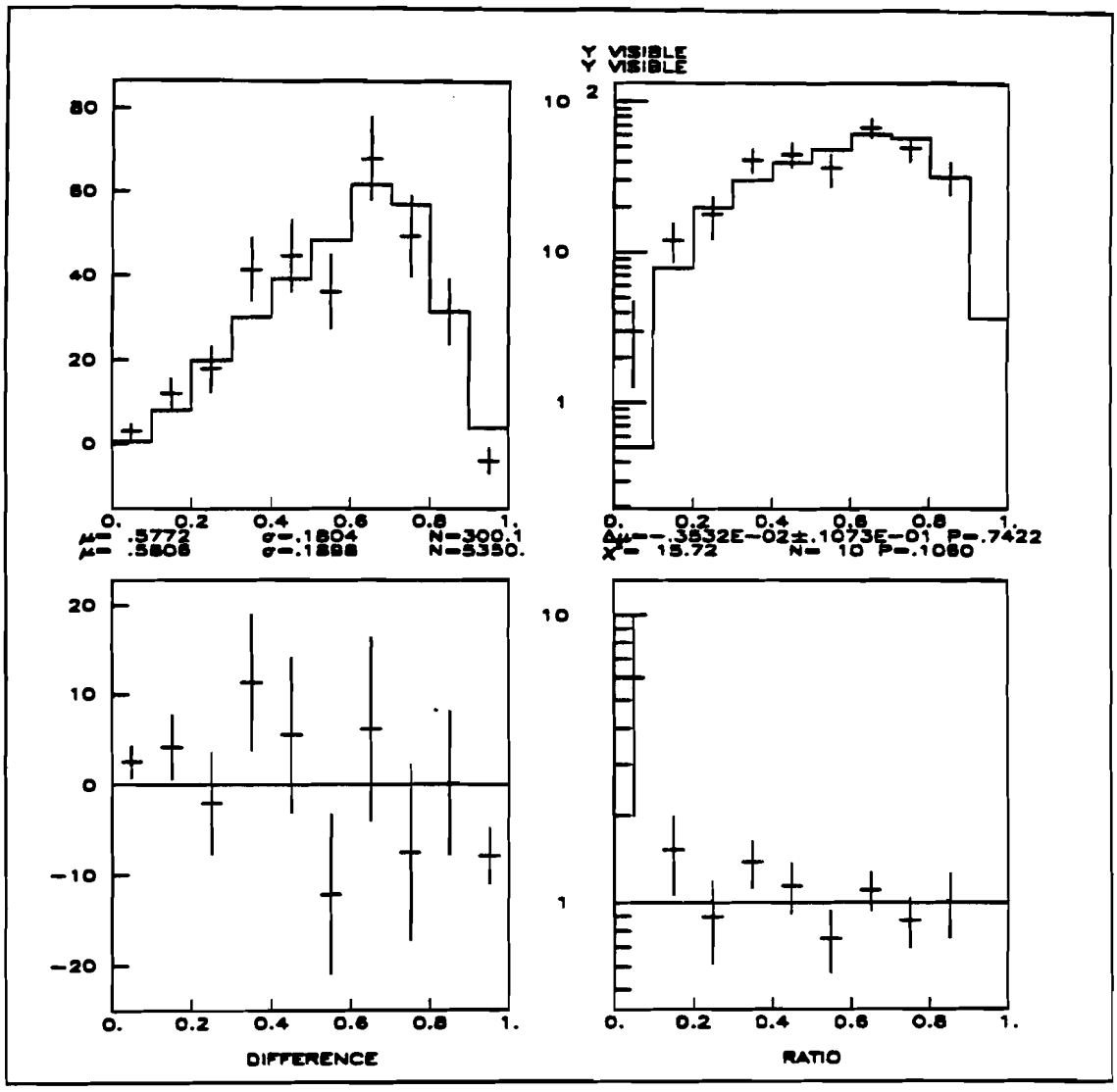

Fig.6.24 $Y_{visible}$. Points with errors represent data, the smooth line is the MC. $\chi^2 = 15.7$ for 10 degrees of freedom.

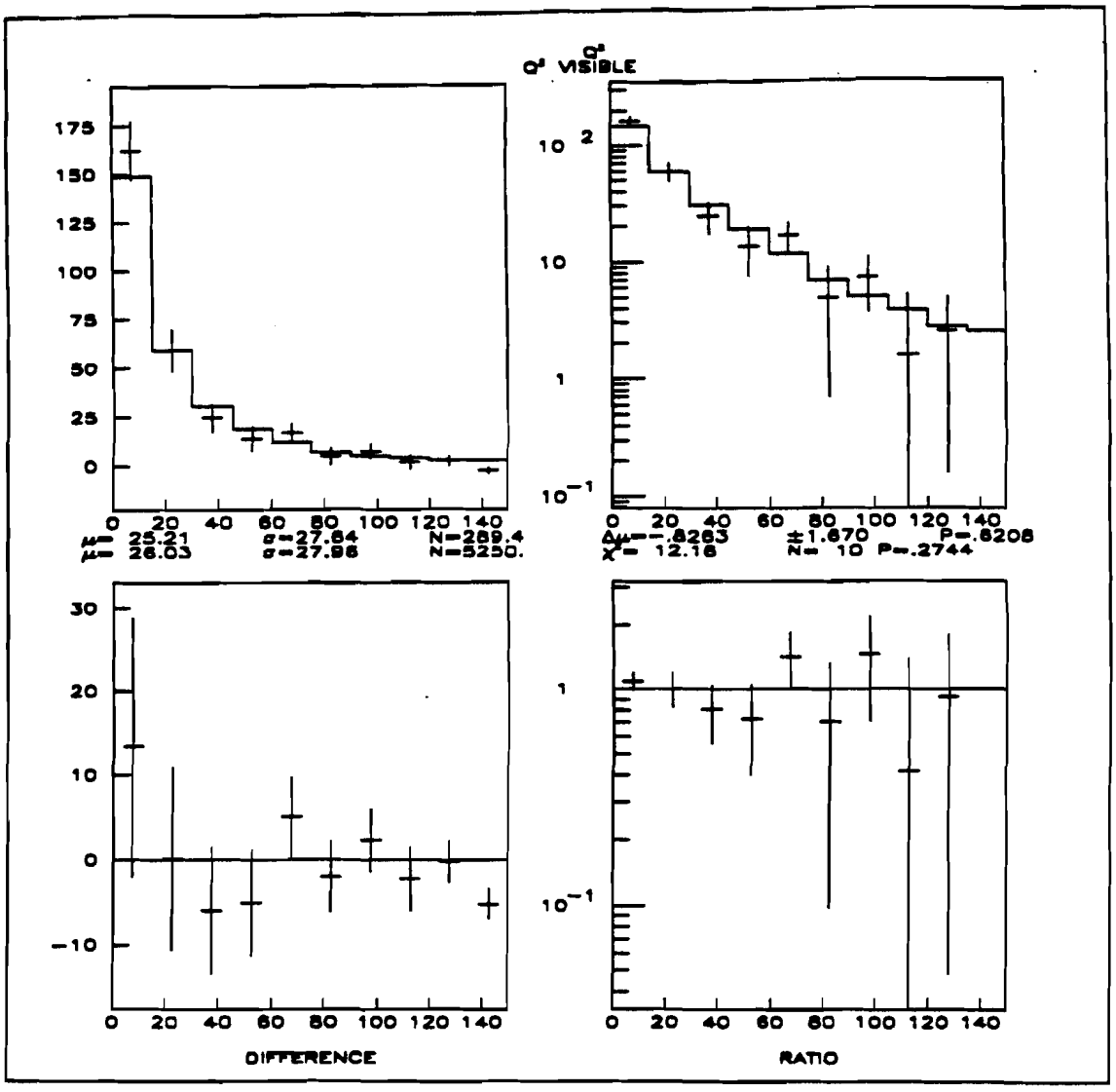

Fig.6.25. $Q^2_{visible}$. Points with errors represent data, the smooth line is the MC. χ^2 = 12.2 for 10 degrees of freedom.

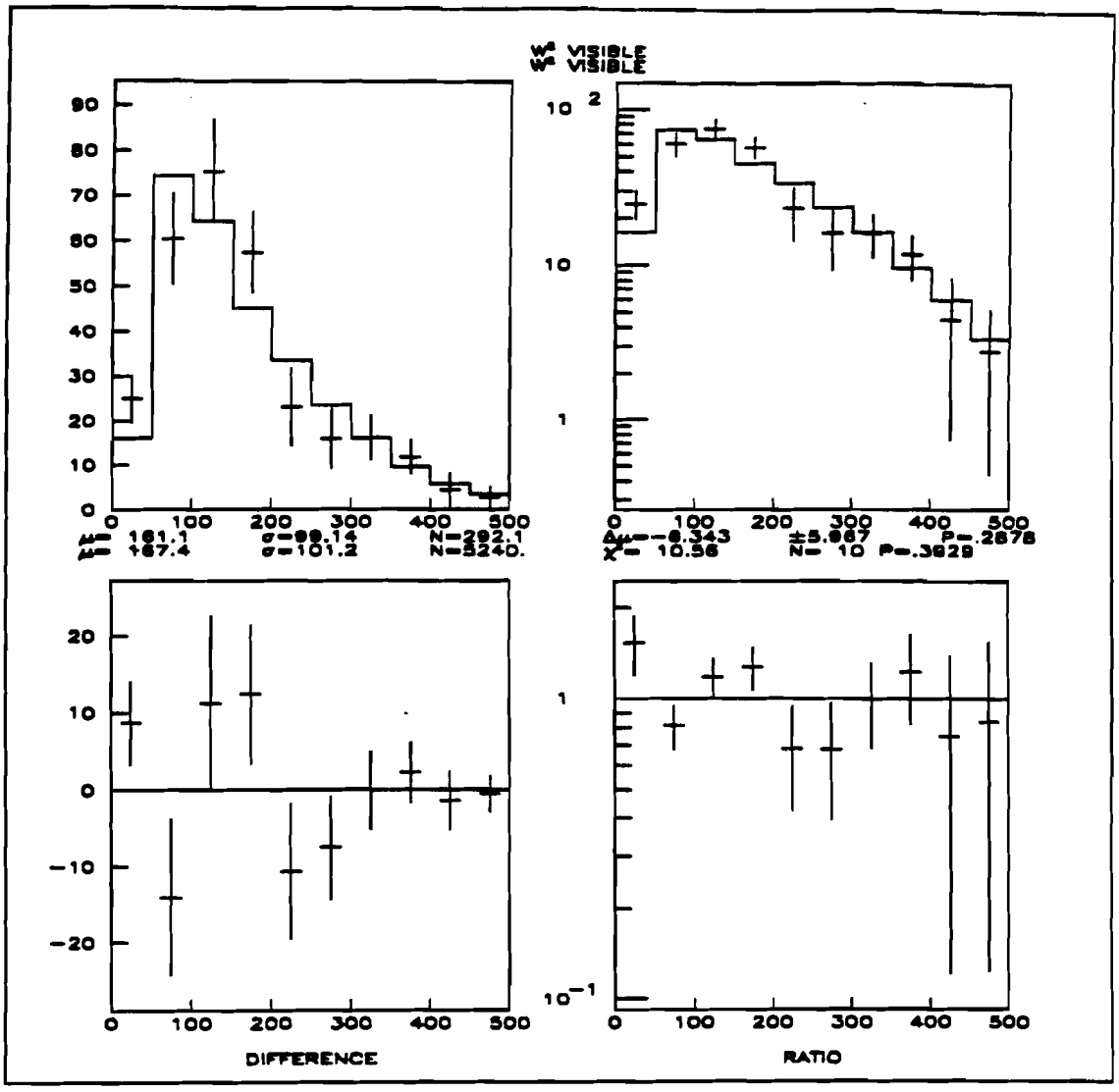

Fig.6.26 $W^2_{visible}$. Points with errors represent data, the smooth line is the MC. $\chi^2 = 10.6$ for 10 degrees of freedom.

6.6. Conclusions.

In this thesis we have described the analysis of neutrino and antineutrino induced opposite sign dimuon events, taken during the 1985 run at Fermilab using the Lab C detector. Our event sample consisted of 300 dimuon events, satisfying $E_\mu > 10$ GeV, $E_{shower} > 10$ GeV, and the fiducial cuts, after the background subtraction. The background due to hadron decays in neutrino showers is calculated to be 23.7% of the raw data sample.

The kinematics of the opposite sign dimuon events were checked against the standard model of opposite sign dimuon production. This model involves creation of the charm quark, its fragmentation into a charm meson (D meson) , and the subsequent semileptonic decay of the charm particle. We find the kinematics of our dimuon data sample to be in good agreement with the predictions of the standard charm production model. The experimentally observable properties of the charm quark fragmentation, such as the experimental fragmentation function (Fig.6.21), are consistent with the Peterson model [6.5] used in our Monte Carlo simulation with the fragmentation parameter $\varepsilon = 0.19$. The transverse momentum distributions of both muons with the respect to the neutrino shower (Fig.6.19 - 6.20), are consistent with the results obtained fr.m e^+e^- experiments [6.7].

The main thrust of this analysis has been to determine the parameters of the standard charm production model, such as the amount of the strange sea inside the nucleon, the semileptonic branching ratio for D meson, the elements of the Kobayashi-Maskawa matrix U_{cd} and U_{cs}, and the mass of the charm quark.

The earliest high statistics determination of χ was done by the CDHS collaboration in 1982[6.1], using a total of 11041 neutrino and 3684 antineutrino dimuon events with $E_\mu > 5$ GeV. They reported the following values of χ and U_{cd}: $\chi = 0.52 \pm 0.09$, and $U_{cd} = 0.24$

$\pm$ 0.03. The CCFR collaboration had a total of 468 opposite sign dimuons with $E_\mu > 4.3$ GeV in 1982 [6.2]. They reported the amount of strange sea of $\kappa = 0.52^{+\ 0.17}_{-\ 0.15}$ using the fixed branching ratio B = 0.109. However their best fit for κ was obtained with B = 0.08. The latest results from CCFR [6.4] indicate $\kappa = 0.46^{+\ 0.13}_{-\ 0.09}$ and B = 0.102 $\pm$ 0.01. Our results for κ at a fixed B of 0.084 are shown in Table 6.4 and are consistent with both the CDHS and CCFR results. The results of the simultaneous fits for B and κ shown in Table 6.7 put the best value of B at B = 0.084 $\pm$ 0.028 $\pm$ 0.014. This value, although consistent with the earlier CCFR results, is somewhat lower than B = 0.109 $\pm$ 0.014, that MARK III obtained [6.6] from studies of e^+e^- collisions. We would like to emphasize, however, that the semileptonic branching ratio measured in this experiment is in fact the average of the branching ratios for various decay modes of $D^\pm$ and D^0 mesons listed in Table 4.2. It is interesting to note that if one assumes that $D^\pm$ and D^0 are produced in equal proportion in neutrino-nucleon scattering, then the average semileptonic branching ratio for all the decay modes becomes B $\approx$ 8.5 %. That value is very close to the branching ratio measured by this experiment.

Our results for U_{cd} and U_{cd} are consistent with the CDHS and are very close to the present world average.

The $2\mu/1\mu$ rate exhibits the characteristic suppression at low neutrino energies due to slow rescaling, and is essentially flat at high energies indicating absence of any additional production channels. We have been able to fit the Monte Carlo calculated dimuon rates to the data to obtain the value of the charm quark mass, which is close to the generally accepted value of $m_c = 1.5\ GeV/c^2$.

Our results and the results of the CDHS and the CCFR collaborations are summarized in Table 6.12

Table 6.12. Comparison of the results of this experiment with the results of CDHS and CCFR. The CCFR results in parentheses represent the latest data yet unpublished.

	Lab C	CDHS	CCFR
# events	300	14700	468 + 1800
x	$0.56 \pm 0.06 \pm 0.07$	0.52 ± 0.09	$0.52\ ^{+0.17}_{-0.15}$
			(0.46 ± 0.1)
B	$0.084 \pm 0.03 \pm 0.014$	----	$0.08\ ^{+0.03}_{-0.02}$
			(0.102 ± 0.01)
U_{cd}	$0.225 \pm 0.038 \pm 0.019$	0.24 ± 0.03	-----
U_{cs}	$0.973 \pm 0.061\ ^{+0.036}_{-0.019}$	> 0.59	-----
M_c	$1.49 \pm 0.92\ ^{+0.35}_{-0.88}$ (2-parm)	-----	-----
(GeV/c^2)	$1.91 \pm 0.28\ ^{+0.45}_{-0.55}$ (1-parm)		

Appendix A.

Event Selection Efficiency.

A.1 Introduction.

To study the efficiency of the event selection and reconstruction software we used Monte Carlo simulations of single muon charged current and opposite sign dimuon events. The physics of the both MCs is described in detail in Chapter IV. The MCs produced "events" in our detector that were as close as possible to the real events, including the full simulation of hadronic showers in the calorimeter and muons in the toroids. We reconstructed these events using the same DST maker as we used for real data. The event selection efficiency is measured by comparing the output of the DST maker with the input. The efficiencies for finding and reconstructing dimuon and single muon charged current events were measured separately.

Since we are interested in the performance of the event selection software, the losses due to the fiducial cuts are not included in the results. There were no other cuts except the requirement that each accepted muon toroid track had at least three hits, not all of them in the same view.

All results are presented in the form of the standard comparison plots. Points with errors represent the output of the DST maker. The smooth line represents the input. The actual efficiency is represented by the ratio plot in the lower right corner of each graph.

A.2. Single Muon Charged Current Events.

The results for Pass A are shown in Fig.A.1 through Fig.A.7. Fig.A.8 through Fig.A.15 show the results after Pass B compared to the original events.

The total efficiency for finding and reconstructing charged current events under the conditions outlined above is found to be about **93%.**

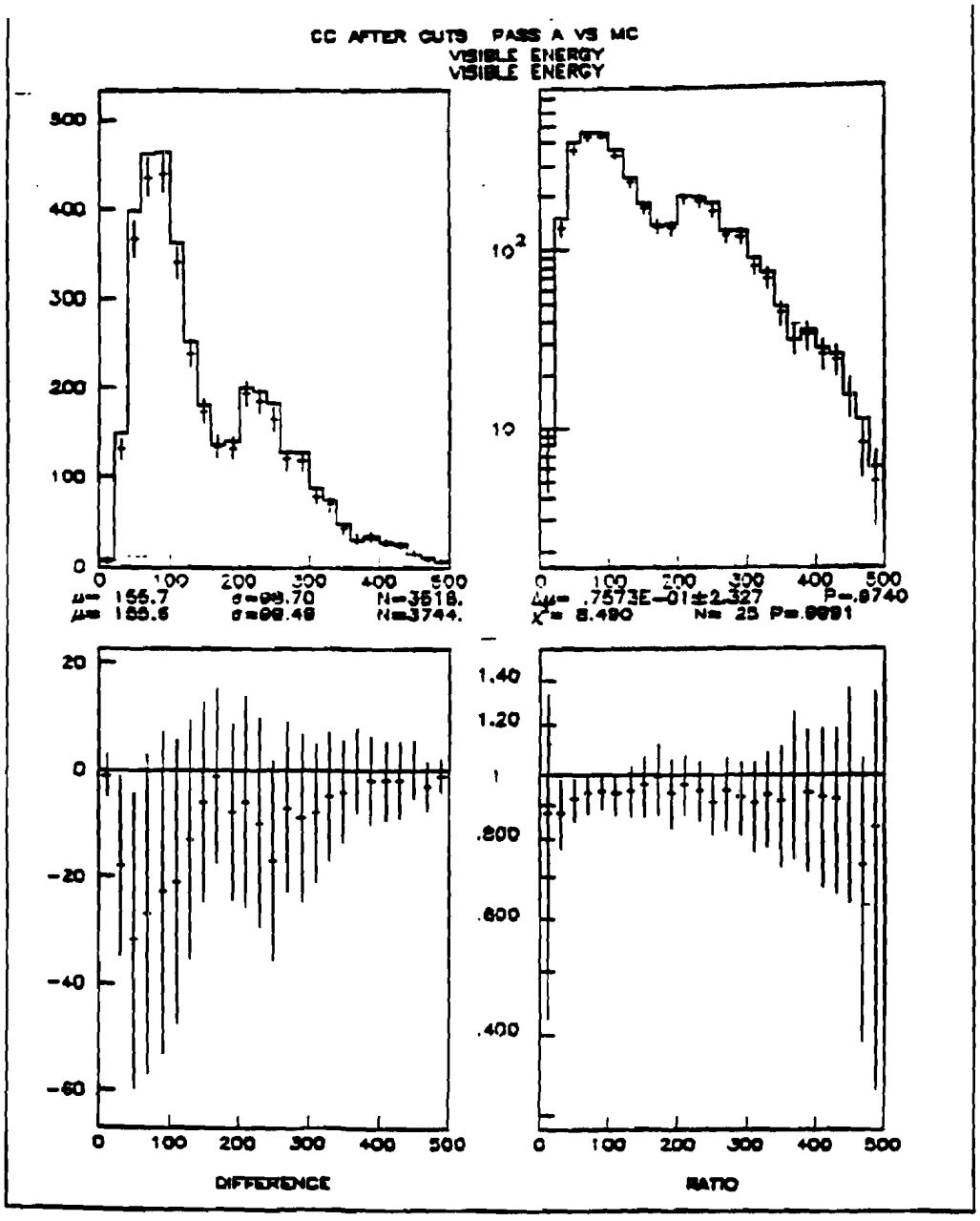

Fig.A.1.Visible energy (in GeV) after Pass A compared with the original MC events.

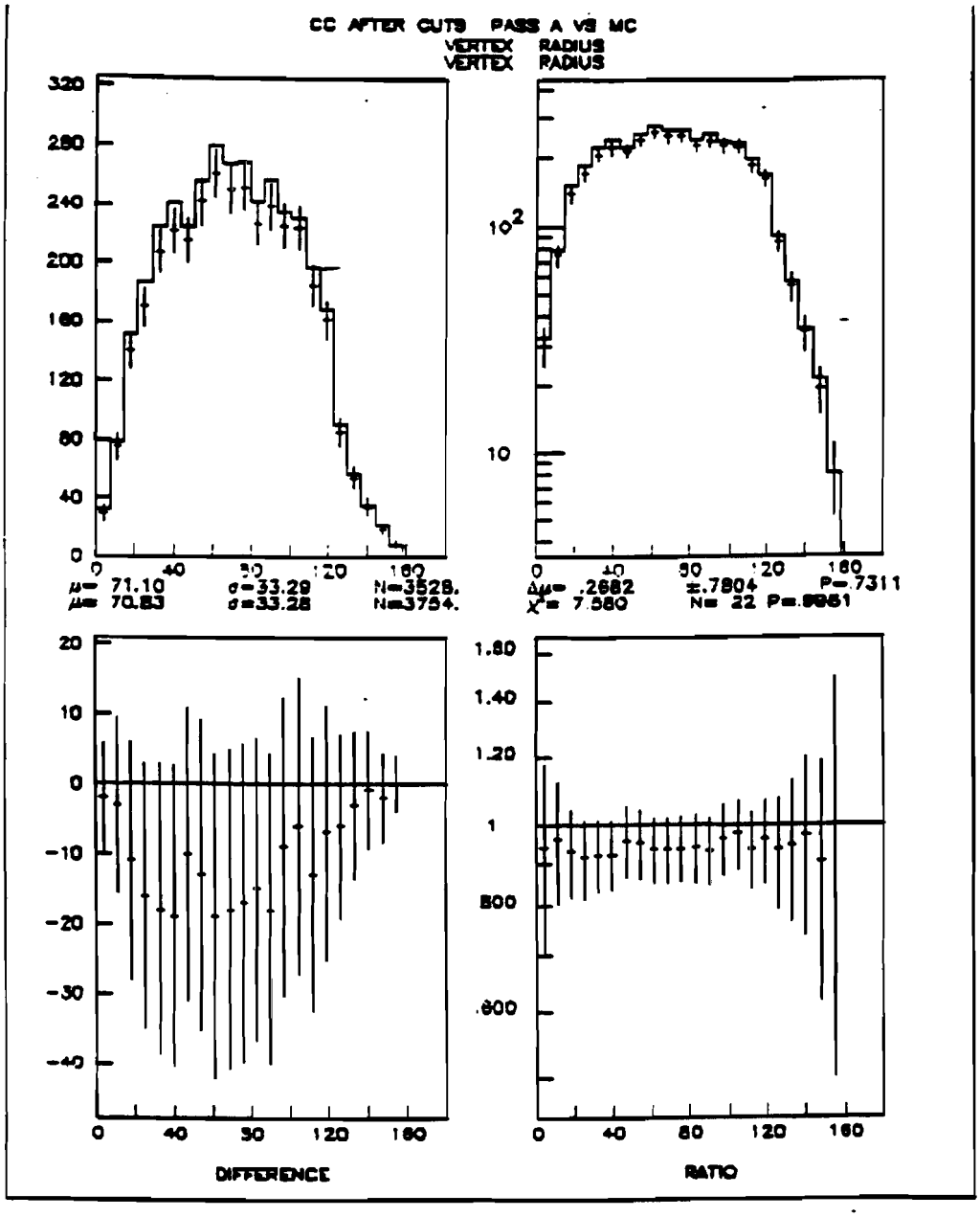

Fig.A.2.Vertex radius (in cm) after Pass A compared with the original MC events.

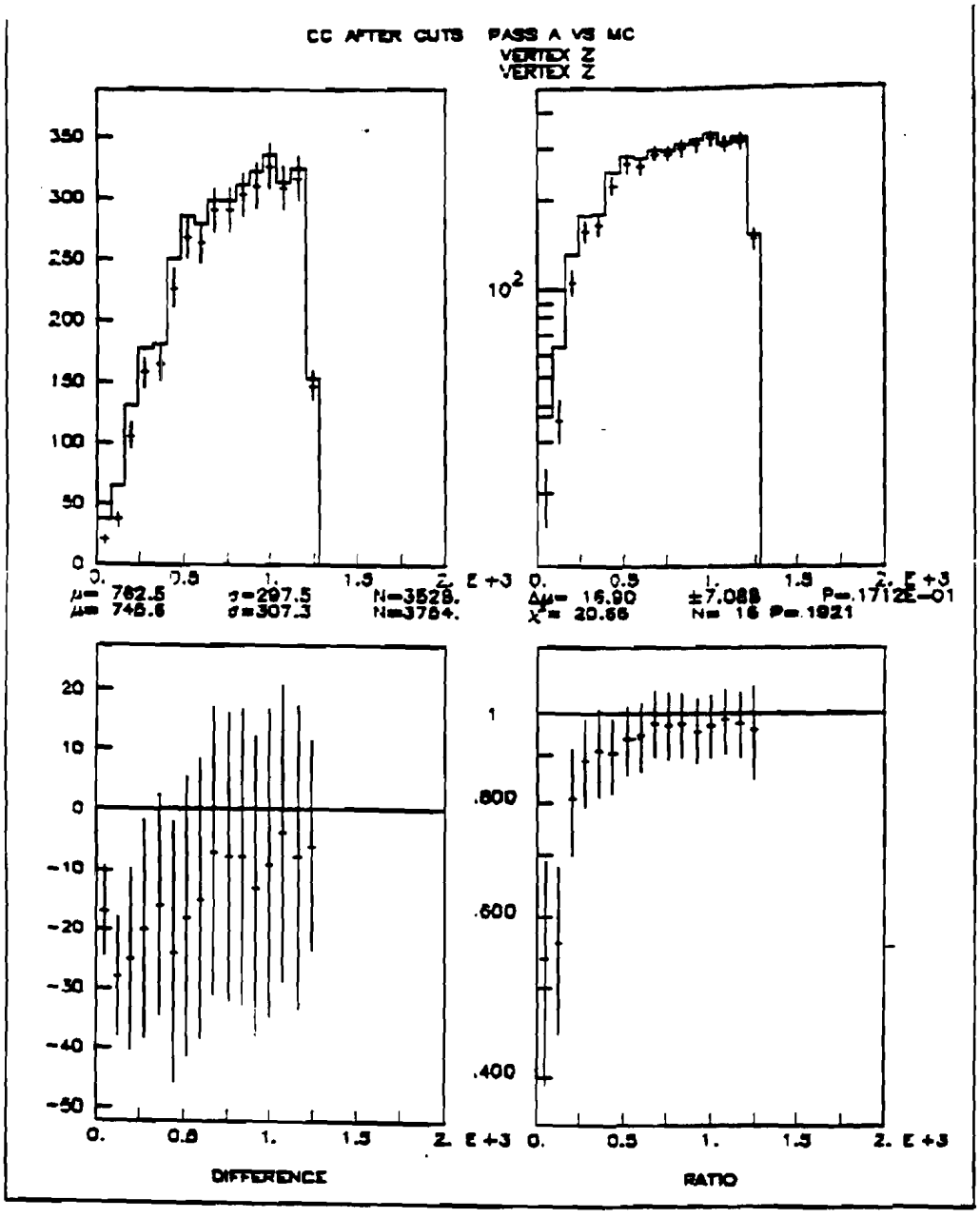

Fig.A.3. Z coordinate of the vertex (in cm) after Pass A compared with the original MC events.

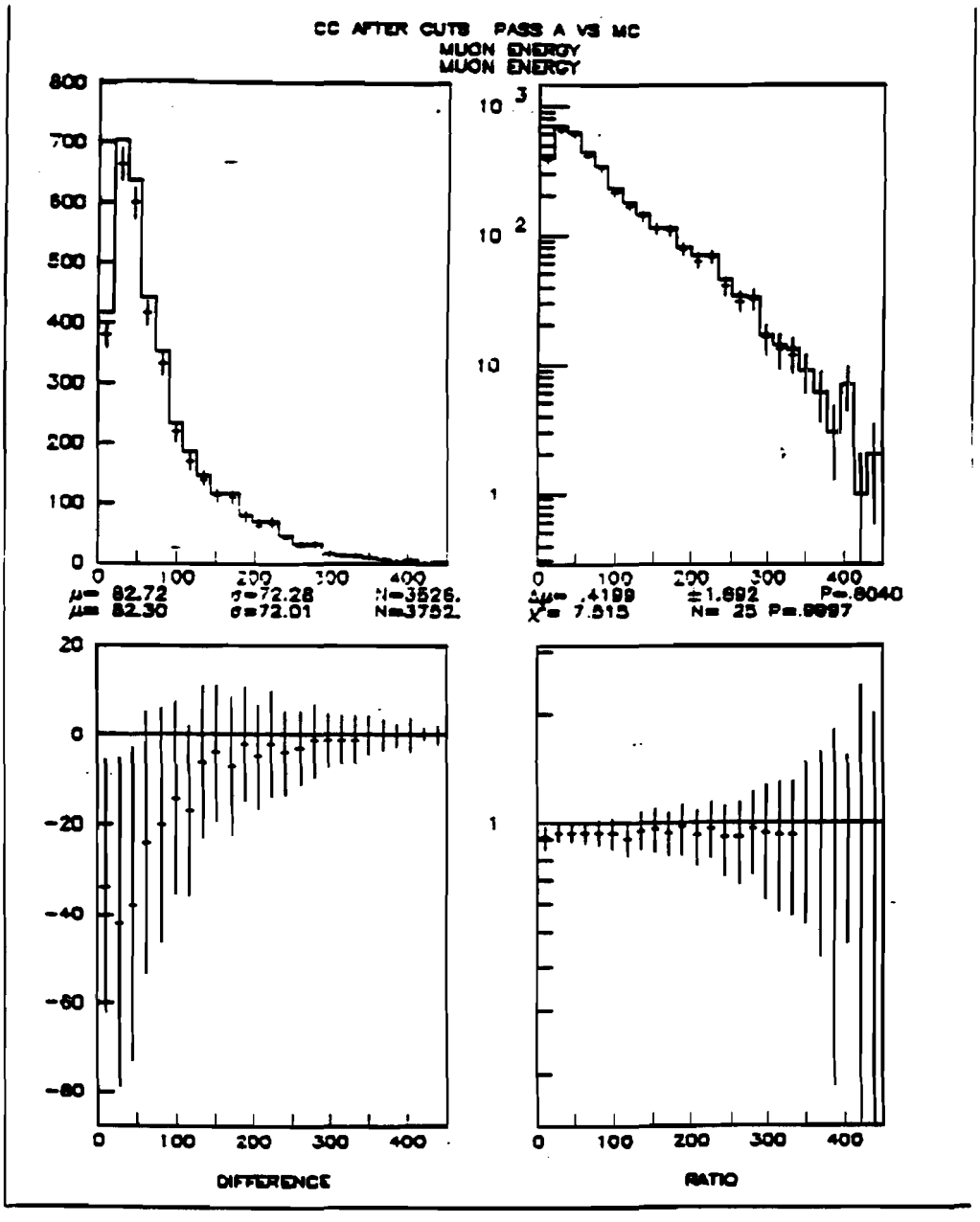

Fig.A.4. The muon energy (in GeV) after Pass A compared with the original MC events.

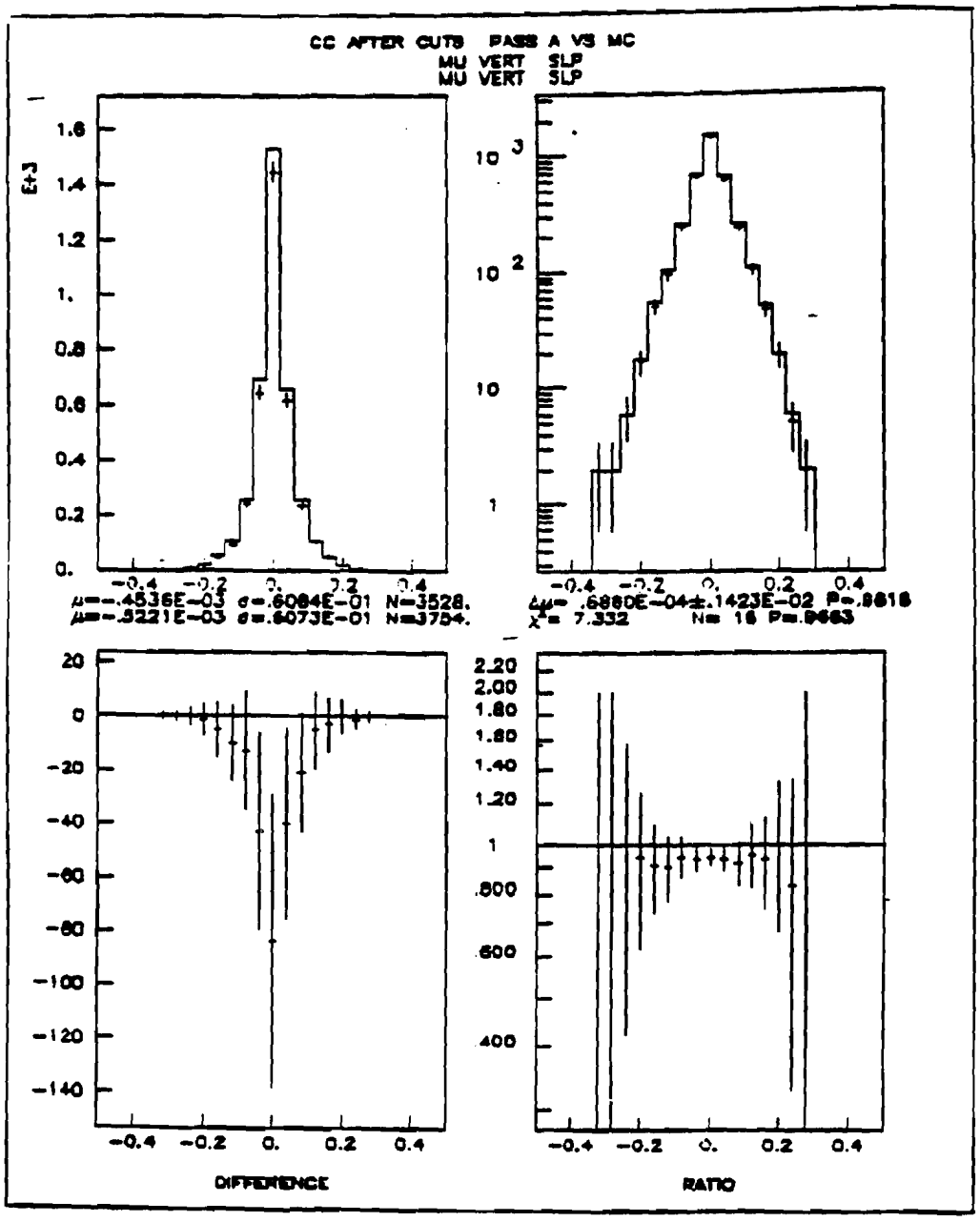

Fig.A.5. The muon vertical slope (in radians) after Pass A compared with the original MC events.

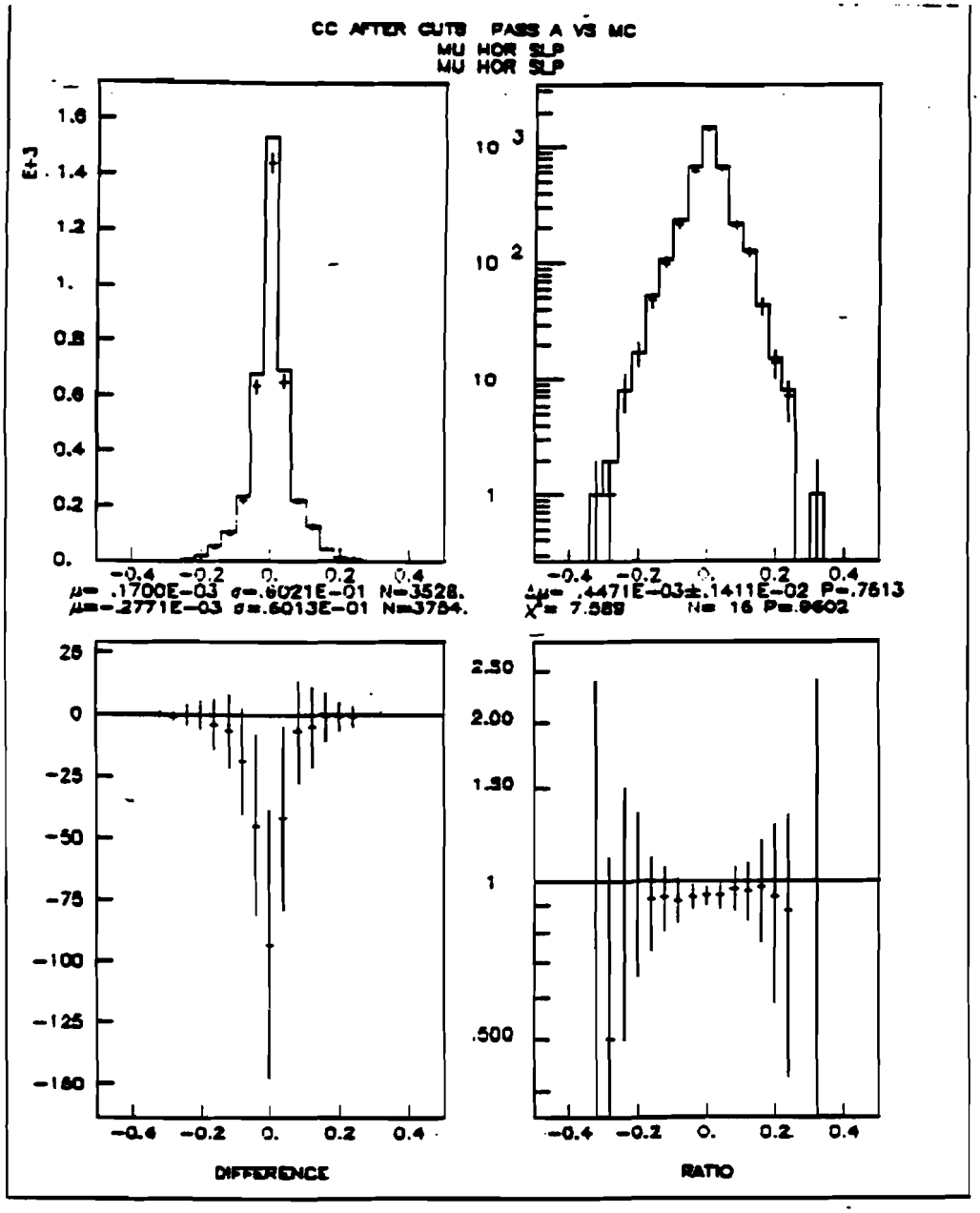

Fig.A.6. The muon horizontal slope (in radians) after Pass A compared with the original MC events.

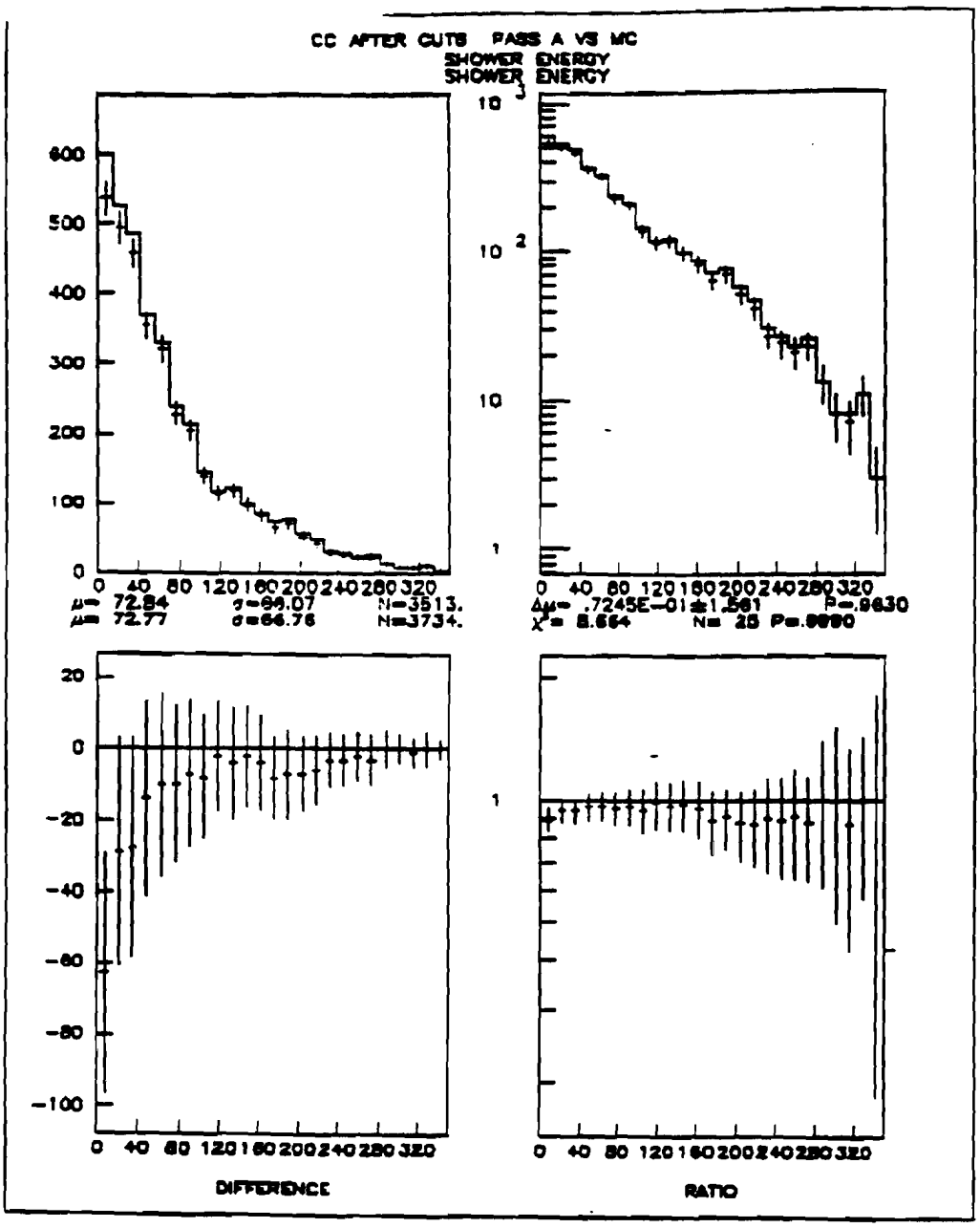

Fig.A.7. The hadron shower energy (in GeV) after Pass A compared with the original MC events.

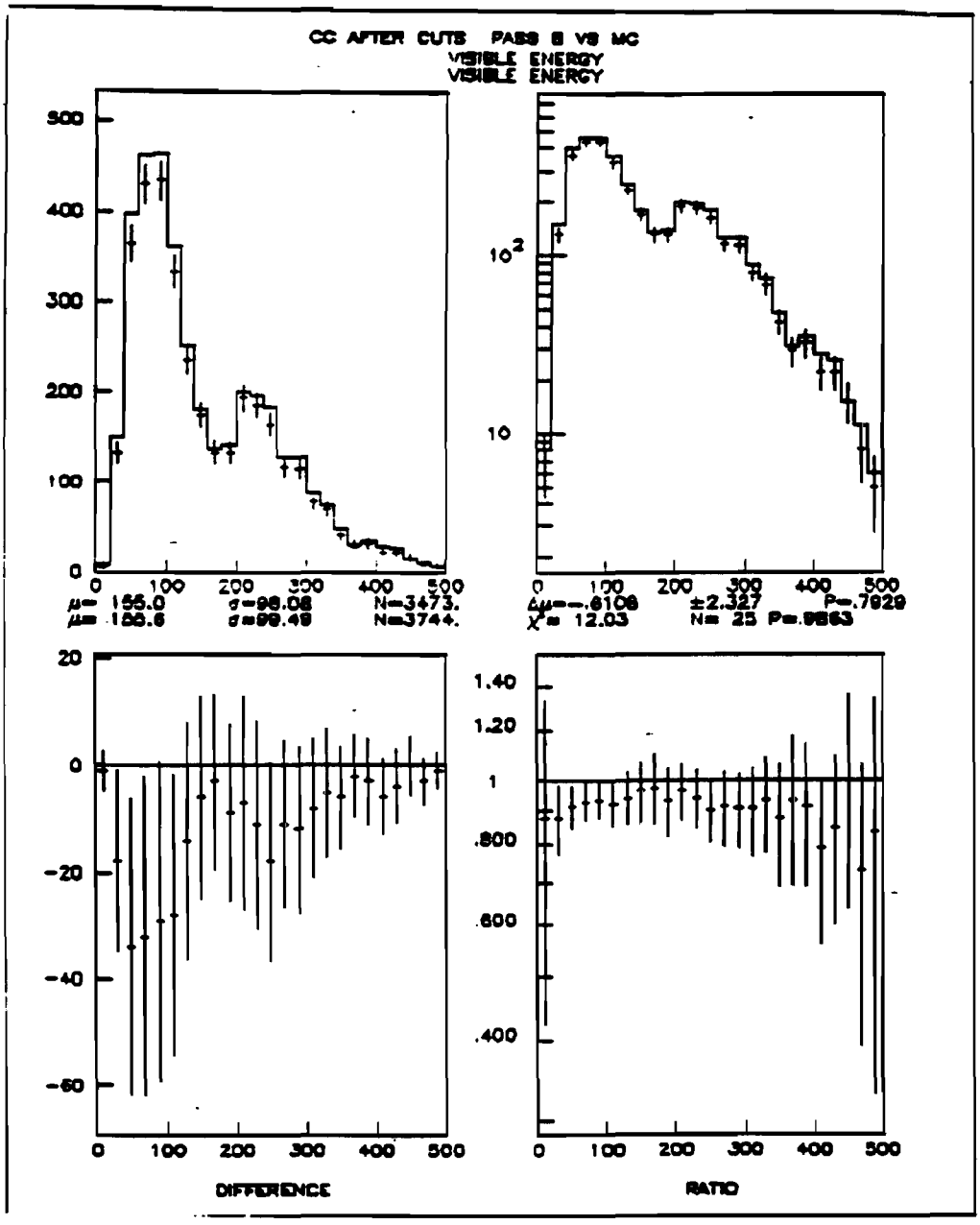

Fig.A.8. Visible energy (in GeV) after Pass B compared with the original MC events.

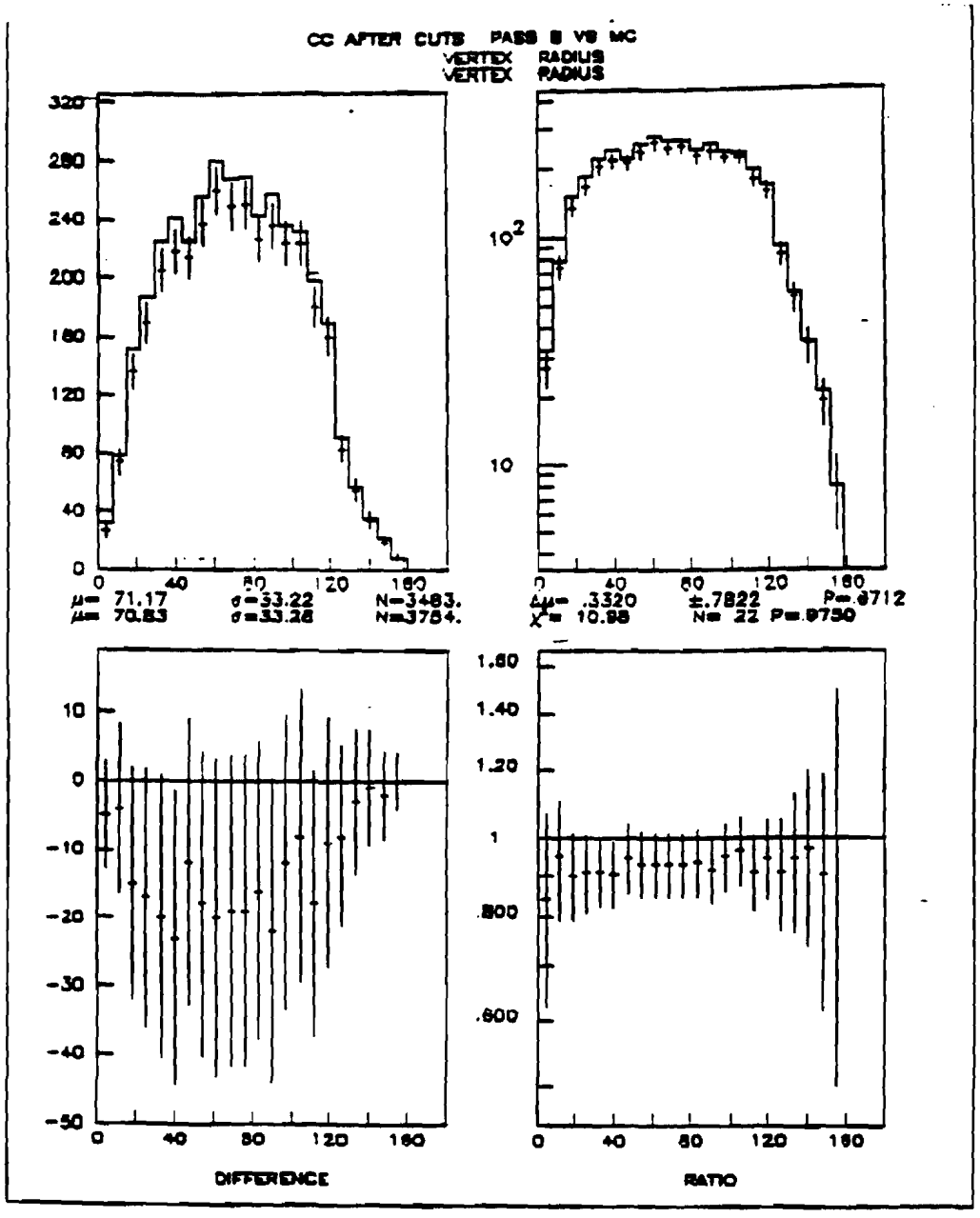

Fig.A.9.Vertex radius (in cm) after Pass B compared with the original MC events.

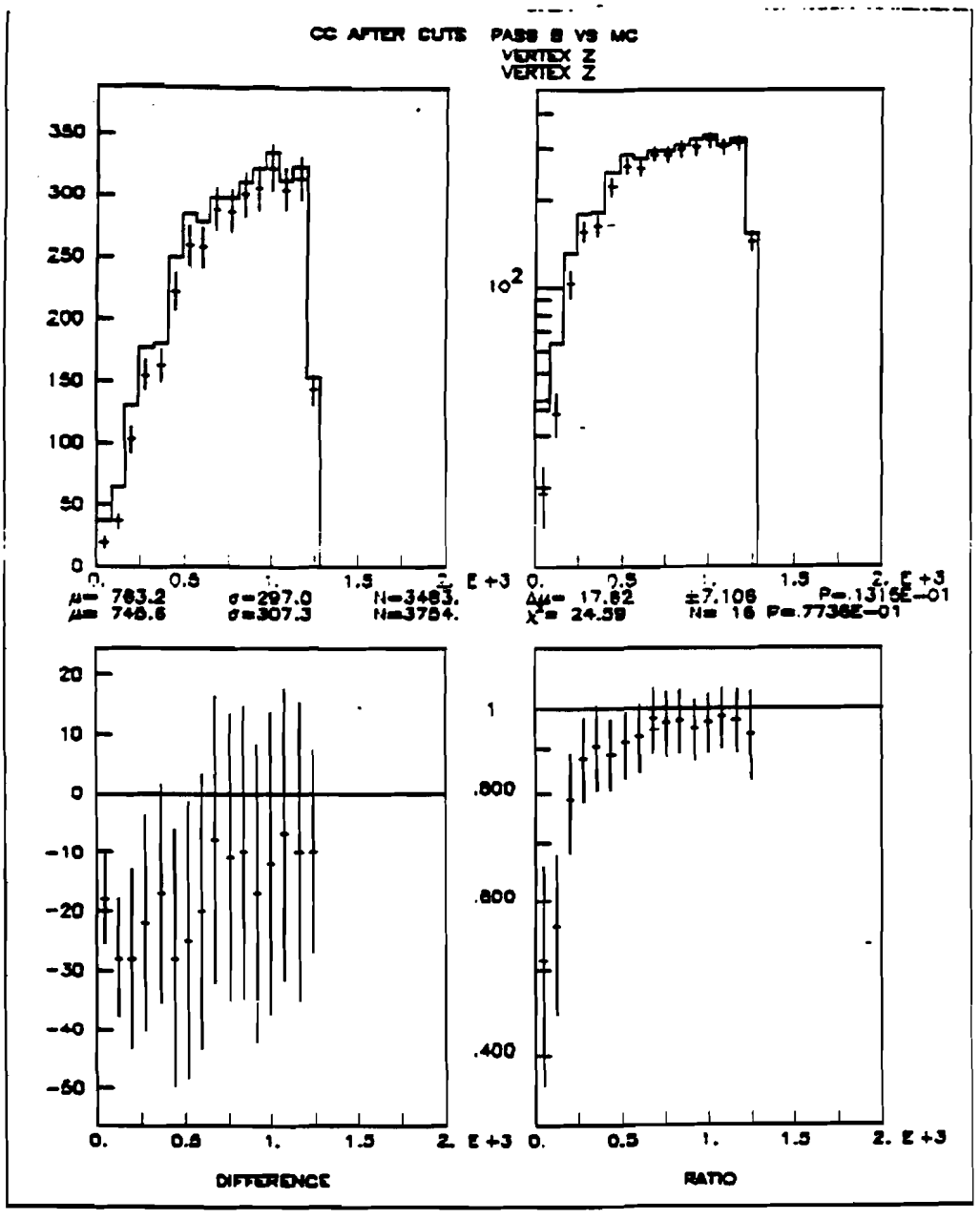

Fig.A.10. Z coordinate of the vertex (in cm) after Pass B compared with the original MC events.

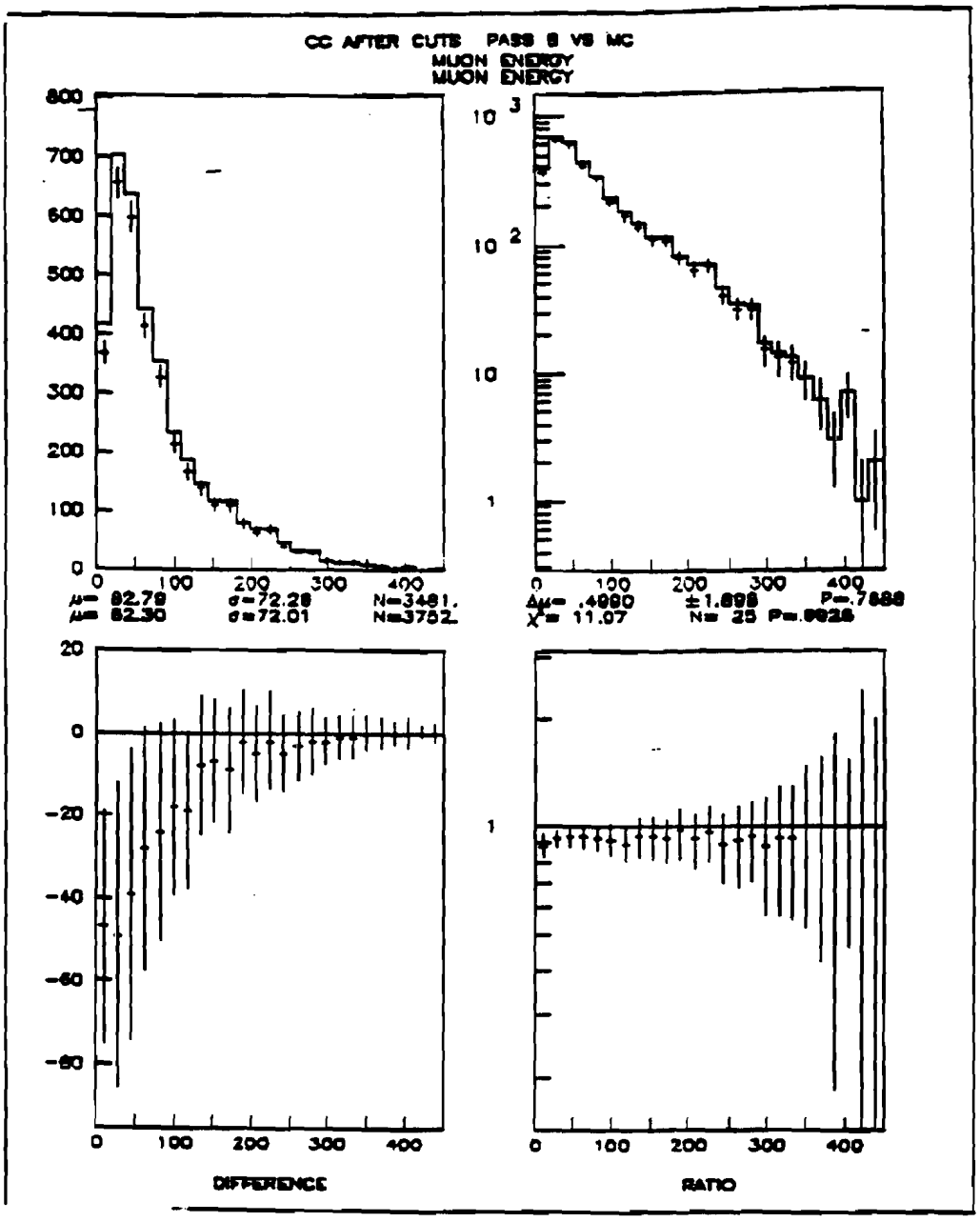

Fig.A.11. The muon energy (in GeV) after Pass B compared with the original MC events.

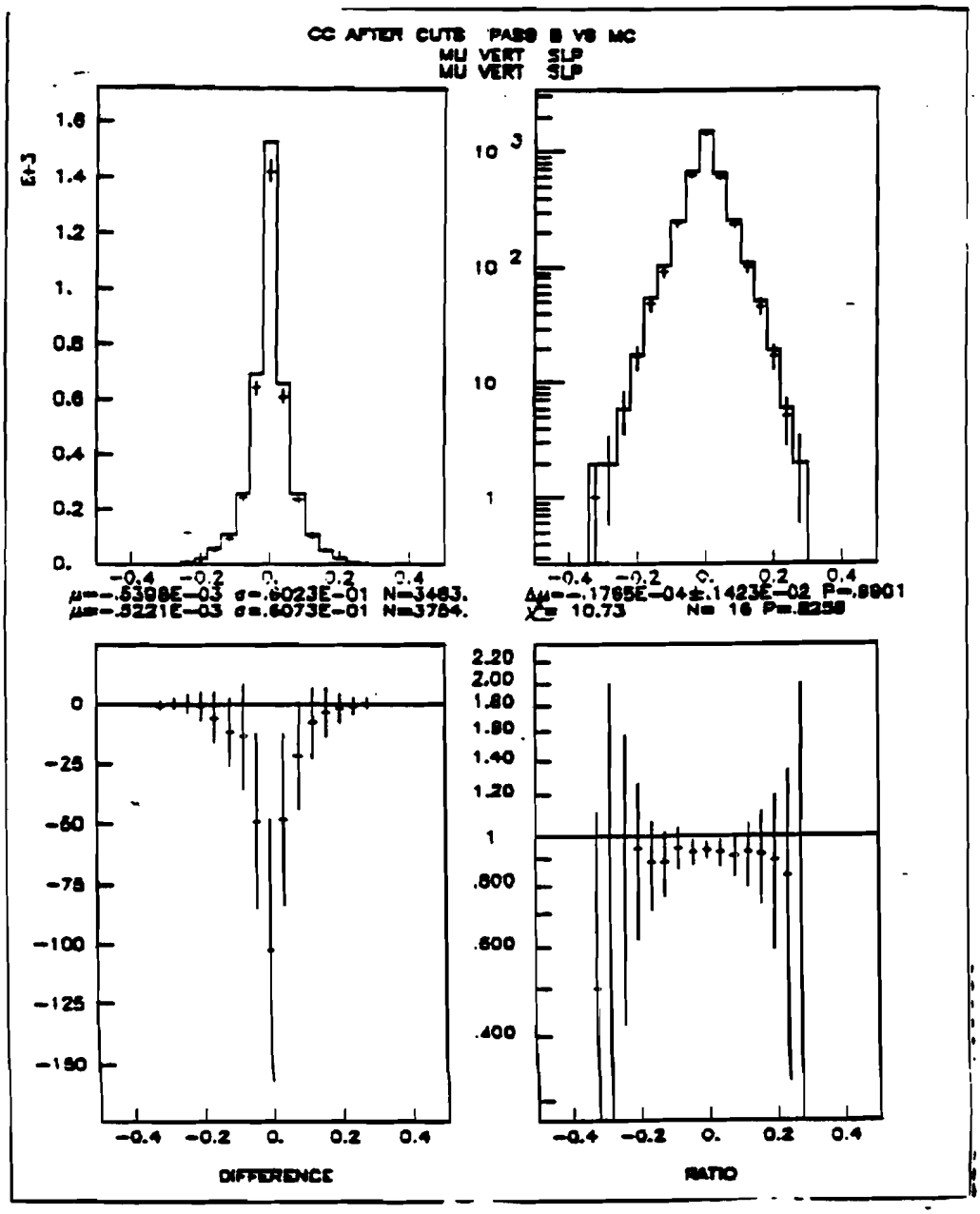

Fig.A.12. The muon vertical slope (in radians) after Pass B compared with the original MC events.

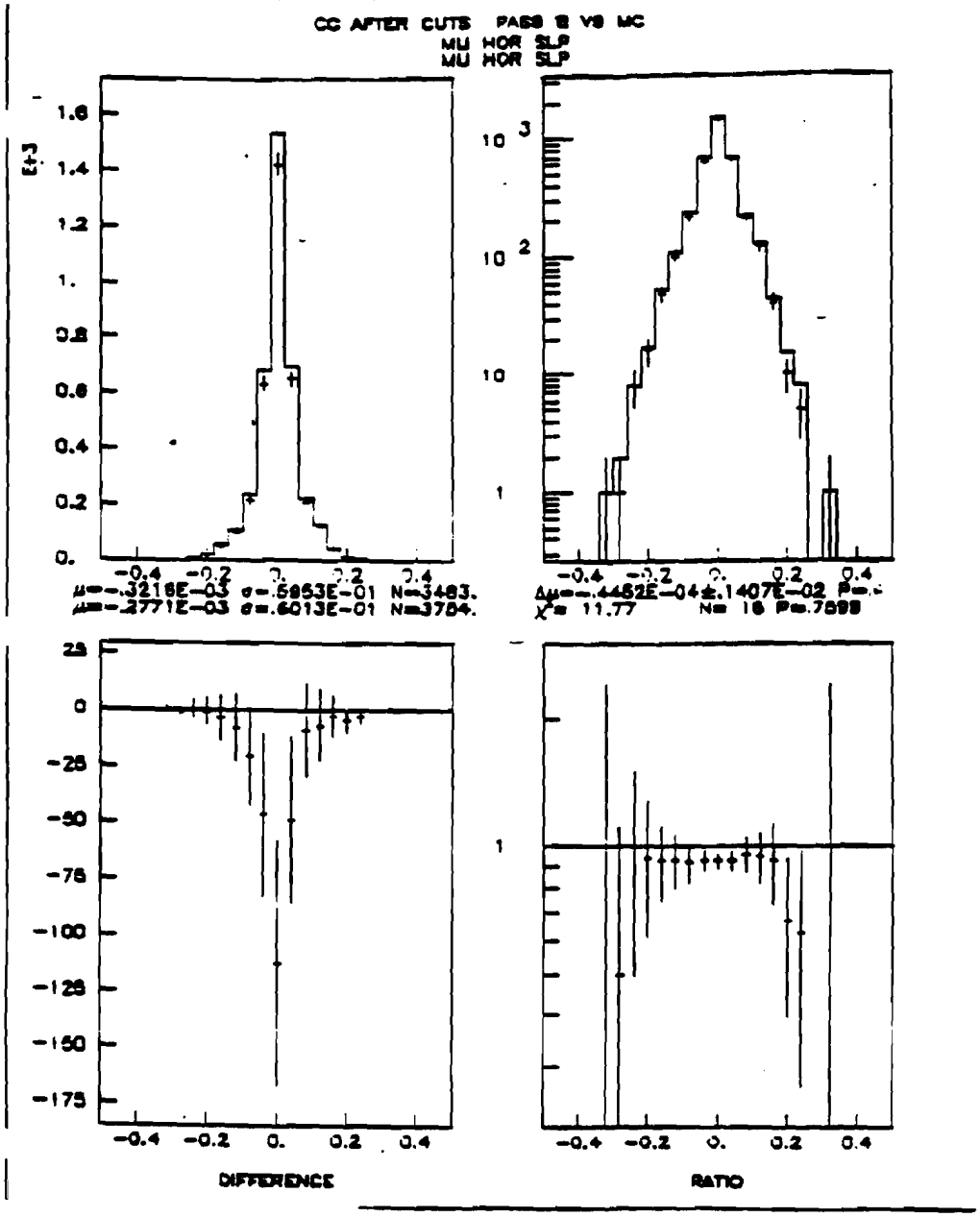

Fig.A.13. The muon horizontal slope (in radians) after Pass B compared with the original MC events.

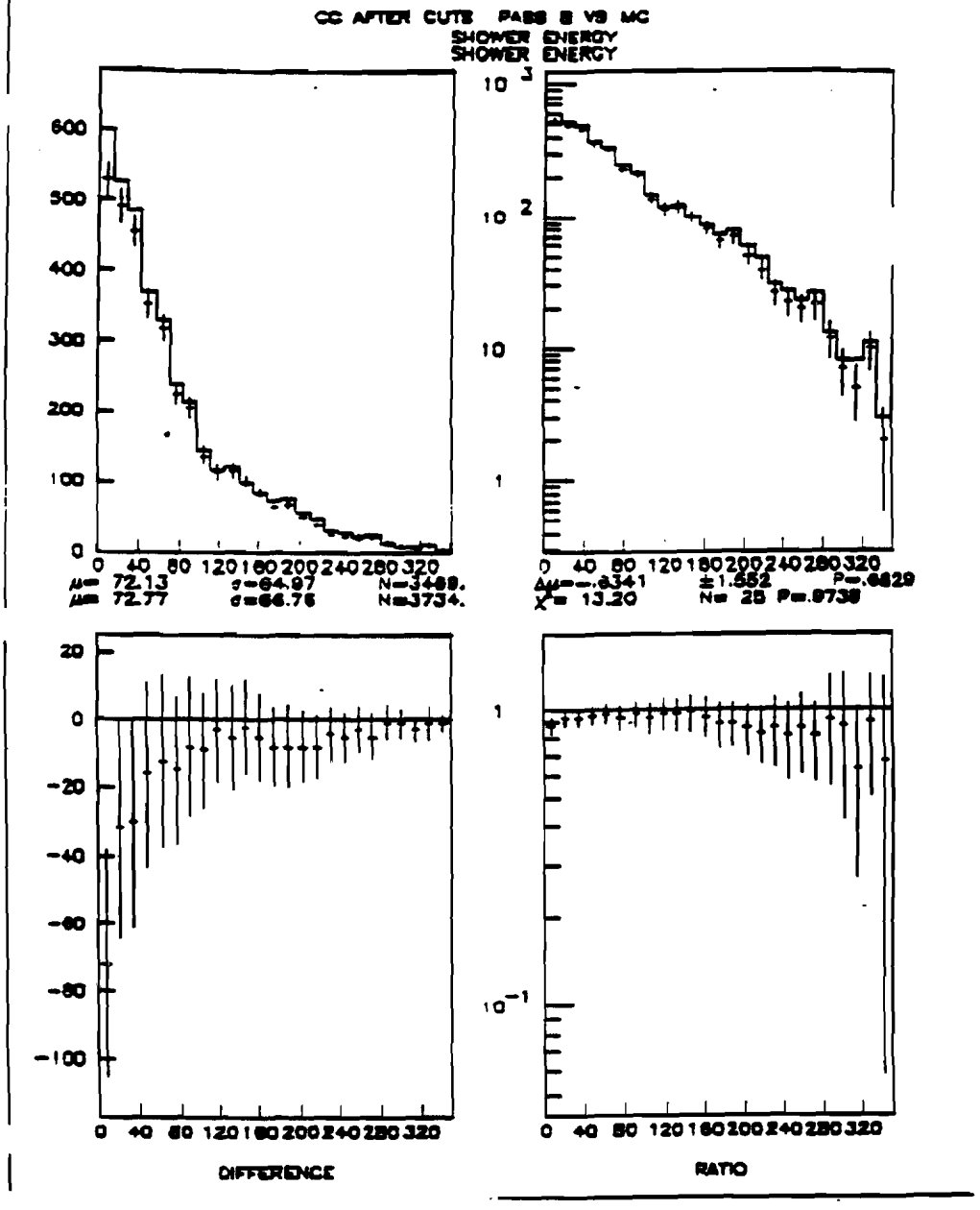

Fig.A.14. The hadron shower energy (in GeV) after Pass B compared with the original MC events.

A.3. Opposite Sign Dimuon Events.

The results for Pass A are shown in Fig.A.16 through Fig.A.19. The results for Pass B versus the original events are shown in Fig.A.20 through Fig.A.23.

The Pass A efficiency is found to be ≈ 88%. The Pass B efficiency is ≈ 80%. The total efficiency for finding dimuons under the conditions outlined in Section A.1 is about 72%.

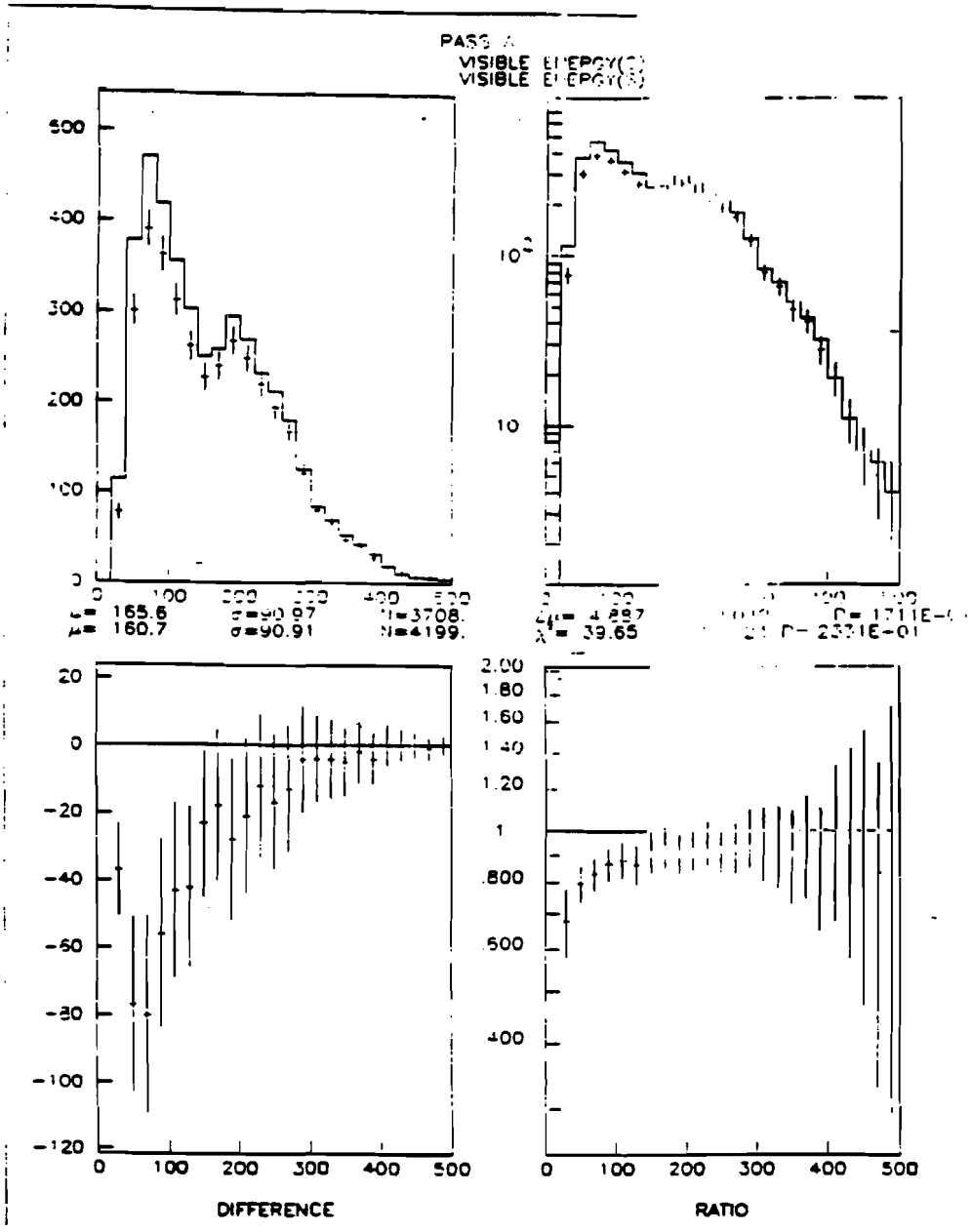

Fig.A.15. Visible energy (in GeV) after Pass A compared with the original MC events.

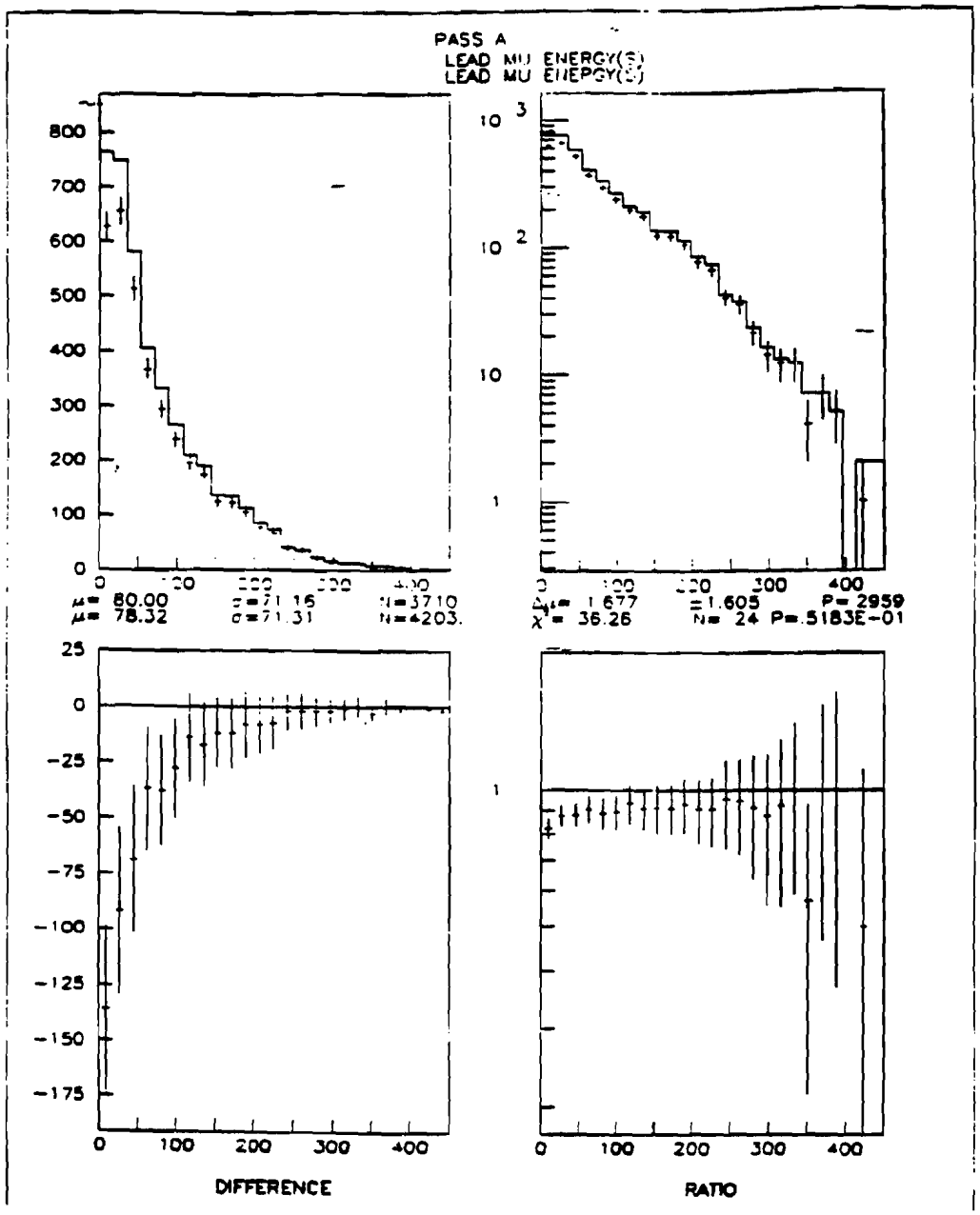

Fig.A.16. Leading muon energy (in GeV) after Pass A compared with the original MC events.

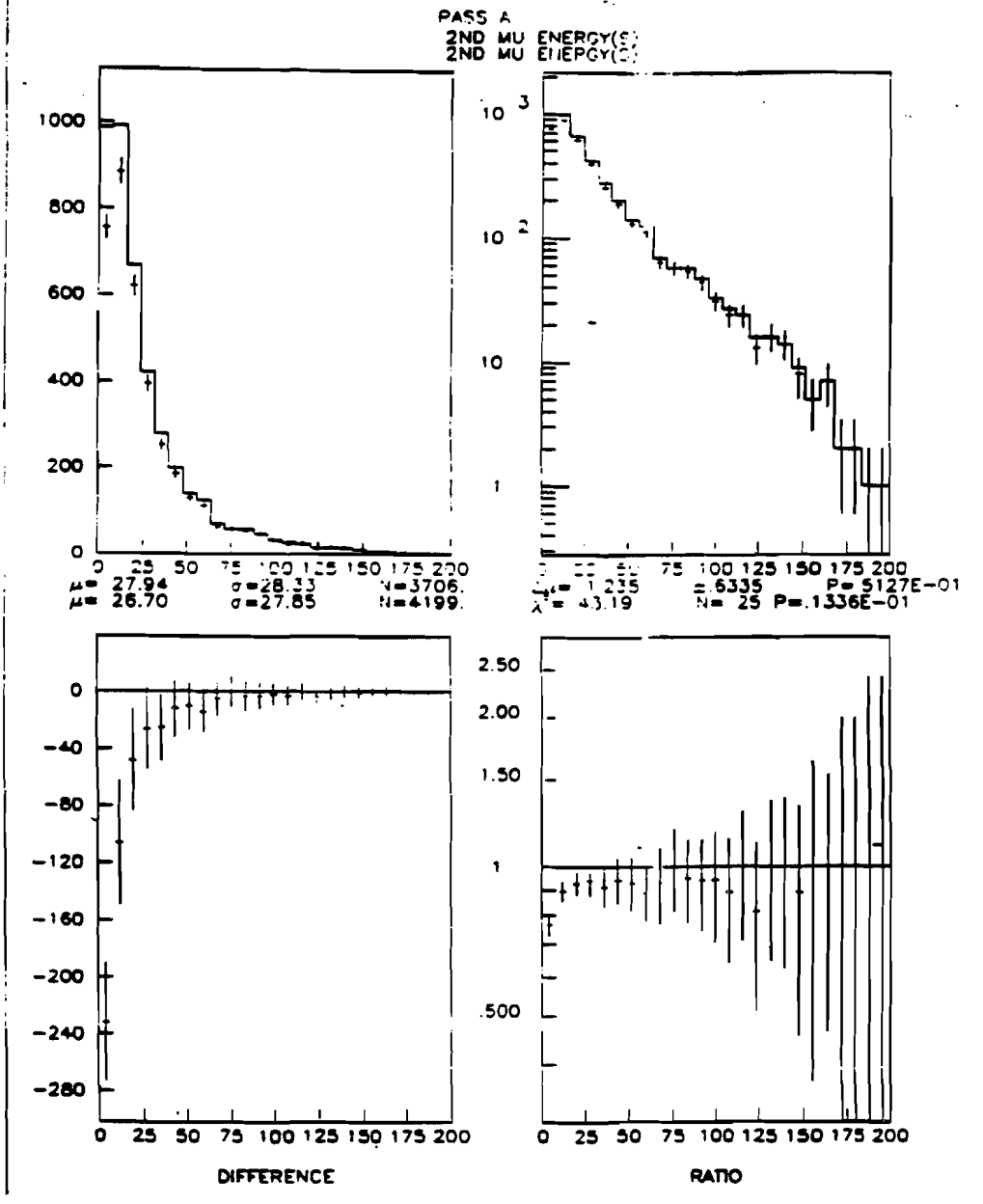

Fig.A.17. Second muon energy (in GeV) after Pass A compared with the original MC events.

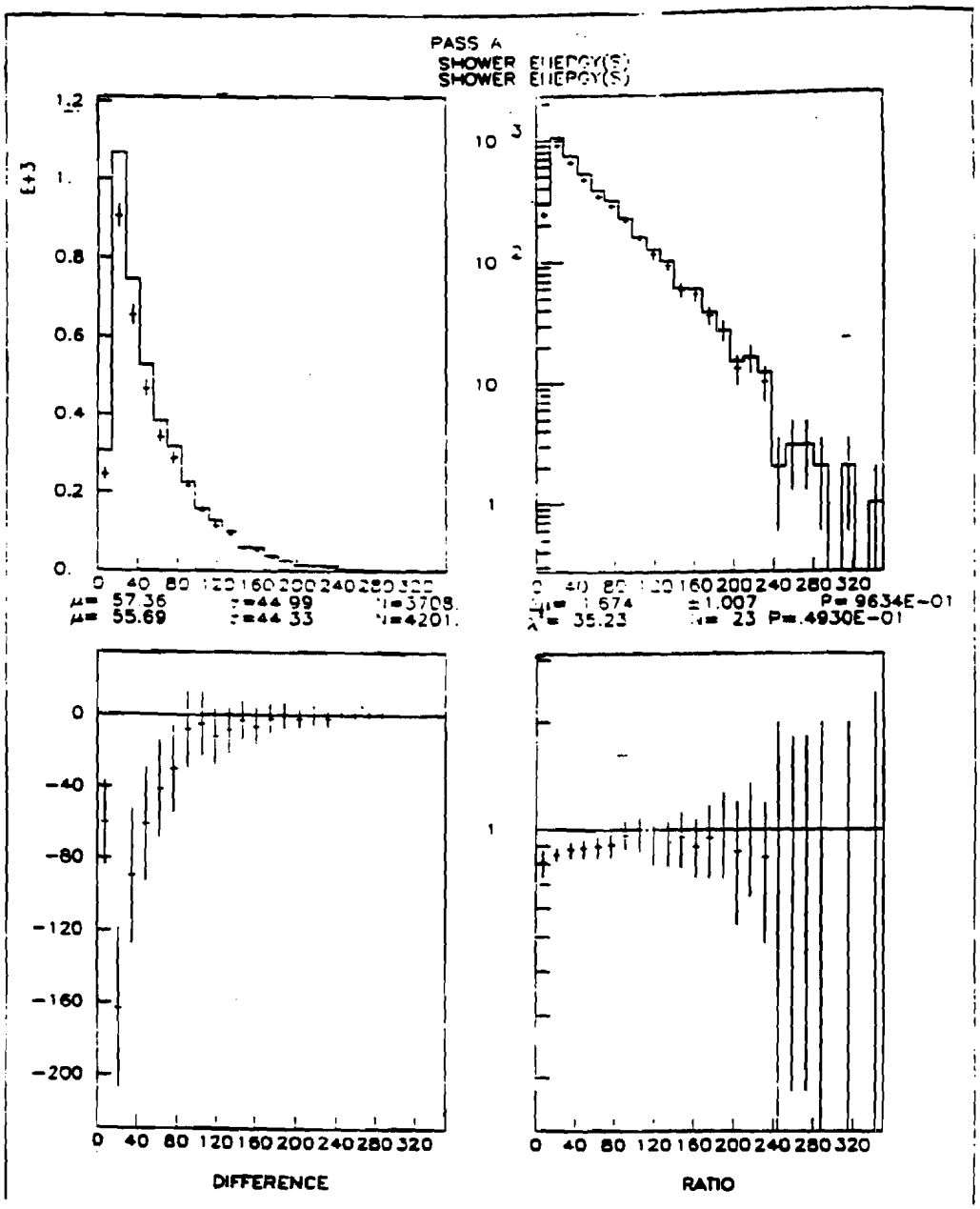

Fig.A.18. Shower energy (in GeV) after Pass A compared with the original MC events.

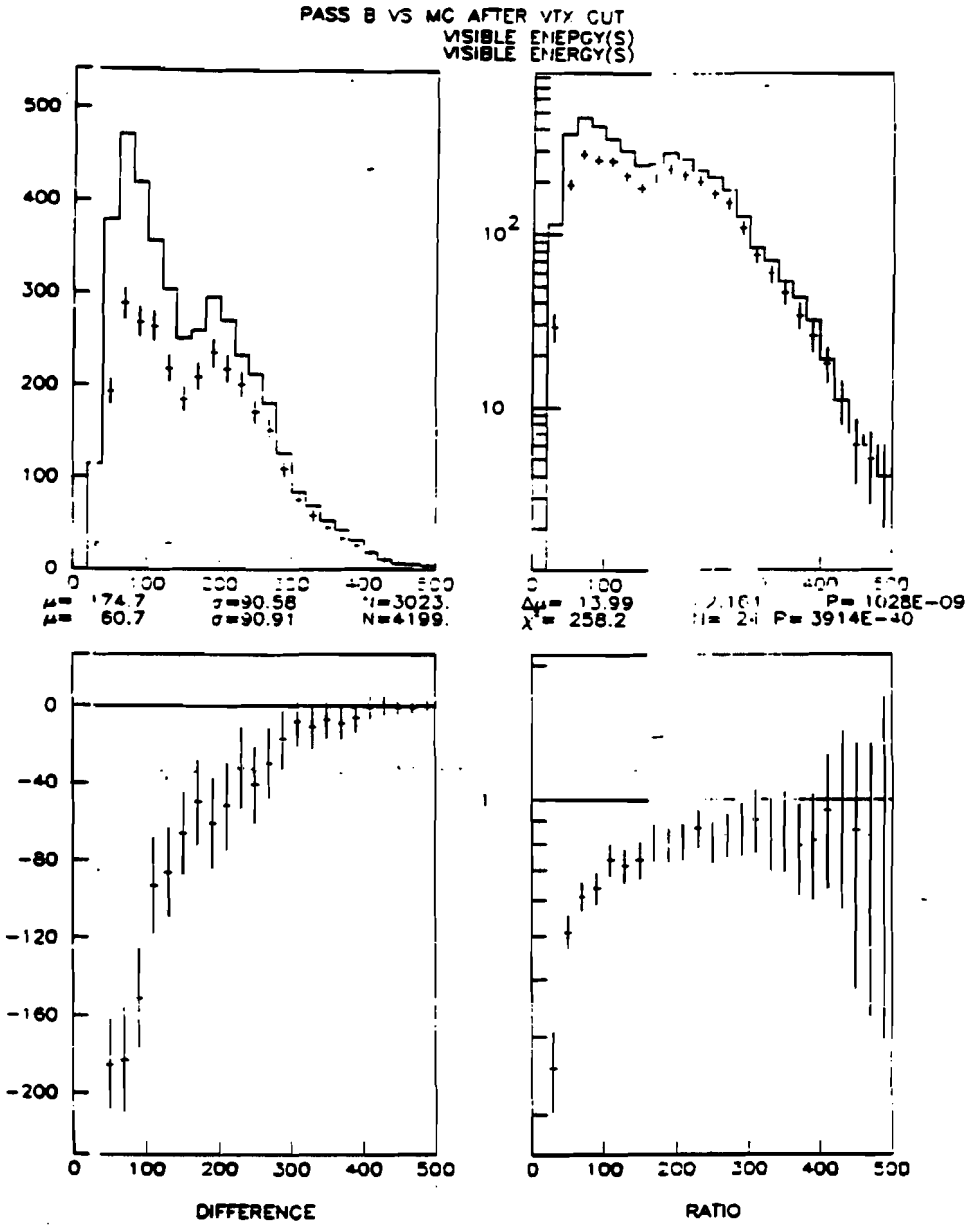

Fig.A.19. Visible energy (in GeV) after Pass B compared with the original MC events.

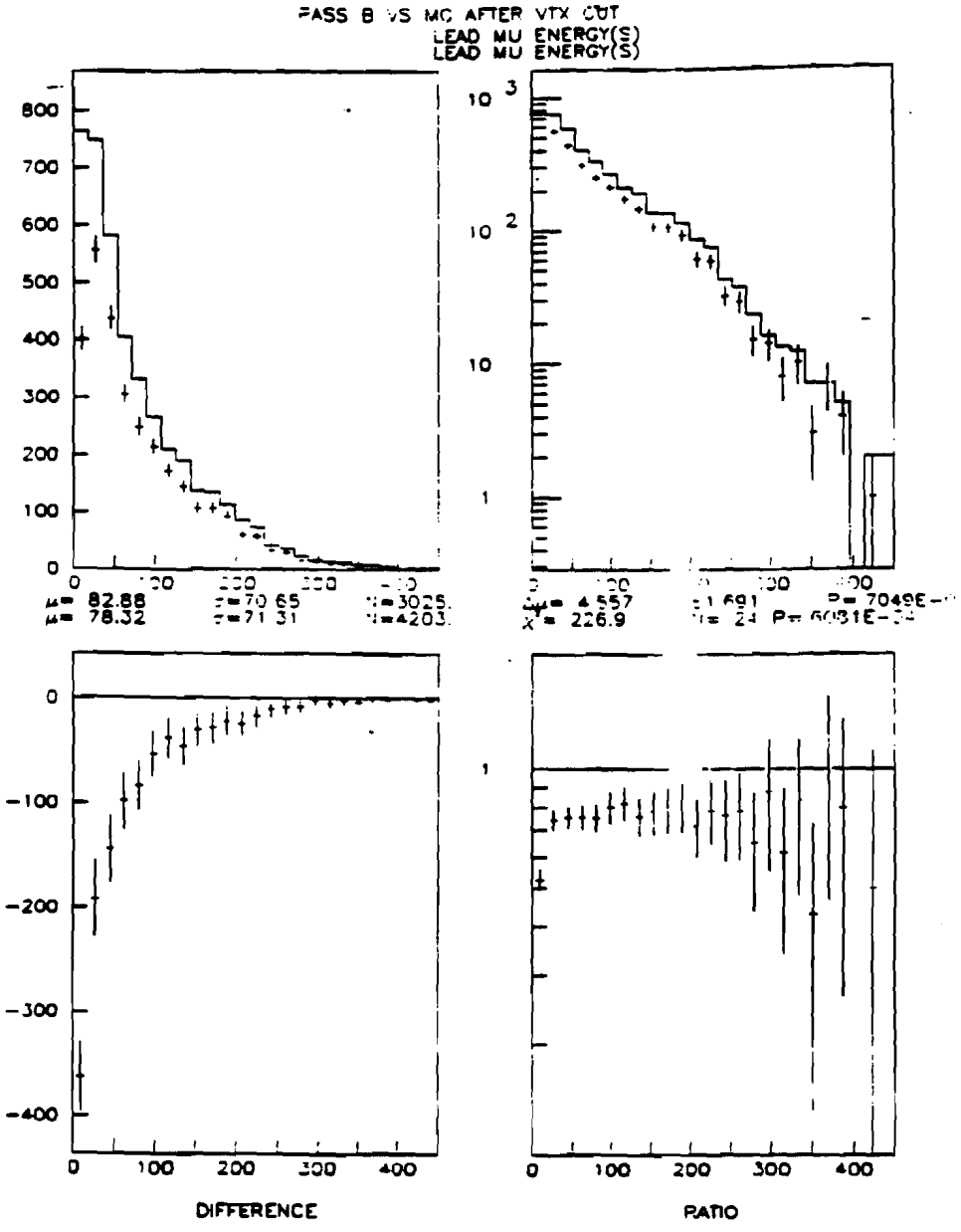

Fig.A.20. Leading muon energy (in GeV) after Pass B compared with the original MC events.

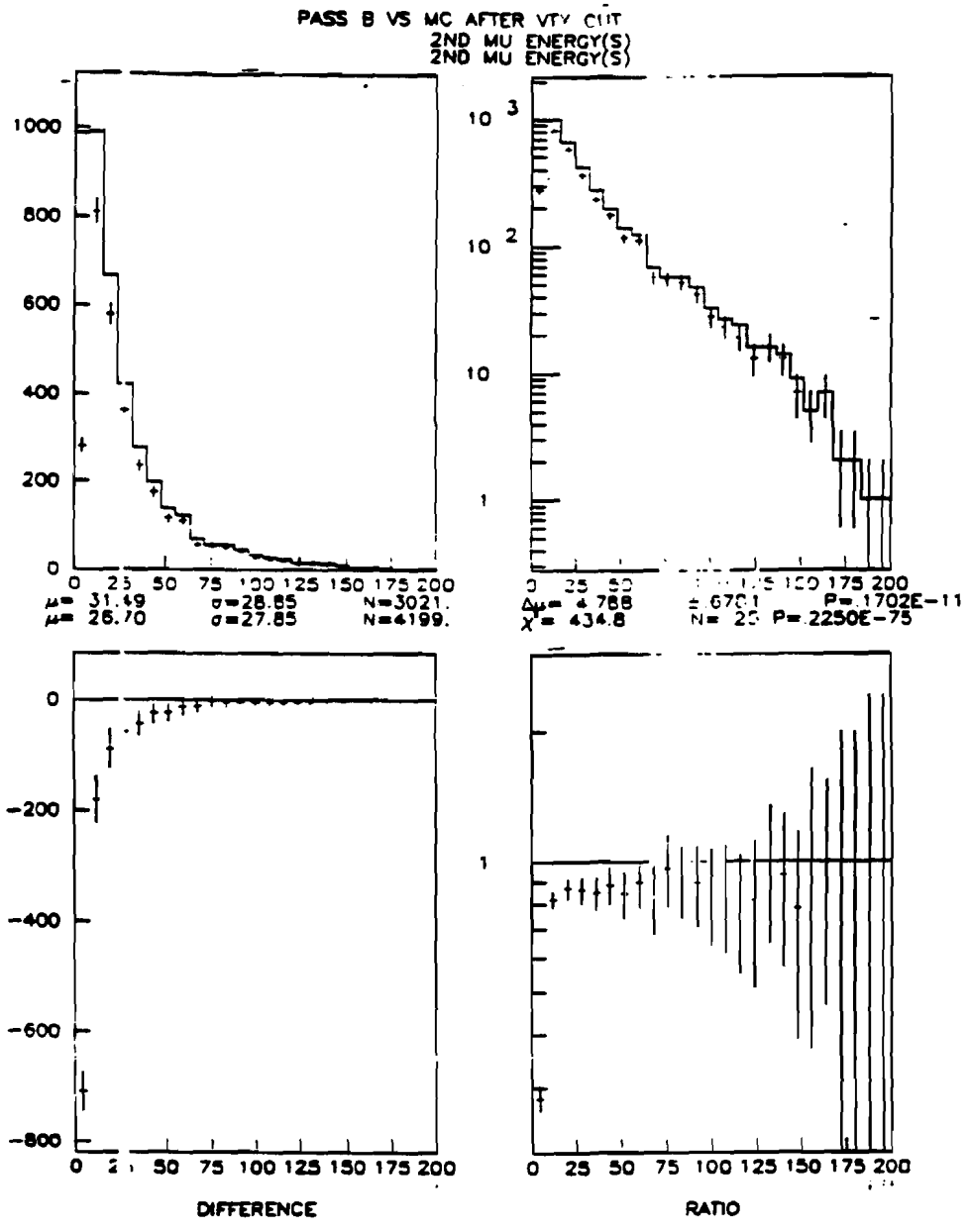

Fig.A.21. Second muon energy (in GeV) after Pass B compared with the original MC events.

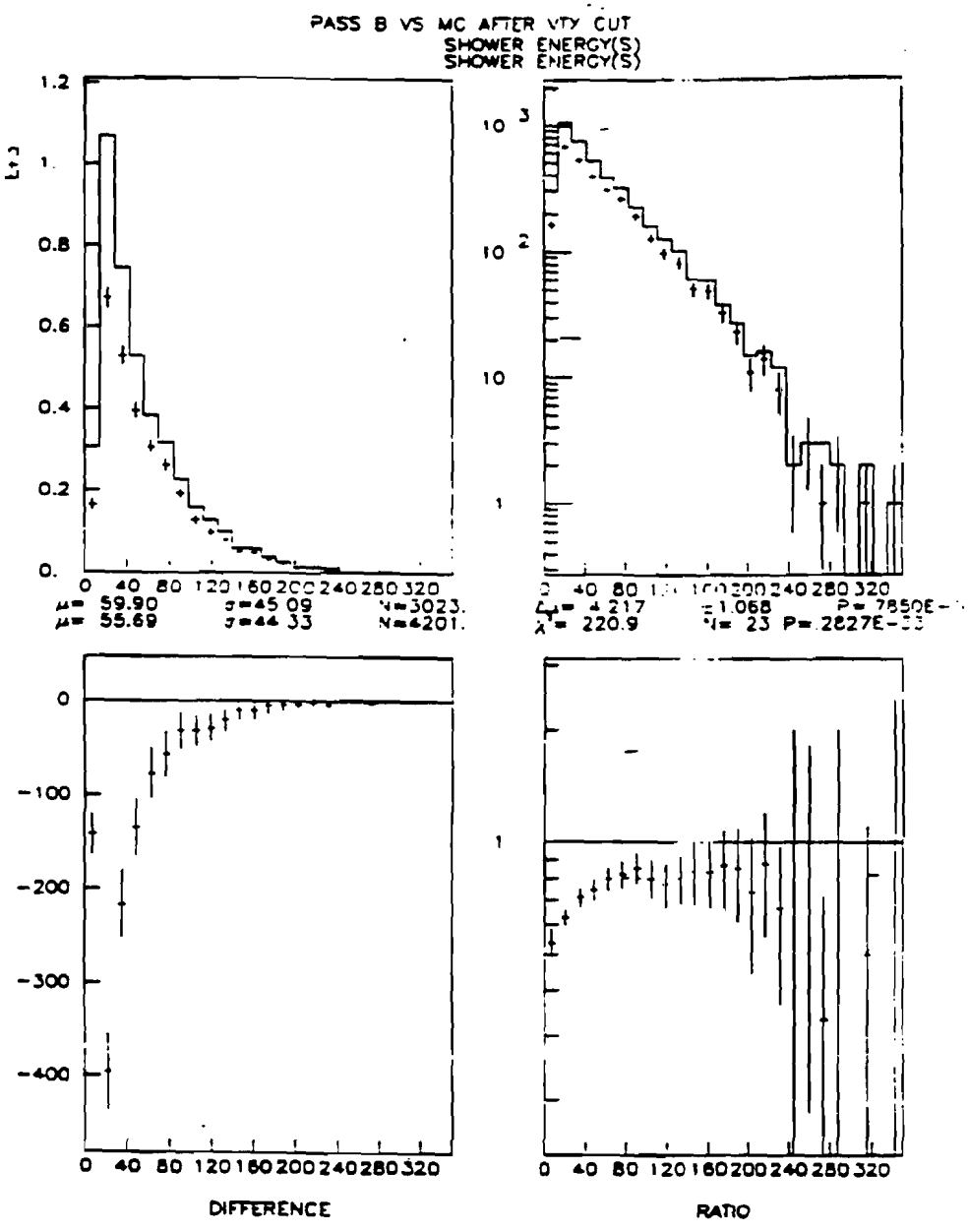

Fig.A.22. Shower energy (in GeV) after Pass B compared with the original MC events.

References.

1.1. Aubert , et al., Proc. XIV Int. Conf. on High Energy Physics, London 1974.

1.2. S. Glashow, J.Iliopoulos, L.Maiani, Phys. Rev. D2,1285 (1970).

1.3. V.Barger, T.Weiler, R.Phillips, University of Wisconsin preprint, COO-881459 (1975).

1.4. A.DeRujula, H.Georgi. S. Glashow, Phys. Rev. Lett. 35, 69(1975).

1.5. R.Turlay, Neutrino Physics, CERN Preprint DPhPE 83-16, November 1983.

1.6. See for example R. Barnett, Phys. Rev. Lett. 36, 1163(1976).

1.7. M.Kobayashi and T.Maskawa, Prog. Theor. Phys. 49, 652 (1973).

1.8. See for example C. Quigg, Gauge Theories of the Strong, Weak and Electromagnetic Interactions, The Benjamin/Cummings Publishing Company 1983.

1.9. H.Georgi and H.Politzer, Phys. Rev. D 9, 416 (1974).

1.10. D.Gross and F.Wilczek, Phys. Rev. D 9, 980 (1974).

1.11. G.Altarelli and G.Parisi, Nucl. Phys., B 126, 298 (1977).

1.12. D.Duke and J.Owens, Phys. Rev. D 27, 508 (1984).

1.13. E.Eichten, I.Hinchliffe, K.Lane, C.Quigg, Reviews of Modern Physics, Vol 56, No.4 (1984), p.579 - 708.

1.14. E.Eichten, Theoretical Expectations at Collider Energies, Fermilab-Conf-85/178-T, 1986.

1.15. E.Eichten, private communication, February 1989.

1.16. H.Abramowitcz, et al., Z.Phys. C 13, 199 (1982).

1.17. H.Abramowicz, et al., Z.Phys., C 17, 283 (1983)

2.1. NCenter Wide Band Neutrino Beam, L.Stutte, Fermilab Technical Memo TM-1305.

2.2. Comparison of Charged Current and Neutral Current structure Functions, T.Mattison, Ph.D. thesis, M.I.T. 1986.

3.1. A. Mukherjee, Azimuthal Energy Flow in Deep Inelastic Neutrino Scattering, Ph.D. thesis, M.I.T. 1986.

4.1."NUADA, the Fermilab Neutrino Flux Program", D.Carey and V.White, 1975.

4.2. NCenter Wide Band Neutrino Beam, L.Stutte, Fermilab Technical Memo TM-1305

4.3. [ref to MC rejection method]

4.4. D.Duke and J.Owens, Phys. Rev. D30, 49, 1984.

4.5. A. Sirlin and W.Marciano, Nucl Phys. B189 (1981).

C.Llewellyn-Smith and J.Wheater, Phys. Lett. 105B 486 (1981).

A.De Rujula, R. Petronzio and A. Savoy-Navarro, Nucl. Phys. B154 394 (1979)

4.6. T.Mattison, Comparison of Charged and Neutral Current Structure Functions, Ph.D. Thesis, M.I.T., 1986.

4.7. C.Petersen et al., Phys. Rev. D27, 105 (1983).

4.8. K. Kleinknecht and R. Renk, Z.Phys. C17, 325 (1983)

4.9. M. Aguilar-Benitez et al., Phys. Lett. 123B, 98 (1984).

M. Aguilar-Benitez et al., Phys. Lett. 123B, 103 (1984)

4.10. D. Coffman, The Properties of Semileptonic Decays of Charmed Mesons, Ph.D Thesis, Caltech 1987.

4.11. V.Barger and R.J.N.Phillips, Phys. Rev. D14, 80 (1976).

5.1. T. Sjostrand, Computer Physics Communications 27 (1932), p.243.

5.2.S.P. Denisov et al, Nuclear Physics B61 (1973) 62-76.

5.3.J.C. Allaby et al, Soviet Journal of Nuclear Physics, vol 13, p.295-304.

5.4.. U. Schneekloth and M. Tartaglia, E733 Memo 88-4.

5.5. K.Lang, "An Experimental Study of Dimuons Produced in High Energy Neutrino Interactions" , Ph.D. thesis, University of Rochester, 1985.

5.6. H. Abramowicz et al, "Experimental Study of Opposite-Sign Dimuon Produced in Neutrino and Antineutrino Interactions", CERN-EP/82-77.

5.7. De Groot et al., Phys. Lett. 86b, 103 (1979).

5.8. B.Schumm,"Like Sign Dimuon Production In High Energy Neutrino Interactions", Ph.D. thesis,University of Chicago, 1988.

5.9. W. Smith, "Review of Multilepton Production", WISC-EX-88-295, Talk presented at the Neutrino-88 Conference in Boston, MA.

5.10. A. Malensek, "empirical Formula for Thick Target Production", Fermilab Report FN-341, 1981.

6.1. R.Abramowitcz et al., Experimental Study of Opposite-Sign Dimuons Produced in Neutrino and Antineutrino Interactions, CERN-EP/82-77, June 1982.

6.2. K.Lang, An Experimental Study of Dimuons Produced in High Energy Neutrino Interactions, Ph.D. Thesis, University of Rochester, 1985.

6.3. F.James., Function Minimization, Proceedings of the 1972 CERN Computing and Data Processing School, Pertisau, Austria, 1972 (CERN 72-21).

6.4. C.Foudas, et al., Neutrino Production of Charm at FNAL E744, Fermilab-Conf-88/160-E.

6.5. C.Peterson et al.,Phys. Rev. D27, 105 (1983).

6.6. R.M. Baltrusaitis et al.,Phys. Rev. Lett. 54, 1976 (1985).

6.7. M. Aguilar-Benitez et al.,Phys. Lett. 123B, 103 (1983).